

Fluidic Devices for Realizing the Shockless Explosion Combustion Process

vorgelegt von
Dipl.-Ing. Bernhard Christian Bobusch
geboren in Berlin

von der Fakultät V — Verkehrs- und Maschinensysteme
der Technischen Universität Berlin
zur Erlangung des akademischen Grades

Doktor der Ingenieurwissenschaften
— Dr.-Ing. —

genehmigte Dissertation

Promotionsausschuss:

Vorsitzender: Prof. Dr.-Ing. R. Liebich (Technische Universität Berlin)
Gutachter: Prof. Dr.-Ing. C. O. Paschereit (Technische Universität Berlin)
Prof. Dr.-Ing. R. Klein (Freie Universität Berlin)
Dr. R. Wozidlo (The University of Kansas)

Tag der wissenschaftlichen Aussprache: 21.01.2015

Berlin 2015

D 83

Vorwort

Die vorliegende Dissertation entstand während meiner Tätigkeit als wissenschaftlicher Mitarbeiter am Fachgebiet für experimentelle Strömungsmechanik des Instituts für Strömungsmechanik und Technische Akustik im Rahmen des von der Deutschen Forschungsgemeinschaft geförderten Sonderforschungsbereiches 1029 “TurbIn - Signifikante Wirkungsgradsteigerung durch gezielte, interagierende Verbrennungs- und Strömungsinstationaritäten in Gasturbinen” an der Technischen Universität Berlin.

Mein besonderer Dank gilt meinem Doktorvater Prof. Dr.-Ing. Christian Oliver Paschereit sowie meinen Gutachtern Prof. Dr.-Ing. Rupert Klein und Dr. René Wozidlo für das mir entgegengebrachte Vertrauen, die Unterstützung, Betreuung und die große Freiheit, die mir im Rahmen meiner Tätigkeit als wissenschaftlicher Mitarbeiter ermöglicht wurde. Prof. Dr.-Ing. Robert Liebich danke ich für die Übernahme des Prüfungsvorsitzes.

Meinem Kollegen Phillip Berndt danke ich für die großartige, unkomplizierte, effiziente und immer sehr spaßige Zusammenarbeit in unserem Projekt zur SEC. Auch Joshua Gray gebührt hier großer Dank für die grandiose Zusammenarbeit zwischen den entsprechenden Teilprojekten. Speziell diesen Beiden aber auch allen anderen Kollegen des SFB verdanke ich viele schöne Zeiten und ein stark von Freundschaft und Kollegialität geprägtes Arbeiten im Rahmen des SFB 1029, wofür ich sehr dankbar bin. An dieser Stelle danke ich auch Prof. Dr.-Ing. habil. Rudibert King als hervorragendem Sprecher des besagten SFB.

Doch auch abseits des SFB im Fachbereich für experimentelle Strömungsmechanik habe ich meine Zeit als wissenschaftlicher Mitarbeiter aufgrund des hervorragenden Teams sowie der stets motivierenden und ausgeglichenen Atmosphäre sehr genossen. Ich bedanke mich bei allen Kollegen (und inzwischen auch Freunden), die mich in dieser Zeit begleitet, unterstützt und gefordert haben. Ein besonderer Dank gilt hier den drei Kollegen, die mich seit meinem ersten Tag als wissenschaftlicher Mitarbeiter als Bürogemeinschaft im CONFET begleitet haben. Bernhard Ćosić, Oliver Krüger und Steffen Terhaar haben mich über die Jahre nicht nur immer wieder motiviert und meine berüchtigte “Laborlaune” ertragen. Durch die stets angeregten, offenen und teilweise kontroversen Diskussionen sowie die weltweit einzigartige Zusammensetzung und Verteilung der persönlichen Fähigkeiten entstanden außerdem viele neue Ideen für Projekte, Veröffentlichungen und Herangehensweisen, die diese Bürogemeinschaft für mich einzigartig gemacht haben. Danke dafür!

Ein sehr großes Dankeschön möchte ich gerne auch den vielen, vielen helfenden Händen, die mit ihrem täglichen Einsatz die Forschung am Fachgebiet für experimentelle Strömungsmechanik auf ihrem hohen Niveau ermöglichen, aussprechen. Hierbei meine ich speziell Robert Bahnweg, Andy Göhrs und Heiko Stolpe, die durch ihre unkomplizierte, kompetente, hilfsbereite und immer motivierende Art so manche Messkampagne gerettet haben. Aber auch allen anderen Werkstatt-, Elektronik-,

Sekretariats- und IT-Mitarbeitern, die aufzuzählen den Rahmen dieser Danksagung sprengen würde, bin ich zu tiefstem Dank verpflichtet.

Neben den Arbeitskollegen danke ich auch der wichtigsten Person in meinem Leben, meiner Verlobten (und hoffentlich bald Frau) Chrischani Perera. Deine Unterstützung, Dein Verständnis und auch Dein unerschütterlicher Glaube an mich haben die Entstehung dieser Arbeit auch in den anstrengendsten Zeiten zu etwas Schönerem gemacht. Ich hoffe, dass ich Dir bei der Erstellung Deiner Dissertation in den kommenden Monaten den Rücken auch nur annähernd so frei halten kann wie Du es für mich getan hast. Vielen, vielen Dank!

Meiner Familie, speziell meinem Bruder und meinen Eltern, möchte ich an dieser Stelle auch herzlichst für die Unterstützung und das Verständnis, gerade in den letzten Monaten vor Abgabe diese Arbeit, danken. Das Wissen, dass ich mich immer auf euch verlassen kann hat mir sehr geholfen.

Bernhard Christian Bobusch

Berlin, im Februar 2015

Zusammenfassung

Die Entwicklung einer effizienten, ressourcenschonenden und damit kostengünstigen Stromerzeugung treibt seit bereits mehr als 100 Jahren die Forschung an. Gerade im Bereich der Gasturbinen werden immer größere Anstrengungen unternommen, um den Wirkungsgrad der Energieumwandlung weiter zu erhöhen. Hierfür verspricht die Gleichraumverbrennung eine enorme Wirkungsgradsteigerung. Die bisher vorgeschlagenen Prozesse der Gleichraumverbrennung haben jedoch einige Nachteile. Der neue und innovative Prozess der Stoßfreien Explosionsverbrennung (Shockless Explosion Combustion, SEC) umgeht einiger dieser Nachteile durch eine innovative Prozessführung. Neben den enormen Vorteilen bringt dieser Prozess aber auch einige Herausforderungen mit sich, die mit traditionellen Bauteilen nicht realisierbar sind. Fluidische Bauteile bieten hierfür enormes Potential, da sie robust sind, ohne bewegliche Teile auskommen und somit eine nahezu unbegrenzte Lebensdauer aufweisen. Außerdem sind diese Bauteile in der Lage, Strömungen mit sehr hohen Temperaturen und Frequenzen zu steuern und zu kontrollieren.

In der vorliegenden Arbeit wird der neue Verbrennungsprozess der Stoßfreien Explosionsverbrennung im Detail vorgestellt. Außerdem werden die Vorteile und die Herausforderungen dieses innovativen Verbrennungskonzepts dargelegt und mit den bereits bekannten Konzepten verglichen. Der Kern dieser Arbeit ist die Entwicklung von drei fluidischen Bauteilen, die den Prozess der Stoßfreien Explosionsverbrennung ermöglichen. Getrieben von den größten Herausforderungen des neuen Verbrennungskonzepts, nämlich: Sehr gute Mischung von Luft und Brennstoff, Strömungsgleichrichtung am Einlass des Verbrennungsrohres sowie die Reflektion der für den Prozess benötigten Druck- und Saugwellen werden fluidische Bauteile experimentell und numerisch untersucht. Für die Verbesserung der Luft-Brennstoff-Vermischung werden fluidische Oszillatoren eingesetzt. Die in dieser Arbeit vorgestellte detaillierte experimentelle und numerische Untersuchung des eingesetzten Oszillators erklärt den zu Grunde liegenden Oszillationsmechanismus und liefert die Sensitivität der Oszillation auf Veränderungen der Geometrie. Eine Untersuchung der Mischungsqualität zeigt die Überlegenheit dieses Eindüsungskonzepts für die SEC.

Für die Strömungsgleichrichtung am Einlass der Brennkammer wird im Rahmen dieser Arbeit eine fluidische Diode entwickelt und untersucht. Die spezielle Geometrie dieses Bauteils sorgt nicht nur für die Strömungsgleichrichtung, sondern auch für die nötige Reflektion der Saug- und Druckwellen innerhalb der Brennkammer.

Außerdem wird im Rahmen dieser Arbeit ein atmosphärischer Prüfstand für die Untersuchung der dem Prozess zu Grunde liegenden Selbstzündung entwickelt. Aufgrund der langen Zündverzugszeiten bei atmosphärischem Druck, muss für diesen Prüfstand ein heißer Luftstrom in sehr kurzer Zeit zum Stillstand gebracht werden, während der elektrische Lufterhitzer weiter durchströmt werden muss. Zu diesem Zweck wird in dieser Arbeit ein fluidischer Schalter entwickelt und untersucht. Der Aufbau und die Inbetriebnahme des Prüfstandes zur Untersuchung von Selbstzündungsprozessen mit ersten Zündversuchen bilden den Abschluß dieser Arbeit.

Basierend auf den entwickelten Bauteilen und mit Hilfe des neuen Prüfstandes ist es möglich Selbstzündungsprozesse mit Hinblick auf die Stoßfreie Explosionsverbrennung schnell und effizient zu untersuchen. Das erarbeitete Verständnis der fluidischen Bauteile trägt außerdem zu einer schnelleren und effizienteren Auslegung dieser Bauteile bei und ermöglicht somit nicht nur den Prozess der Stoßfreien Explosionsverbrennung, sondern auch die Anpassung dieser Bauteile an andere Prozesse.

Abstract

The depletability of resources as well as the efficient and economic generation of electrical power is driving the scientific community since more than 100 years. Especially in the field of gas turbines, the efforts to even further increase the efficiency of such systems are tremendous. The constant volume combustion (CVC) is one possibility to create a step-change in the efficiency of gas turbine systems. By utilizing a completely new process it enables new possibilities for future optimizations. However, most of the known CVC processes imply significant drawbacks. In the presented thesis the new and innovative shockless explosion combustion (SEC) is introduced. Employing naturally occurring unsteady effects in the combustor it overcomes most of the detriments of known systems. The SEC process is shown and discussed in detail in the first sections of this thesis.

Even though the SEC avoids several drawbacks, new challenges arise from the SEC as well as it is making strict demands on the mixing quality and the flow rectification at the upstream end of the combustion tube. Due to the hot gases and the high frequencies involved in the SEC process, traditional parts are not able to fulfill these requirements for a sufficiently long time. However, fluidic devices are able to withstand the harsh environment of such a combustor and fulfill the requirements of the SEC. By abandoning any moving parts in their setup they provide a very high reliability at an almost infinite lifetime.

In the presented thesis three fluidic devices are developed and investigated to match the requirements of the SEC process. In order to create the necessary mixing quality of fuel and air fluidic oscillators are used. The presented detailed experimental and numerical investigation reveals the underlying oscillation mechanism and the influence of the main geometrical parameters on the overall performance of the device. A mixing investigation is subsequently showing the ability of the fluidic oscillator to fulfill the high demands on the mixing quality. For the challenge of the high-frequency flow rectification a fluidic diode is developed and investigated. It is shown that the device is able to create the required performance and to reflect the pressure and suction waves needed by the process.

Additionally, a test rig for the investigation of auto-ignition events is designed and developed. In order to investigate the ignition behavior of relevant fuels it is necessary to stop a high temperature stream of air within a very short time. Since no valve is able to withstand this temperature and fulfill this task, a fluidic switch is developed and investigated. This device is able to switch the hot main air flow between two separate flow paths in 7 ms. Combining all the developed devices in the new test rig the first ignition tests within this SEC ignition test rig are conducted and presented.

Based on the presented results and by employing the new test rig it is possible to investigate the auto-ignition behavior of relevant fuels flexibly and efficiently. The created deeper understanding of the different fluidic devices not only enables the SEC process but also allows for a faster and more efficient adaption of these devices to different tasks and applications.

Contents

1	Introduction	1
1.1	Background	4
1.1.1	Shockless Explosion Combustion Process and its Challenges .	5
1.1.2	Fluidic Devices and their History	11
1.1.3	Main Equations and Numerical Modeling of Turbulent Flow .	15
2	Fluidic Oscillator	25
2.1	State of the Art	25
2.2	Flow Inside and Function of a Fluidic Oscillator	29
2.2.1	Experimental Setup and Instrumentation	29
2.2.2	Data Analysis	31
2.2.3	Internal Flow and Underlying Mechanism	34
2.2.4	Numerical Confirmation of Oscillation Mechanism	43
2.3	Geometry Parameters Affecting the Oscillation Structures	44
2.3.1	Numerical Tools	44
2.3.2	Geometry Parameters	45
2.4	Mixing Enhancement in the SEC-Configuration	59
2.4.1	Experimental Setup	61
2.4.2	Experimental Results	66
2.5	Intermediate Conclusion	75
3	Fluidic Diode	79
3.1	State of the Art	80
3.2	Design of the Diode	84
3.3	Steady Investigation	87
3.3.1	Experimental Setup	87
3.3.2	Assessment of the Diodicity	90
3.3.3	Steady Flow Field and Validation of the Numerical Model . .	92
3.4	Transient Investigation	96
3.4.1	Computational Domain and Boundary Conditions	96
3.4.2	Flow Field During Ignition and Blow Down	99

3.5	Intermediate Conclusion	105
4	Fluidic Switch	109
4.1	State of the Art	109
4.2	Geometric Design	112
4.3	Investigation of the Switching Process	116
4.3.1	Experimental Investigation	116
4.3.2	Numerical Investigation	121
4.4	Intermediate Conclusion	129
5	Shockless Explosion Combustion Ignition	131
5.1	The Shockless Explosion Combustion Test Rig	131
5.2	Fuel Injection Curves and Timings	136
5.2.1	Fuel Injection Curve	136
5.2.2	Fuel Valve Response	139
5.2.3	Timing of Test Rig Control Signals	142
5.3	Ignition Investigations	145
5.3.1	Ignition Characteristics	145
5.3.2	Performance of the Fluidic Devices	150
5.4	Intermediate Conclusion	154
6	Concluding Remarks	157
	Bibliography	159

List of Figures

1.1	SEC -Process	7
1.2	Fluidic divider	12
1.3	COANDA-Effect	13
1.4	Bistable switch	13
1.5	Fluid Oscillator by Warren (1962)	14
1.6	Tesla diode	15
1.7	Scroll diode	15
2.1	Different types of fluidic oscillators	27
2.2	Sketch of the used oscillator	28
2.3	Sketch of experimental setup	30
2.4	Oscillator geometry and pressure tabs	31
2.5	Energy of POD modes	33
2.6	POD modes	33
2.7	Phase portrait of POD modal amplitudes	34
2.8	Dominant oscillation frequency vs. Reynolds number.	35
2.9	Fluidic glossary	36
2.10	Flow field inside the fluidic oscillator	37
2.11	Feedback channel mass flow	38
2.12	Pressure time traces	40
2.13	Mass flow fluctuations	41
2.14	Feedback channel mass flows	44
2.15	Setup of the different outlet geometries.	46
2.16	Velocity distribution for different outlets	47
2.17	Vorticity in the outlet region	48
2.18	Pressure and pressure loss time traces	49
2.19	Geometrical setup for the different inlet wedges distances.	50
2.20	Mass transport through the feedback channels	51
2.21	Minimum recirculation bubble size	51
2.22	Geometric setups of the different outlet nozzles.	52
2.23	Velocity magnitude at the outlet nozzle.	53

2.24	Pressure distribution around the outlet nozzle	54
2.25	Geometries of the different feedback channels.	56
2.26	Pressure loss across the feedback channel	56
2.27	Frequencies for different aspect ratios	58
2.28	Sketch of the test rig.	61
2.29	Cut through the fuel inlet	62
2.30	Injection disk models	63
2.31	Time averaged concentrations	67
2.32	Spatial unmixedness parameter	68
2.33	Ranges of spatial unmixedness parameter	70
2.34	Spatial unmixedness parameter for the rectangular orifices	71
2.35	Frequency ranges of the fluidic oscillators	72
2.36	Spatial unmixedness parameter for the fluidic oscillators	73
2.37	Spatial unmixedness of rectangular orifices and fluidic oscillators	75
3.1	Tesla diode	80
3.2	Vortex diode	81
3.3	Cascade diode	82
3.4	Scroll diode	83
3.5	Proposed fluidic diode inlet section (isometric)	85
3.6	Proposed fluidic diode inlet section (cut)	86
3.7	Test rig for fluidic diode	88
3.8	Setup of the experimental investigation	88
3.9	Pressure loss coefficient of the fluidic diode	91
3.10	Diodicity of the fluidic diode	91
3.11	Computational domain for the steady investigation	93
3.12	Flow field comparison in forward direction	94
3.13	Flow field comparison in backward direction	95
3.14	Velocity profiles of the fluidic diode	96
3.15	Computational Domain for the transient investigation	97
3.16	Pressure time trace of ignition	98
3.17	Transient flow field of the fluidic diode (first part)	100
3.18	Transient flow field of the fluidic diode (second part)	103
4.1	Sketch of a fluidic amplifier	110
4.2	Examples of fluidic amplifiers	111
4.3	Parameters of the bistable fluidic amplifier	112
4.4	Geometry of fluidic switch (rendered)	113
4.5	Geometry of fluidic switch (drawing)	114
4.6	Photograph of the fluidic switch	115
4.7	Experimental setup of switching tests	118
4.8	Example measurement of switching process	119

4.9	Limits of switching	120
4.10	Limits of switching against momentum	121
4.11	Control velocity time trace	122
4.12	Overview on the computational grid	123
4.13	Initial state of fluidic switch	124
4.14	Initial state of fluidic switch (pressure distribution)	125
4.15	Internal states of the switching process	127
4.16	Final state of fluidic switch	128
5.1	Sketch of the developed test rig	132
5.2	Measurement section of test rig	134
5.3	Photograph of the test rig	134
5.4	Photograph of the test rig in upstream direction	135
5.5	Ignition time delay of DME in air	137
5.6	Ignition time delay of DME in air at 739 K	138
5.7	Target fuel and Φ curve	139
5.8	Valve response to pulse	140
5.9	Valve response to pulse (start up)	141
5.10	Valve response to ramp	142
5.11	Flow paths in the test rig	143
5.12	Control signal timings	144
5.13	Category 1 ignition	146
5.14	Category 2 ignition	147
5.15	Category 3 ignition	148
5.16	Pressure time trace during switching	151
5.17	Axial shifting of the fresh charge	153

List of Tables

1.1	SEC combustor parameters	8
2.1	Flow rates and Reynolds numbers	35
2.2	Investigated aspect ratios	57
2.3	Injector geometries	64
3.1	Investigated flow rates of the diode	89
3.2	Operating conditions of pressure measurement	90
4.1	Operating conditions of fluidic switch	117
5.1	Influence of fuel injection duration	149
5.2	Influence of switching time delay	150

List of Acronyms

CAD	<u>C</u> omputer <u>A</u> ided <u>D</u> esign
CFD	<u>C</u> omputational <u>F</u> luid <u>D</u> ynamics
CVC	<u>C</u> onstant <u>V</u> olume <u>C</u> ombustion
DDT	<u>D</u> eflagration to <u>D</u> etonation <u>T</u> ransition
DME	<u>D</u> imethylether
DNS	<u>D</u> irect <u>N</u> umerical <u>S</u> imulation
FFT	<u>F</u> ast <u>F</u> ourier <u>T</u> ransform
JDA	<u>J</u> et <u>D</u> eflection <u>A</u> ngle
NTC	<u>N</u> egative <u>T</u> emperature <u>C</u> oefficient
PDC	<u>P</u> ulsed <u>D</u> etonation <u>C</u> ombustion
PIV	<u>P</u> article <u>I</u> mage <u>V</u> elocimetry
PLIF	<u>P</u> lanar <u>L</u> aser <u>I</u> nduced <u>F</u> luorescence
PMT	<u>P</u> hotomultiplier <u>T</u> ube
POD	<u>P</u> roper <u>O</u> rthogonal <u>D</u> ecomposition
RANS	<u>R</u> eynolds <u>A</u> veraged <u>N</u> avier- <u>S</u> tokes
SEC	<u>S</u> hockless <u>E</u> xplosion <u>C</u> ombustion
SST	<u>S</u> hear <u>S</u> tress <u>T</u> ransport

Nomenclature

C	dye concentration
J	jet in cross flow momentum
R	ideal gas constant in J/molK
Re	Reynolds number
S_{ij}	strain rate tensor
St	Strouhal number
T	Temperature in K
T_{osc}	period time in s
U	Voltage in V
U_t	total unmixedness parameter
U_x	spatial unmixedness parameter
X	mass fraction
a_i	modal amplitudes of the POD
d_h	hydraulic diameter in mm
f	frequency in Hz
f_i	body forces in N
k	turbulent kinetic energy in m^2/s^2
l_{tube}	length of the combustion tube in m
p	pressure in kg/ms^2

t	time in s
u_i	velocity vector in m/s
x_i	spatial coordinate vector in m
Φ	equivalence ratio
$\Phi_i(\vec{x})$	spatial modes of the POD
Θ	diodicity coefficient of a fluidic diode
δ_{ij}	Kronecker-delta
ε	eddy dissipation rate k in m^2/s^2
η'	bulk viscosity in $\text{kg}/\text{m s}$
η	dynamic viscosity in $\text{kg}/\text{m s}$
κ	adiabatic index
λ_i	eigenvalues of the POD
μ_t	eddy viscosity as defined by BOUSSINESQ in $\text{kg}/\text{m s}$
ν	kinematic viscosity in m^2/s
ω	characteristic frequency of the energy dissipating eddies
φ	phase angle of the PIV snapshots in deg
π_{ij}	total stress tensor
ρ	density in kg/m^3
σ	variance
τ_{ign}	ignition delay time in s
τ'_{ij}	Reynolds stress tensor in $\text{kg}/\text{m s}^2$
τ_{ij}	viscosity tensor in $\text{kg}/\text{m s}^2$
ξ	Residual in POD -formulation
ζ	pressure loss coefficient
$(...)'$	fluctuations of value
$(...)_{i/j}$	coordinate indexes
$\overline{(...)}$	mean value

CHAPTER 1

Introduction

The idea of a modern gas turbine system dates back to the year 1791 in which John Barber claimed a patent [9] that basically describes the idea and function of a gas turbine system:

“It consists of a metallic vessel called a retort, so contrived that (when heated by a circumambient fire) coal, wood, oil or any other combustible matter may be put therein, and the smoke or vapor therein collected may be brought out by a small pipe, and conveyed in a regular stream into another metallic vessel called an exploder, by means of an air pump and a compressor or regulating bellows, which pipe opposing its orifice to another similar pipe which enters the exploder (on the opposite side from the pipe which brings in the inflammable vapour from the retort) and injects by similar means a proper quantity of atmospheric or common air, causing an admixture of the two airs, which, so mixed, will take fire on application of a match or candle to the mouth of the exploder, and rush out with great rapidity in one continued stream of fire, so long as the exploder is supplied with proper quantities of the respective airs. The fluid stream is also considerably augmented both in quantity and velocity by water injected into the exploder by means of another small pipe entering therein, which water is also intended to prevent the inward pipes and the mouth of the exploder for melting by the velocity and intensesness of the issuing flame. This water, as well as the airs, are forced into the exploder by means of a pump, which in lieu of common crank carries upon the axis of one of its wheels two esses or double portions of circles, whereby a more regular motion is procured than can be done by any crank work. This engine is wrought by the stream issuing from the mouth of the exploder, and may be applied to grinding, rolling, forging, spinning, and every other mechanical operation; and the fluid stream may be injected into furnaces for smelting metallic ores, or passed out at the stern of any ship, boat, barge, or other vessel, so as by an opposing and impelling power directed against the water carrying such vessel, the vessel with its contents may be driven in any direction whatsoever.” — JOHN BARBER 1791

Unfortunately, materials fulfilling the thermo-physical requirements were not available at that time and, thus, the system described by John Barber could not be built. The idea of the gas turbine to convert the chemical energy bond in the fuel to mechanical or electrical energy was incorporated again towards the end of the 19th century as better materials became available. In 1903 Jens William Ægidius Elling invented a compressor with an efficiency between 85% and 87% that allowed the construction of the first gas turbine producing net power. Due to the low efficiency of the compressor, the overall efficiency of the machine was very poor and, thus, his work received almost no consideration.

At the same time, Hans Holzwarth built the first constant volume combustion gas turbine in the year 1905 ([43]). The needed pressure for the turbine was created by the constant volume combustion in closed vessels and, thus, cut the need for the compressor. The efficiency of his gas turbine was around 13%. Since the beginning of the 20th century, research and development of energy conversion systems were driven by the depletability of resources, in this case fossil fuel, the negative consequences of the pollutant emissions from burning these fuels, and the high volatility of the fuel costs. Owing to the rapid increase in efficiency of the compressors and the lower complexity of a constant pressure combustion system, the industrial focus was shifted from constant volume combustion to constant pressure combustion gas turbines in the following years. Better materials, turbine blade cooling, high efficiency airfoils in the turbo-parts, and higher pressure ratios of the compressor led the way to higher efficiency in gas turbines. The development results in today's efficiencies of gas turbine systems of around 40% for single cycle application and slightly above 60% for combined cycle operation incorporating an additional steam cycle.

Nevertheless, the idea of the pressure gain combustion (i.e., constant volume combustion) remained in the focus of the scientific community. This non-steady combustion process was and is associated with higher efficiency, less emissions, and, due to the non-implicit need of compressor or turbine (in case of thrust generation), a very simple and economic configuration. This motivated the development and utilization of the first pulse jet engine, the ARGUS AS 014, as thrust generator for the FISELER FI 103 ("flying bomb") in Germany in the 1940s. This engine only consisted of a tube with mechanical one way valves to control the inflow, a fuel injection, and a spark plug for the startup of the system. The combustion in pulse jet engines is based on the acoustic resonance of the combustion tube. For startup the tube is filled with a combustible mixture, which is ignited using the spark plug. The combustion or "explosion" creates a pressure increase that pushes the combustion products out of the tube generating thrust. A mechanical one way valve prohibits that the reactants may exit the tube through the inlet. Due to the fast blow-down of the pressure pulse, the pressure in the tube decreases below the inlet pressure and, thus, sucks a fresh fuel-air mixture into the tube. In the tube it is ignited by either the spark plug (in the startup phase) or by the hot environment and residual gases from the previous cycle. Later on, valveless pulse jet concepts

were invented and investigated because mechanical valves limited the operational time of the engine to a maximum of around 60 min. Unfortunately, pulse jet engines had a poor fuel efficiency and very high emissions, which mainly stemmed from their lack of controllability as self-controlling systems.

Nonetheless, the expected increase in efficiency of a pressure gain, constant volume combustion is still one of the main advantages of such systems [17, 24, 48, 82, 105] and kept them in the focus of research all over the world. Heiser and Pratt reported a thermodynamic cycle analysis regarding the constant pressure, constant volume (CVC), and pulsed detonation combustion (PDC) in 2002 [41] for both the ideal and the real cycles. They conclude that the ideal PDC-cycle has a thermal cycle efficiency between 40% and 80% depending on the temperature ratio across the compressor. This increase in thermal efficiency makes constant volume combustion, in the mentioned study in the form of a PDC, very desirable for the gas turbine community. Several types of pressure gain combustors, suitable for a gas turbine system, were proposed and investigated in the last decades. Pulse combustors, pulse detonation engines, rotating detonation engines, and wave rotors are the main types of these devices¹.

In the present work the innovative shockless explosion combustion (SEC), a variant of constant volume combustion, is introduced. This process combines the advantages of a pulsed combustor (i.e., no shock waves) with a real constant volume combustion approach (e.g., PDC). The details of this new and innovative system will be discussed in Sec. 1.1.1. The main challenges arising by this process are the fast and reliable preparation of the fuel–air mixture and the opening and closing of the combustion tube inlet. In addition, the hot main air mass flow must be switched between two flow paths in the required combustion test rig. All mentioned tasks require the handling and fast controlling of large mass flows with very high temperatures, which cannot be achieved using traditional mechanical parts or existing techniques. The inherent robustness, cheapness and reliability of fluidic devices is promising to fulfill such requirements not only in the context of constant volume combustion systems. In this thesis special fluidic devices are developed and used to overcome the challenges in a test rig for the shockless explosion combustion

Fluidic devices were invented in the 1960 by the United States Military as a robust and easy way to control and steer rockets. Several of these devices, such as switches, diodes, triodes, amplifiers, oscillators, and so on exist, which are able to conduct simple analogue or digital tasks. Working with a fluid instead of electricity and omitting any moving parts, it was possible to create extremely robust systems that work similar to electronic circuits. The details of these devices can be found in Sec. 1.1.2. However, since the electronics massively improved in terms of robustness, cheapness, size, availability, and reliability the fluidic devices are not used to create

¹ The details, advantages and drawbacks of these combustion systems can be found in Sec. 1.1.1

calculating or controlling circuits any more. In the current work three of these devices and their unique features are adapted to overcome the challenges of preparing the fuel–air mixture (fluidic oscillator), represent the opening and closing of the combustion tube (fluidic diode) and switching high mass flows of hot air (fluidic switch). All of these devices are not only able to withstand the harsh environment of a test rig for a reasonable time, but are also robust enough to be used in industrial gas turbine systems regarding the required reliability, lifetime and maintenance intervals.

The contents of this thesis are separated into five chapters. In the current chapter (subsequent to this motivation) the background of the shockless explosion combustion process, the fluidic devices and the governing equations including the used numerical approaches provide an introduction to the topics of this thesis. Each of the subsequent chapters is dedicated to one of the used fluidic devices and their performance in the context of the SEC. In the second chapter the fluidic oscillator is presented and investigated by itself experimentally and numerically. In addition its ability to enhance the mixing quality in the given SEC inlet geometry is shown. The third chapter introduces the fluidic diode and the corresponding flow field, again, numerically and experimentally. The fourth chapter is dedicated to the fluidic switch that is needed in the SEC test rig to switch high mass flows of hot air. Finally, the presented devices are tested in the first ignition tests for the SEC giving the final approval of their efficiency in the context of a combustion test rig. This is presented in the fifth chapter.

1.1 Background

Prior to investigating the different fluidic devices and their suitability to overcome the challenges introduced by the shockless explosion combustion, an introduction to the SEC, the history of fluidic devices, and the general mathematical background including the numerical approaches are given in this section. Since the challenges regarding the SEC process are the primary motivation for the usage of fluidic devices, the details, advantages and disadvantages of the SEC will be presented in the first part of this section. Beginning from an overview of pressure rising combustion systems, it will be shown that the SEC implies several promising advantages, especially for the usage in gas turbines. This part is based on a publication from Bobusch *et al.* [14].

Subsequently, a historical overview on fluidic devices is presented. As the first fluidic devices date back to the 1960s a vast variety of different approaches, geometries and devices have been invented. A general overview on the background of these devices and the main underlying mechanisms will be shown together with the historical development arising from simple flow configurations.

The last part of this section is dedicated to the governing equations, characteristic dimensionless quantities and the numerical approach used in the investigations. Since the employed approaches are common in the field of flow dynamics only a

brief overview is given in this part. For further details the reader is referred to the literature cited.

Altogether this section is giving the background information needed for the understanding of the following chapters and the challenges, which arise from the SEC.

1.1.1 Shockless Explosion Combustion Process and its Challenges

Several approaches to realize a pressure gain combustion or a quasi-CVC-process in a gas turbine were proposed, developed and investigated in the last decades. Pulsed combustors, pulse detonation combustion, rotating detonation combustion, and wave rotors are the main types of these devices.

As stated in the introduction, pulsed combustion was the first technique to realize a pressure gain combustion. Starting in the 1940s several papers were published and patents claimed describing and investigating different ways of pulsed pressure gain combustion (e.g., [51–53, 66, 68, 70, 77, 80]). In 1986 Putnam *et al.* [77] published an overview on the work of several research groups on pulsed combustors. However, even though these systems create a pressure gain in the combustion chamber, they cannot be considered as constant volume combustion. In most of them a deflagration wave is responsible for the chemical reaction, which is slow enough to give the products of the chemical reaction enough time to expand while the flame is propagating through the mixture. Thus, the volume increases during the combustion process and no CVC is achieved.

An overview on the technique of PDC was published in 2004 by Roy *et al.* [81], whereas Wolański published an overview on the detonative propulsion in 2013 [106]. In a pulsed detonation combustor a detonation wave is responsible for the combustion of the fresh fuel–air mixture. Due to the very high velocity of the detonation wave (e.g., around 2000 m/s for hydrogen–air flames), the mixture is burnt quasi-instantaneously and the volume of the mixture does not change during the combustion process. However, the detonation wave is also responsible for drawbacks of this combustion system. First of all a reliable initiation of the detonation wave is a challenge itself. Since direct initiation of a detonation wave is extremely energy consuming, most of the PDC systems rely on the deflagration to detonation transition process (DDT). This process occurs when a deflagration wave is accelerated by regions of high turbulence in the flow (mostly generated by obstructions in the detonation tube) until finally a detonation wave occurs. Accordingly, the volume needed to accelerate the deflagration wave and create the detonation cannot be considered as constant volume combustion. In addition, the detonation wave causes a very strong and sharp pressure peak (i.e., shock wave), which is harmful for the turbine and other parts of the engine. Lastly, the detonation wave is accompanied by moving flow trailing the wave. The corresponding kinetic energy may not be fully converted to technical work by the turbine and, thus, might be lost.

In order to partly avoid the mentioned losses and the pulsed nature of the PDC-concept, the rotating detonation engine was suggested. An analysis on the respective engine concepts, their modeling, and the corresponding challenges was published by Lu *et al.* [63] in 2011. A continuous detonation wave is employed in this type of combustion system that travels around an annular chamber perpendicular to the main flow direction. The fresh fuel–air mixture is constantly injected into the combustion chamber to stabilize and maintain the detonation wave. This supply of fresh mixture presents the main challenge of these devices. Depending on the radius of the annular chamber and the speed of the detonation wave, the time for mixing the fuel and air is extremely short. In addition, these devices still employ a detonation wave implying a shock wave, including the losses associated with it. Since the shock wave is constantly traveling around the combustion chamber and, thus, into the turbine inlet, significant problems regarding the cooling of the blades and rotor may occur.

The fourth mentioned CVC-process is the wave rotor technology. In 2006 Akbari *et al.* [3] published an extensive review on the wave rotor technology and its applications including an overview on the historical development of this technique. In the wave rotor a mechanically closed chamber is employed to realize CVC. The wave rotor consists of a moving barrel of tubes in which the combustion process takes place without detonation or shock waves. Accordingly, the mentioned losses for the PDC are not present in these devices. However, the combustion tubes in the barrel need to be mechanically sealed on both ends during the combustion process. This seal is difficult to realize in gas turbines, especially regarding the maintenance intervals and lifetime of these systems. Additionally, the cooling of this moving barrel is a challenging task.

Following these points, the optimal pressure gain combustion system needs to fulfill the following points:

1. constant volume combustion,
2. without shock waves and the associated losses, and
3. no moving parts in the main air path.

The presented Shockless Explosion Combustion process (SEC) uses several physical properties of the fuel–air mixture to get close to this optimal pressure gain combustion and will be presented in the subsequent section.

Combustion Process

Identical to other CVC-approaches the SEC is based on an unsteady, cyclic combustion process that takes place in a combustion tube. A first overview of the main process phases is shown in Fig. 1.1. In contrast to the wave rotor technology the combustion tube of the SEC is open at the downstream end and acoustically closed on the

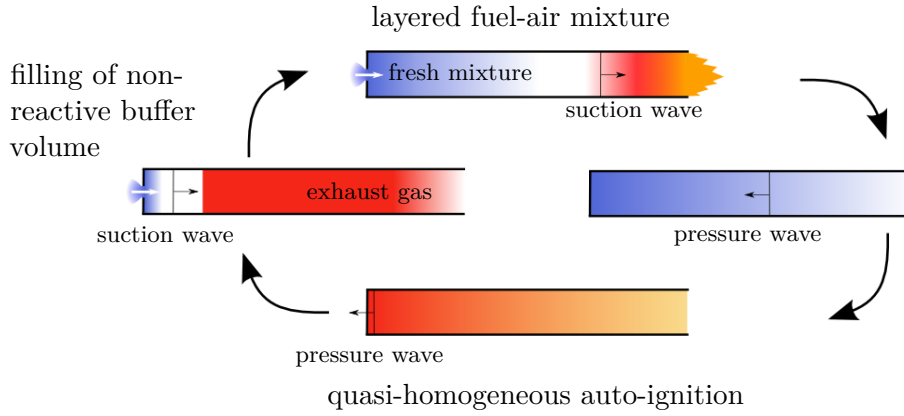


Figure 1.1: Process cycle of the shockless explosion combustor.

upstream end. This acoustic boundary condition is needed, as the process is based on a pressure wave oscillating inside the combustion tube. From Fig. 1.1 the four phases of the SEC can be identified. At the moment when the pressure at the inlet of the combustion tube drops below the plenum (i.e., compressor outlet) pressure, due to the reflected pressure wave from the previous cycle, fresh air is drawn into the combustion tube. A small non-reactive air volume is created to separate the new charge from the hot exhaust gases. While the low pressure suction wave is still causing an air inflow, fuel is injected into the air stream. The fresh air is drawn from a plenum downstream of the compressor and, thus, has a temperature several hundred Kelvin above ambient temperature, depending on the pressure ratio of the compressor. As the suction wave reaches the open downstream end of the combustor it is reflected as a compression wave and traveling upstream to the tube inlet. The now increasing pressure cuts off the inflow. At this point a part of the tube volume is filled with a combustible fuel-air mixture. The high temperature of the inlet air results in the auto-ignition of the fuel-air mixture succeeding the ignition delay time τ_{ign} . However, to assure a CVC the volume of the reactants needs to be burnt instantaneously to keep the gases from expanding before the combustion process is completed. The only way to realize such an instantaneous combustion simultaneously throughout a given volume is a homogeneous auto-ignition with subsequent very rapid energy release on sub-acoustic time scales. Thus, the ignition delay time τ_{ign} of the fresh mixture needs to be adjusted to match the residence time inside the combustion tube. This is done by an equivalence ratio stratification along the tube axis. The equivalence ratio is defined as follows:

$$\Phi = \frac{X_{\text{fuel}}/X_{\text{oxidizer}}}{(X_{\text{fuel}}/X_{\text{oxidizer}})|_{st}}. \quad (1.1)$$

where X_{fuel} and X_{air} denote the mass fractions of fuel and air in the mixture respectively and st denotes the stoichiometric mixture. In addition, the combustion process is tuned to match the oscillating pressure inside the tube. As the suction wave that generated the inflow is reflected at the open end of the tube, it travels upstream as a pressure wave. The moment when this compression wave reaches the acoustically closed (i.e., sufficiently reflective for acoustic waves) upstream end, the fuel–air mixture is burnt completely and instantaneously creating a significant, but rather smooth (i.e., without shocks), pressure rise that amplifies the pressure wave in the tube. The pressure wave is reflected at the acoustically closed upstream end, travels downstream in the tube and is reflected as a suction wave by the open end of the tube, restarting the process cycle.

Due to the coupling of the combustion process and the acoustic resonance of the combustion chamber, the firing frequency can be determined by the tube length and the mean temperature inside the tube. For each ignition event, the pressure fluctuation needs to travel four times from one end of the combustion tube to the other, resulting in:

$$f = \frac{\sqrt{\kappa R \bar{T}}}{4 l_{\text{tube}}}. \quad (1.2)$$

Where f denotes the firing frequency, κ denotes the adiabatic index, R the ideal gas constant, \bar{T} the mean temperature and l_{tube} the length of the combustion tube. Since the exact gas composition in the exhaust gases is not known at this point, the values of air are used for κ and R . According to this estimation, the firing frequency will be around 250 Hz for a tube length of around 80 cm at a mean temperature of 1700 K. A simple calculation of the main process parameters provides an estimate of the power of such a combustion system, fueled with dimethyl ether (DME) at 30 bar inlet pressure. The corresponding values are summarized in Tab. 1.1.

Table 1.1: Estimated operating parameters of one SEC-tube burning DME at an inlet pressure level of 30 bar.

length in mm	800	equivalence ratio	1
diameter in mm	40	average temperature in K	1700
filling ratio in %	0.4	frequency in Hz	258
intermediate air volume ratio	0.05	thermal power in MW	11

Regarding the operation of a gas turbine based on CVC, turn–down and part–load are crucial parameters of a combustion system. Two possible ways to operate such a system at part–load are proposed: lowering the mean equivalence ratio or reducing the volume of the combustible mixture by increasing the buffer volume. The first option is expected to result in a reduced combustor temperature and thus in lower firing frequencies. In contrast to that the firing frequency and combustor temperature

will only slightly change for the latter part-load operation possibility. However, for both operational strategies the pressure increase across the combustor will be lower.

Advantages of the SEC Process

The proposed cycle has several advantages in comparison to other CVC approaches. These advantages are most likely to result in an overall efficiency increase for the SEC.

1. **Smooth pressure rises** — In contrast to PDC or rotating detonations, no detonation or shock waves are employed in the SEC cycle. The detonation wave is accompanied by a shock wave, which is responsible for very high temperatures in the reaction zone. In addition, the shock waves are harmful for the machine, especially to the turbine section, not only from the mechanical point of view but also regarding the aerodynamic performance of the turbine blades. In contrast to that, the SEC only results in a smooth rise of pressure that is generated during the combustion process.
2. **Lower exergy losses** — The detonation in a PDC is accompanied by a significant amount of kinetic energy, which is introduced by the detonation wave. Unfortunately, this kinetic energy is most likely lost in the process since it is difficult to convert this energy to mechanical work in the turbine [73]. The shockless explosion combustor will not induce as much kinetic energy. Thus, the exergy losses associated with the kinetic energy behind the detonation wave are not present in the SEC.
3. **No DDT-losses** — Since a direct ignition of a detonation is extremely energy consuming, pulsed detonation combustors are most likely to employ a deflagration to detonation transition. In order to achieve this transition, at least a small distance is needed, which is directly associated to losses because no constant volume combustion is achieved in this region. For the SEC, these losses do not exist due to the homogeneous auto-ignition that does not require any developing distance.
4. **Mechanical integrity** — The proposed system mainly consists of a stationary tube without any moving parts or internal obstacles for flame acceleration. Therefore, it is easy to realize the cooling of the combustion chamber and to integrate such a device in a gas turbine system. No seals against moving parts are necessary and no obstacles inside the combustor require cooling. This ensures a long lifetime and long maintenance intervals for such systems.
5. **Filling against a positive pressure gradient** — Every pressure gain combustion reaches a critical point when the increased static pressure is retained downstream of the combustor, for example by a plenum, critical nozzle or turbine. If the static

pressure downstream of the combustion tube is higher than the pressure at the inlet, the tube must be filled against a positive pressure gradient. The SEC resolves this task by employing the unsteady pressure in the combustion tube. At the moment the suction wave reduces the combustor pressure below the upstream plenum pressure, the combustion tube is filled in line with the pressure gradient. Hence, the solution to filling the combustor against a positive pressure gradient is implicated in the process itself.

Following these points, the SEC process is a significant improvement to the pressure gain combustion cycles found in literature. The lack of shock or detonation waves reduces the technical problems of mechanical integrity, cooling and sealing. In addition, the losses of the combustion system are reduced, whereas the homogeneous auto-ignition creates a real CVC with the accompanied pressure rise.

Challenges in the SEC Process

Among the numerous challenges arising from the application of the SEC concept, two major ones will be addressed in the current thesis:

1. Provision of a high mixing quality, as required for homogeneous ignition, in the very limited available time.
2. Development of a back pressure valve, which is capable of handling the necessary high frequencies.

The first of the mentioned issues is the most crucial regarding the SEC process. A correct, exact and reliable conditioning of the mixture is needed to avoid premature ignition resulting in inefficient deflagrations or harmful detonation waves. Since the fuel is injected into the hot air stream of the compressor, fast and good mixing is needed in the radial plane of the combustor. Additionally, the mixing in the axial direction must be much lower to create the needed equivalence ratio stratification for a quasi-homogeneous auto-ignition. Only if these two points are fulfilled, premature ignition (that will result in harmful and unwanted detonation events or in inefficient deflagrations) in one or more locations can be avoided. In contrast to these demands of high mixing quality in the reactant volume, a film of non-reactive pure air is needed along the hot walls and as a buffer volume for the exhaust gases of the previous cycle to inhibit ignition at the hot gases or the hot surfaces of the combustion tube. This demand for a high mixing quality can, as shown in the present work, be realized by using fluidic oscillators. These devices are able to produce a fast and good mixing due to the oscillating jet they produce. The details of this approach are contained in chapter 2.

Besides the equivalence ratio, the temperature of the fuel-air mixture is the second main parameter determining ignition delay time. Since it is not possible to precisely

control the temperature of the fresh fuel–air charge in the extremely short time given by the chemical time scales, fuels with a less pronounced coupling between the temperature and the ignition time delay will be used for the first ignitions. By employing fuels with a negative temperature coefficient (NTC) behavior it is possible to even cross out the temperature dependency of the ignition time delay in a certain temperature range (see [16]). The NTC behavior describes a region of temperatures in which the ignition delay time increases for increasing temperature. The usage of special fuels allows to neglect the ignition time delay dependencies on pressure and temperature, as it is shown by Cai and Pitsch [16]. Accordingly, the equivalence ratio is the only parameter left that governs the ignition delay time in the fresh charge. The fuel used in this work is dimethylether (DME), which features such a behavior in the range of approximately 690–770 K for an equivalence ratio of one and at atmospheric pressure. Details on the ignition time delay of the used fuel and its dependency on the temperature are discussed in chapter 5.

The second challenge is the design of a back pressure valve that is able to handle hot flows at frequencies around 250 Hz for an adequate time. The inlet of the combustion tube needs to be opened when the suction wave is creating the necessary inflow and to be closed, when the combustion takes place to avoid a back flow. In addition, the pressure wave in the tube must be reflected by the upstream end of the combustor. In the first years of pulsed combustors, mostly reed valves have been used to assure this behavior at the combustor inlet. However, these devices are not able to withstand the harmful, hot environment of such a combustion tube for a long time. A fluidic diode without any moving parts is developed to deliver the desired inlet characteristics for the SEC and withstand the combustor environment for a long time. The details and characteristics of this fluidic diode can be found in chapter 3.

1.1.2 Fluidic Devices and their History

Around the year 1960 the United States Military was looking for a robust and easy way to control and steer rockets. Unfortunately, the electronics at that time were neither reliable nor robust enough to fulfill this task. Consequently, the DIAMOND ORDNANCE FUZE LABORATORIES (later: HARRY DIAMOND LABORATORIES) invented and developed a way to complete easy calculation and control tasks using fluids and devices without any moving parts — the fluidic devices. A figure of one layer of such a “fluidic computer” is shown in Fig. 1.2. The layer shown in this figure is a subsystem that performs a divide by ten operation. For every ten input pulses this circuit delivers one output pulse. Input and output pulses enter and leave the subsystem perpendicular to the plane of the system. The main input of the subsystem, for example, is located on the long straight channel running from left to right in the middle of the circuit. Ten identical logic elements are arranged in 5 pairs each containing two steady input streams, two outputs, eight control jets, and eight open vents. This Figure is cited from a work published by Angrist in 1964 [5]. In

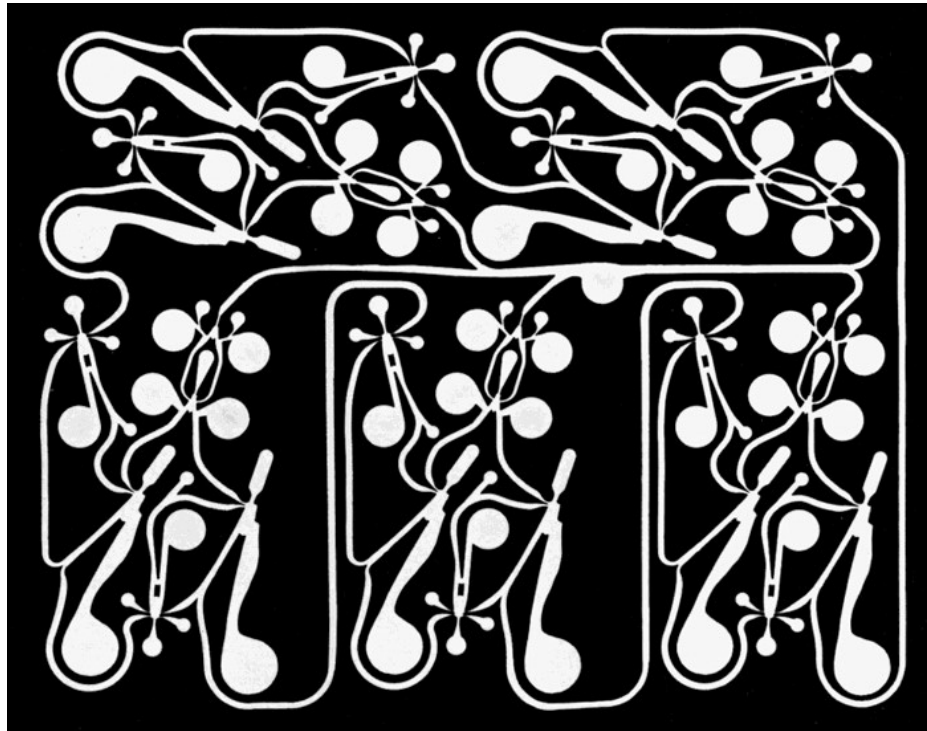


Figure 1.2: Fluidic circuit that performs a divide by ten operation ([5])

this work the basic underlying principle of a fluidic amplifiers, the COANDĂ-Effect, is explained and several effects regarding fluidic amplifiers are discussed.

In the following years the electronic systems compensated the lack of robustness and reliability. This paved the way for the usage of these components in most of the computing and controlling applications. The fluidic devices sank into oblivion since they were not needed anymore. In recent years the fluidic devices regained attention of the scientific community as they can be used as actuators in a broad variety of fluid dynamic applications.

Fluidic devices are a family of several components, just as the corresponding electronic modules. A broad variety of parts, such as diodes, triodes, switches, oscillators, amplifiers, and so on, are known and for each part several designs exist. However, all of these devices have one thing in common: the absence of any moving parts. Once pressurized with the main mass flow, they will fulfill their task, for example creating an oscillating jet, on their own without any need for intervention from outside the system. The first fluidic part, the fluidic amplifier was disclosed in 1960 by the said DIAMOND ORDNANCE FUZE LABORATORIES. It is based on the COANDĂ-Effect that causes a jet emanating from a nozzle to attach to a close surface. A sketch visualizing this effect is shown in Fig. 1.3. In this figure a jet emanating

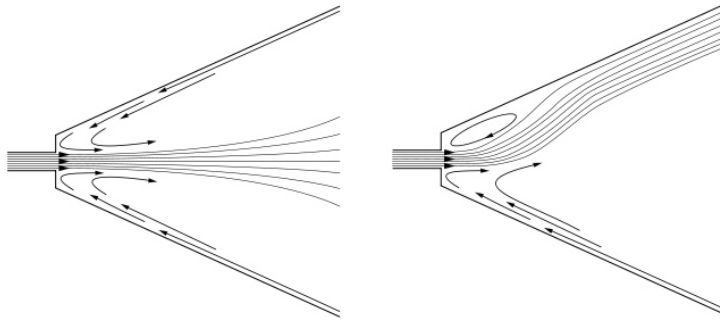


Figure 1.3: COANDĂ-Effect of a jet emanating from a nozzle

from a nozzle directly after starting the flow is shown on the left side. The flow direction is from left to right and the jet is streaming without any change in direction into the surrounding. On both sides of the jet, entrainment causes a back flow along the walls, thus, lowering the pressure on both sides of the jet at the nozzle exit. Due to turbulent fluctuations this pressure will be lower on one side than on the other, causing a movement of the jet to this side. This movement brings the jet closer to the wall, creating an even lower pressure on this side. Finally, the jet is attaching to one of the two sides and a low pressure bubble is created at the jet exit. This flow situation is shown in Fig. 1.3 on the right side.

Based on this effect the fluidic amplifier or bistable switch was invented. An example of a simple bistable switch is shown in Fig. 1.4. This bistable switch is

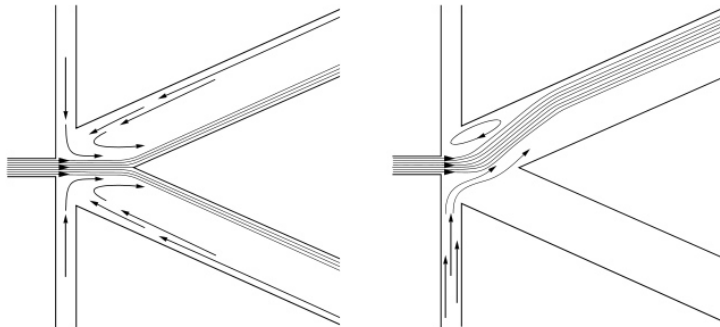


Figure 1.4: Sketch of a bistable fluidic switch

basically the same configuration as in Fig. 1.3 with two additional control ports on both sides of the main jet. In the left part of Fig. 1.4 the control ports are opened to the ambient pressure. The entrainment of the main jet induces a small flow inwards. When now a control pressure or flow is applied to one of the control ports, the jet

bends towards the other side and attaches to the surface of the outlet. Hence, it is possible to switch the jet from one outlet to the other by applying small control pulses to the control ports. This behavior is used with some additional geometric parameters and flow features in chapter 4. In this section a fluidic switch is used to control high mass flows of hot air in the surrounding of a SEC test rig. A more detailed overview on the different possible geometries for fluidic switches and their features can be found in said section.

If the control ports of the bistable switch are somehow connected to the outlets or to each other, a fluidic oscillator is created. This device creates a self-induced and self-sustaining oscillation of the main jet. A sketch of such a device, where the control ports are connected to each other, was published in the patent of Warren in 1962 [103] and is shown in Fig. 1.5. Based on the bistable switch and these first

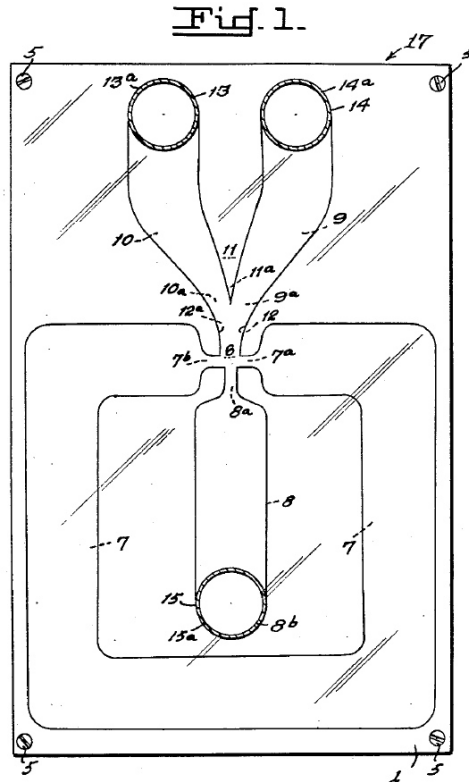


Figure 1.5: A “Fluid Oscillator” as it was patented by Warren in 1962 [103]

oscillators, a vast amount of different fluidic oscillator geometries have been invented over the last decades. In the presented work these devices are used to enhance the passive scalar mixing between two fluids (see Sec. 2). In the mentioned section a more detailed introduction into the different types of fluidic oscillators and their possible applications is presented as well.

In the year 1920 Nicolai Tesla claimed a patent that included a flow geometry now known as the “Tesla diode” [96]. This geometry is shown in Fig. 1.6. The

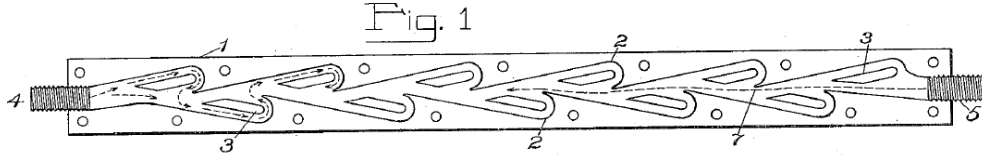


Figure 1.6: A “Tesla diode” as it was patented by Nikolai Tesla in 1920 [96].

shown geometry was the first realization of a fluidic diode as it creates a much higher pressure loss when the flow is directed from left to right than it creates for a flow from right to left. This resistance ratio or diodicity is defined as the pressure loss coefficient in one direction divided by the other direction and is around 4 [55] for the shown device. Another known geometry for a fluidic diode is the so called scroll diode as it is shown in Fig. 1.7. A fluidic diode is used in this work to rectify the main flow in the SEC combustion tube as the combustion will create a short moment of positive pressure gradient. The details of the used device and a more detailed description of fluidic diodes are presented in Sec. 3.

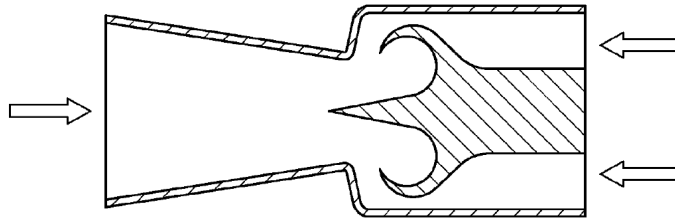


Figure 1.7: A scroll diode as it was shown in Kirshner and Katz [55]

The mentioned three fluidic devices are investigated and employed to create a test rig for the SEC in this work. All of these parts (bistable switch, fluidic oscillator, and fluidic diode) are used in the SEC test rig to fulfill a task traditional parts are not able to accomplish or withstand for a sufficiently long time. Each device, its corresponding flow field, and the most important geometrical features will be discussed in the following chapters. In addition, the task that is accomplished with each device regarding the SEC is discussed and shown.

1.1.3 Main Equations and Numerical Modeling of Turbulent Flow

Fluid mechanical phenomena can be described mathematically by the balance equations for mass and momentum. Starting from these equations several characteristic dimensionless quantities and simplified equations for specific flow situations were derived in the past. In the present work the BERNOULLI equation was utilized for the

evaluation of experimental results, characteristic dimensionless parameters were employed for the design of the test rigs and numerical simulations were carried out using the Reynolds Averaged Navier Stokes equations (RANS). All these representations will be presented in this section using the Einstein notation.

Mass Balance

The balance equation of mass in the local form is also known as the continuity equation in the field of fluid mechanics. It states that the mass transport into and out of the infinitesimal volume element is equal to the total change in mass of the element. This is defined mathematically as follows

$$\frac{\partial \rho}{\partial t} + \frac{\partial}{\partial x_i}(\rho u_i) = 0. \quad (1.3)$$

In the present work water is used as fluid for most investigations and even if air is used the fluid can be treated as incompressible as long as the Mach number is sufficiently low. For a stationary, incompressible flow the constant density leads to:

$$\frac{\partial u_i}{\partial x_i} = 0. \quad (1.4)$$

Momentum Balance

The momentum balance equation describes the change in the momentum of a control volume over time under the influence of external forces. It is defined as:

$$\frac{\partial}{\partial t}(\rho u_i) + \frac{\partial}{\partial x_j}(\rho u_i u_j) = \rho f_i + \frac{\partial}{\partial x_j}(\pi_{ji}),$$

where f_i denotes specific body forces on the control volume and π_{ij} denotes the stress tensor. This tensor can be expressed by the viscosity tensor τ_{ij} .

$$(\pi_{ji}) = -p\delta_{ij} + \tau_{ij}$$

By only regarding NEWTONian fluids, this viscosity tensor τ_{ij} can in turn be represented by the following ansatz.

$$\tau_{ij} = \eta \left(\frac{\partial u_j}{\partial x_i} + \frac{\partial u_i}{\partial x_j} \right) + \eta' \frac{\partial u_l}{\partial x_l} \delta_{ij}$$

In this equation the term η' denotes the bulk viscosity. For incompressible fluids this last term is equal to zero due to the continuity equation 1.4. Finally wrapping up

these steps one yields the NAVIER-STOKES equations for incompressible, NEWTONian fluids.

$$\frac{\partial}{\partial t}(\rho u_i) + \frac{\partial}{\partial x_j}(\rho u_i u_j) = \rho f_i - \frac{\partial p}{\partial x_i} + \eta \frac{\partial^2 u_i}{\partial x_j \partial x_j} \quad (1.5)$$

These equations describe all fluid mechanical phenomena including turbulence and even acoustics if compressibility is considered. However, analytical solutions to the NAVIER-STOKES equations are only known for very simple flow configurations. Therefore, numerical methods are mostly used to solve these equations.

BERNOULLI Equation

In order to align the pressure measurements with the PIV measurements for the internal flow structures of the fluidic oscillator (see, Sec. 2.2), the BERNOULLI equation is used. This equation was introduced in the 18th century and can be derived from the NAVIER-STOKES Equations 1.5 by only considering a rotational free flow $\vec{\nabla} \times \vec{u} = 0$. This simplification yields:

$$\rho \frac{u_i^2}{2} + p = \text{const.}, \quad (1.6)$$

which is known as the BERNOULLI equation.

Reynolds Averaged NAVIER-STOKES Equations

A common simplification for the NAVIER-STOKES equations is the PRANDTL ansatz, which decomposes the velocity components and the pressure into a mean and a fluctuating value.

$$u_i = \bar{u}_i + u'_i, \quad p = \bar{p} + p'$$

This ansatz is now inserted in Eq. 1.5, which yields the Reynolds Averaged NAVIER-STOKES equations (RANS):

$$\frac{\partial \bar{u}_i}{\partial t} + \bar{u}_j \frac{\partial \bar{u}_i}{\partial x_j} = f_i - \frac{1}{\rho} \frac{\partial \bar{p}}{\partial x_i} + \nu \frac{\partial^2 \bar{u}_i}{\partial x_j \partial x_j} - \frac{\partial}{\partial x_j} \overline{u'_j u'_i}.$$

These equations are identical to the NAVIER-STOKES equations except for the last term. This term can be rewritten to use the formulation of the Reynolds stress tensor τ'_{ij} which then yields:

$$\frac{\partial \bar{u}_i}{\partial t} + \bar{u}_j \frac{\partial \bar{u}_i}{\partial x_j} = f_i - \frac{1}{\rho} \frac{\partial \bar{p}}{\partial x_i} + \nu \frac{\partial^2 \bar{u}_i}{\partial x_j^2} - \frac{\partial}{\partial x_j} (\overline{\tau_{ij}} + \overline{\tau'_{ij}}). \quad (1.7)$$

In contrast to the NAVIER-STOKES equations 1.5, which together with the continuity equation creates a set of four equations with four unknowns, the RANS equations include five new unknowns due to the Reynolds stress tensor τ'_{ij} . Thus, this set of equations is not solvable unless further assumptions for the stress tensor are made. This problem is known as the *closure problem* that creates the necessity of turbulence models for the solution of the system. The turbulence model used in this work, the SST-model introduced by Menter [65], will be introduced in the following section.

Numerical Approach and Turbulence Modeling

Besides the direct numerical simulation (DNS), which means a direct numerical solution of the NAVIER-STOKES equations 1.5, several methods are known to solve the RANS equations instead with less computational costs. As stated in the previous section, the RANS set of equations consists, together with the continuity equation, of 4 equations with 9 unknowns. Thus, a turbulence model is needed to reduce the number of unknowns and create a solvable system. In this work the shear stress transport model SST as introduced by Menter in 1993 [65] is used. This turbulence model is based on the closure ansatz of BOUSSINESQ, who stated a dependency of the Reynolds stresses $-\rho\overline{u'_i u'_j}$ and the strain rate tensor S_{ij} :

$$-\rho\overline{u'_i u'_j} = 2\mu_t S_{ij} - \frac{2}{3}\rho k\delta_{ij}.$$

In this case μ_t denotes the eddy viscosity that is usually calculated by the turbulence model. The second summand assures the satisfaction of the definition of the turbulent kinetic energy k .

$$k = \frac{\overline{u'_i u'_i}}{2}$$

Altogether this yields:

$$-\rho\overline{u'_i u'_j} = \mu_t \left(\frac{\partial \bar{u}_i}{\partial x_j} + \frac{\partial \bar{u}_j}{\partial x_i} - \frac{2}{3} \frac{\partial \bar{u}_k}{\partial x_k} \right) - \frac{2}{3}\rho k\delta_{ij}.$$

This heavy simplification implies several advantages and disadvantages. On the one hand, the description of the turbulence motion as a viscous effect analogous to the molecular viscosity reduces the computational effort. On the other hand, the postulated dependency between the Reynolds stresses and the strain rate tensor does not necessarily hold. Hence, this modeling ansatz fails for certain flow situations.

However, several turbulence models based on this simplification exist. The used SST model is based on two two-equation turbulence models, the $k\varepsilon$ and the $k\omega$ model. All of the following mathematical descriptions are based on reference [6].

The $k\varepsilon$ model is the most commonly used turbulence model. In order to close the set of RANS and continuity equations two partial differential equations are introduced, which describe the change in the turbulence kinetic energy k and the isotropic dissipation rate ε .

$$\begin{aligned}\frac{\partial}{\partial t}(\rho k) + \frac{\partial}{\partial x_j}(\rho k \bar{u}_j) &= \frac{\partial}{\partial x_j} \left[\left(\mu + \frac{\mu_t}{\sigma_k} \right) \frac{\partial k}{\partial x_j} \right] + P_k + P_b - \rho \varepsilon - Y_M + S_k \\ \frac{\partial}{\partial t}(\rho \varepsilon) + \frac{\partial}{\partial x_j}(\rho \varepsilon \bar{u}_j) &= \frac{\partial}{\partial x_j} \left[\left(\mu + \frac{\mu_t}{\sigma_\varepsilon} \right) \frac{\partial \varepsilon}{\partial x_j} \right] + \rho C_1 S \varepsilon - \rho C_2 \frac{\varepsilon^2}{k + \sqrt{\nu \varepsilon}} + \\ &+ C_{1\varepsilon} \frac{\varepsilon}{k} C_{3\varepsilon} P_b + S_\varepsilon.\end{aligned}$$

Several unknown parameters are introduced together with this formulation. These parameters must be empirically derived from simple flow configurations and treated as constants. By changing these values it is possible to adjust the model for a given flow configuration, which casts doubt on the universality of the model. The mentioned constants are derived from the following flow situations:

- $C_{1\varepsilon}$: homogeneous shear flow
- C_2 : dissipation of homogeneous grid turbulence
- turbulent PRANDTL number σ_ε : logarithmic region of a turbulent wall shear flow

The other parameters are defined as follows:

$$\begin{aligned}C_1 &= \max \left[0.43, \frac{\eta}{\eta + 5} \right] \\ \eta &= S \frac{k}{\varepsilon} \\ S &= \sqrt{2 S_{ij} S_{ij}}.\end{aligned}$$

The values P_k and P_b in the equations denote the production of turbulent kinetic energy from the velocity gradients and the body forces, respectively. The anisotropic parameter C_μ is derived by a dimensional analysis of the eddy viscosity. Accordingly,

the model of the turbulent viscosity yields:

$$\begin{aligned}\mu_t &= \rho C_\mu \frac{k^2}{\varepsilon} \\ C_\mu &= \frac{1}{A_0 + A_s \frac{kU^*}{\varepsilon}} \\ U^* &\equiv \sqrt{S_{ij}S_{ij} + \tilde{\Omega}_{ij}\tilde{\Omega}_{ij}} \\ \tilde{\Omega}_{ij} &= \Omega_{ij} - 2\varepsilon_{ijk}\omega_k \\ \Omega_{ij} &= \overline{\Omega_{ij}} - \varepsilon_{ijk}\omega_k,\end{aligned}$$

where $\overline{\Omega_{ij}}$ denotes the averaged rotation tensor in a coordinate system that rotates with an angular velocity of ω_k . The remaining parameters are given by

$$\begin{aligned}A_0 &= 4,04 \\ A_s &= \sqrt{6} \cos \phi \\ \phi &= \frac{1}{3} \cos^{-1}(\sqrt{6}W) \\ W &= \frac{S_{ij}S_{jk}S_{ki}}{\tilde{S}^3} \\ \tilde{S} &= \sqrt{S_{ij}S_{ij}} \\ S_{ij} &= \frac{1}{2} \left(\frac{\partial \bar{u}_j}{\partial x_i} + \frac{\partial \bar{u}_i}{\partial x_j} \right).\end{aligned}$$

For the presented work the following values for the empirical constants are used:

$$\begin{aligned}C_{1\varepsilon} &= 1.44 \\ C_2 &= 1.92 \\ \sigma_k &= 1.0 \\ \sigma_\varepsilon &= 1.3\end{aligned}$$

The main drawback of this turbulence model lies in the vicinity of the walls, where the profiles of turbulent kinetic energy and the dissipation show step gradients. To sufficiently resolve these gradients a very fine mesh is needed in these regions. In order to overcome this disadvantage, the SST model “switches” to a $k\omega$ model in these regions by making use of a blending function.

The $k\omega$ model is using the turbulent kinetic energy k and the specific eddy viscosity ω . This specific eddy viscosity is a quantity that describes the characteristic frequency

of the energy dissipating eddies.

$$\omega = \frac{1}{C_\mu} \frac{\varepsilon}{k}$$

The mathematical description of the used SST model is summed up in the following. The kinematic eddy viscosity can be calculated by:

$$\nu_T = \frac{a_1 k}{\max(a_1 \omega, SF_2)}.$$

Whereas the turbulent kinetic energy is calculated by:

$$\frac{\partial k}{\partial t} + \bar{u}_j \frac{\partial k}{\partial x_j} = P_k - \beta^* k \omega + \frac{\partial}{\partial x_j} \left[(\nu + \sigma_k \nu_T) \frac{\partial k}{\partial x_j} \right]$$

and the specific dissipation is defined by

$$\frac{\partial \omega}{\partial t} + \bar{u}_j \frac{\partial \omega}{\partial x_j} = \alpha S^2 - \beta \omega^2 + \frac{\partial}{\partial x_j} \left[(\nu + \sigma_\omega \nu_T) \frac{\partial \omega}{\partial x_j} \right] + 2(1 - F_1) \sigma_{\omega 2} \frac{1}{\omega} \frac{\partial k}{\partial x_i} \frac{\partial \omega}{\partial x_i}.$$

The remaining parameters are defined as follows.

$$\begin{aligned} F_2 &= \tanh \left[\left[\max \left(\frac{2\sqrt{k}}{\beta^* \omega y}, \frac{500\nu}{y^2 \omega} \right) \right]^2 \right] \\ P_k &= \min \left(\tau_{Tij} \frac{\partial \bar{u}_i}{\partial x_j}, 10\beta^* k \omega \right) \\ F_1 &= \tanh \left\{ \left\{ \min \left[\max \left(\frac{\sqrt{k}}{\beta^* \omega y}, \frac{500\nu}{y^2 \omega} \right), \frac{4\sigma_{\omega 2} k}{\text{CD}_{k\omega} y^2} \right] \right\}^4 \right\} \\ \text{CD}_{k\omega} &= \max \left(2\rho\sigma_{\omega 2} \frac{1}{\omega} \frac{\partial k}{\partial x_i} \frac{\partial \omega}{\partial x_i}, 10^{-10} \right) \\ \phi &= \phi_1 F_1 + \phi_2 (1 - F_1) \end{aligned}$$

The used empirical constants are the baseline settings of ANSYS CFX and, thus:

$$\begin{aligned}\alpha_1 &= \frac{5}{9} \\ \alpha_2 &= 0.44 \\ \beta_1 &= \frac{3}{40} \\ \beta_2 &= 0.0828 \\ \beta^* &= \frac{9}{100} \\ \sigma_{k1} &= 0.85 \\ \sigma_{k2} &= 1 \\ \sigma_{\omega 1} &= 0.5 \\ \sigma_{\omega 2} &= 0.856.\end{aligned}$$

All presented numerical results within this work were calculated using the program package ANSYS CFX 14.5, which discretizes the equations presented above by employing the finite volume approach on unstructured computational grids. The required meshes were created using ICEM CFD 14.5.

REYNOLDS number

The Reynolds number Re is used to characterize flow situations and to assure the comparability of scaled model experiments and the full scale situation. It denotes the ratio between inertia and viscosity effects of a given flow situation and is defined as follows:

$$Re = \frac{ul}{\nu}, \quad (1.8)$$

where u denotes the flow velocity, ν the kinematic viscosity and l a characteristic length of the flow situation. Since mainly flows on the inside of certain geometries (e.g., tubes) are investigated in this work, this characteristic length is mostly given by the hydraulic diameter d_h of the given flow situation.

STROUHAL number

Like the Reynolds number the Strouhal number is a dimensionless quantity. It is also known as the dimensionless frequency and defined as:

$$St = \frac{fl}{u}, \quad (1.9)$$

where f denotes the frequency of the oscillation. The other parameters are similar to the Reynolds number. In the presented investigations the Strouhal number was used to scale the oscillations in the pulsating SEC combustor to the used water test rig. By taking into account both the Reynolds number and the Strouhal number, it is possible to scale the used test rig, flow velocities and other parameters to assure comparability between the different fluids (i.e., water and air).

CHAPTER 2

Fluidic Oscillator

This chapter addresses the main challenge in the SEC process, the mixing. A quasi-instantaneous fuel-air mixing with very low spatial deviation is needed to avoid premature ignition of the combustible mixture. In the present work spatially oscillating jets are investigated as fuel injectors for the SEC configuration. It is known from Literature (e.g., [59]) that the mixing quality close to the injection position can be significantly improved by employing spatially oscillating jets as injectors. One promising way to generate robust and reliable spatially oscillating jets are fluidic oscillators, due to the absence of moving parts.

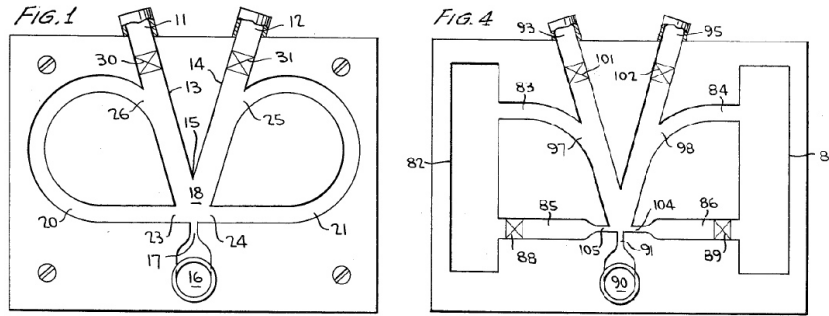
In order to create the optimal fuel injection system, the underlying processes and mechanisms of the fluidic oscillator must be understood. This is assured by first performing an experimental analysis of the internal flow structures of the device. Next, this experimental study is used to validate the numerical tools and to conduct a numerical parametric study of several geometry parameters. The deeper understanding obtained from the simulations allows to create fluidic oscillators with the needed performance for the purpose of fuel injection in the SEC configuration. This chapter is divided in four sections. Following the literature review on fluidic oscillators and their applications, an experimental investigation of the internal flow structures and the underlying oscillation mechanism of the used oscillator geometry are presented. The validated numerical parametric study on the influence of several geometrical parameters is shown in the third section of this chapter. Finally, two fluidic oscillator geometries are designed and tested against several common injection geometries in a water test rig to quantify the mixing performance of these configurations.

2.1 State of the Art

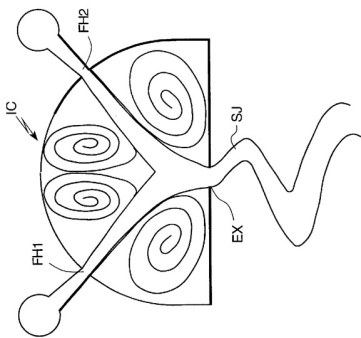
Fluidic oscillators are devices that emit an either continuous, but spatially oscillating, a temporarily oscillating, or a spatially and temporary oscillating jet when pressurized

with a fluid. The oscillation is entirely self-induced and self-sustaining. Because these actuators are almost arbitrarily scalable (i.e., from sub-millimeter up to meter), do not contain any moving parts, are capable of exerting high momentum, and can, depending on the material, sustain almost any fluid or temperature, they inherit several crucial advantages over traditional flow control devices. Their simplicity, reliability, and low maintenance have sparked the current interest in these devices as a viable actuator, especially from the industrial point of view. Based on the COANDĂ-Effect (see Sec. 1.1.2) the fluid amplifier, also known as fluidic amplifier or bistable switch, was created. The fluidic oscillator was then derived from these devices by either adding some kind of feedback or connection between the control ports of the bistable switch. Later on, a third type of fluidic oscillator was invented, the so called vortex interaction oscillator. One example for a very simple fluidic oscillator is shown in Fig. 1.5. For this type of oscillator the control ports of the bistable switch are connected to each other. If now the main jet is attached to either side, the pressure at the control port of this side will decrease, resulting in a flow from one control port to the other. This flow is creating a lower pressure on the other side and raises the pressure on the side where the jet is attached. Thus, the jet switches to the other side and restarts the process. This oscillator was already patented in 1962 by Warren [103].

Four examples for the feedback and vortex interaction types of oscillators are summarized in Fig. 2.1. In Fig. 2.1a examples for the feedback type of fluidic oscillators are shown as they were published in the patent from Campagnuolo [18] in 1970. In both oscillator models a part of the outlet flow is redirected upstream and guided through the control ports of the device. In the design on the left of Fig. 2.1a the fluid is directed directly to the power nozzle (i.e., main jet inlet). In the other design (i.e., on the right side) the feedback flow is directed into a volume, from which a flow is fed to the control ports if the pressure in the volume is sufficiently high. Hence, the volume creates a capacitor like effect. The other two parts of Fig. 2.1, namely 2.1b and 2.1c, are examples for the feedback free or vortex interaction oscillator. Both devices are employing different underlying mechanisms to create the oscillatory flow. The oscillator on the left (i.e., Fig. 2.1b) relies on the interaction of two jets in a chamber to create the oscillatory motion. Hence, this oscillator is also called “jet interaction oscillator” and was patented by Raghu in 2001 [78]. In order to visualize the internal dynamics of this system, Gregory *et al.* [36] used pressure sensitive paint and colored water. They concluded that the underlying oscillation mechanism is based on two counter-rotating vortices inside the interaction chamber. The second feedback free oscillator (see Fig. 2.1c) was first patented as a “Fluidic Oscillator Flowmeter” in 1981 [10]. By integrating the geometry shown in Fig. 2.1c into a flow passage it is possible to measure the flow rate in the passage by monitoring the frequency of the pressure in the chamber. In 2002 Uzol and Cameci [99] investigated the internal flow structure in this configuration both, numerically and experimentally. They revealed that, like for the jet interaction oscillator, the underlying oscillation



(a) Oscillators with two feedback channels as patented by Campagnuolo in 1970 [18].



(b) Feedback free oscillator as patented by Raghu [78].



(c) Feedback free oscillator as patented by Bauer in 1981 [10].

Figure 2.1: Different types of oscillators: 2.1a oscillators with two feedback channels and 2.1b/2.1c feedback free oscillator.

mechanism is based on the dynamics of two vortices inside the main chamber of the geometry.

The oscillator geometry used in this work is shown in Fig. 2.2. A configuration with two feedback channels similar to the one of Campagnuolo (Fig. 2.1a) is used. Guyot *et al.* [40] incorporated this fluidic oscillator in an atmospheric model gas turbine combustor to suppress thermoacoustic instabilities, whereas Lacarelle *et al.* [59] employed it for mixing enhancement studies. Due to the experience gained with this oscillator type, this geometry was chosen to be investigated, adapted and used for the current work. In contrast to the geometry of Campagnuolo, the used oscillator has two distinct regions of separation downstream of the control ports. Hence, the detailed underlying oscillation mechanism is not completely obvious. However, the main mechanism of this oscillator follows the idea of the first fluidic oscillators and, thus, can be described as follows. Due to the bistable COANDA-Effect the fluid

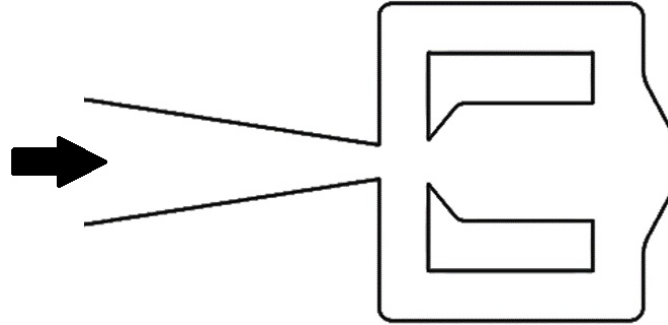


Figure 2.2: Sketch of the used oscillator geometry.

emanating from the power nozzle¹ attaches to one side of the main chamber. On the downstream side of the main chamber a small part of the fluid is guided through the feedback channel in the upstream direction. This volume flow causes the main jet from the power nozzle to switch to the other side of the main chamber and, thus, re-initiates the process. Consequently, the jet is leaving the outlet at varying jet deflection angles (JDA). Depending on the oscillator type, the specific geometry and the volumetric flow rate, main oscillating frequencies of the presented devices vary between less than 10 Hz [99, 101] up to the order of 20 kHz [37]. Several different oscillator geometries have been developed and patented in recent years (e.g., [30, 78]). Each of these different actuators provide individual outlet flow properties. The jet may, for example, exit into an unobstructed area where it can move continuously from side to side (sweeping jet actuators) or it may be obstructed by a wedge which separates the exit area into two discrete outlets.

In the past fluidic oscillators have mostly been utilized with liquids as a working fluid (e.g., [88]) for applications such as windshield washers, sprinklers, shower heads, and jacuzzis. However, recent research on separation [83], noise [79], and combustion [40] control applied air and other gases as a working fluid. Significant aerodynamic improvements were achieved with fluidic oscillators by controlling flow separation over the flap of several two-dimensional airfoils such as a NACA 0021 airfoil [75] or a generic airfoil [107], and three-dimensional models such as a 1/10th-scale powered V-22 model [83], λ -Wing [97] and a vertical tail model [84]. Possible applications are not just limited to modern aviation. Other areas of interest include turbomachinery [20], vehicle aerodynamics [89], and wind turbines [21]. In recent years several studies on the internal flow field (numerical) and the external flow field (numerical and experimental) of a fluidic oscillator were carried out (e.g., [12, 27–29, 31–33, 37, 67, 72, 99, 100]). In addition, other researchers (e.g., [7, 13]) altered the geometry of a fluidic oscillator (e.g., the feedback tube size) and studied

¹ A glossary of the different parts and regions inside the fluidic oscillator can be found in Fig. 2.9

the changes in global quantities such as the oscillation frequency. However, so far the internal flow field of such a device has mainly been examined numerically (e.g., [27, 29, 31–33, 67, 100]). Unfortunately, little detail regarding the internal flow mechanisms has been extracted from numerical studies as some uncertainty regarding the validity of the calculations remains. The first experimental investigation of the detailed internal flow patterns of the chosen device were published by Bobusch *et al.* [12] and confirmed by additional experiments of [28, 72]. An overview of the research on fluidic oscillators was published by Gregory and Tomac in 2013 [35]. In this work they give an overview of the history of different fluidic oscillators as well as their applications in the field of active flow control.

2.2 Flow Inside and Function of a Fluidic Oscillator

Before designing a fuel injection system for the SEC process one needs to understand the internal flow structures and the sensitive geometrical parameters of the fluidic oscillator. This knowledge is needed to create a fluidic oscillator with the desired properties. The internal flow structures of a fluidic oscillator are investigated experimentally by making use of different measurement techniques. Experiments are challenging due to the optical accessibility of the small internal geometry and the needed time resolution for capturing the high frequency oscillations. A simplified approach was used in the current work employing an enlarged oscillator which uses water as a working fluid to reduce its oscillation frequency. In the following sections the experimental setup, the data analysis, and the results are presented and discussed to identify the underlying oscillation mechanism for the used oscillator. This section is based on and was partly published by Bobusch *et al.* in 2013 [12].

2.2.1 Experimental Setup and Instrumentation

In 2009 Guyot *et al.* [40] incorporated a fluidic oscillator in an atmospheric model gas turbine combustor to suppress thermoacoustic instabilities by modulating parts of the fuel (natural gas) flow. They found out that additional tubing at the outlets of this oscillator inhibits the oscillations of the device. Due to this undesired effect this oscillator geometry was selected for a detailed analysis in order to understand and suppress the reasons for this behavior. Note that the oscillator used in this section has a slightly different outlet region than the one shown in Fig. 2.2, because additional tubing was needed for the purpose of suppressing thermoacoustic instabilities. It will be shown later (see Sec. 2.3.2) that this change in the outlet region has no influence on the internal flow structures of the device.

The internal flow structures of this device were investigated using Particle Image Velocimetry PIV. In order to simplify this measurement approach, water was employed as working fluid, since it was shown by Guyot *et al.* [40] that the oscillating frequency is independent of the fluid's compressibility. Several advantages follow from this

choice. First, the frequency of the oscillation is decreased for the same mass flow. Second, the refractive index of water is very close to the one of acrylic glass, thus reflections and scattering inside the actuator were reduced. An actuator similar to the design of Guyot *et al.* was manufactured out of acrylic glass. However, even though employing water as fluid and a background subtraction, some regions inside the oscillator (e.g., close to the outlet nozzle) were disturbed by refracted light. The oscillator was positioned in a water tank 40 outlet diameters underneath the surface. This ensures a constant pressure and density field at the outlet of the actuator. The oscillator was fed by a pump in a closed loop configuration, adjusting the volumetric flow rate using a needle valve and a flow meter. A sketch of the experimental setup can be found in Fig. 2.3.

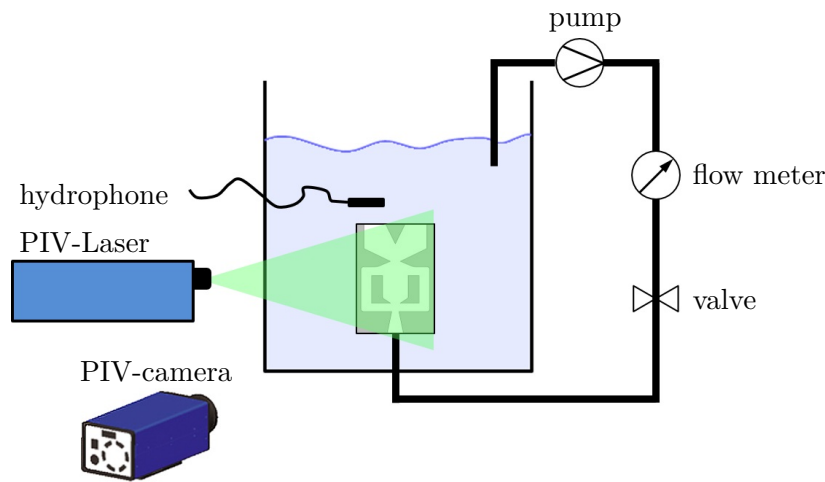


Figure 2.3: Sketch of experimental PIV-setup including the flow circuit and the measurement equipment (not to scale).

In addition to the PIV-measurements, pressure sensors and a hydrophone were used to further characterize the internal flow of the device. The hydrophone was placed downstream of the oscillator’s outlet to measure the oscillating frequency. It was assured that the hydrophone does not disturb the flow by mounting it at a sufficient distance to the outlets. Due to the high turbulence levels in the flow field, it was not possible to employ the hydrophone signal as a trigger source for the other measurement techniques. Thus, the PIV snapshots, taken at random internal flow states, were phase averaged using the Proper Orthogonal Decomposition (POD), which is explained in Sec. 2.2.2.

The laser sheet for the PIV-measurements entered the oscillator from one side, whereas the camera was placed outside the tank perpendicular to the laser sheet. The pictures were background corrected and possible perspective distortions were compensated using the known oscillator geometry. At each operating condition

(i.e., flow rate) 750 image pairs were recorded at a sampling rate of approximately 4.5 Hz. Employing the non-constant sampling rate of the used PIV-system, phase locking of the measurement frequency and the oscillation was avoided. Seeding was introduced in form of silver coated hollow glass spheres with a diameter of $15\ \mu\text{m}$ and with the approximations of Melling [64] a negligible error due to slip of the particles was ascertained. A final interrogation size of $16 \times 16\ \text{px}$ with a window overlap of 50 % resulted in a spatial resolution of 0.56 mm.

The pressure measurements were carried out by using two dynamic pressure sensors with a range of $\pm 1\ \text{bar}$. The pressure tabs and the geometry of the investigated fluidic oscillator are depicted in Fig. 2.4. Since only 2 pressure sensors were available one sensor was placed at the reference position (see position “ref” in Fig. 2.4), while the other one was consecutively connected to each pressure port. Unused pressure tabs were sealed. Finally, the pressure time traces were aligned by making use of the simultaneously recorded reference signal (“ref”). The pressure was measured relative to the static pressure at the oscillator’s outlet in quiescent surrounding. Stainless steel tubes with a length of 12 mm and an inner diameter of 1 mm were used to connect the pressure sensors to the internal flow volume of the oscillator, resulting in a time delay of the signals of approximately $8\ \mu\text{s}$ or $1/6250$ of an oscillation cycle. Thus, the time delay is several orders of magnitude smaller than the expected oscillation time scales. The pressure signal was recorded at every position for a period of 64 s with a sampling rate of 2048 Hz. For both, pressure sensors and hydrophone, the voltage signal was directly recorded using a 16 bit A/D-converter and later transformed to a pressure signal using the corresponding calibration functions.

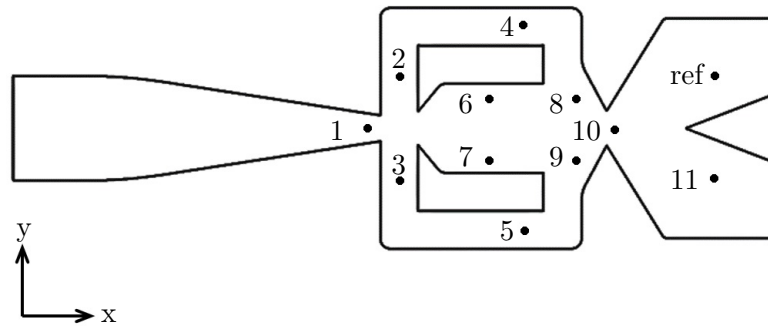


Figure 2.4: Fluidic geometry and pressure measurement locations (not to scale).

2.2.2 Data Analysis

The lack of a trigger signal for the PIV measurements made it necessary to reconstruct the phase information of the internal jet oscillations from the captured velocity data using the method of POD. The POD separates a vector or scalar field into its mean

value and the fluctuations in the field in form of higher modes. These higher modes are sorted by the descending amount of (kinetic) energy captured within them. In the context of the presented results, the POD method allows to reconstruct the phase angle information for each randomly taken PIV snapshot. Since the POD is used only for the PIV measurements in this section, the mathematical description of the method is only briefly discussed. The detailed mathematical formulation for the POD in the field of fluid dynamics can be found in Holmes *et al.* [42]. An example for the reconstruction of the modes in a turbulent swirling jet using the POD framework was presented by Oberleithner *et al.* [71].

Following the POD method, an instantaneous velocity field $\vec{u}(\vec{x}, t_k)$ at $t = t_k$ can be represented by the sum of the mean velocity field (i.e., $\overline{\vec{u}(\vec{x})}$) and the fluctuations, which are expressed by an orthonormal basis. This yields

$$\vec{u}(\vec{x}, t_k) = \overline{\vec{u}(\vec{x})} + \sum_{i=1}^N a_i(t_k) \vec{\Phi}_i(\vec{x}) + \xi, \quad \text{with } i = 1 \dots N \quad (2.1)$$

where the summation limit N corresponds to the number of measurements (i.e., PIV snapshots) at uncorrelated times t_k with $k = 1 \dots N$.

The calculation of the spatial modes $\vec{\Phi}_i(\vec{x})$ is based on the minimization of the residual error ξ in Eq. 2.1, which leads to an eigenvalue problem that can be solved for the eigenvalues λ_i with $i = 1 \dots N$ and the eigenvectors $a_i(t_k)$. The eigenvalues represent twice the fluctuation energy of the corresponding mode; hence, the sum of all eigenvalues equals twice the total fluctuation energy of the flow field. The spatial POD modes can be derived from the fluctuation snapshots as a linear combination weighted by the corresponding modal amplitudes $a_i(t_k)$:

$$\vec{\Phi}_i(\vec{x}) = \frac{1}{N\lambda_i} + \sum_{i=1}^N a_i(t_k) (\vec{u}(\vec{x}, t_k) - \overline{\vec{u}(\vec{x})}) \quad (2.2)$$

As a consequence it is possible to investigate the kinetic fluctuation energy captured within each mode ($\lambda_i/2$). This kinetic energy is plotted in Fig. 2.5. To enhance the visibility the zeroth mode (i.e., the mean flow field) is omitted in this plot and the sum of the higher modes ($i = 1 \dots N$) is normalized to 100%. From Fig. 2.5 it is evident that the first four modes contain most of the fluctuation energy (i.e., 53.4%), which indicates large coherent structures in the flow field or an oscillatory behavior. This can be confirmed by plotting the axial component of the spatial POD modes one and two $\vec{\Phi}_{1,2}(\vec{x})$. This plot can be found in Fig. 2.6. As one can see, both modes resemble parts of the oscillatory movement in the main chamber. The first two modes correspond to the deflection of the jet and an axial wave, which propagates through the main chamber of the oscillator. This axial wave will be discussed in more detail in a subsequent section. However, since these modes contain similar amounts of energy an oscillatory behavior between these two flow states is most likely.

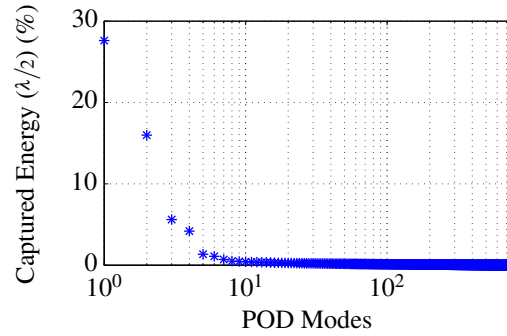


Figure 2.5: Energy captured in each POD mode.

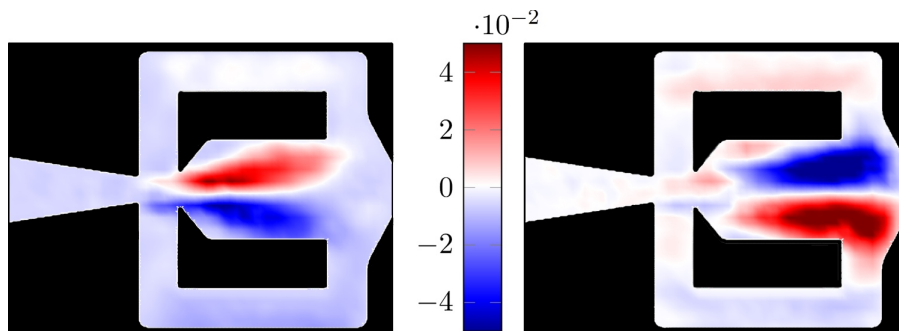


Figure 2.6: Axial component of POD modes 1 and 2 in arbitrary units.

In order to finally confirm the oscillatory relationship between these modes a phase portrait between the corresponding modal amplitudes a_1 and a_2 for all PIV snapshots is plotted in Fig. 2.7. As the circular pattern reveals, the two modes are coupled and represent the switching behavior inside the oscillator. Since an analysis of the relationships of higher modes did not show such a dominant coupled behavior, it is concluded that the internal flow field oscillation is represented by mode one and two. Following Fig. 2.7 the correlation between the modes one and two includes information regarding the phase angle of each snapshot. This angle can be calculated using Eq. 2.3:

$$\varphi_k = \arctan \left(\frac{a_1(t_k)}{a_2(t_k)} \right), \quad (2.3)$$

which allows for the phase-averaging of the PIV measurements. Following Eq. 2.3 a phase angle of 0° represents a pure POD mode two while 90° corresponds to a pure mode one. From a physical point of view the first POD mode describes the maximum lateral deflection of the jet from the mean flow (i.e., center line). A phase angle of 0° corresponds to the jet being attached completely to one of the walls in the main chamber, accordingly. However, to realize the phase-averaging of the PIV snapshots they were sorted according to their phase angles and averaged within a

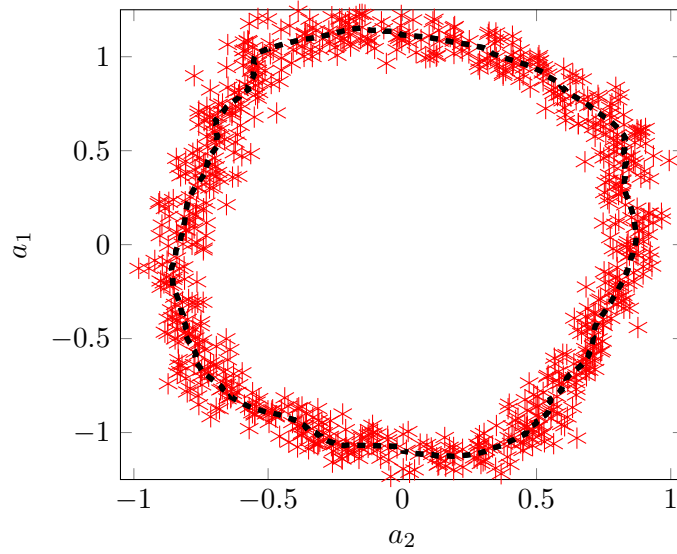


Figure 2.7: Phase portrait of POD modal amplitudes a_1 and a_2 for all snapshots.

certain range. Ostermann *et al.* [72] compared several phase averaging methods for determining the internal and external flow structures of a fluidic oscillator. They concluded that an averaging window size of $\pm 3^\circ$ gives the best balance between biasing the results and creating a smooth velocity field. However, by evaluating several possible averaging window sizes it was assured that the averaging process did not disturb the results significantly, even though a window size of $\pm 5^\circ$ was chosen for the shown phase-averaged velocity plots.

In order to align the uncorrelated pressure measurements with the PIV data the BERNOLLI equation was used (see Eq. 1.6). The velocity peaks in the time history at the reference position (see Fig. 2.4) were identified and correlated to the time history of the pressure measurements at the reference position. Subsequently all other pressure tab locations were aligned to the reference position that was recorded simultaneously. As a result a complete and phase-correlated data set including velocity and pressure information was created, which will be discussed in the following section.

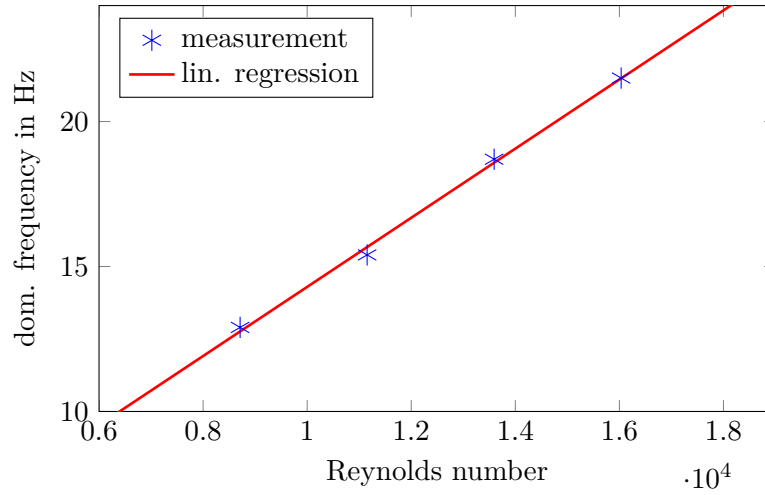
2.2.3 Internal Flow and Underlying Mechanism

In order to investigate the internal flow structures and the underlying oscillation mechanism, the oscillator was investigated for four different volumetric flow rates. These flow rates are summarized together with the corresponding Reynolds numbers in Tab. 2.1. The Reynolds numbers are based on the hydraulic diameter d_h of the quadratic power nozzle and are all well within the turbulent flow regime.

Table 2.1: Flow rates and Reynolds numbers of the experimental investigations.

volume flow rate L/h	Reynolds number
80.9	8711
103.5	11152
126.3	13593
148.8	16034

The frequency for each operating condition was calculated using the hydrophone data and a spectral analysis. From literature (e.g., [31, 39]) it is known that the frequency of such a device is linearly dependent on the Reynolds number for flows, which can be considered incompressible. This behavior was confirmed as the plot in Fig. 2.8 clearly shows. However, for the investigation of the flow field and pressure

**Figure 2.8:** Dominant oscillation frequency vs. Reynolds number.

data only the maximum flow rate of 148.8 L/h is used in this work since the other flow rates yield similar results.

For a detailed discussion of the flow patterns inside the oscillator several parts, regions, directions, and names need to be defined, which is done in the glossary shown in Fig. 2.9. The flow enters the oscillator from the left, whereas the oscillator consists of the power nozzle (a), the main chamber (b), the two inner blocks (c) with the main chamber inlet wedges (d), the two feedback channels (e), the outlet nozzle (f) and the two outlet regions (g) separated by the splitter plate (h). The key flow regions are the main jet (i) and the recirculation bubble (j). Due to the fact that the feedback channel flow is oriented upstream (i.e., from right to left), the channel inlet (k) is defined downstream of the main chamber and the channel outlet (l) is defined at the power nozzle. The orientation of the inlet and outlet faces of the feedback channels is consistent with the feedback channel control volume (i.e.,

- | | |
|-------------------------------|-----------------------------|
| a - power nozzle | g - outlet region |
| b - main chamber | h - splitter plate |
| c - inner blocks | i - main jet |
| d - main chamber inlet wedges | j - recirculation bubble |
| e - feedback channels | k - feedback channel inlet |
| f - outlet nozzle | l - feedback channel outlet |

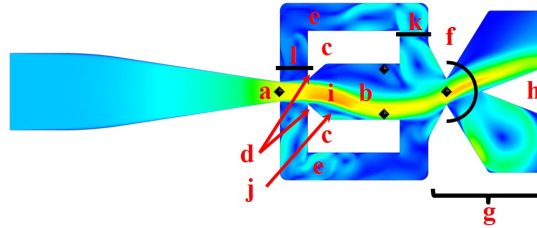


Figure 2.9: Characteristic parts and flow regions inside fluidic oscillator.

an inflow is quantified as negative for flow entering the feedback channels and an outflow is quantified as positive for flow leaving the feedback channels).

Figure 2.10 gives a first overview on the oscillation process inside the fluidic oscillator. Half of an oscillation period is shown in phase angle steps of 30° . The plots a-g illustrate the velocity magnitude of the flow field normalized by the maximal velocity as false colors complemented by corresponding streamlines. The plots h-n visualize the respective vorticity distribution. As depicted in the pictures, the main jet switches from the lower inner block of the oscillator at 0° to the upper inner block at 180° . The switching mechanism is mainly based on a recirculation bubble, which is formed between the jet and the lower block inside the main chamber of the oscillator. This recirculation bubble is visible in Fig. 2.10a and also in the corresponding vorticity plot. The jet is bent downwards at that instance and impinges the wall at the outlet nozzle below the centerline. Thus, part of the flow is diverted in the upstream direction through the lower feedback channel. In addition, a small vortex is generated at the lower feedback channel inlet due to the cavity that is formed by the geometry. The jet exits the outlet nozzle through the upper outlet port, completely attached to the splitter plate, whereas a strong vortex is created in the lower outlet port. This vortex entrains fluid from downstream of the oscillator and thus, is responsible for the sensitivity of the oscillator regarding downstream tubing. Fluid that is pushed into the attached tube at one instance will be sucked back into the oscillator during the following half of the oscillation cycle. As this quasi synthetic jet behavior was already revealed numerically for this type of oscillator [31], it might be alleviated

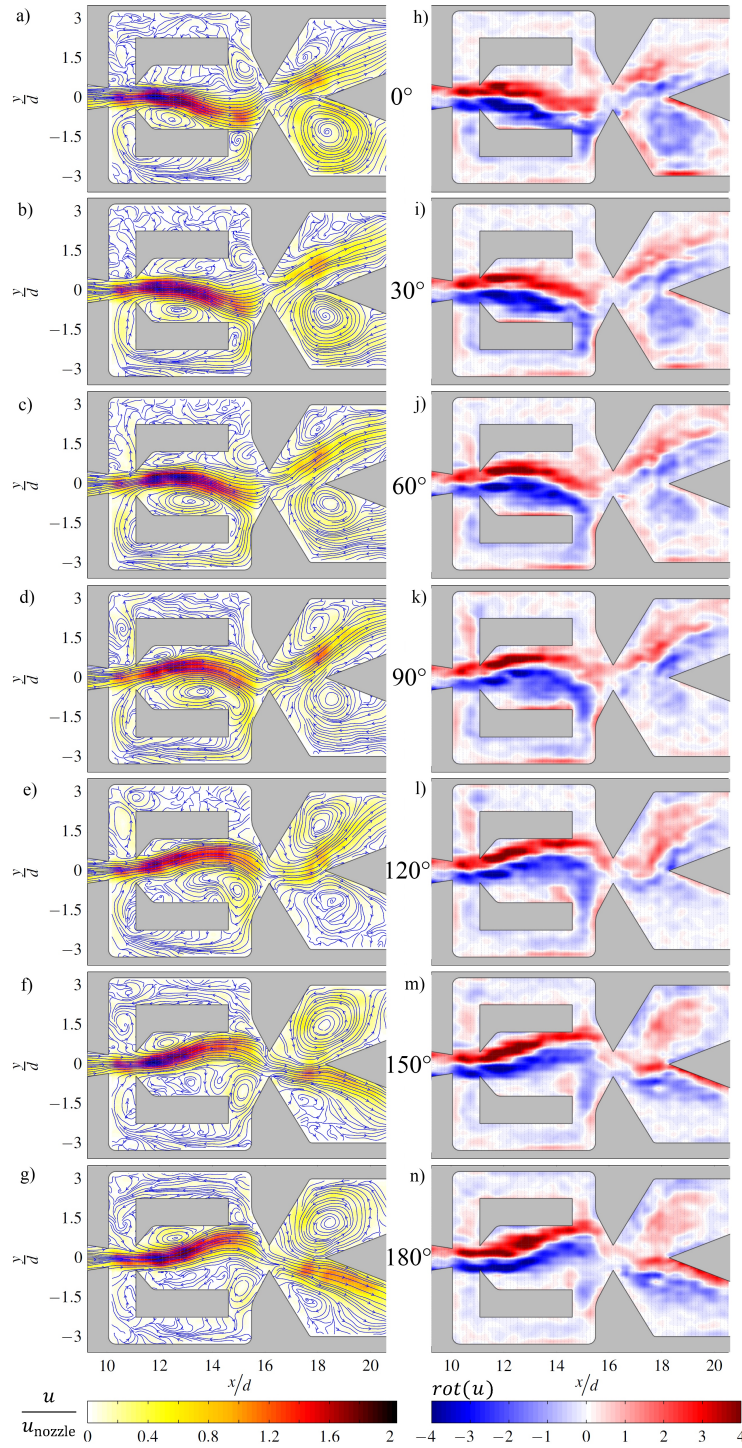


Figure 2.10: Flow field inside the fluidic oscillator for half an oscillation cycle; *left* - velocity magnitude with superimposed streamlines at 7 phase angles φ (a-g), *right* - vorticity at respective phase angles (h-n).

by altering and streamlining the outlet geometry to prevent the development of the meant vortex for applications where downstream tubing is required.

In the subsequent phase angles $\varphi = 30^\circ \dots 90^\circ$ (see Fig. 2.10b-d) the transport of fluid through the lower feedback channel is evident. It enters the main chamber and is fed into the main recirculation bubble mentioned earlier. Consequently, this recirculation region grows and extends downstream, whereby it pushes the main jet to the other side of the main chamber. The growing recirculation region is also visible in the corresponding vorticity plots. According to this, it is expected that the main jet is not only bent by the lateral momentum leaving the feedback channel but also by the growing recirculation bubble that increases the pressure at the lower inner block of the oscillator. Additionally, the entrainment of the jet creates a low pressure region at the upper block enhancing the switching movement even further.

As the jet is pushed to the upper inlet wedge (see $\varphi = 60^\circ \dots 120^\circ$), a small portion of the flow is separated by the main chamber inlet wedge and penetrates the upper feedback channel in the downstream direction. This behavior can be seen by the streamlines and the increased vorticity in that region. For a more detailed view on this phenomenon the mass flow into and out of the lower feedback channel for a complete oscillation cycle is shown in Fig. 2.11. As the jet is pushed upwards away from the lower block (as shown in Fig. 2.10a-g) the mass transport through the feedback channel is completely directed upstream. Due to the mentioned phenomenon a reverted flow through the feedback channel can be observed in Fig. 2.11 for phase angles between $\varphi = 200^\circ \dots 320^\circ$. This behavior is likely to delay the switching of the jet since the outflow at the feedback channel inlet (close to the outlet nozzle) hinders the attachment of the jet in that region. Additionally the mentioned undesired flow goes along with an increase in pressure loss inside the oscillator. The influence of the main chamber inlet wedge distance on the oscillation parameters is investigated in Sec. 2.3.2. As expected the frequency of the oscillation is increased for a larger distance of these wedges.

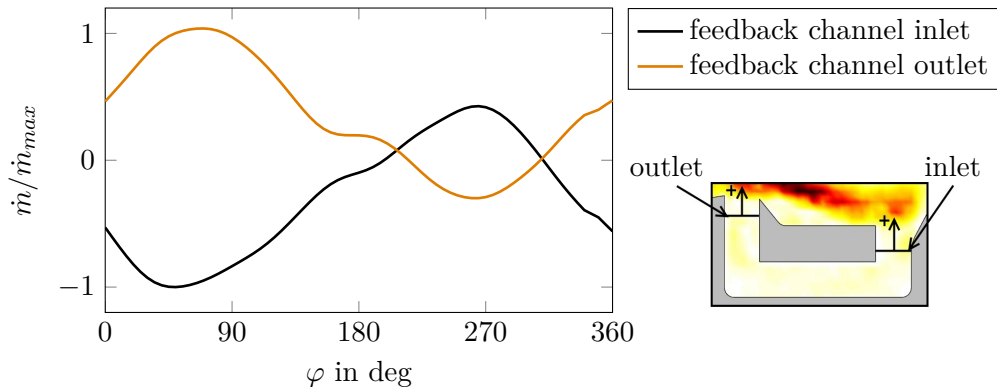


Figure 2.11: Mass flow in lower feedback channel during one complete oscillation cycle.

With further increasing phase angle (up to $\varphi = 90^\circ$, see Fig. 2.10d) the large vortex in the lower outlet port weakens as the jet starts to switch between the two outlet ports. Even though, the jet is already detached from the lower block at this instance, the jet impinges the wall below the outlet nozzle with increasing steepness and is directed through the upper outlet port. Due to this increasing inclination angle the jet detaches from the flow diverter in the upper outlet and deflects even further. According to this finding, the maximum jet deflection at the outlet is reached during the internal switching process and not, as commonly believed, while the jet is fully attached to one of the inner blocks. Therefore, the use and definition of frequently referenced characteristic time scales such as transmission and switching time (see [55]) have to be reconsidered for this type of oscillator when external jet properties are analyzed. It is possible to alter the correlation of the internal and external jet location by changing the outlet nozzle geometry and respective wall angles, as shown in Sec. 2.3.2. Besides this, it is evident that the emanating jet neither attaches to the outer walls of the outlet nozzle nor the downstream walls of the outlet nozzle even at the largest deflection angles. Therefore the shape of the outlet nozzle on the downstream side (i.e., the diverging part of the nozzle) has no influence on the jet deflection and the jet deflection angle is prescribed by the internal geometry of the outlet nozzle. Thus, no diverging part at the outlet nozzle is required to enable oscillations. The same findings were presented for an enlarged fluidic oscillator using air as fluid by Gärtlein *et al.* in 2014 [28]. Changes in the geometry in that region were investigated numerically, which is shown in Sec. 2.3.2, to verify these assumptions.

At a phase angle of $\varphi = 120^\circ$ (see Fig. 2.10e) the main recirculation bubble has moved downstream to the inlet of the lower feedback channel inlet where it pushes the jet away from the lower wall of the outlet nozzle. Even though parts of the jet still impinge on this wall the amount of fluid emanating from the lower outlet port is increasing. Thus, the vortex in the lower outlet port has almost disappeared whereas the respective vortex in the upper outlet is growing. Further increasing the phase angle to $\varphi = 150^\circ$, the main recirculation region moves into the inlet of the lower feedback channel completely pushing the jet away from the lower outlet nozzle wall. Located in the feedback channel inlet this vortex weakens, as visible in the corresponding vorticity distribution (Fig. 2.10m) and the decreasing mass transport (see Fig. 2.11). However, as the jet completely attaches to the upper block the recirculation zone in the upper part of the oscillator is created and fed by the increasing flow through the upper feedback channel. At a phase angle of $\varphi = 180^\circ$ (see Fig. 2.10h/n) the switching process from the lower to the upper block is completed as the jet is emanating from the lower outlet port entirely. The recirculation zone in the main chamber is growing and the mass transport through the upper feedback channel is increasing, showing the same flow state as for $\varphi = 0^\circ$ but mirrored at the centerline of the fluidic oscillator. Similar internal dynamics were found by Gärtlein *et al.* [28] in 2014 for an enlarged fluidic oscillator. Like in

the presented work they used PIV measurements to assess the internal and external flow field of the oscillator. Their results confirmed the presented findings regarding the underlying oscillation mechanism for air and the potential sensitive regions for geometrical changes.

The additional pressure measurements underline the mentioned findings. The pressure time traces for all pressure tabs are shown in Fig. 2.12 against the phase angle φ . To allow a better comparison between the flow fields in Fig. 2.10 and the pressure measurements the phase angles shown in the flow field plots are indicated by vertical dashed lines.

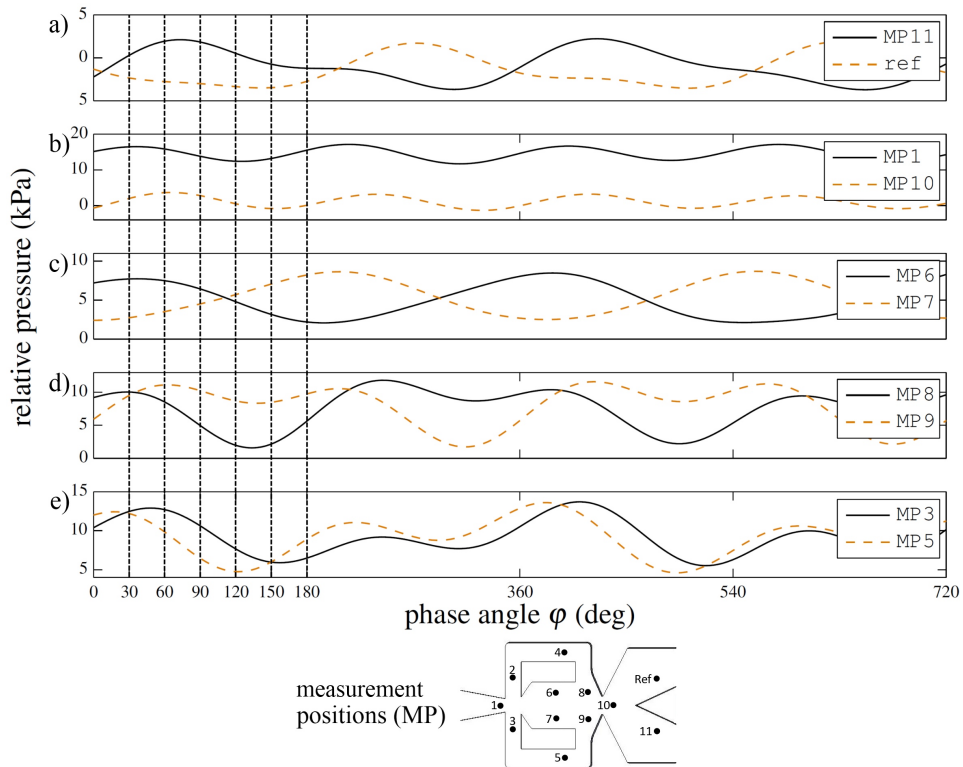


Figure 2.12: Pressure time traces at various locations (dashed lines indicate phase angles of Fig. 2.10).

On top of Fig. 2.12 the pressure fluctuations in the outlets of the oscillator are shown in subplot a. As expected the oscillatory behavior of the flow field and the 180° phase shift between the outlets is evident in the pressure measurements. The sustained low pressure at the reference location is caused by the presence of the high velocity jet as well as the strong recirculating flow. On the centerline the two pressure signals at the power and outlet nozzle show an almost identical peak-to-peak fluctuation at different mean pressure levels. Additionally a small phase shift can be observed in Fig. 2.12 that matches the convective time lag between the power

and outlet nozzle, whereas the difference in the mean pressure of around 15 kPa corresponds to the pressure loss between these two points. Note that the pressure on the actuator's centerline fluctuates with twice the frequency of the outlet pressure ports, because the jet internally passes the centerline twice in one oscillation period. First, when switching from one side to the other and again while switching back. Since water is used for the presented experiments, the flow can be considered incompressible and, thus, the fluctuations on the centerline of the actuator prove the existence of axial pumping of mass flow. The term axial pumping describes an oscillatory mass flow at the outlet of the actuator. This mass flow is depicted in Fig. 2.13 that illustrates the oscillations in mass flow and jet velocity normalized by their maximum values. The data is extracted at a cross-section through pressure port MP10. Again, twice the overall oscillation frequency is observed in the mass flow and the velocity. The phenomenon of axial pumping was already similarly deduced from numerical

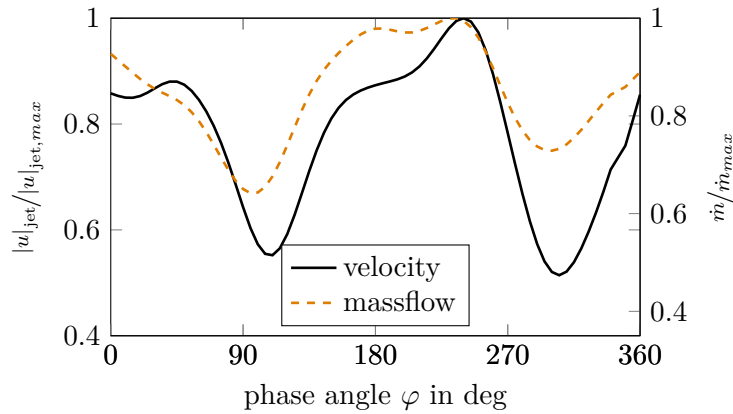


Figure 2.13: Mass flow fluctuations (“axial pumping”) downstream of outlet nozzle.

studies by Gokoglu et al. [31]. The main reason of this phenomenon is found in the oscillatory behavior itself. Since the jet is bending to either side, a small amount of energy is needed to bend the jet. This energy must be provided by the main jet because of the self-sustaining nature of the oscillation. Hence, the total pressure loss of the oscillator is fluctuating in time. The origin of the behavior is confirmed by the fact that jet velocity is minimal during the jet's largest deflection angle at around 90° . At this stage the steepest jet impingement on the inside wall of the outlet nozzle is observed, which relates to a velocity stagnation and pressure increase in this area and, thus, reduces the mass flow. Since both values, velocity and mass flow, attain their extreme values simultaneously, the exerted momentum resembles the same oscillation, which may affect the controlling efficacy in control applications of this device either in a positive or negative way. Unfortunately, the reduced quality of the PIV data in the vicinity of the outlet nozzle implies uncertainty regarding the quantitative accuracy of Fig. 2.13. But based on the consistency between the

pressure and flow field data a high confidence in the qualitative description of the oscillations in mass flow and jet velocity exists.

The pressure inside the main chamber is shown in Fig. 2.12c for the two pressure ports MP6 and MP7. For a phase angle of 0° the jet is fully attached to the lower block at MP7 resulting in a minimal pressure value. As the jet is switched to the upper block the growing recirculation bubble (see Fig. 2.10a-g) creates a continuously increasing pressure at MP7, which again indicates the “pushing” behavior of the main recirculation region. At MP6 the opposite pressure trend can be observed. This includes the decreasing pressure due to the jet entrainment as the jet is moving upwards between $\varphi = 30^\circ$ and 120° . The two pressure tabs further downstream MP8 and MP9 (shown in Fig. 2.12d) are affected not only by the jet’s velocity but also by the proximity to the local stagnation region of the inner nozzle walls. The impingement of the jet below the outlet nozzle creates high velocities at MP9 for a phase angle of 0° resulting in a low pressure at this position. The stagnation point that is accompanied by this impingement is moving upwards together with the jet in the subsequent phase angles. As it passes MP9 a pressure peak at this location is observed at a phase angle of 60° . From this time on the pressure at MP9 decreases temporarily before the jet switches to the upper block. The increasing velocity in the vicinity of MP8 is visible as a pressure minimum at $\varphi \approx 150^\circ$.

Finally, the pressure measurements in the feedback channels (see Fig. 2.12e) further underline the previously mentioned arguments. As the jet remains attached to the lower block, the jet creates a back pressure inside the feedback channel as visible in the pressure maximum at MP5 that coincides with the maximum at MP1. As the jet is moving away from the lower block, the pressure inside the lower feedback channel decreases. The positive pressure gradient inside the feedback channel is represented by the apparent difference in the first pressure minima between MP3 and MP5. Again, the phase shift between these two pressure tabs correlates well with the convective time delay, which can be seen as further evidence that the jet’s oscillation is caused by streaming flow through the feedback channel and not by a pressure wave. In addition, Fig. 2.12e reveals that the pressure inside the feedback channel attains two local maxima and minima within one oscillation period. One of the two oscillations corresponds to the switching process where mass is transported in the upstream direction through the feedback channel. This is followed by a back flow in the opposite direction as parts of the main jet are guided into the feedback channel outlet by the main chamber inlet wedges. In this part of the oscillation the pressure gradient reverses with the pressure at MP5 being higher than at MP3.

Now knowing the internal dynamics of the flow and pressure field inside the fluidic oscillator and, it is possible to create a validated numerical model. This model is then used in the next section to investigate the oscillation mechanism and later on the influence of the identified sensitive geometrical regions on the flow field.

2.2.4 Numerical Confirmation of Oscillation Mechanism

For a further investigation and proof of the experimental findings regarding the switching mechanism a numerical simulation was performed for different mass flows. The details and the experimental validation of these simulations were part of a broad parametric study published by Krüger *et al.* [57] and Bobusch *et al.* [13] and will be presented in the following section (2.3.1). However, since the results of these investigations support the experimental findings of the previous part they will be presented here.

Three different main flow rates were simulated. The baseline case and two configurations with $\pm 20\%$ volumetric flow rate. The linear dependency between the volumetric flow rate and the dominant oscillation frequency was confirmed by these simulations, which gives, together with the validation, confidence in the results of the numerical investigations.

From the experimental data it was stated that the switching of the jet is governed by the growing recirculation bubble and not the momentum exchange at the power nozzle. In order to verify this statement the mass transport through the feedback channel during one oscillation cycle was observed for the three different mass flows. For each time step the instantaneous mass flow rate through the feedback channel outlet was calculated from the velocity of the incompressible and isothermal flow and the area of the flow passage. If the growing recirculation bubble is the governing oscillation mechanism, it is expected that the mass, which is transported through the feedback channel in one oscillation cycle, is nearly constant for all flow rates. This is due to the fact that the minimal and maximal volume of the recirculation region in the main chamber is constant for all flow rates, because the geometry is not changing. The resulting mass flow time traces are plotted in Fig. 2.14, where the left plot denotes the mass flow in kg/s versus the period time $T_{osc} = 1/f$. It is obvious that the peak mass flow leaving the feedback channel outlet is increasing with main volume flow. Recall that the different flow rates result in different frequencies, which were normalized for this plot with the period time T_{osc} .

However, by additionally normalizing the mass flow with the frequency (see Fig. 2.14, right) the three curves collapse in one single curve, giving evidence that the mass transport through the feedback channel per oscillation cycle is constant for all investigated flow rates. Thus, the growth of the recirculation bubble is the dominant oscillation mechanism for this type of oscillator. This will be further verified in the subsequent section 2.3, as geometry changes affect the minimal and maximal bubble size and, thus, the mass transport needed per oscillation cycle.

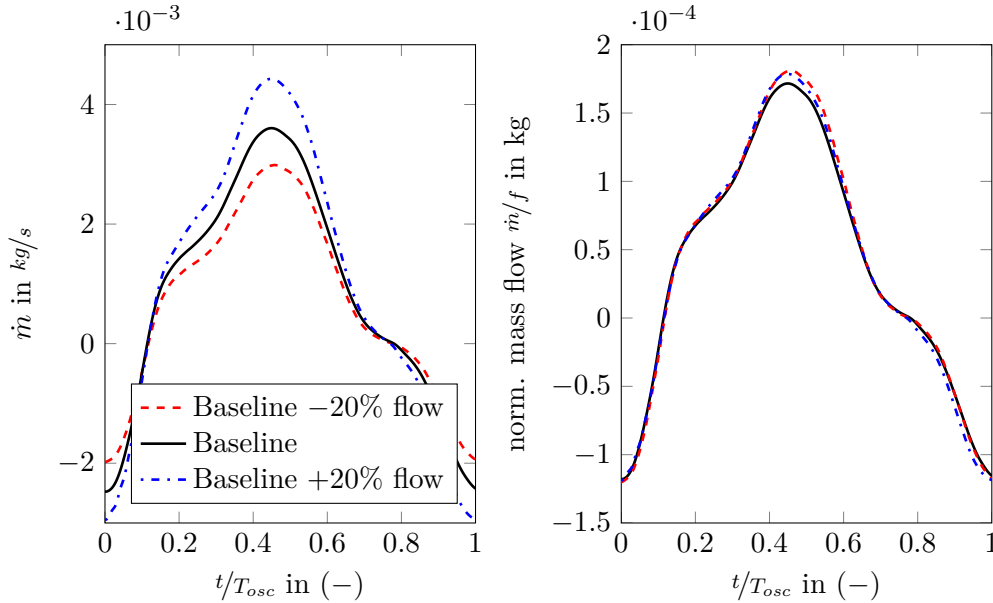


Figure 2.14: Mass flow through the feedback channels for the three flow rates.

2.3 Geometry Parameters Affecting the Oscillation Structures

Subsequent to the experimental discovery of the underlying oscillation mechanism one needs to understand the different influences of the geometrical parameters of the fluidic oscillator, in order to design a device with the desired oscillatory behavior. Several possible regions of high sensitivity regarding geometrical changes were revealed by the experimental investigations, but since an experimental parametric study is associated with high costs and time consuming experiments, the influence of these regions was determined using a numerical approach. Following the definition and validation of the numerical tools, the influence of geometrical parameters regarding the internal flow structures and the overall oscillation parameters is investigated. This section is based on and was partly published by Bobusch *et al.* in 2013 [13].

2.3.1 Numerical Tools

Prior to conduct a parametric study of the oscillator geometry using numerical simulations the numerical tools and programs need to be defined and validated. In order to do so a grid sensitivity analysis was performed and several numerical models were compared with the experimental data obtained in Sec. 2.2. It was possible to simulate the flow of the fluidic oscillator with a deviation of only 2% from the experimental results regarding the dominant oscillation frequency. The details of the validation can be found in the work of Krüger *et al.* [57], whereas the mathematical

description of the validated numerical approach can be found in Sec. 1.1.3. Since only small geometric variations were investigated, the author is confident that the numerical results are reliable and accurate even with an altered geometry.

The numerical investigations were carried out using ANSYS CFX 14.5 and the ANSYS WORKBENCH. A parameterization of the oscillator's geometry allows easy changes in the ANSYS WORKBENCH. The computational grid was generated using the ANSYS MESH tool consisting of around 550,000 non-structured quadrangular elements. The grid was extruded in the third dimension by one cell, because the used solver is not able to work on pure two-dimensional grids. Thus, all simulations were done in a quasi two-dimensional manner. This simplification of the three-dimensional flow field of the oscillator is validated in the mentioned paper by Krüger et al. [57]. In addition, the almost negligible influence of the aspect ratio of the device will be shown later in this section (see Sec. 2.3.2).

To minimize the influence of the boundary conditions an inflow and an outflow region were added to the oscillator geometry. The inlet was set to the needed mass flow of 148.8 L/h whereas the outlet was simulated as an opening to atmospheric pressure. In the third dimension symmetry boundary conditions represent an infinite depth of the geometry, whereas all walls were set to non-slip walls. In order to allow the comparison with the experimental data of Sec. 2.2 water was used as working fluid and the temperature was set to 293 K. Turbulence modeling was done using the Shear-Stress-Transport model from Menter [65] that is described in more detail in Sec. 1.1.3.

As for the previous section the definition of the parts, regions and directions inside the fluidic oscillator can be found in Fig. 2.9. Again the spatial coordinates were normalized by the hydraulic diameter of the power nozzle and the velocity plots are normalized by the theoretical power nozzle velocity defined by the area of the power nozzle and the volumetric flow rate of the incompressible water.

2.3.2 Geometry Parameters

In the following a parametric study on the influence of different geometrical parameters will be presented based on pressure and velocity data at several positions inside the oscillator. Additionally, frequency and JDA are used as global oscillation parameters. The positions at which these values are evaluated are shown in Fig. 2.9 as black lines and points. The main frequency was calculated from the axial velocity time trace at two points in the main chamber by making use of Fast Fourier Transform (FFT). From the half circle around the center of the outlet nozzle the JDA was calculated with the jet axis defined as the maximum of the velocity magnitude. In addition, velocity and pressure were evaluated at the feedback channel's inlet and outlet. The definition of the normal vectors regarding these "surfaces" is the same as in Sec. 2.2 (i.e., the normal vector points outwards the feedback channel volume). The pressure loss of the oscillator was calculated using the two points in the power and outlet

nozzle of the device. The oscillator was fed with the same mass flow as for the previous section (i.e., 148.8 L/h).

Influence of Outlet Geometry

One of the first regions of interest identified in Sec. 2.2 was the outlet geometry, particularly the diverging part of the outlet nozzle and the subsequent flow diverter. Since the two separate outlets are not useful for all applications the flow diverter or splitter plate was removed in a first test case. Additionally small outlets are often desirable, for example in flow control or fuel injection. Thus, the diverging part of the outlet nozzle was removed, creating the outlet opening at the narrowest location of the outlet nozzle. The resulting three different outlet geometries are shown in Fig. 2.15 together with the corresponding oscillation frequency and the JDA. Note that for case (a) the circle for the calculation of the JDA is upstream of the splitter plate and, thus, inside the oscillator. As already stated in Sec. 2.2 the investigated changes on the outlet geometry have a negligible influence in the main oscillation parameters frequency and JDA. For the sake of computational costs, the shortest oscillator geometry will be used as the baseline case for the rest of the investigations. Therefore the three different outlet geometries will be addressed as a) baseline with splitter plate, b) baseline with diffuser, and c) baseline.

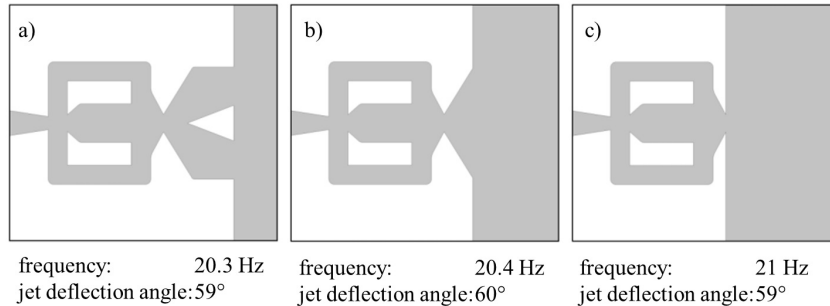


Figure 2.15: Setup of the different outlet geometries.

A more detailed insight into the flow downstream of the oscillator the velocity magnitude in this region is depicted in Fig. 2.16. Each plot was created at the maximum JDA of the respective configuration. It is evident that neither for the case with (2.16a) nor without (2.16b) the splitter plate the jet attaches to the diverging part of the outlet nozzle. Accordingly, this part of the outlet is not needed to enable the oscillation, as it was already mentioned in Sec. 2.2 and confirmed by Gärtlein *et al.* [28]. Since it allows a much easier integration of these devices as fuel injectors the outlet opening can be opened to a full 180° without altering the oscillation characteristics.

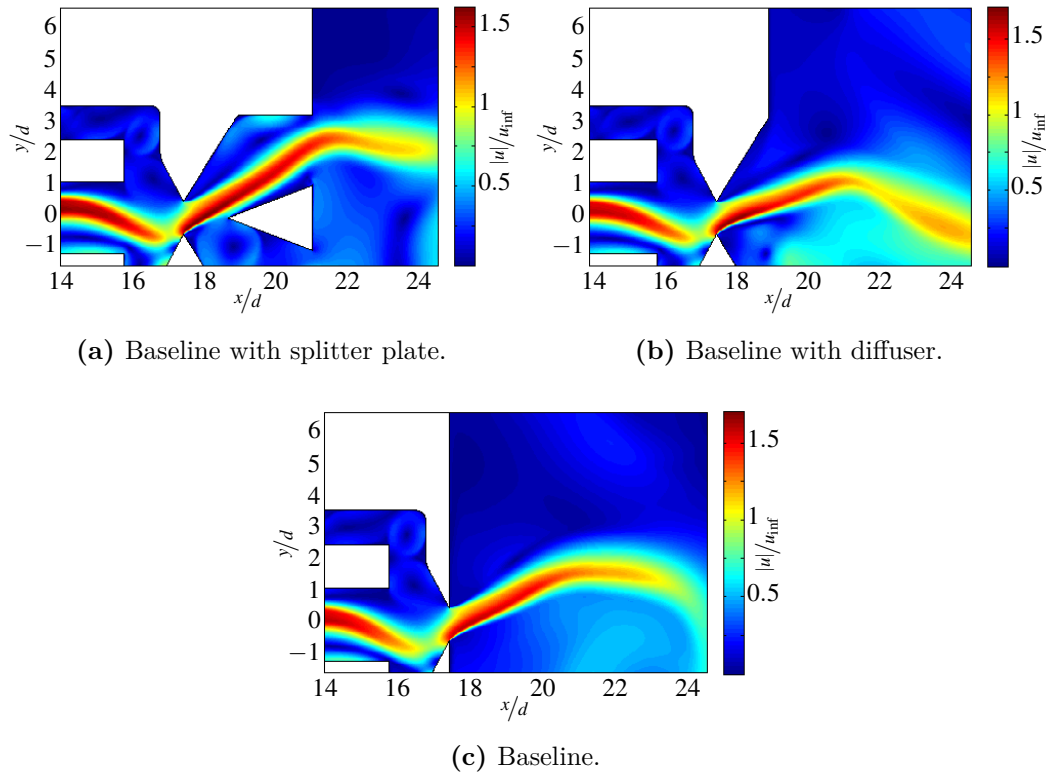


Figure 2.16: Velocity magnitude at the outlet region with maximum JDA for three outlet geometries.

An additional phenomenon associated with the outlet geometry is revealed by Fig. 2.16. The cavity vortex in the inactive outlet, as described in Sec. 2.2 can be seen in Fig. 2.16a at the bottom of the picture. Without the splitter plate still a region of high velocity gradients exist in this area (see Fig. 2.16b), whereas this behavior cannot be observed without the diverging part of the outlet nozzle as visible in Fig. 2.16c. For a further investigation of this effect, the vorticity in the outlet region and downstream of the oscillator is shown in Fig. 2.17 for the baseline case with diffuser and the baseline case. In contrast to Fig. 2.16 the vorticity in the outlet region of the oscillator is shown at the moment of the internal jet attachment and not the maximum JDA in order to enhance the visibility of the mentioned effect. For the baseline case with the diffuser (see Fig. 2.17a) a small vortex is visible in the diverging part of the outlet nozzle below the main jet. This vortex is likely to stem from the jet entrainment that creates a flow along the vertical outlet wall towards the jet. At the corner to the diverging part of the outlet nozzle the flow separates and creates a cavity vortex at this location. This behavior was confirmed experimentally

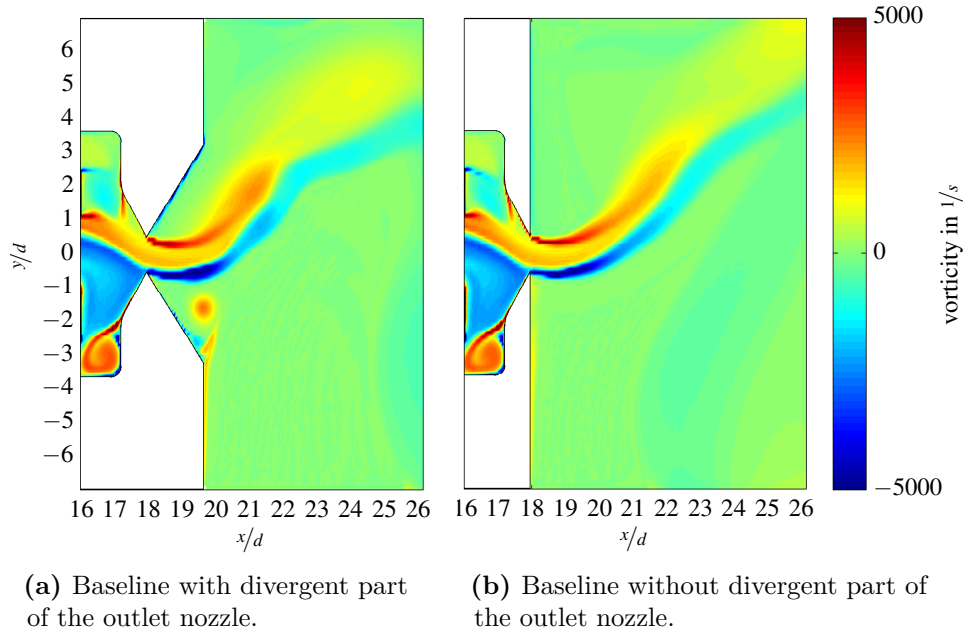


Figure 2.17: Vorticity in the outlet region and downstream of the oscillator.

by Gärtlein *et al.* [28] using a very large oscillator and high speed PIV measurements. Note, that the influence of this outlet behavior is still visible well downstream of the oscillator as the jet bending outside of the oscillator is influenced by this small cavity vortex. For the baseline case (see Fig. 2.17b) the cavity vortex at the outlet nozzle is not observed. It might be possible to even enhance this effect by creating a more distinguished cavity in the region of the outlet nozzle. However, the influence of this behavior on specific applications of these devices is part of future work and not within the scope of this thesis.

As for every flow situation or device pressure loss is an important parameter. In case of the fluidic oscillator the phenomenon of axial pumping is an additional effect that might be crucial for some applications of these devices. As written in Sec. 2.2 axial pumping occurs when the overall pressure loss fluctuates with time, resulting in a oscillating jet momentum at the outlet for a given supply pressure. In order to investigate these two effects, pressure loss and axial pumping, the pressure in the inlet and outlet nozzle was evaluated for the different oscillator geometries. The corresponding time traces of the pressure and the instantaneous pressure loss (i.e., the difference between the two measurement positions) are depicted in Fig. 2.18. For all three outlet geometries the mean pressure loss remains nearly constant at around 5600 Pa, whereas axial pumping is obviously present for all three cases. This can be seen by the three green curves, which resemble the pressure loss across the device.

The amplitude of this oscillating pressure loss is similar for all outlet configurations at around 4900 Pa resulting in a velocity magnitude fluctuation of $\approx \pm 10\%$ in the jet downstream of the outlet nozzle. This oscillation stems from the change in the lateral velocity component, whereas the axial component in the outlet nozzle and, thus, the mass flow through the oscillator remains constant, due to the boundary conditions and the incompressible flow.

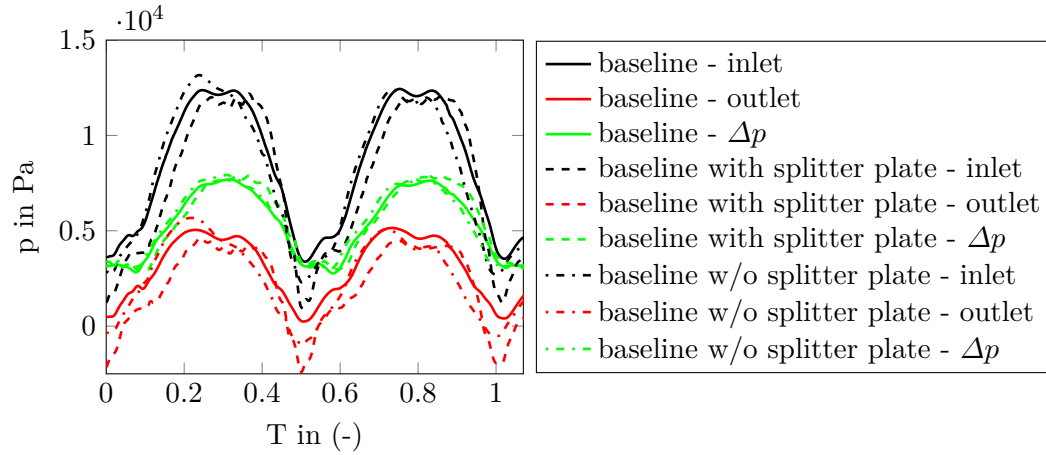


Figure 2.18: Time traces of pressure and pressure loss inside the oscillator for the three outlet geometries.

Influence of the Main Chamber Inlet Geometry

The main chamber inlet geometry, i.e., the main chamber inlet wedges, are expected to have a significant influence on the oscillation as they are responsible for an undesired backflow in the feedback channels (see Sec. 2.2). In the aforementioned section it was suspected that an increase in the distance of the main chamber inlet wedges will increase the oscillation frequency of the device. Additionally, the experiments showed that a small portion of the main jet is separated by these wedges creating the said undesired back flow in the feedback channels, counteracting the main oscillation by inhibiting the attachment of the main jet to the inner block of the oscillator. In order to investigate the influence of this region to the internal flow structures the distance between the main chamber inlet wedges was changed. The resulting geometries are shown in 2.19 together with the overall flow parameters obtained from the respective simulations.

As already expected from the experimental investigations, the oscillation frequency increases with the distance between the main chamber inlet wedges. However, this increase in frequency is not linearly coupled with said distance. The reversed flow in the feedback channels is reduced significantly as can be seen in Fig. 2.20 in the lower negative mass flow through the feedback channel outlet. Figure 2.20 shows the mass

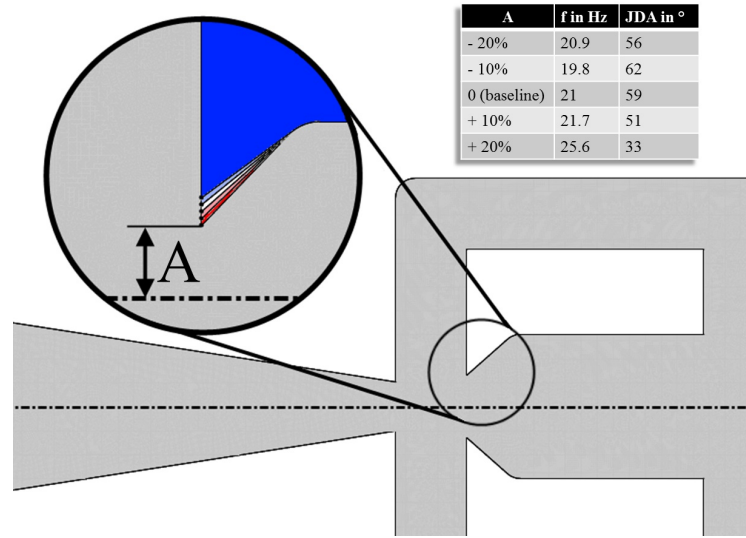


Figure 2.19: Geometrical setup for the different inlet wedges distances.

flow rate through the feedback channel in one oscillation cycle, similar to Fig. 2.14. This reduction in mass flow is accompanied by the mentioned increase in frequency since the reversed flow inhibits the jet attachment in the mixing chamber.

In addition, Fig. 2.20 (right) reveals a change in the mass transport per oscillation cycle for the different configurations. It is visible, that the total amount of transported mass in one oscillation (i.e., the integral under the curves) decreases with decreasing distance between the main chamber inlet wedges. This change in the mass transport needs to be accompanied by a change in either the minimum or the maximum size of the recirculation bubble if the identified oscillation mechanism holds. In order to investigate this, the minimal recirculation bubble size is shown in Fig. 2.21. On the left side the minimal distance between the main chamber inlet wedges is shown, whereas the maximum distance is shown on the right side of the figure. By comparing the two images it is observed that the minimal size of the recirculation region is a lot bigger for the left picture, since the jet is not attaching completely to the inner block. Accordingly, less mass is needed to switch the jet to the other side, because the maximum size of the recirculation region is governed by the distance of the inner blocks. This said distance is not changed though and, thus, the mass transport needed is defined by the minimal size of the recirculation region.

However, this behavior counteracts the expected increase in frequency due to the lower back flow in the feedback channels for a wider distance between the wedges. Even though the reversed flow in the feedback channels is less for the wider inlet wedge distance, a larger amount of mass transport is needed for switching the jet. This counteracting mechanism is responsible for the increase in frequency for the

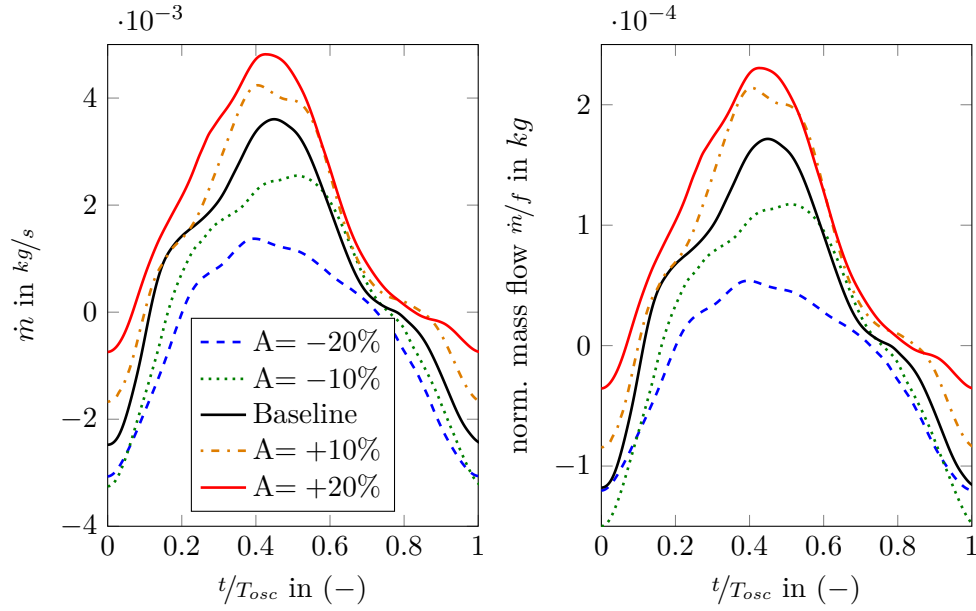


Figure 2.20: Mass transport through the feedback channels for the different inlet wedges.

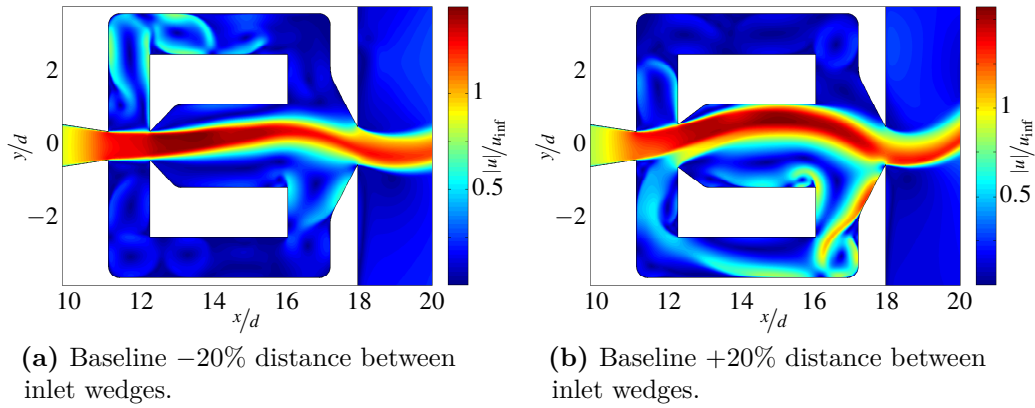


Figure 2.21: Minimum recirculation bubble size for the different inlet wedge distances.

smallest inlet wedge distance, because the needed mass for switching the jet is reduced significantly.

Figure 2.21 also indicates that the jet attachment in the mixing chamber differs for various distances between inlet wedges. The changed attachment topology results in different *JDA*s at the oscillator's outlet. For a larger wedge distance the more upstream wall attachment inside the mixing chamber causes the jet to impinge the surface at the outlet nozzle at a different angle, resulting in a smaller *JDA*. This behavior is consistent up to a decrease of the inlet wedges distance of -20% . For this case, the jet attachment in the mixing chamber is so weak, that the *JDA* is decreasing again.

Influence of Outlet Nozzle Geometry

The outlet nozzle region is another area of interest that was identified by the experimental investigations. Two different changes in the geometry were investigated to see their influence on the flow of the oscillator. First, the angle of the converging section of the outlet nozzle was changed, whereas in a second step the outlet nozzle width was changed. Both changes are visualized in Fig. 2.22 A and B respectively, again, together with the global oscillation parameters frequency and *JDA*.

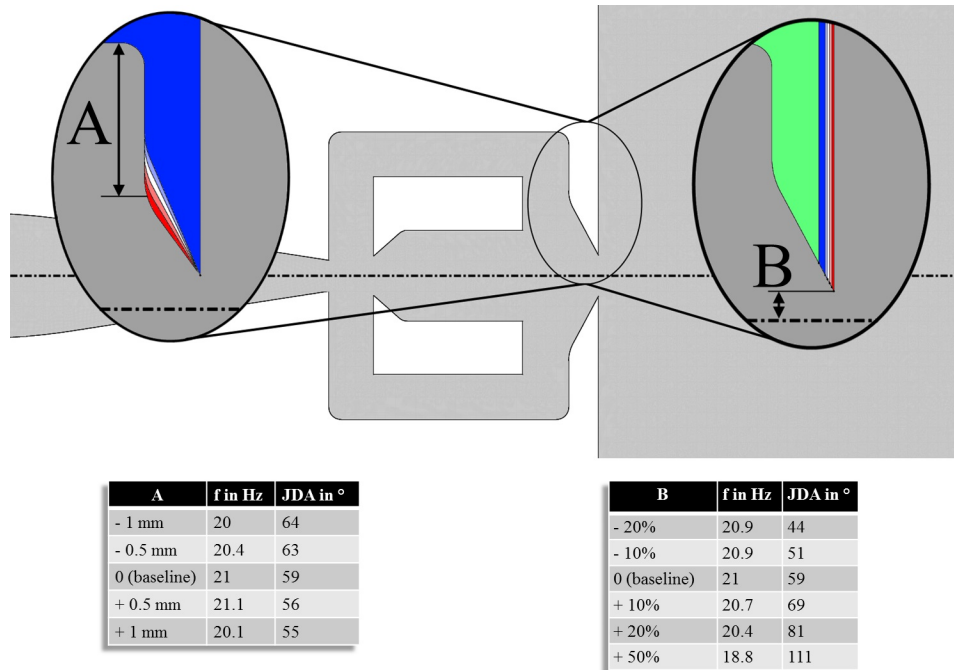
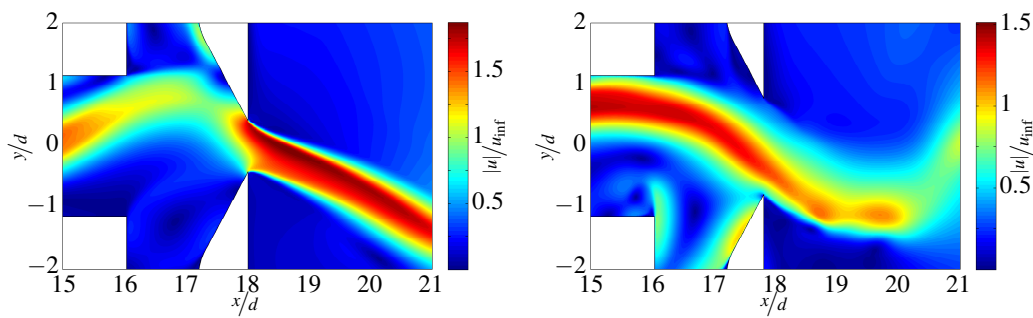


Figure 2.22: Geometric setups of the different outlet nozzles.

Other than expected the frequency is almost constant for all configurations (A and B) except for an outlet opening increase of 50 %, whereas the JDA is very sensitive to changes in that region. For changes in the angle of the outlet nozzle (see Fig. 2.22 A) this sensitivity is expected, since the wall that guides the jet through the outlet nozzle has a different angle itself. Thus, the changes in the JDA follow the changes in the outlet nozzle angle. For the different outlet openings (Fig. 2.22 B) the link between the JDA and the changes in the geometry is not as direct. In Fig. 2.23 the velocity magnitude in the outlet region is plotted for the maximal JDA for both, smallest and largest, outlet nozzle widths.



(a) Baseline with a 20% smaller outlet nozzle.

(b) Baseline with a 50% wider outlet nozzle.

Figure 2.23: Velocity magnitude at the outlet nozzle for different outlet nozzle widths.

Two findings can be drawn from Fig. 2.23: First, the two configurations reach their maximum JDA at different internal flow states. Second, the emanating jet is accelerated in the outlet nozzle for the smaller configuration (Fig. 2.23a). The changes in the JDA for the different outlet nozzle widths are explained by the latter observation. The main jet impinges the wall besides the outlet nozzle and is guided to the outlet nozzle parallel to the wall, i.e. with a defined lateral velocity component. By decreasing the outlet nozzle width the axial velocity component is increased in the nozzle due to the constant inflow and incompressibility of the fluid. Thus, for smaller outlet nozzles the increased axial velocity component is responsible for a smaller JDA compared to wider nozzles. The first finding verifies the statement in Sec. 2.2 that the correlation of the internal and external switching can be altered by changing the outlet nozzle geometry. This behavior was also expected by Gärtlein *et al.* [28] in 2014. For an increase in the outlet nozzle diameter, the maximum JDA is reached when the jet is fully attached to one of the inner blocks, while this is not the case for a smaller outlet nozzle. In Fig. 2.23b it can be found that the jet is not impinging on the outlet nozzle wall but is leaving the oscillator without an additional change in direction at this location. Accordingly, the maximum JDA is correlated to

the internal geometry and flow state alone, whereas Fig. 2.23a reveals that this is not the case for the smaller outlet nozzle. In this case the maximum JDA is created by a redirection of the main jet at the outlet nozzle wall. Thus, the highest JDA is reached at the moment the main jet hits the outlet nozzle wall perpendicularly, which is different from the moment of internal attachment.

This difference in the creation of the maximum JDA can also be found in the pressure distribution around the outlet nozzle that is shown in Fig. 2.24, again for the smallest and widest outlet nozzle configuration at the phase of the maximum stagnation pressure. For the configuration with the smaller outlet nozzle the impingement of the

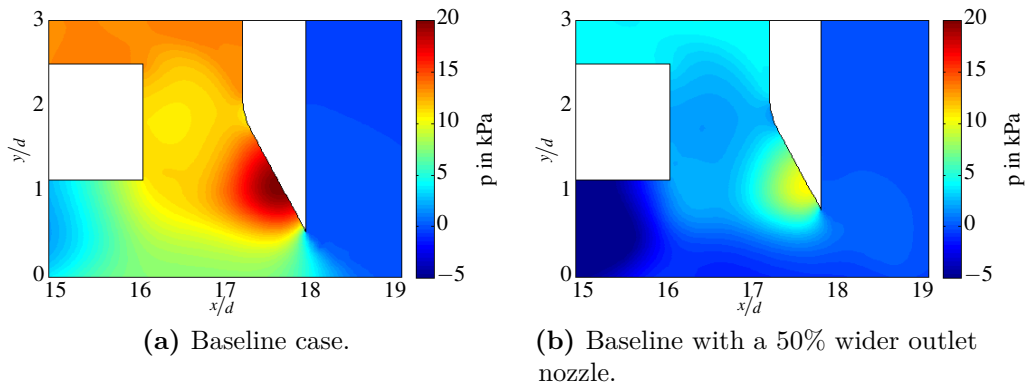


Figure 2.24: Pressure distribution around the outlet nozzle for maximum stagnation pressure for different outlet nozzle widths.

jet at the outlet nozzle wall can be seen in the higher stagnation pressure at that point, whereas this pressure is a lot smaller for the widest outlet configuration. Additionally, this distribution reveals the reasons for the lower frequency incorporating the wider outlet nozzle. The lower pressure at the feedback channel inlet reduces the driving pressure gradient inside of the feedback channel and, thus, reduces the mass transport velocity through said channel. Accordingly, the frequency of this configuration is reduced. This change in the stagnation pressure goes along with a corresponding change in the overall pressure loss of the oscillator. However, the amplitude of the axial pumping is only slightly changing. As the JDA is increasing for the case with the widest outlet nozzle, the amplitude of the axial pumping is slightly increasing. As already mentioned in Sec. 2.2 this is explained by the needed momentum for bending the jet.

However, from the data for these configurations it was possible to verify the driving oscillation mechanism employed in this oscillator, again, like for the previous configurations. The corresponding mass transport plots are omitted, because no additional information is inherent in these plots.

Influence of Feedback Channel Geometry

The feedback channels are, as the main feedback path, widely expected to be the most important parameter affecting the oscillation parameters of the oscillator. Depending on the feedback mechanisms identified in the past (e.g., [19, 35, 54, 87, 101]) for different types of actuators it is expected that either the length or the volume of the feedback channels is expected to be the governing parameter. In order to investigate the influence of a change in the volume and the length of the feedback channels both geometrical changes are investigated separately. Three different parameter changes in the feedback channel geometry are investigated: the length, the volume, and the overall shape of the channels. First, the feedback channels were changed to a round setup. For this simulation the length of the feedback channel (both the inner and outer wall length) were, as well as the overall channel volume, kept constant. In a second step the feedback channel length was increased. Accordingly, the diameter was decreased to keep the feedback channel volume constant. The last step was a variation of the feedback channel volume for a constant length. Since only two-dimensional simulations were performed, it was only possible to keep one length of the feedback channel constant: the inner or the outer wall. In this case the inner wall was kept constant whereas the outer wall was shifted. All three variations and the corresponding overall flow parameters (i.e., frequency and JDA) are shown in Fig. 2.25.

As the oscillation parameters frequency and JDA reveal, each change in the feedback channel configuration is accompanied with changes in the oscillation. For round feedback channels the frequency is decreased while the JDA is almost constant. Whereas the reasons for the constant JDA are expected to lie in the unchanged outlet nozzle geometry, the reasons for the decreasing frequency are not completely understood. Since incompressible water is used as working fluid for the numerical simulations, no convective time lag can be present in the feedback channel. Hence, the pressure loss in the feedback channel should be the driving parameter for the oscillating frequency. In order to investigate this, the pressure difference between the feedback channel inlet and outlet is plotted in Fig. 2.26 for all configurations. Like the mass transport plots the x-axis represents one oscillation period. Due to the decrease in frequency, an increase in the pressure loss is expected for the round feedback channels. This is visible in Fig. 2.26 (left) in the peak pressure difference across the feedback channel. However, as the other plots in Fig. 2.26 reveal the direct dependency of the frequency on the pressure is not found consistently for all feedback channel configurations. An increase in length increases the pressure loss and thus decreases the frequency of the oscillation for the +4 mm case. In contrast to that, the pressure loss profile is only shifted in time for the +8 mm case, but still the frequency is decreased.

A similar non-conclusive behavior can be found for an increasing feedback channel volume. For volume changes up to 25% the pressure loss across the feedback channel

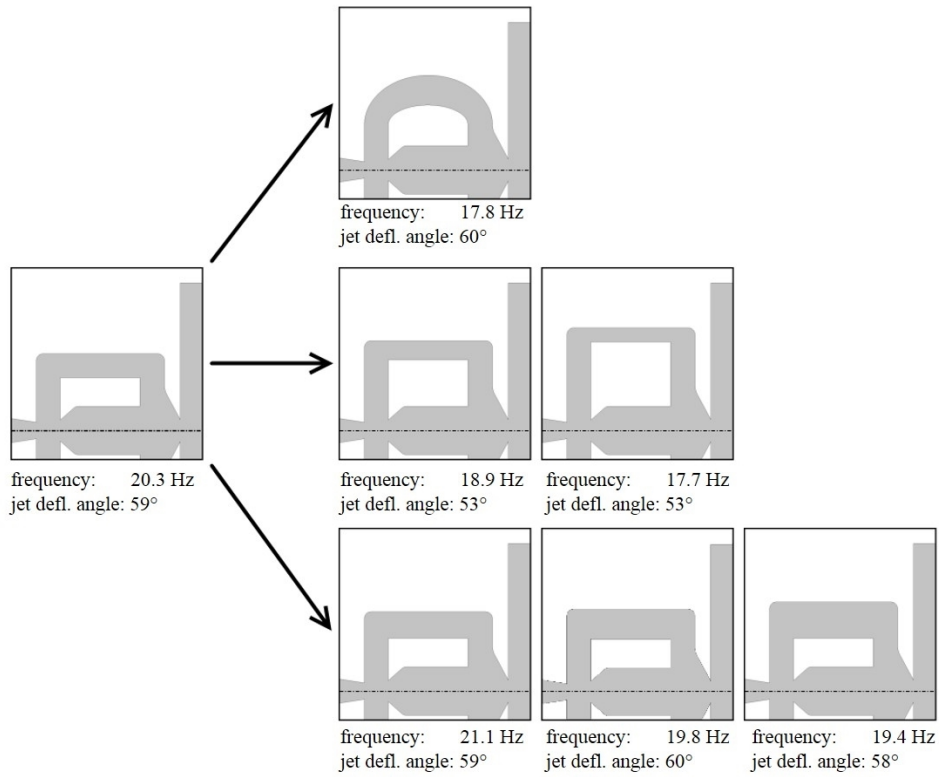


Figure 2.25: Geometries of the different feedback channels.

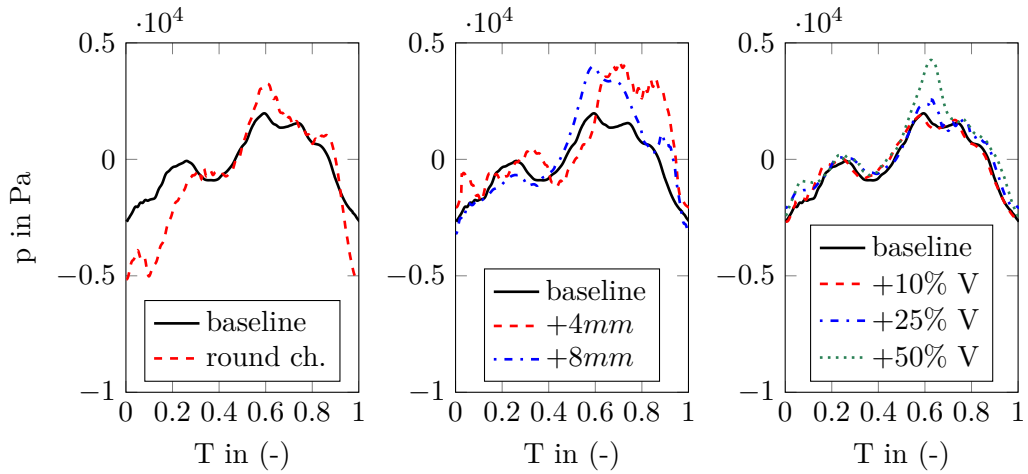


Figure 2.26: Pressure loss across the feedback channel for the different feedback channel geometries.

is almost constant, whereas the frequency is changing. Since no significant changes are observed in the mass transport through the feedback channels per oscillation cycle, these plots are omitted. However, according to these findings, the reasons for the changes of the frequency are not caused by a single change in one of the flow paths. They are rather a consequence of several changes within the internal flow structures of the fluidic oscillator that cannot be identified with the available data.

Influence of Aspect Ratio

In order to finalize the parametric study of the oscillator's geometry and control the two dimensional numerical approach, the influence of different aspect ratios of the fluidic oscillator is investigated. The aspect ratio of the oscillator is defined as the ratio between the power nozzle width and the depth of the oscillator geometry. The influence of the aspect ratio on the oscillation parameters of the oscillator is an inherent three-dimensional phenomenon and, thus, cannot be evaluated using the two-dimensional numerical approach. Hence, the influence of the aspect ratio was evaluated experimentally. The oscillator geometry was manufactured out of acrylic glass with 5 different aspect ratios. The experimental setup was identical to the setup of Sec. 2.2, that is the oscillator is placed inside a water tank with a sufficiently large distance to the water surface. The oscillation frequency was determined using a hydrophone measurement in the outlet region of the oscillator (see Fig. 2.3). All configurations were tested using water with a temperature of ≈ 290 K and the volumetric flow rates were measured with a calibrated rotameter. The different configurations and their respective Reynolds numbers (based on the hydraulic diameter) are listed in Tab. 2.2.

Table 2.2: Aspect ratios, the volumetric flow rates and the Reynolds numbers of the investigated configurations.

aspect ratio	volume flow rates L/h	Reynolds numbers
0.25	90 – 155	10800-18660
0.5	90 – 250	9000-25000
1	90 – 250	6700-18000
1.25	90 – 312	6000-20800
2	90 – 500	4500-25000

The resulting frequencies for the different aspect ratios are plotted against the flow rate in Fig. 2.27a. Again, one can see the frequency's linear dependency on the volumetric flow rate. As expected the frequency ranges for the different aspect ratios are different, because the velocity inside the oscillator at the same flow rate is higher for smaller aspect ratios. Following this, the frequency versus flow rate plots should collapse to one single line if the frequency is plotted against the jet velocity that can be calculated by the flow rate and the cross-sectional area of the

oscillator. This plot is shown in Fig. 2.27b. The three higher aspect ratio oscillators collapse to one single curve, whereas the two smaller aspect ratios show a little higher slope in the frequency – flow rate dependency. This stems from the boundary layer effects on the upper and lower wall of the oscillator’s geometry. The boundary layers reduce the effective oscillator height and increase the jet velocity more than the area reduction alone. Accordingly, the frequency increases. For higher aspect ratios these boundary layer effects are less significant. This finding verifies the validity of the

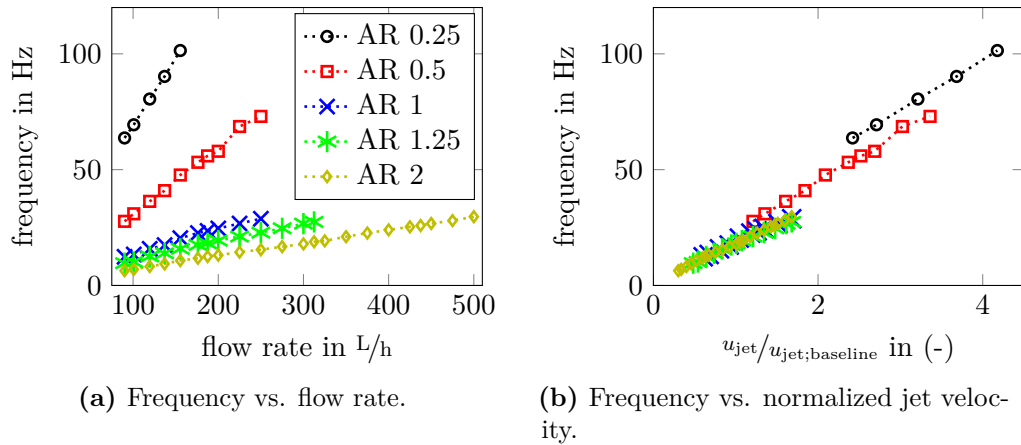


Figure 2.27: Frequencies of the different aspect ratio fluidic oscillators vs. the flow rate or jet velocity, respectively.

two-dimensional approach, since a change in the aspect ratio only results in a shift of the oscillation parameters. If now the jet velocity inside the oscillator is kept constant, the oscillatory parameters remain constant as well. In addition to the verification of the two-dimensional approach this finding confirms the found switching mechanism. The scaling of the oscillators depth goes along with an identical scaling of the main recirculation region in the mixing chamber, thus, for the same jet velocity the mass which is transported through the feedback channels is scaled with the same factor and the oscillation frequency of the device remains constant.

Following the findings of the numerical and experimental parametric study, it is possible to design and tune the geometry of the fluidic oscillator to exhibit the needed flow and oscillatory parameters. Knowing the target values for the frequency, volume flow, pressure loss, and jet deflection angle it is possible to create the needed fluidic oscillator based on the knowledge that is gained in this chapter. This knowledge is now used to create the needed fluidic oscillators for the mixing of fuel and air in the SEC process. The resulting mixing enhancements are investigated in the next section.

2.4 Mixing Enhancement in the SEC-Configuration

By knowing the underlying oscillation mechanism (see Sec. 2.2) and the effects of changes in the most sensitive regions of the geometry, it is not only possible to create a fluidic oscillator with the desired oscillation parameters but also to predict the internal flow structures of this device using the validated numerical model. Based on this experience, two oscillator geometries were designed. The goal was to create oscillation frequencies in the range of 10-100 Hz for the target volumetric flow rates of water.

The corresponding frequencies for the SEC test rig are in the range of 1-10 kHz, while keeping the presented dimensionless parameters (Reynolds and Strouhal number) of the SEC process constant. Since the estimated firing frequency for the SEC is around 250 Hz (see Sec. 1.1.1) the oscillation frequency must be sufficiently high to assure a multitude of oscillation cycles during one combustor filling. The outlet nozzle of the oscillators was designed to create a jet deflection angle of approximately 60° to cover a broad area in the mixing section. These fluidic oscillators were then integrated in the SEC mixing test rig employing three different aspect ratios to investigate their ability to create the needed mixing quality for the SEC¹.

In 2012 Lacarelle *et al.* [59] published a work on the enhancement of the passive scalar mixing using fluidic oscillators. They investigated the mixing properties of a spatially oscillating jet in contrast to a steady round jet in a cross flow configuration. Their configuration featured a rectangular test section in a water test rig, where the jets emanated from a central lance outwards. The experiments showed that an oscillating jet not only increases the passive scalar mixing between the tracer dye and the flow but also reduces the mixing quality's dependency on the jet in cross flow momentum. These results are very promising regarding the SEC process since a high mixing quality close to the injection position is needed in this combustion process. In addition, this high quality mixing must be independent from the jet in cross flow momentum because the amount of fuel injected must be adjusted even during the injection process to create the necessary stratification of equivalence ratios (see 1.1.1). However, even though the results of Lacarelle *et al.* are promising the SEC-configuration is different. The SEC process takes place in a narrow tube and the fuel is injected inwards from the outside walls in contrast to the outwards directed injection of Lacarelle *et al.* This inward directed injection in the narrow flow passage leads to a collision of the jets in the middle of the tube, resulting in a different flow situation. In addition, the short filling time per combustion cycle results in very high velocities for fuel and air (close to 250 m/s for the air) in the combustion configuration. Thus, the findings of Lacarelle *et al.* need to be reevaluated and verified for the SEC configuration.

¹ This section is based on and was partly published by Bobusch *et al.* in 2014 [15]

The details of the SEC process can be found in Sec. 1.1.1. As a quick recap a brief summary of the mixing requirements of this new combustion technique is shown here:

1. The mixing needs to be very fast in order to avoid premature ignition (i.e., regions where the ignition delay is too short).
2. The mixing must be homogeneous in the radial plane of the combustion tube.
3. The axial stratification of equivalence ratio demands for very low mixing in the axial direction.
4. The mixing must be independent from the fuel volume flow (i.e., jet in cross flow momentum) to have a broad range of possible equivalence ratios for base load, part load, and idle operation.

In order to verify the findings of Lacarelle *et al.* [59] and to investigate the mixing capabilities of other injection geometries several jet in cross flow configurations are investigated in this section. The tested setups are: 1 – round jet, 2 – rectangular jet, 3 – slit, and 4 – the spatially oscillating jet (i.e., fluidic oscillator). Since the jet in cross flow configuration is the least complex, most robust and most common way to mix two fluids, a vast variety of investigations were published in the past decades. The round jet in cross flow was not only investigated as a steady jet (e.g., [4, 49, 50, 86]) but also as a modulated/pulsed jet (e.g., [26, 44, 45]). The rectangular jet in cross flow is not as thoroughly described as the round jet, but recently this configuration was analyzed more extensively as well (see [76, 104]). The slit injection can be seen as a two-dimensional jet in cross flow with infinite depth or discrete jets with infinite small spacing. Regarding the spatially oscillating jet in cross flow only a few publications can be found. Nathan *et al.* [69] extensively investigated jet parameters and their impact on the mixing for an co-flow configuration. Several oscillating devices, mechanical and fluidic, were tested. It was shown that the oscillation enhances the mixing especially close to the fuel inlet. The already mentioned work of Lacarelle *et al.* [59] not only confirmed these findings in a cross flow injection, but also found that the spatial oscillation reduces the dependency of the mixing quality on the jet in cross flow momentum, as already mentioned.

Following these publications the spatially oscillating jet in cross flow injection is the most promising configuration to fulfill the demands of the SEC. In order to compare and assess the mixing quality of the different configurations they were investigated using a water test rig that is described in the next section. It is known from literature (e.g., [23, 60]) that the mixing of water with dye is a good indicator for the fuel-air mixing in combustion systems. In addition the usage of water as the main fluid reduces the needed flow velocities for the same Reynolds and Strouhal number (see Sec. 1.1.3).

2.4.1 Experimental Setup

A model of the fuel injection section of the SEC setup was built in order to investigate the mixing processes inside the combustion tube. In Fig. 2.28 a sketch of the experimental setup and in Fig. 2.29 a more detailed cut through the dye inlet section is shown. The combustion tube has an inner diameter of 40 mm, a length of about

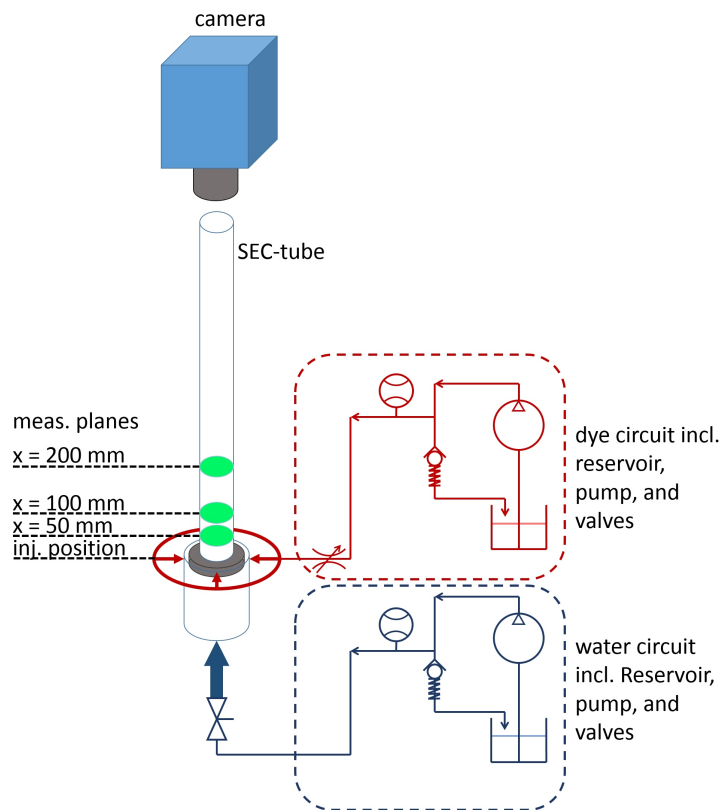


Figure 2.28: Sketch of the test rig.

800 mm, and is made of acrylic glass. Upstream of the main tube the injection section is located with two inlets. First, the axial main inlet controlled by a 25 mm on/off-valve, followed by a diffuser to increase the inner diameter up to the mentioned 40 mm without flow separation at the walls. Second, the radial dye inlet that is realized by making use of interchangeable disks for the fuel injection. This disk is shown in Fig. 2.29 in yellow for a better visibility. More details and pictures of the investigated injection disks will be shown later in this section. The two inlets are connected to two separate water circuits, which are both equipped with pressure driven valves in the circuit to generate the needed constant pressure upstream of the control valves. As already mentioned the main inlet was driven by an on/off valve whereas the fuel line was controlled using an electrically driven proportional valve.

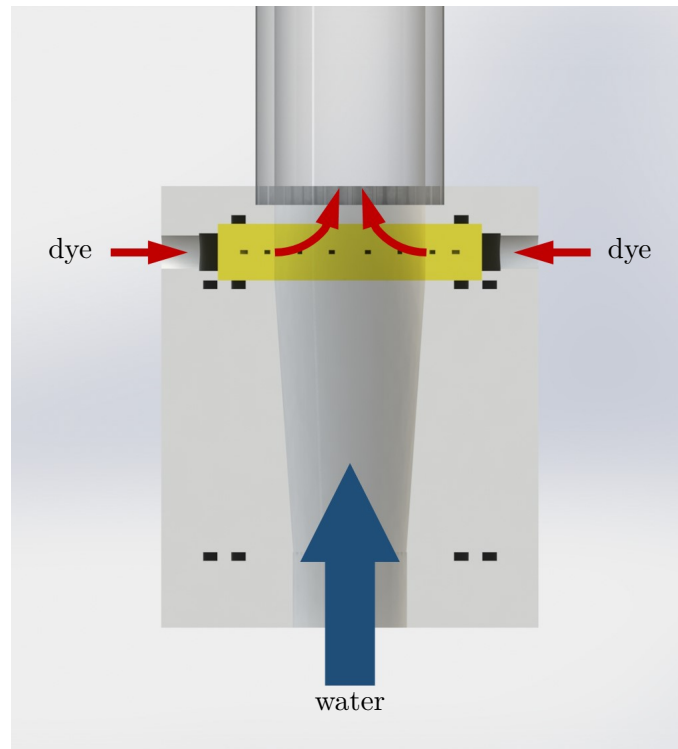


Figure 2.29: Cut through the fuel inlet section of the water test rig.

Injection Configurations

Four main types of injection geometries, denoted as “round”, “rectangular”, “slit” injections, and “spatially oscillating (fluidic)” jets were investigated. This resulted in 21 different configurations (see Tab. 2.3), since different sizes and numbers of injectors for each type were employed to create a broad variety of configurations. The spatially oscillating jets were created using fluidic oscillators, which were, as mentioned above, designed based on the numeric parametric study. The overall geometry was scaled and adapted to fit the injection setup and to create frequencies in the range of 10 – 100Hz for the desired volumetric flow rates. These frequencies correspond to frequencies around 1 – 10kHz for the SEC test rig with similar Reynolds and Strouhal numbers (based on the SEC process). The type of oscillators used was described in detail in Sec. 2.2. The oscillatory parameters of the scaled devices were determined by numerical simulations, which were carried out with a validated numerical model (see Sec. 2.3). The oscillation frequency was calculated from the numerical simulations using a velocity time trace inside the main chamber.

For each main type several different cross-sectional areas were tested to create a wide range of jet in cross flow momentums as well as different frequencies for the

fluidic oscillators. The jet in cross flow momentum J is defined as follows

$$J = \frac{\rho_{\text{jet}} u_{\text{jet}}^2}{\rho_{\text{cross flow}} u_{\text{cross flow}}^2}, \quad (2.4)$$

where u_{jet} denotes the jet flow velocity and $u_{\text{crossflow}}$ the main flow velocity. In addition to the different cross-section areas, different amounts of injection ports were used to investigate the influence of their radial distribution and further increase the range of J . This broad range of momentum ratios is needed in the SEC process as the fuel mass flow is changed within each injection cycle, as mentioned in Sec. 1.1.1. A summary of all investigated configurations including the main flow parameters is presented in Tab. 2.3. The Reynolds number of the main flow was $Re = 31,280$ and thus, a fully turbulent flow was assured. The presented aspect ratio of the rectangular orifices and the fluidic oscillators is defined as the ratio between the axial and the circumferential side of the rectangular channel $AR = l_{\text{axial}}/l_{\text{circ}}$. To give an idea of the different injection geometries a three-dimensional model of four of the used injector disks is shown in Fig. 2.30. For better visibility of the fluidic oscillator, a cut was made through the material to show the geometry. Even though the slit injection (shown in blue in Fig. 2.30) is fed through discrete ports an even velocity distribution along the slit was assured.

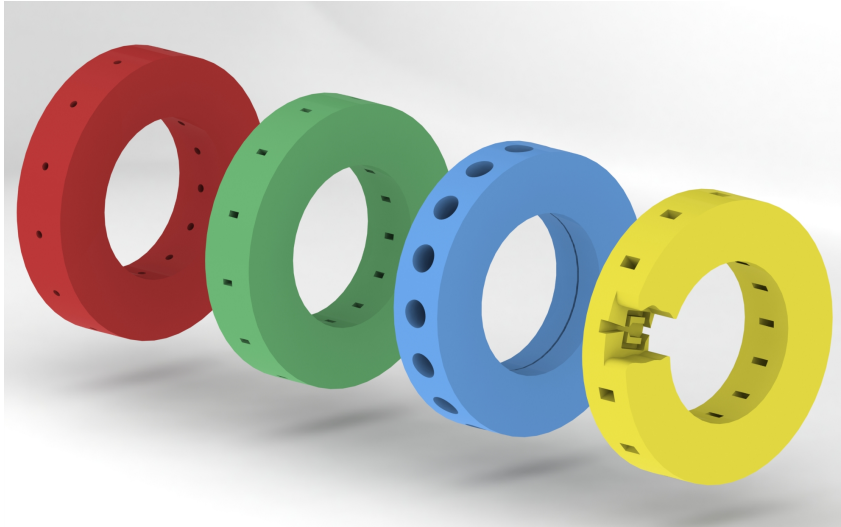


Figure 2.30: Colored CAD-Models of the four different injector types (from left to right): round holes (red), rectangular holes (green), slit (blue), and fluidic oscillator (yellow).

Measurement Technique and Unmixedness Parameter

Table 2.3: Investigated injector geometries including the main parameters. All units in mm or mm² respectively.

Disk	Outlet geom.	Outlets	Type	d_h	A_{Outlet}	aspect ratio	$Re_{\text{jet; min}}$	$Re_{\text{jet; max}}$	J
⊙small;13	round	13	orifice	1.40	20.01	—	4479	11143	16.7-103.6
⊙medium;13	round	13	orifice	1.90	36.86	—	3542	8371	5.7-34.2
⊙large;13	round	13	orifice	2.40	58.81	—	3059	7519	2.7-16.0
⊙small;7	round	7	orifice	2.00	21.99	—	6249	14485	13.2-82.4
⊙medium;7	round	7	orifice	2.60	37.17	—	4916	11361	5.8-31.2
⊙large;7	round	7	orifice	3.30	59.87	—	3787	9984	2.2-15.0
▣small;13	rectangle	13	orifice	1.26	21.06	0.72	3909	9493	15.8-93.4
▣medium;13	rectangle	13	orifice	1.69	37.83	1.29	3359	7138	6.4-32.6
▣large;13	rectangle	13	orifice	2.00	58.89	2.015	2548	5732	2.6-13.4
▣small;7	rectangle	7	orifice	1.73	21.28	0.76	5574	12668	14.1-87.9
▣medium;7	rectangle	7	orifice	2.29	37.66	1.345	4183	9983	4.5-31.0
▣large;7	rectangle	7	orifice	2.71	58.80	2.1	3308	8127	2.4-14.7
⇔small;13	rectangle	13	fluidic osc.	1.31	23.17	0.72	3430	8092	11.2-62.5
⇔medium;13	rectangle	13	fluidic osc.	1.78	41.61	1.29	2943	7223	4.4-26.7
⇔large;13	rectangle	13	fluidic osc.	2.17	68.21	2.015	1889	5618	1.2-10.9
⇔small;7	rectangle	7	fluidic osc.	1.79	23.20	0.76	4098	11088	8.6-62.6
⇔medium;7	rectangle	7	fluidic osc.	2.40	40.90	1.345	3303	9726	3.1-26.7
⇔large;7	rectangle	7	fluidic osc.	2.87	64.09	2.015	2516	7828	1.3-12.2
≡small	slit	1	—	0.40	25.13	—	893	2728	8.2-76.3
≡medium	slit	1	—	0.60	37.70	—	867	2701	3.4-33.3
≡large	slit	1	—	0.80	50.27	—	891	2674	2.0-18.4

Planar Laser Induced Fluorescence (PLIF) was employed to investigate the mixing quality of the different configurations. At three axial positions downstream of the dye injection radial planes were investigated with a high-speed camera from the downstream side of the tube. A shutter frequency of 500 Hz minimizes the blurring of the image due to too long exposure times.

For each of these 21 configurations, 6 fuel flow rates were investigated at the mentioned three axial positions. Recording 1,632 snapshots for each of these tests over 615,000 pictures were taken in total. Each picture was corrected for background reflections and normalized using a homogeneous picture with the maximum dye concentration. It was assured that the dye concentration was low enough to be well within the linear regime of the fluorescence response. From the normalized images containing pixel values between 0 and 1, the two unmixedness parameters U_x and U_t were calculated, which represent the spatial and the temporal mixing quality respectively. Based on the work of Danckwerts [25], the parameters are defined as follows:

$$U_x = \frac{\sigma_x^2}{\sigma_0^2} = \frac{\sigma_x^2}{C_\infty(1 - C_\infty)}, \quad (2.5)$$

$$\text{where} \quad \sigma_x^2 = \frac{1}{N_i - 1} \sum_{i=1}^{N_i} (\bar{C}(i) - C_\infty)^2. \quad (2.6)$$

The mixture variance of the temporally averaged concentration field $\bar{C}(i)$ is denoted by σ_x^2 . The temporally averaged concentration field $\bar{C}(i)$ itself is recorded by the N_i camera pixels and is defined in Eq. 2.6. The variance of an unmixed stream (σ_0^2) is calculated from the dye concentration C_∞ in the pure “fuel” stream. The spatial unmixedness parameter U_x represents the average spatial mixing quality and gives a value between 0 (perfectly mixed) and 1 (not mixed at all). The temporal unmixedness is investigated using the parameter U_t , which employs the variance of all the concentration records. It is defined as:

$$U_t = \frac{\sigma_t^2}{\sigma_0^2} = \frac{\sigma_t^2}{C_\infty(1 - C_\infty)}, \quad (2.7)$$

$$\text{where} \quad \sigma_t^2 = \frac{1}{N_i N_t - 1} \sum_{i=1}^{N_i} \sum_{t=1}^{N_t} (C(i,t) - C_\infty)^2. \quad (2.8)$$

N_t is the number of snapshots recorded during one measurement sequence (1,632 in this work). According to Eq. 2.8, U_t captures both spatial and temporal fluctuations in the concentration. These unmixedness parameters can be used as a first measure to evaluate the mixing quality of a given injector geometry.

2.4.2 Experimental Results

Remember that the SEC raises some critical claims on the mixing process as stated in Sec. 1.1.1. By making use of the definitions and parameters introduced in the last section it is possible to reduce these claims to two values. First an almost instant mixing with a high spatial mixing quality close to the injection position (i.e., a low U_x), and, second, a mixing quality that is independent from the volumetric flow rate of the fuel (i.e., independent of J). For giving a first impression of the experimental results, pictures of the averaged and normalized concentration field C in the first measurement plane are shown in Fig. 2.31 for the four main configurations together with the corresponding concentration histograms. For a good first overview for each of the four main injector classes a representative case was selected. Due to reflections on the inside of the combustion tube only half of the measurement plane was evaluated and plotted here. The time averaged concentration for the round jets in cross flow is shown in the top row of Fig. 2.31. The concentration is higher at the outside of the measurement plane, whereas it is lower than the mean value on centerline of the tube. The histogram on the right side of the plot reveals a rather broad distribution of concentrations. The spatial unmixedness parameter of this configuration is $2.718 \cdot 10^{-3}$. For the rectangular jets in cross flow (the second row from the top) the concentration seems to be more even in the measurement plane and, thus, the spatial unmixedness parameter for this configuration is $1.149 \cdot 10^{-3}$. Accordingly, the histogram of the concentration on the right side of the plot displays a much sharper peak. However, like for the round jets a region of high concentration can be found in the vicinity of the wall. This region of high fuel concentration has to be seen critical, because a cooling film of pure air at the wall is needed for the SEC process. With such a region of high concentration close to the wall it is more likely that a combustible mixture is formed between the wall cooling film and the main flow.

For the third main configuration, the fluidic oscillators (third row from the top) the concentration is well distributed inside of the combustion tube resulting in a spatial unmixedness parameter of $0.6958 \cdot 10^{-3}$. The corresponding histogram has an almost rectangular shape around the mean value with a little narrower distribution than for the rectangular jets in cross flow. In the bottom row of Fig. 2.31 the concentration distribution of disk $=_{\text{small}}$, i.e., a slit with an hydraulic diameter of 0.4 mm, is shown. The concentration is a little less evenly distributed than for the fluidic oscillators (disk $\Leftrightarrow_{\text{small};13}$) as can be seen in the histogram on the right side of the time averaged concentration field. This results in an unmixedness parameter of $1.425 \cdot 10^{-3}$. Again, as for the round and rectangular jet in cross flow a region of higher concentration can be found near the wall of the tube.

However, even though Fig. 2.31 gives a first impression of the results the vast amount of data (see Tab. 2.3) demands for a more global investigation of the different mixing qualities, especially from the SEC point of view. This investigation is based

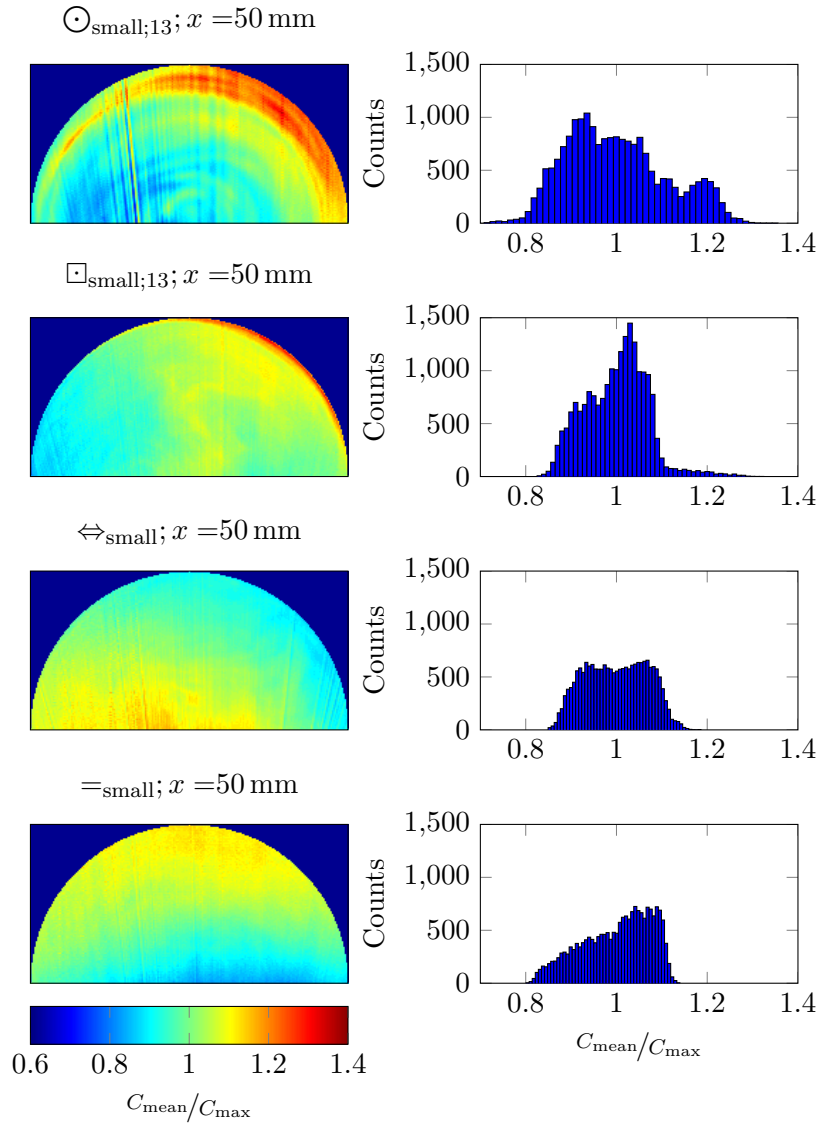


Figure 2.31: Time averaged concentration at measurement plane $x = 50$ mm for disks $\odot_{\text{small};13}$, $\square_{\text{small};13}$, $\Leftrightarrow_{\text{small};13}$, and $=_{\text{small}}$

on the defined unmixedness parameter. Incorporating the 21 different configurations (see Tab. 2.3) a broad area of different jet in cross flow momentums J was realized for each configuration. This range can be divided into three sub ranges, since three different sizes for each main configuration (e.g., round holes) were tested. With each configuration 6 different dye flow rates and, thus, momentum ratios were investigated. In Fig. 2.32 the spatial unmixedness parameter U_x at the first measurement plane, i.e., 50 mm downstream of the injection position, is plotted versus the jet in cross flow momentum for every configuration divided in the said three sub regions.

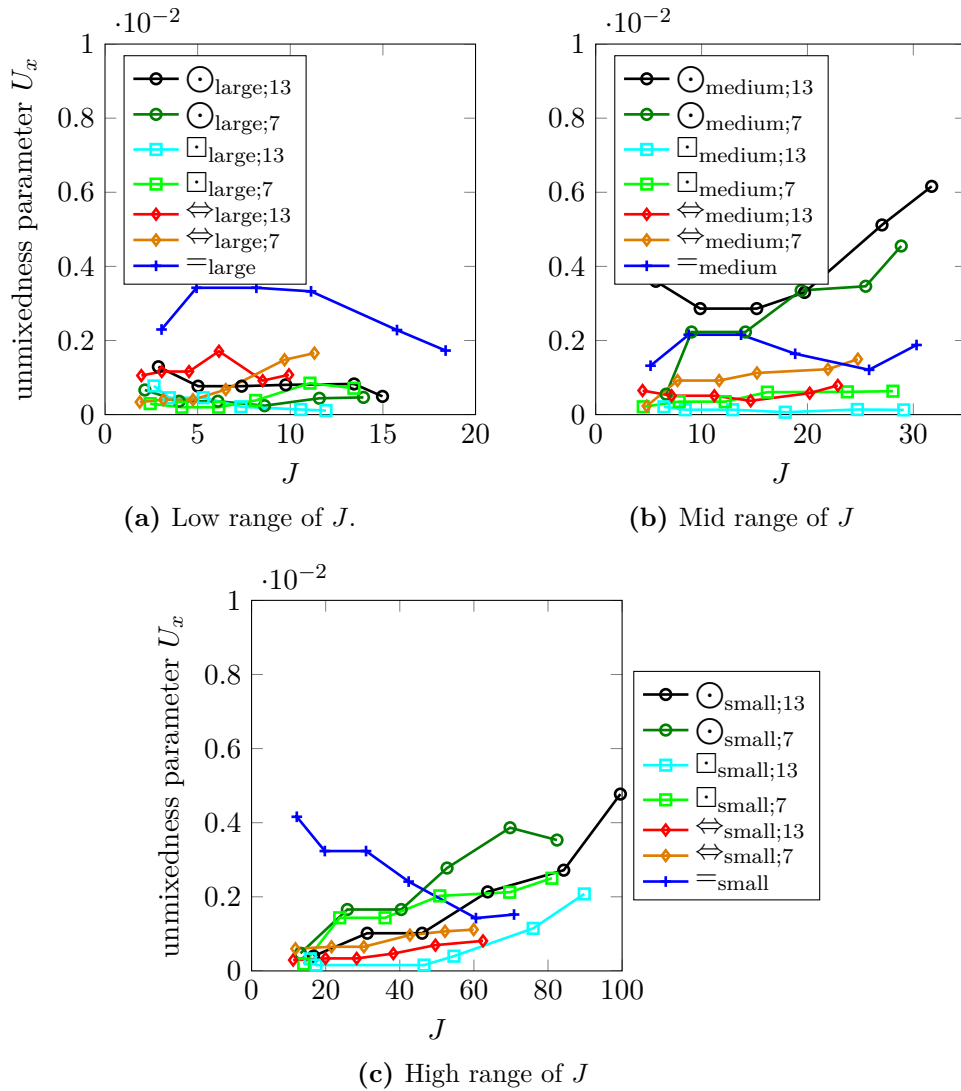


Figure 2.32: Spatial unmixedness parameter U_x at measurement plane $x = 50$ mm for all injection disks.

Several conclusions can be drawn from Fig. 2.32. For the lowest jet in cross flow momentum region (see Fig. 2.32a) it is found that the slit injection (marked with crosses) creates a much lower mixing quality than all the other configurations. The rest of the configurations are pretty similar, however the fluidic oscillators seem to result in a slightly lower mixing quality (higher U_x) than the rectangular and round holes. For the middle region of J (Fig. 2.32b) the slit injection gives a low mixing quality again. Only the round holes are creating a far worse mixing quality in this region. The reason of these results for the round jet in cross flow injection is not completely understood, but it seems that the collision of the multiple jets in the center of the mixing section creates different effects for different regions of J . The rectangular jets and the fluidic oscillators create similar mixing qualities in the same range of U_x as for the first range of J . For the highest range of J (see Fig. 2.32c), the dependency of the jet in cross flow momentum J is clearly visible for all configurations except the fluidic oscillators. The slit injection creates an increasing mixing quality whereas the round and rectangular holes create a decreasing mixing quality with increasing J . The fluidic oscillators result in an almost independent mixing quality that is higher than the round jets, the slit injection and one configuration employing rectangular holes. Unfortunately, it was not possible to further increase the momentum ratio for the fluidic oscillators. However, due to the slope of the unmixedness curves it is assumed that the mixing quality will only slightly decrease for higher momentum ratios J .

Wrapping up the conclusions drawn from Fig. 2.32 it can be stated that the slit injection is not only creating a worse mixing quality than, for example, the fluidic oscillators but also a mixing quality dependent on the jet in cross flow momentum. The same was found for the round jets. These preliminary results confirm the findings of Lacarelle *et al.* [59], who found out that a spatially oscillating jet in cross flow results in an increased passive scalar mixing compared to a steady jet. The dependency of U_x on the jet in cross flow momentum J results in a broad range of unmixedness parameters for the two configurations slit and round jet, which is even more evident by grouping together all configurations of the same type and plotting the ranges of unmixedness parameters they create. This is done in Fig. 2.33, where disks 1 – 6 (i.e. all round jets) are summed up in the black range, 7 – 12 (rectangular jets) in the red, 13 – 18 (fluidic oscillators) in the green, and finally the slits (19 – 21) in the blue range. The slits and the round holes give a lower mixing quality than the rectangular holes and the fluidic oscillators. The rectangular holes show a better mixing quality (lower unmixedness parameter) on the lower side of the range than the fluidic oscillators but a worse mixing quality than the fluidic oscillators for the upper boundary of the range. Crossing out the round jets and the slit injection configuration the rectangular jets and the fluidic oscillators are left to be further investigated to find out the configuration best suited for the SEC.

Due to the different injection disks and configurations several parameters and their influence on the mixing can be investigated besides the jet in cross flow momentum J .

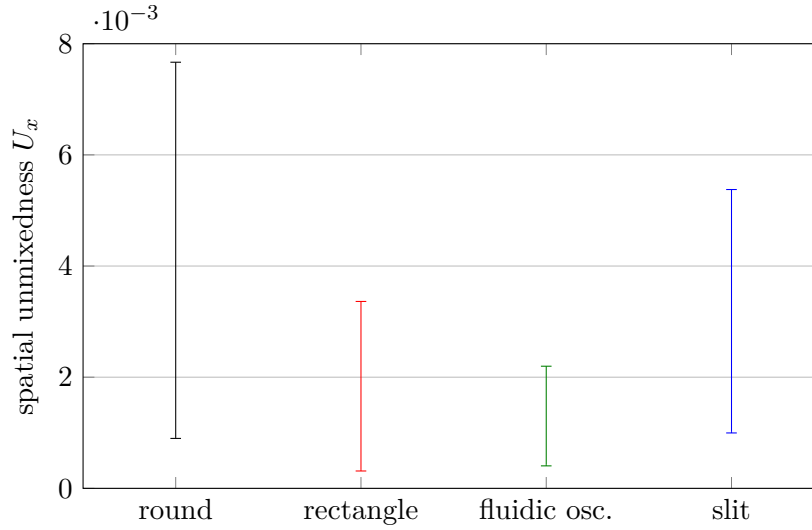


Figure 2.33: Ranges of spatial unmixedness parameter U_x at measurement plane $x = 50$ mm for the four different geometries: round jet, rectangular jet, fluidic oscillator, and slit.

In addition, to the total number of injection points and the aspect ratio of the injector geometry for both types of disks, the frequency of the oscillators that is depending on the volumetric flow rate and the geometry of the device is an interesting parameter. At first the influence of the total number of injection openings is shown in Fig. 2.34 in form of the unmixedness parameters for the three disks with 13 rectangular holes and the disks using 7 rectangular holes at the three different measurement planes. Depending on the downstream distance of the investigated measurement plane the influence of the difference in the number of injection ports is more or less clear. For the SEC a quasi-instantaneous mixing is needed, so the first measurement plane (plain lines) is of dominant interest. For the highest range of J (see Fig. 2.34c) the mixing quality of disk $\square_{\text{small};13}$ employing 13 injection ports is higher for the full range of jet in cross flow momentums J . This behavior is also observable for the disks with the medium range of J (i.e., disk $\square_{\text{medium};13}/\square_{\text{medium};7}$ in Fig. 2.34b). Only for the lowest range of J (Fig. 2.34a) no clear trend can be found. In this range of jet in cross flow momentums $\square_{\text{large};13}$ (i.e., 13 injection ports) performs worse than $\square_{\text{large};7}$ with 7 injectors at low values of J . This behavior changes as the mixing quality decreases for $\square_{\text{large};7}$ with increasing J , whereas the opposite behavior can be found for $\square_{\text{large};13}$.

Regarding the other two measurement planes the difference in mixing quality vanish resulting in similar mixing qualities for the most downstream plane (dotted lines). Following these findings it can be stated that a higher number of injection ports is leading to a better mixing quality for the given injection situation. For the

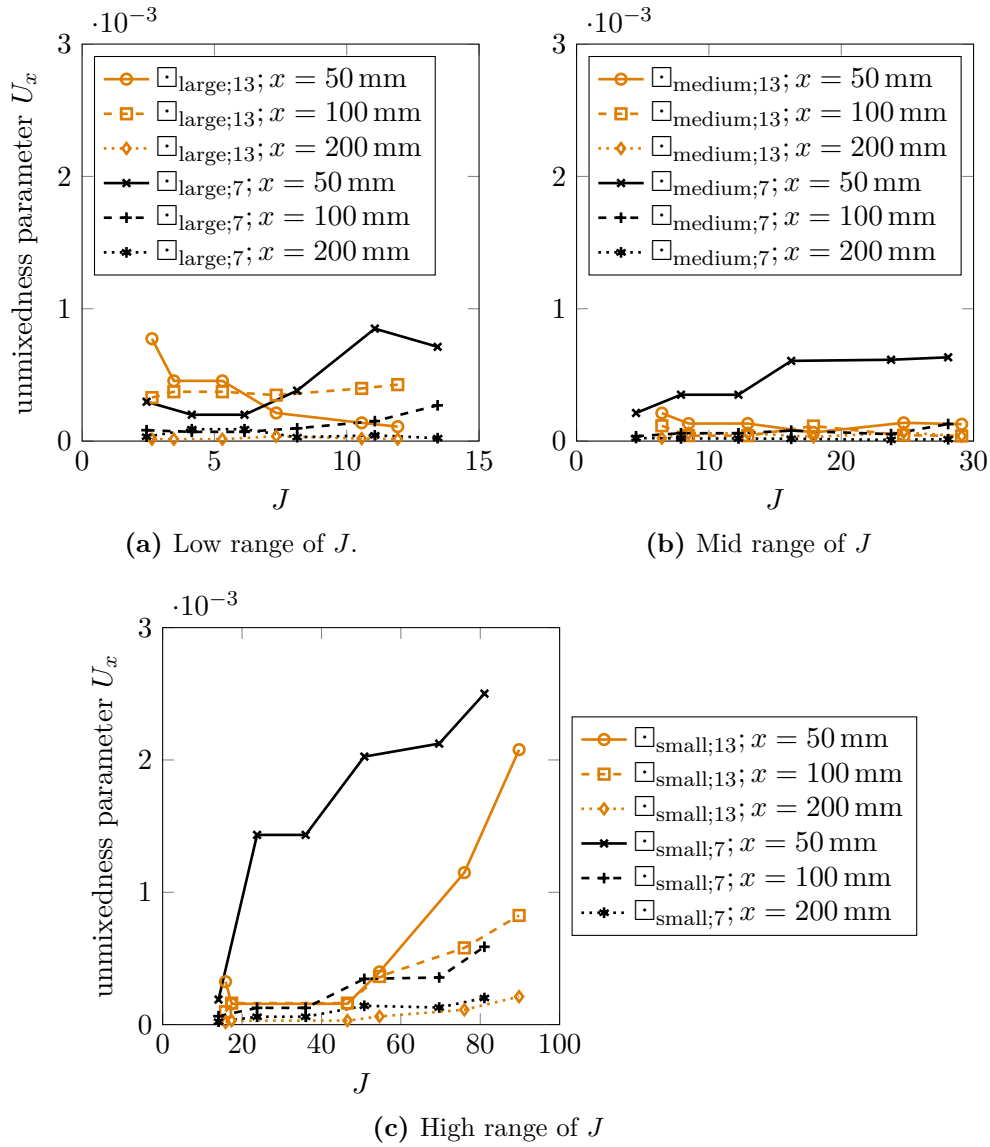


Figure 2.34: Spatial unmixedness parameter U_x at the different measurement planes for all disks with rectangular orifices.

fluidic oscillators this comparison is not that simple, since bigger oscillator geometries are needed for the case with less injectors and the frequencies of these oscillators are lower. To gain a deeper insight into the mixing mechanisms of the spatially oscillating jet two oscillators with different geometrical dimensions and three different aspect ratios were manufactured. Note that the range of possible volumetric flow rates is defined by the dye pump of the system, which results in a different frequency range for all disks.

From literature, it is known that the frequency of these oscillators scales linearly with the volumetric flow rate [12, 13]. The frequency of the used oscillators was calculated from numerical simulations of the flow using the validated approach presented in Sec. 2.3.1. Each geometry was simulated with different volumetric flow rates resulting in a flow rate – frequency function that was evaluated for all flow rates used in the experimental mixing investigations. Following the linear dependency of the frequency on the volumetric flow rate, the dependency of the frequency on the jet in cross flow momentum ratio J is of quadratic nature. For a better illustration of the frequency ranges, J is plotted against the numerically determined frequency in Fig. 2.35 for all disks. Fig. 2.35 shows that the six different disks can be divided

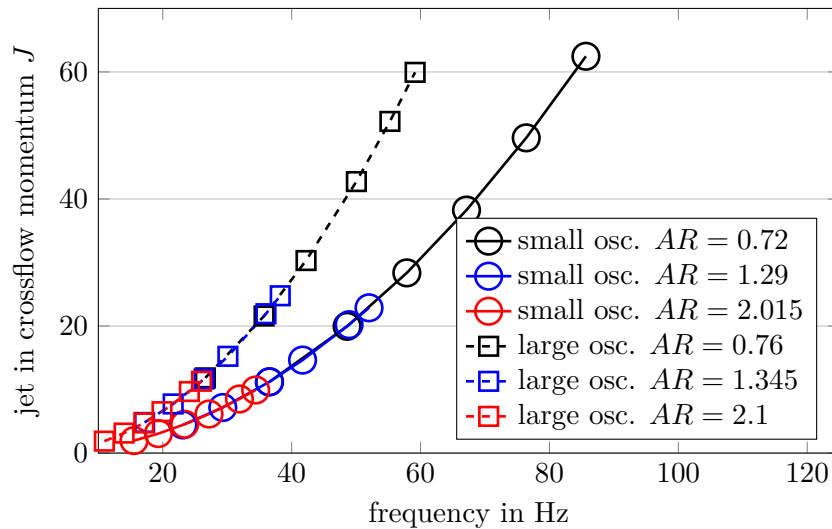


Figure 2.35: Frequency of the fluidic oscillators for the different geometries and different values of J , derived from numerical simulations.

into two groups: the disks with 13 oscillators (smaller geometry) and the disks with 7 oscillators (larger geometry). Within these two groups the oscillator's geometry is the same, only the aspect ratio and, thus, the jet in cross flow momentum J changes. As expected, the frequency created by the larger oscillators (i.e., disks $\Leftrightarrow(\dots);7$) is smaller for the same J . Please note, that Fig. 2.35 shows an idealized numerical result. Following the findings of Sec. 2.3.2 the frequencies of the smaller aspect ratio

oscillators ($\Leftrightarrow_{(small);13/7}$) will not follow the line as perfectly as shown, but will create a higher frequency than expected by the numerical simulations.

Keeping this in mind, the mixing performances of the fluidic oscillator disks were compared to see the impact of this change in injection geometry. The spatial unmixedness is plotted against J in Fig. 2.36. Several findings can be extracted

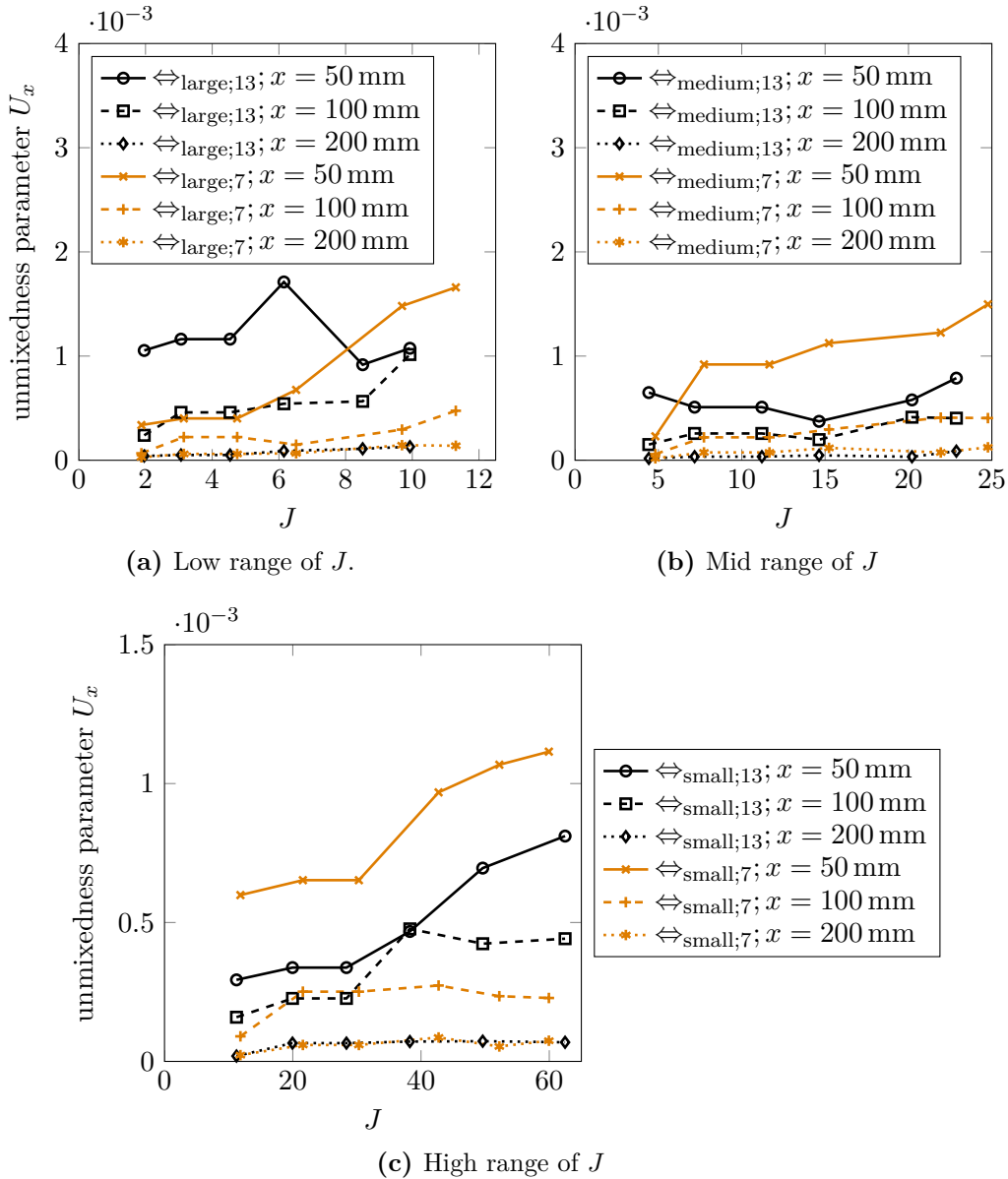


Figure 2.36: Spatial unmixedness versus J of all fluidic oscillator disks for the three measurement planes.

from these results. First, it can be stated that a higher oscillation frequency will generate a better mixing quality (i.e., lower unmixedness parameter). This can be seen by comparing the unmixedness parameter of e.g. disk $\Leftrightarrow_{\text{medium};7}$ (solid orange line in Fig. 2.36b) and $\Leftrightarrow_{\text{small};7}$ (solid orange line in Fig. 2.36c). For identical values of J disk $\Leftrightarrow_{\text{medium};7}$ creates a higher unmixedness than disk $\Leftrightarrow_{\text{small};7}$. Remember, for the same J and, thus, the same jet velocity and jet penetration, they create slightly different frequencies due to the boundary layers, as it was shown in Sec. 2.3.2. This observation can be found by comparing the other pair of corresponding disks with lower aspect ratio, i.e., $\Leftrightarrow_{\text{medium};13}$ and $\Leftrightarrow_{\text{small};13}$. This finding presumably is the reason for the lower dependency between mixing quality and jet in cross flow momentum. As the mixing quality is mostly lower for higher J (see Fig. 2.32), the frequency is increasing for a higher J and, thus, both effects cancel each other out. This results in a less pronounced dependency of the mixing quality on the jet in cross flow momentum J for the fluidic oscillator injection configuration.

The second finding found in Fig. 2.36 confirms the results already found for the rectangular jet. The disks with 13 injection ports (i.e., disk $\Leftrightarrow_{\text{small};13}$ - $\Leftrightarrow_{\text{large};13}$) produce a higher mixing quality than the ones with only 7 injection ports. This seems to be reasonable since the fuel (in this case dye) is more evenly distributed in the radial plane. Again, like for the rectangular jets, this trend is not clear for the lowest range of J where the two different injection configurations create different dependencies on the jet in cross flow momentum. In addition, this finding may be altered if different fluidic oscillators are incorporated for the generation of the spatially oscillating jets, because different jet deflection angles or oscillatory patterns may have an influence on the mixing behavior.

The third finding confirms the findings of Lacarelle *et al.* [59] as the mixing quality converges for both configurations as the mixture is convected downstream. Lacarelle *et al.* stated that the mixing enhancement of the fluidic oscillators compared to plain round jets is most pronounced close to the injection plane. This behavior is favorable for the SEC as an almost instant mixing in the radial plane is needed. After investigating the different mixing characteristics of the rectangular jets and the fluidic oscillators the two types of injectors were compared to finally find the best suited injection configuration for the SEC. For doing so the unmixedness parameter for the two most promising injection disks were plotted in Fig. 2.37 against the jet in cross flow momentum J , for the most critical high range of J .

Remember that the injection geometry for the SEC-process needs to be as independent from the jet in cross flow momentum as possible, since the total volume flow of the fuel is depending strongly on the fuel composition, which, again, is depending on the overall combustion conditions. Now looking at Fig. 2.37 it is found that this behavior is best represented by the fluidic oscillators (orange lines). As observable in the black curves, the strong dependency of the mixing quality on J for the rectangular jets is found even in the most downstream measurement plane. In contrast to that, the mixing quality of the fluidic disk ($\Leftrightarrow_{\text{small};13}$) is almost independent from the jet

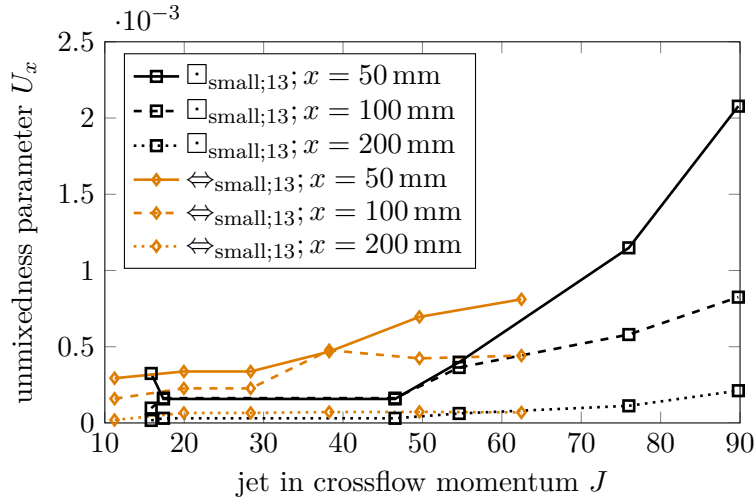


Figure 2.37: Spatial unmixedness versus J of disks $\square_{\text{small};13}$ and $\diamond_{\text{small};13}$ for the three measurement planes.

in cross flow momentum J . This independence even increases when the mixture is transported downstream. This favorable behavior outbalances the marginally better mixing quality of the rectangular jets for smaller values of J . In addition, the fluidic oscillators create a broad room for future optimizations, whereas the rectangular orifices cannot be further optimized. Following these observations, disk $\diamond_{\text{small};13}$ is the most suitable injection configuration of the investigated geometries. In future investigations the oscillatory parameters (e.g., the jet deflection angle, frequency, and the sweeping pattern) should be in the main focus, as they may allow further increases in the mixing quality.

2.5 Intermediate Conclusion

The innovative constant volume combustion process SEC has very high and specific demands for the fuel–air mixing. The fluidic oscillator is a promising device for meeting the stringent fuel injection requirements of the SEC process.

However, to design an optimal fluidic oscillator configuration for the given injection situation the underlying flow structures and oscillation mechanisms of the fluidic oscillator used have to be understood. This task was accomplished by an experimental assessment of the flow inside the oscillator using PIV and pressure measurements (Sec. 2.2). These first experimental investigations of the flow inside a fluidic oscillator of this type revealed the underlying oscillation mechanism and several regions of interest for possible optimizations of the geometry. The oscillation of the given type of oscillator is based on a recirculation region in the main chamber that pushes the jet

to the other side of the internal geometry as it grows and extends downstream. This recirculation bubble is fed from the feedback channels with a small portion of the main jet, providing the needed fluid volume to increase the size of the recirculation region in the main chamber. This needed flow volume is determined by the minimal and maximal size of the recirculation region and, hence, constant for a given geometry. In addition, it was shown that the internal dynamics are not necessarily directly linked to the external movement of the oscillating jet, as the moment of maximum jet deflagration inside and outside of the oscillator is not always identical. Changes in the identified sensitive regions of the oscillator's geometry (i.e., the feedback channels, the main chamber inlet wedges, and the outlet nozzle) were expected to alter these characteristics and further underline the presented findings.

The experimental data set paved the way for the validation of numerical tools for a further investigation of the influence of several geometrical parameters on the overall oscillation performance of the device (see Sec. 2.3). The broad parametric study of the fluidic oscillator and the influence of the most sensitive geometrical regions not only confirms several assumptions of the experimental investigations but also lead to a deeper understanding of the oscillation mechanism inside the fluidic oscillator itself. It was found that the assumptions based on the experimental investigations held. Changes in the geometry of the main chamber, for example a change in the size of the main chamber inlet wedges, were accompanied by the expected changes in the frequency and pressure loss of the fluidic oscillator. By increasing the distance between the main chamber inlet wedges it was not only possible to reduce an undesired back flow (i.e., in the downstream direction) in the feedback channels but also to alter the minimum size of the recirculation region and, thus, the needed volume for pushing the jet to the other side. As a consequence the frequency of the oscillator and the pressure loss change. Altering the outlet nozzle of the oscillator did not only allow to change of the maximum jet deflection angle but also to alter the link between the internal and the external jet movement of the fluidic oscillator. When the outlet nozzle diameter was increased by 50% the maximum jet deflection downstream of the oscillator was reached as the jet was fully attached to one side of the main chamber. Based on these experiences and results it is possible to design a fluidic oscillator for a given task and the required oscillation parameters. If, for example, an oscillator creating a higher frequency with a lower pressure loss is needed it is possible to adjust the feedback channels, the main chamber inlet wedges, and the outlet geometry of the oscillator following the presented findings to create such a fluidic oscillator.

In order to investigate the mixing performance and mechanisms of spatially oscillating jet in the SEC setup several injection configurations were investigated in a water test rig (see Sec. 2.4) employing planar laser induced fluorescence. It was shown that spatially oscillating jets in cross flow created by fluidic oscillators are able to create a fuel-air mixture fulfilling the required mixing characteristics. In contrast to a slit injection or the round jet in cross flow, fluidic oscillators allow the creation

of a very high mixing quality already close to the fuel injection plane. In addition, the mixing quality is independent from the jet in cross flow momentum for these types of injectors. The results indicate that this behavior stems from the increasing oscillation frequency of the fluidic oscillators. A higher jet in cross flow momentum leads to a higher volumetric flow in the oscillator and, thus, a higher oscillating frequency. By comparing different sizes of fluidic oscillators, it was possible to show that higher frequencies are favorable for the mixing process. However, since higher frequencies lead to smaller geometries for the fluidic oscillators the pressure loss of the fuel injection system will increase and might contradict the advantages of a higher mixing quality. Hence, the optimal oscillator design must to be created based on the given investigations for every new injection configuration.

Now, if one transfers these results to the SEC test rig situation, several changes and effects set in. First of all the working fluid is changed to a stream of cold gaseous fuel, which must be injected and mixed with a hot air stream. Due to the design of the test rig regarding the Reynolds and Strouhal numbers the main fluid dynamic effects will remain the same. However, since the range of volumetric flow rates for the fuel was not finally known at the moment of the mixing investigations the fluidic oscillators may be rescaled and redesigned for the final SEC test rig. The frequency of the fluidic oscillators needs to be increased, because the final SEC process will achieve frequencies of approximate 250 Hz, resulting in injection durations of around 1-2 ms. In this time scale the oscillators must be able to create an oscillatory flow and complete several oscillations. In addition, the fuel flow rate will change dynamically during this injection period to create the desired equivalence ratio stratification. Due to these requirements a frequency of at least around 10 kHz is needed for the fluidic oscillators to guarantee a minimum of 10 oscillations during each filling cycle of the SEC process. Based on the presented findings it is possible to design and characterize the needed fluidic oscillators fast and reliable by making use of the validated numerical tools. It is expected that the main chamber inlet wedges, the feedback channel geometry and maybe the outlet nozzle geometry will be adapted to the needed oscillation parameters of the SEC test rig. The distance between the main chamber inlet wedges will be increased, the feedback channels “streamlined” and the outlet nozzle geometry changed for a larger jet deflection angle to create the needed increase in mixing quality. Even for a change in the geometry (e.g., the size) of the SEC combustion tube the presented findings will allow for a quick and reliable adaption of the injection configuration.

Summing up the results of this section, it is possible to create a fuel injection configuration that is very promising to not only create the necessary mixing quality for the SEC process in the experimental scale but also to withstand the harsh environment of the combustion process over a long period of operation. Together with the following chapters a test rig for the first SEC ignition tests is created, which finally show the performance of the fluidic oscillators for mixing enhancement in the SEC setup.

CHAPTER 3

Fluidic Diode

From the beginning of pressure gain or pulsed combustion, the reliable, robust and long-lasting control of the inlet flow is one key factor for stable operation of the combustion system. Regarding the SEC process this is the case, too. Several ideas and devices for fulfilling this task have been developed and presented in the past. In the first widely used pulsed combustion system (i.e., the pulse jet; see Sec. 1.1.1), for example, very simple one-way valve configurations were used to force the hot combustion products through the exhaust pipe. Due to their moving parts and the hot exhaust gases, these valves were not suitable for long-term operation. Hence, valveless pulse jet engines were developed in the first decade of the 20th century, together with their valved counterparts. The valveless incorporate a secondary flow path to purge the combustion induced reversed flow and guide them to the exhaust of the system. This setup allows for a much longer lifetime of the device but reduces the maximum achievable thrust and pressure gain.

In later developments of pulsed combustors for gas turbine application, the problem of flow rectification reoccurs. Kentfield *et al.* [53] suggested a so called thrust-augmenter flow rectifier setup similar to the bypass systems of the valveless pulse jets. In their system the reversed flow induced by the pressure gain combustion is guided into a channel and transported to the downstream side of the combustion tube. In 1977 they filed a patent [51] for this device. However, two main drawbacks exist for this configuration. First, as stated in the patent, it was not possible to create a significant pressure gain in the valveless combustor. For a positive static pressure gradient across the combustor (including the bypass), the flow in the bypass will be reversed. Hence, hot reaction products are transported upstream, reducing the possible pressure gain of the system. Second, the pressure wave that is created by the combustion is not reflected at the inlet of the combustion tube. Instead it is guided into the bypass channel and transported downstream. Thus, the mentioned valveless bypass systems are not suitable for the SEC process due to the loss of the

necessary pressure wave. A flow rectifying setup without any moving parts is needed that is able to reflect the pressure and suction waves imperative for the SEC process.

In this chapter a fluidic diode is proposed and designed to match this task. As a fluidic device it works completely without moving parts and, thus, is capable of handling the harsh environment of the SEC combustor for a sufficient time. The first section of this chapter is dedicated to the history and current state of fluidic diodes. As most other fluidic devices, its first publication dates back to the early last century. Hence, several different geometries of such flow rectifiers exist. In the second section, the idea and geometrical design of the proposed fluidic diode is presented. Besides preventing a reversed flow of the hot combustion products the proposed diode is able to provide the needed reflection of the pressure and suction waves as well as prevent misfires in the combustion tube. The designed fluidic diode is subsequently investigated experimentally by water channel experiments and numerical simulations.

3.1 State of the Art

In 1920, long before the first fluid logic or fluidic system was created, Nikola Tesla filed a patent called “Valvular Conduit” in which he described a way to create a valve like behavior in the absence of any moving parts. The main sketch of this patent is shown in Fig. 3.1¹. As the fluid passes through the diode from left to right,

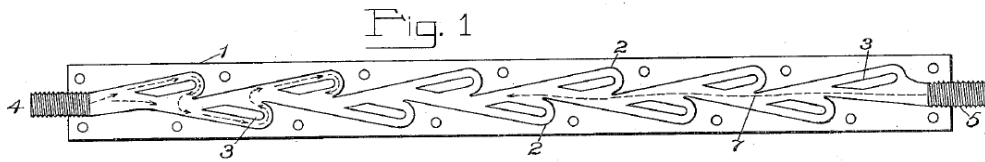


Figure 3.1: A “Tesla diode” as it was patented by Nikolai Tesla in 1920 [96].

part of the main flow is separated and guided into one of the curved side channels (number 2 in the sketch). In this channel the flow is redirected upstream and pushes the flow into the corresponding side channel on the other side of the main flow path. The dashed arrows on the left side of Fig. 3.1 illustrate this behavior. If the fluid is entering Tesla’s “valvular conduit” from the other side (i.e., from right to left), it is able to almost freely pass the device without any redirecting. This is illustrated by the long dashed arrow beginning at the right inlet of the diode (number 5). Hence, the pressure loss across the device is depending on the flow direction. This so-called diodicity is a measure of the performance of such a device. It is defined as the ratio

¹ This Sketch was already shown in the introduction but as the flow inside the device is described here, it is shown again to improve readability.

of the pressure loss coefficients in the two directions.

$$\Theta = \frac{\zeta_{\text{backward}}}{\zeta_{\text{forward}}}, \quad (3.1)$$

$$\text{with: } \zeta = \frac{2\Delta p}{\rho \bar{u}^2} \quad (3.2)$$

Following the calculations of Kirshner and Katz [55], the tesla diode typically creates a diodicity coefficient of up to 4, that is, the pressure loss coefficient in the reversed flow direction is four times larger than the forward pressure loss coefficient. Beginning with Tesla's invention, several geometries for fluidic diodes were developed in the following decades.

The vortex diode is one of these other geometries that creates a valve-like behavior. In 1929 Dieter Thoma filed a patent called "Fluid Lines" [98] in which he described this type of diode. The sketch from this patent is shown in Fig. 3.2. In this figure

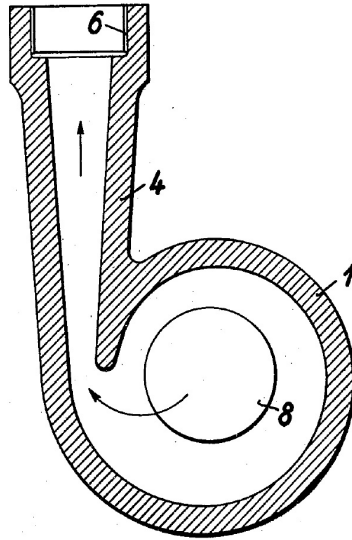


Figure 3.2: A vortex diode as it was patented by Dieter Thoma in 1929 [98].

the geometry of the vortex diode with its inlets (6 and 8) as well as the straight duct (4) and the vortex chamber (1) is depicted. If fluid is fed into the geometry through inlet 8 and thus, in the forward direction, it can leave the device easily through the straight duct as it is illustrated by the two arrows. If fluid is entering the device in the reversed direction (i.e., from port 6 to port 8) it enters the vortex chamber tangentially. This tangentially oriented velocity creates a strong vortical flow inside the round vortex chamber. As a result of the vortical flow, the radial pressure distribution features a very low pressure region in the center of the vortex. This low pressure region reduces the pressure level at the outlet (8) of the diode and

thus creates a high pressure loss. Following the work of Baker [8] this type of diode is able to create a diodicity coefficient of up to $\Theta = 50$. Since none of the fluidic diodes is completely closed for one of the two flow directions they can also be used as switchable resistances in a given flow path. Due to their inherent robustness, they are able to control the flow of a molten metal stream as it was shown by Tesař in 2003 [91]. In 2014 Koli *et al.* [56] presented a combination of a vortex diode and another fluidic device to modulate the cooling airflow of an aero engine. They employed a fluidic switch (see chapter 4) to change the flow path in the vortex chamber between a purely radial (low resistance) to a tangential (high resistance) inlet. This simple approach allows to increase the turbine cooling air if needed (e.g., for take-off) and save the cooling air to enhance efficiency when redundant.

Baker published a comparison of different fluidic diodes in 1967 [8]. In his work he introduced another type of fluidic diodes, which he called the “Fluid Rectifier”. Later on this type of diode was called “cascade diode” (e.g., by Kirshner and Katz [55]). This diode is based on a cascade of radial blades that will create a swirling flow for the reversed flow direction whereas a flow separation occurs on the first blade for the forward direction. A sketch of Baker’s device can be found in Fig. 3.3. The shown

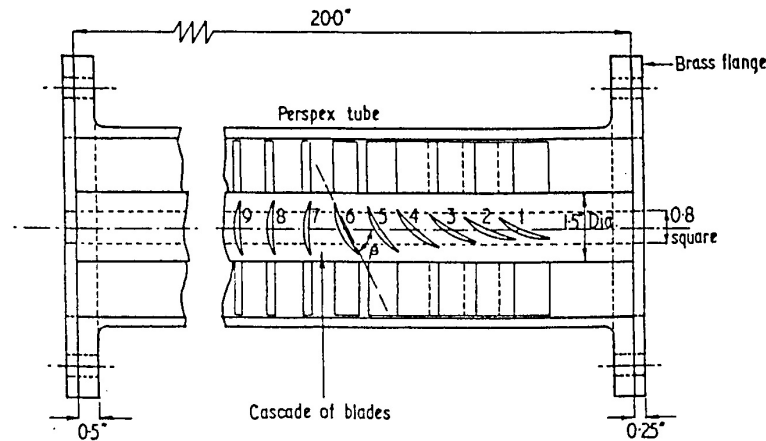


Figure 3.3: A cascade diode as it was investigated by P.J. Baker in 1967 [8].

cascade diode consists of a straight duct equipped with 9 blade stages, with four blades each. If the flow is entering the device in the forward direction (i.e., from left to right) it hits blade 9 with an angle of attack of 90° and a separation bubble downstream of this blade is formed. Accordingly, the flow faces a blockage of the passage by the blade itself and the accompanied separation region behind the blade, which creates a certain pressure loss. Flow entering the diode in the other direction (i.e., from right to left) faces a completely different setup. The fluid approaches the first blade with an angle of attack of 12° . Due to the low angle of attack no separation occurs downstream of the blade, but a certain angular momentum is

applied to the flow. The following blades feature an increasing angle of attack to amplify this angular momentum. This setup creates a highly swirling flow inside the duct. This redirection of the flow and the increased tangential velocity creates a pressure loss in the reversed direction that is significantly higher than the one in the forward direction. By increasing the number of blades, it is possible to create diodicity coefficients of up to 350 for this type of diode. The shown cascade diode consisting of 9 blades creates a diodicity coefficient of 31 as measured by Baker [8].

Unfortunately, none of the already presented fluidic diodes is suitable for the task of flow rectification in the SEC process. Since the SEC is based on pressure and suction waves traveling through the combustion tube, the flow rectifier must reflect a pressure or suction wave just like a closed end. For all diodes shown, the pressure wave coming in the reversed flow direction would not be reflected but rather redirected and dissipated inside the different fluidic diode geometries. This redirection and dissipation of the acoustic energy significantly reduces the reflected pressure wave that is needed for the next filling process. Hence, a different geometry for the fluidic diode has to be used in the SEC setup. One geometry to potentially fulfill this task is the so called “scroll diode”. A sketch of such a diode is shown in Fig. 3.4¹. The

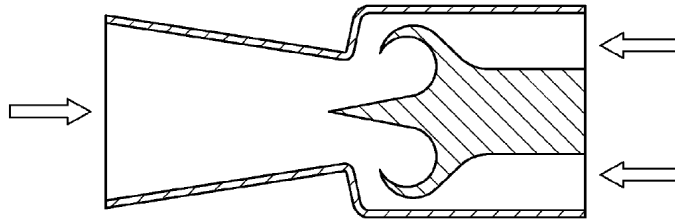


Figure 3.4: A scroll diode as it was shown in Kirshner and Katz [55]

scroll diode consists of a straight (two-dimensional) duct with a tulip like geometry on the centerline of the device, the center body. As the flow enters the diode in the forward direction (i.e., from left to right in the sketch) it faces a smooth redirection of the flow around the center body. Two separation regions on the downstream side are formed. If the flow is directed in the backward direction it faces the two almost circular slots, redirecting the flow backwards and thus “blocking” the flow passage around the center body. Due to the high flow resistance in the forward direction, the diodicity coefficient of the shown diode is 6.6 as measured by Baker [8]. The scroll diode, consisting of a center body that creates a physical wall for the flow in the backward direction is the only geometry, which may be able to sufficiently reflect the pressure and suction waves associated with the SEC. Based on the idea of the scroll diode a fluidic diode was designed that not only creates the diodicity effect

¹ Again, this sketch was already shown in the introduction but it is also shown here to improve readability.

but also reduces the chance of misfiring events in the SEC process. The design and performance of this fluidic diode is shown in the following sections.

3.2 Design of the Diode

In order to create an inlet geometry for the SEC combustion tube, several objectives must be met by the flow rectification setup. Beside the needed one-way valve behavior the following characteristics have to be realized by the fluid diode:

1. sufficient prevention of a reversed flow inside the combustion system,
2. reflection of the pressure wave created by the ignition of the mixture,
3. realization of a minimal inlet pressure loss in order to ensure the needed filling velocity of the combustor,
4. ability to withstand the very high temperatures of the combustion (i.e., no moving parts or parts that penetrate into the reaction zone), and it must be
5. assimilable to a gas turbine system (i.e., no direct connection to the downstream side of the combustor).

Following the findings of Sec. 3.1 a fluidic diode based on the idea of the scroll diode was created. Several designs were evaluated numerically to create an inlet geometry that not only fulfills the mentioned tasks associated with the SEC process but also allows for the integration of the oscillating fuel injection (see Sec. 2.4) and the required film cooling on the inside of the combustion tube. An overview of the resulting final design is shown in Fig. 3.5 and a more detailed cut view on the flow path can be found in Fig. 3.6. The inlet geometry is divided in three different parts (diode, fuel injection, and transition section) and each part is depicted in false colors to enhance visibility. For both pictures the main flow is directed from left to right (i.e., the forward direction). The combustion tube has an inner diameter of 40 mm and is attached on the right or downstream side of the inlet section. In Fig. 3.6 it is shown connected to the transition section (red part) of the geometry. On the upstream side of the geometry the main flow inlet is connected with an inner diameter of 30 mm. This inlet consists of a large Y-type main control valve in the water channel setup and a fluidic switch (see chapter 4) in the combustion test rig. The diode itself is shown in blue in Figs. 3.5 and 3.6. Similar to the scroll diode, the designed fluidic diode consists of a center body on the central axis of the tube. The fluidic diode is designed to create a minimal pressure loss in the forward direction (i.e., from left to right) and a significantly higher pressure loss in the backward direction. In the design of the diode section, it was assured that the cross-sectional area of the flow passage around the center body is constant. Both parts, the outer wall and the shape of the center body, are based on a sine or cosine

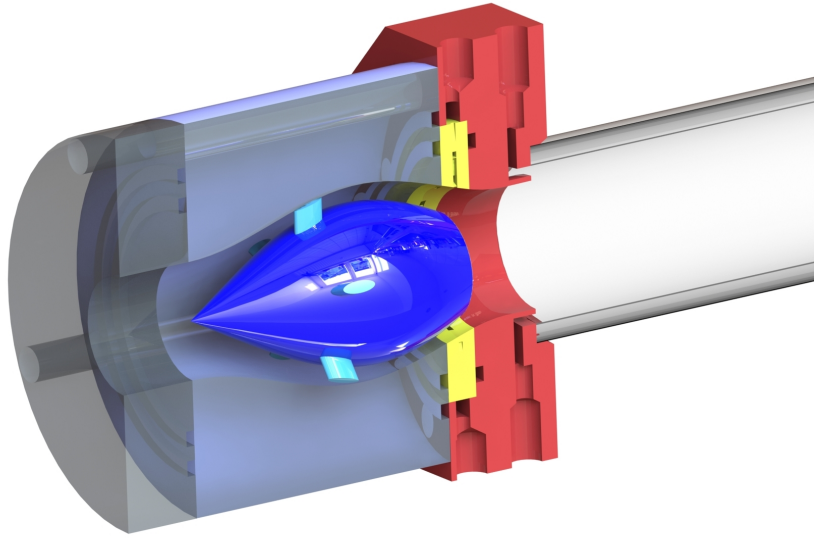


Figure 3.5: Isometric view of a cut through the inlet section, including the proposed fluidic diode (blue), the fuel injection (yellow) and the transition piece with the film cooling inlet (red). Note, that the center body is omitted from the cut.

function, respectively. On the downstream side, the center body features a spherical cavity that fulfills several purposes. The details of this geometrical feature will be discussed later in this section. The center body itself is fixed in the center of the flow passage by five elliptical tacks for the water channel investigation and four tacks for the final combustion tests. These tacks are shown in cyan in Fig. 3.5.

Downstream of the fluidic diode, the fuel injection section is shown in yellow. The fuel is injected by means of spatially oscillating jets (created by fluidic oscillators), as it was proposed in chapter 2. The inner wall of the fuel injection disk was adapted to match the overall shape of the flow passage. This maintains the decreasing diameter in this part of the inlet section. Downstream of the fuel injection section, the transition to the combustion tube is shown in red in Fig. 3.6. In this section the diameter of the cross section is further decreasing, creating a step at the inlet of the combustion tube (see on the right side of Fig. 3.6). At this position the cooling flow is injected flush to the inner wall of the combustion tube through a slot of 2.5 mm to separate the fresh fuel air mixture from the hot surfaces on the inside of the combustion tube. As already mentioned, the outer wall of the flow passage follows a cosine wave, whereas the diameter of the center body is following a sine wave. Both waveforms were adapted to maintain the above mentioned constant cross-sectional area. Downstream of the center body a jump in the cross-sectional area is located until the fuel injection and transition piece decrease the inner diameter

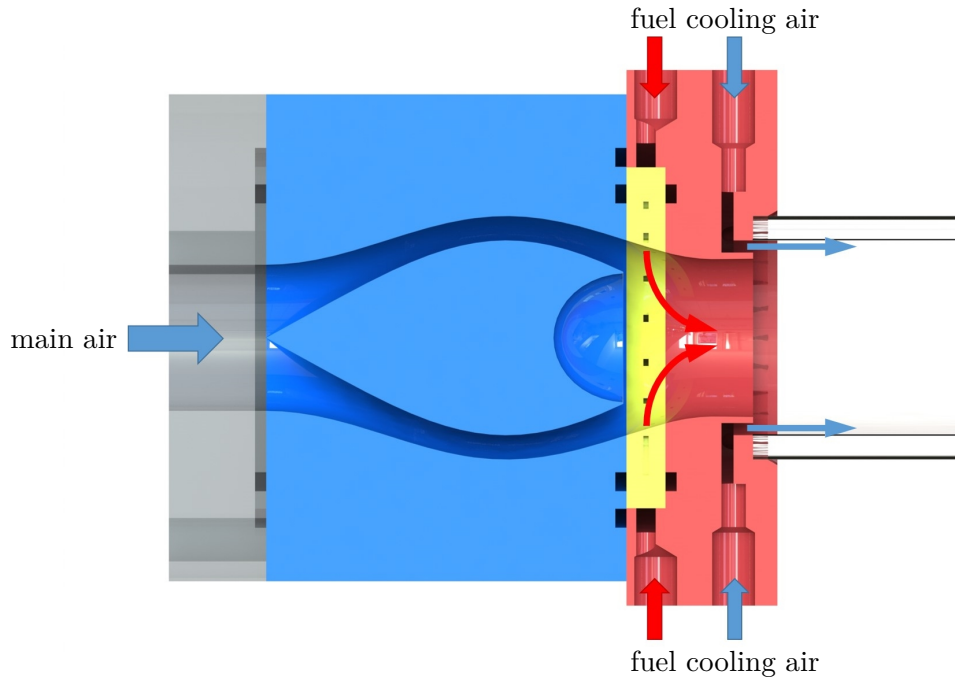


Figure 3.6: Cut through the centerline of the inlet section, including the proposed fluidic diode (blue), the fuel injection (yellow) and the transition piece with the film cooling inlet (red).

again. This design of the flow passage is used in order to avoid any non-geometry induced separation inside the fluidic diode.

Whereas the physical wall created by the center body reflects the pressure and suction waves, which are needed for the SEC process, the mentioned spherical cavity or cusp on the downstream side of the center body is a special design feature that fulfills two different objectives in the context of the SEC. First, the cusp increases the reversed pressure loss because it redirects parts of the backwards directed flow. Second, the spherical shape of the cavity focuses the incoming pressure waves into a single point, assuring the ignition and burning of possible misfiring charges in the combustion tube. Achasov *et al.* [1, 2] investigated the reflection and focusing of shock waves from concave curvilinear surfaces in order to initiate a detonation in a combustible fuel air mixture. Based on these investigations, Levin *et al.* [62] investigated a new approach to create a self-inducing pulsed detonation combustion. They employed two supersonic jets emanating inwards into a half-spherical resonator chamber. The shocks created by the colliding jets are then focused by the spherical resonator surface, thereby igniting a detonation in the focus of the chamber. The same principle is used in the presented device. Even though no shock waves are present in the combustion tube, the spherical cavity will focus the pressure wave in

the focal point. Recall, the combustion inside the SEC tube relies on a homogeneous auto-ignition throughout the whole fuel-air mixture. This auto-ignition shall occur as the pressure wave inside the combustion tube reaches the upstream end (i.e., the fluidic diode). If the auto-ignition is to fail, the pressure wave is reflected and focused at the fluidic diode, creating a pressure peak in one single point. This pressure peak serves as an emergency ignition source and ignites the combustible mixture. Note, that the focusing point of the spherical cavity is upstream of the fuel injection. This is intended since no combustible mixture should be in the focal point of the cusp during normal operation. However, in a misfiring charge it is assumed that the fresh fuel-air mixture is slightly pushed in the upstream direction by the impinging pressure wave forming a combustible mixture in the focal point of the fluidic diode. Even though, no pressure rising CVC is created in this particular (misfiring) cycle, the shock focusing character of the inlet section assures the combustion of the fresh charge and prevents the ingestion of a combustible mixture into the turbine plenum.

3.3 Steady Investigation

During the design process of the presented SEC inlet section several geometries were evaluated numerically. In order to verify the reliability of these results, the final diode geometry is validated experimentally in the water channel presented in Sec. 2.4. This section is dedicated to the experimental investigation of the steady flow in the fluidic diode and the associated validation of the numerical simulations. Besides the validation of the numerical model, the experimental investigation assesses the performance (i.e., diodicity) of the developed fluidic diode.

3.3.1 Experimental Setup

The steady flow field inside the fluidic diode was investigated using PIV measurements at one side of the center body for both flow directions. The diode was mounted in the water channel test rig, presented in Sec. 2.4. To give an idea of the setup used in this section, a sketch of the layout is shown in Fig. 3.7. Note that in this steady investigation only the fluidic diode (the blue part of Fig. 3.5) is investigated in order to neglect influences of the wall cooling section on the performance of the device itself. A sectional view through the detailed geometrical setup is shown in Fig. 3.8.

Like in the previous chapter, air was substituted by water as working fluid. This results in lower velocities and frequencies at the same Reynolds and Strouhal numbers, which significantly enhances the measurement quality. The seeding is less challenging due to the higher density of the water and PIV measurements are significantly improved, because the refractive index of acrylic glass is very close to the one of water. The dye circuit of the test rig was not used and the outlet of the combustion tube was connected to the main water reservoir to create a closed-loop setup. The water was seeded using silver coated hollow glass spheres with a nominal diameter of

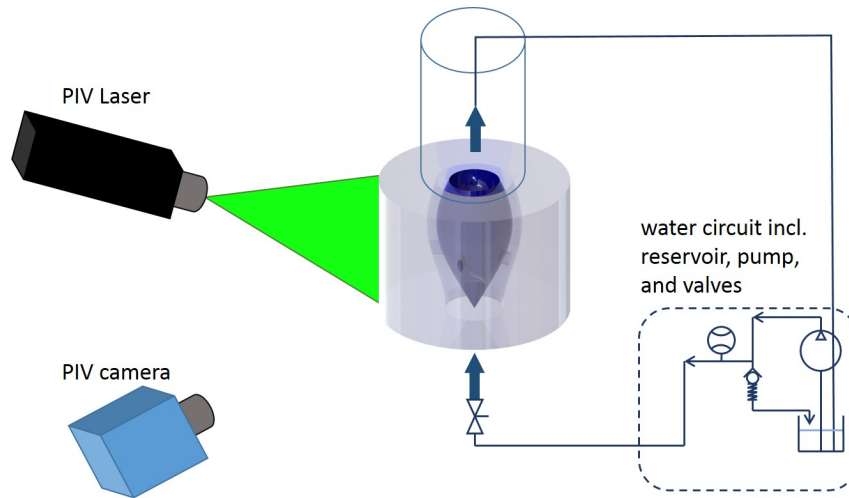


Figure 3.7: Sketch of the experimental setup for the validation of the fluidic diode.

$15\ \mu\text{m}$. A high-speed PIV-system consisting of a ND:YLF – Laser (Neodymium-doped yttrium lithium fluoride) at 527 nm and a high speed active pixel sensor (CMOS-sensor) camera was used. For each of the three investigated flow rates, 3640 PIV snapshots were recorded for both, the forward and the backward flow direction. A measurement frequency of 2000 Hz was used. In order to reduce the reflected and scattered light emanating from the center body of the fluidic diode, it was coated with a specially structured paint. After a primer layer, the center body was lacquered with matte black paint. Prepared with these sub-layers, the center body was coated with a clear two-component lacquer mixed with Rhodamine 6G dye, which has a high

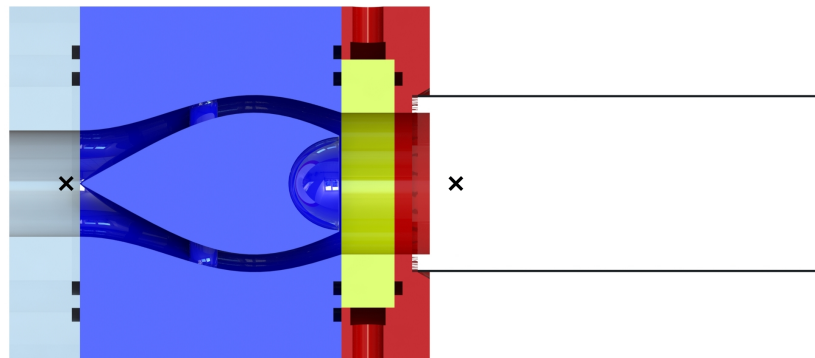


Figure 3.8: Geometrical setup of the diode section for the experimental investigations.

absorption for the used laser wavelength. Excited with the laser light at 527 nm it fluoresces at higher wavelengths (around 550 nm) that can easily be filtered by using a band pass filter centered at the laser wavelength. However, due to the high laser intensity, the Rhodamine deteriorated with time and the intensity of the reflected and scattered light increased. Thus, the pictures were corrected for background light and the distortion that was created by the curved surface of the diode. The resulting snapshots were evaluated employing a final interrogation area of 16×16 pixel with an overlap of 50%. Subsequently, the results were filtered for outliers and interpolated. This process results in a spatial resolution of approximately 0.5 mm in the axial and radial direction.

The flow rates of the PIV investigation are shown in Tab.3.1 together with the Reynolds number (based on the diameter of the combustion tube). The water had a temperature of approximately 295 K. The flow rates were obtained by measuring the time it took to fill a 50 L water tank. In order to switch the direction of the flow, the connections at the main pump were switched. Hence, the flow direction was inverted without any change in the overall setup of the test section.

Table 3.1: Flow rates and Reynolds numbers at the investigated operating conditions of the fluidic diode.

no.	direction	\dot{V} in L/s	$\overline{ u _1}$ in the Diode in m/s	Re
1	forward	0.6	0.84	21217
2	forward	0.84	1.18	29804
3	forward	1.01	1.42	35860
4	backward	0.58	0.82	20748
5	backward	0.83	1.18	29704
6	backward	0.97	1.37	34607

In addition to these measurements, the pressure loss across the fluidic diode for a range of mass flows was measured to calculate the diodicity of the device. The mass flows used for this test are summarized in Tab. 3.2. Smaller steps in the volumetric flow rate are utilized in order to give a more detailed idea of the Reynolds number dependency. The pressure loss was measured using two pressure tabs, one upstream of the diode and one downstream in the combustion tube. The positions of the two pressure tabs are shown in Fig. 3.8 as black crosses. Stainless steel tubes with an inner diameter of 1 mm are glued into the setup flush with the inner wall. A differential pressure sensor was connected to both pressure ports and the pressure difference was measured. Due to the different diameters of the flow section upstream and downstream of the diode, the data was corrected for the dynamic pressure and the hydrostatic pressure difference. Based on this pressure loss data, the diodicity, as it is defined in Eq. 3.1, was calculated.

Table 3.2: Flow rates, velocities, Reynolds numbers and results of the pressure loss measurements of the fluidic diode.

no.	direction	\dot{V} in $10^{-3}\text{m}^3/\text{s}$	$\overline{ u }_z$ in m/s	Re	Delta p	ζ
1	forward	0.20	0.29	7248	361	8.743
2	forward	0.39	0.55	13913	163	1.074
3	forward	0.60	0.84	21217	139	0.392
4	forward	0.69	0.97	24549	154	0.325
5	forward	0.77	1.09	27377	309	0.525
6	forward	0.84	1.18	29804	242	0.347
7	forward	0.96	1.36	34208	548	0.596
8	forward	1.01	1.42	35860	326	0.323
9	forward	1.03	1.46	36747	533	0.502
10	forward	1.06	1.50	37760	655	0.585
11	backward	0.31	0.44	11042	338	3.531
12	backward	0.42	0.59	14889	545	3.129
13	backward	0.51	0.72	18021	857	3.356
14	backward	0.58	0.82	20748	1018	3.007
15	backward	0.62	0.88	22250	1091	2.804
16	backward	0.70	0.99	24892	1323	2.716
17	backward	0.77	1.09	27461	1503	2.535
18	backward	0.83	1.18	29704	1699	2.450
19	backward	0.92	1.30	32642	2082	2.486
20	backward	0.94	1.33	33501	2113	2.395
21	backward	0.97	1.37	34607	2324	2.469

3.3.2 Assessment of the Diodicity

The steady state performance of a fluidic diode is metered by the diodicity of the device, which is defined in Eq. 3.1. It is derived from the pressure loss coefficients in both directions that were measured in the water channel test rig. The results of the pressure loss measurements are shown in Tab. 3.2 together with the corresponding operating conditions. Additionally, the pressure loss coefficient ζ is plotted against the Reynolds number for the forward and backward direction in Fig. 3.9. In addition to the measured data (shown as symbols), a power function fit for the data is plotted. As for the original scroll diode investigated by Baker [8], the developed geometry is showing an almost constant pressure loss coefficient in both directions for Reynolds numbers greater than 10,000. However, in contrast to the scroll diode investigated by Baker, the presented fluidic diode has a significantly lower pressure loss coefficient in both directions. Accordingly, the required very low pressure loss was accomplished by the proposed design utilizing a constant cross-sectional area in the fluidic diode.

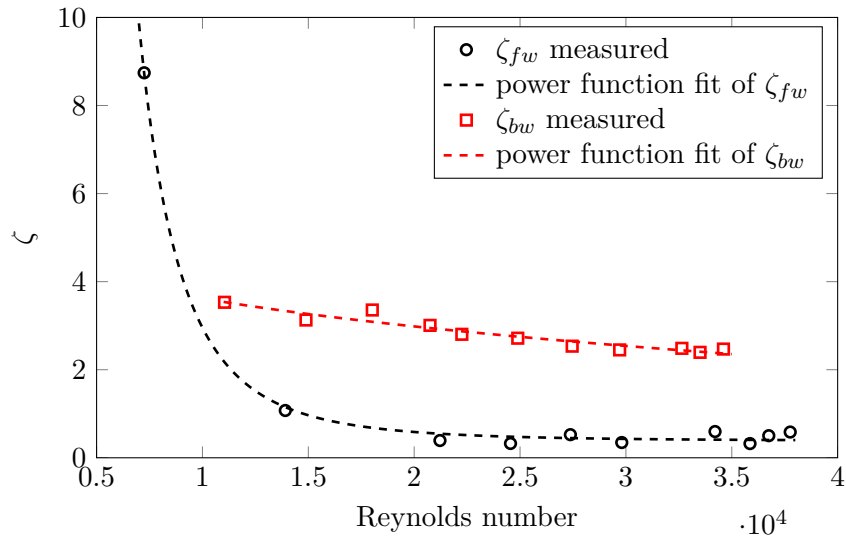


Figure 3.9: Measured pressure loss coefficients of the fluidic diode in both directions, forward (fw) and backward (bw).

Based on the fitted power functions, it is possible to calculate the diodicity for the presented fluidic diode. This curve is shown in Fig. 3.10. As expected from the pressure loss coefficients in the two directions, the diodicity is increasing with Reynolds number in the lower Reynolds number regime. At a Reynolds number

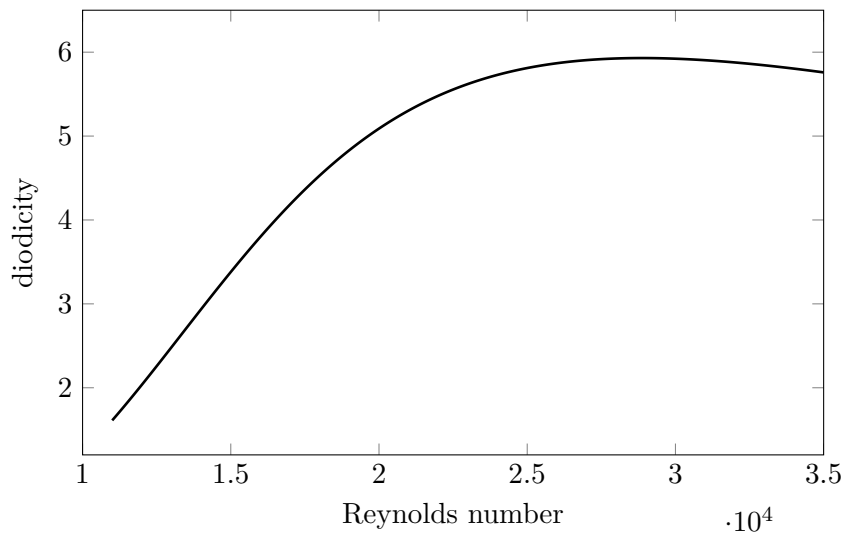


Figure 3.10: Diodicity of the fluidic diode for the investigated range of Reynolds numbers.

of around $Re = 22,000$, it reaches its maximum value of 5.9 and is only slightly decreasing for higher Reynolds numbers. This value of the diodicity is close to the value of the original scroll diode of 6.6 found by Baker [8]. In contrast to the presented design, the original scroll diode features multiple severe changes in the cross-sectional area, whereas the presented geometry only has a single area jump right downstream of the center body. In the original scroll diode the backwards directed flow is entirely guided onto the center body. In the investigated setup of the developed design part of the flow can enter the passage around the center body directly without any redirection. In the complete SEC inlet section setup this direct flow without redirection is reduced due to the decreasing diameter in the mixing section (see red part in Fig. 3.6), which guides the reversed flow into the cusp of the center body. Accordingly, the diodicity is expected to increase even further for the complete setup. Nevertheless, already the presented pressure loss measurements show that the proposed geometry of the fluidic diode has the desired very low pressure loss in the forward direction with almost the same performance (i.e., diodicity value) than the original scroll diode.

3.3.3 Steady Flow Field and Validation of the Numerical Model

Beside the assessment of the performance of the fluidic diode, the steady flow field inside the device was investigated using PIV measurements. Since, the transition pieces upstream and downstream of the fluidic diode did not allow for measurements in these areas, only the velocity field in the passage between the center body and the outer wall was measured (the area inside the blue dashed rectangle in Fig. 3.11). Additionally, the sealing cords blocked the view on the most downstream part of the fluidic diode. The experimental assessment of the flow field within the diode was performed to validate the numerical model. Subsequently, the numerical model is then used to assess the internal structures during a transient ignition event (i.e., a pressure rise at the outlet), because these structures are extremely difficult to obtain experimentally. Since all flow rates gave similar quantitative results, only the highest flow rate of $1 \cdot 10^{-3} \text{ m}^3/\text{s}$ is shown and discussed in this work.

The numerical approach validated in this section is based on the unsteady RANS equations together with the SST turbulence model, as they are presented in Sec. 1.1.3. The simulations were conducted using the ANSYS CFX 14.5 software package. The computational grid was created with ICEM CFD and consisted of 2,126,773 nodes. The domain and the computational grid is shown in Fig. 3.11 together with the regions for the different boundary conditions. The inlet for the forward direction is denoted as a green line, and the outlet for the same direction as a red line. For the other flow direction, these boundary conditions were flipped. In the discussion of the results, the two sides will be denoted with respect to the normal (forward) flow direction. This means that the “upstream” side of the domain and the center body is on the left hand side whereas the “downstream” side is on the right hand side of

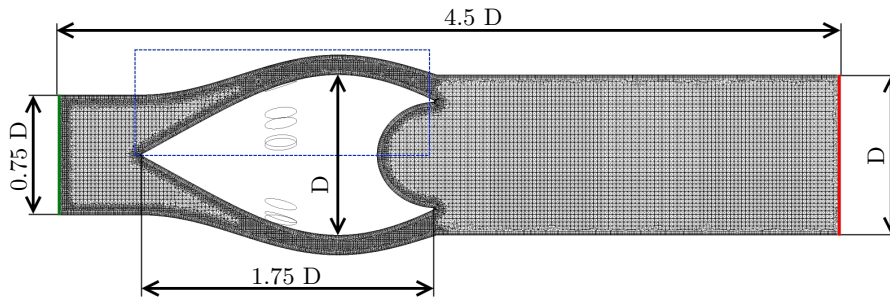


Figure 3.11: Overview of the computational domain of the fluidic diode including the dimensions and the region of the different boundary conditions.

the figures even for the reversed flow case. In order to validate the experimentally obtained flow fields, a water flow rate of $1 \cdot 10^{-3} \text{ m}^3/\text{s}$ was numerically simulated for both flow directions at a fluid temperature of 295 K. This flow rate was set as a boundary condition at the inlet of the device whereas the outlet was defined as an opening to ambient pressure. The walls were treated as smooth non-slip walls. These settings result in a Reynolds number of around 35,000 based on the diameter of the combustion tube.

To give a first overview on the flow field of the fluidic diode, the results for the two flow directions are plotted as a false color plot of the velocity magnitude in Fig. 3.12 and 3.13. In order to gain visibility and comparability, the PIV data is plotted within the results of the numerical simulations (the area of the PIV measurement is shown by the blue dashed rectangle). The white area in the PIV data is due to the tacks that hold the center body blocking the view in the measurements (see Fig. 3.5). The same tacks are responsible for the area of increased velocity in the numerical data below the center body. However, it was assured that the plane in which the CFD data is plotted is at the same distance to the tacks as the PIV measurement plane. The two flow fields are significantly different. In the forward direction the measured velocities are higher than the velocities calculated from the flow rate by a factor of 1.4 in the mean value. This severe deviation between the measurements and the numerical simulation is assumed to stem from an asymmetry in the inflow of the fluidic diode in the experiments. Upstream of the fluidic diode, a large (25 mm) Y-type valve is located. This valve creates an asymmetric inflow into the fluidic diode, resulting in significantly higher local velocities than expected. This non-symmetric behavior decreases as the flow is passing the center body, but is still noticeable on the downstream side of it. Despite the quantitative differences, both, the numerical simulation and the PIV measurements, allow for the qualitative assessment of the flow field within the fluidic diode. As planned in the design phase,

no flow separation neither at the surface of the center body nor at the outer walls is observed. Downstream of the center body, the flow separates and creates a large recirculation region. This recirculation region is depicted by the black line of zero axial velocity in Figs. 3.12 and 3.13. In the final SEC environment a shorter axial extent of the recirculation region is required, because the fuel injection is located in this region. However, it is expected that the axial extent of the recirculation region will be reduced by the converging part of the mixing section (see the red part in Fig. 3.6). In addition, the fuel injection is realized in a jet in cross flow type injection, which introduces radial momentum within the mixing section, pushing the flow from the diode towards the centerline. This will create a more even inflow into the center of the combustion tube.

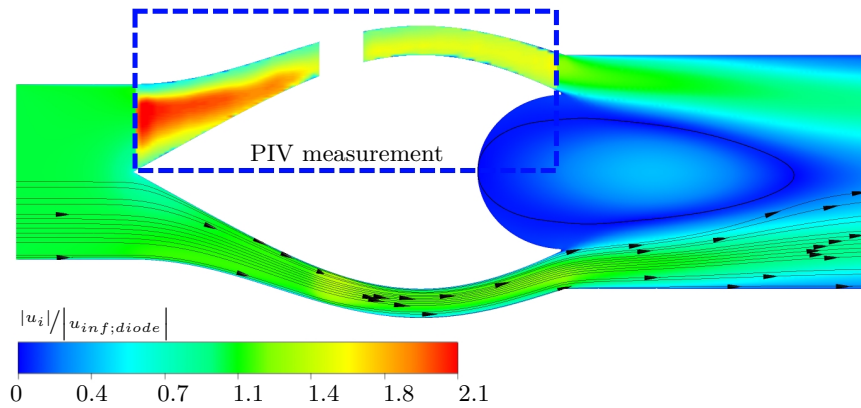


Figure 3.12: Flow field as measured by PIV (in the blue dashed rectangle) and calculated by the numerical simulation in the forward direction.

For the measurements in the reversed direction, no asymmetry is present in the inflow, because the combustion tube with a length of approximately 1 m causes a perfectly symmetrical inflow into the fluidic diode. Accordingly, the PIV measurements are in very good agreement with the numerical simulation. Again, the line of zero axial velocity is shown as a black solid line. It can be seen, that the recirculation region that was observed in the forward direction is not present anymore. The flow is penetrating the cusp on the downstream side of the center body and is directed into the outer passage. A small region of separated flow is located on the center body surface directly at its “downstream” (i.e., right) side. This flow separation and the strong deflection of the main flow is desired, as it increases the pressure loss of the fluidic diode in the backward direction. It may be possible to further increase the size of this recirculation bubble, for example using a shallower cusp or a different axial positioning of the center body. This will not necessarily increase the diodes performance (i.e., diodicity) due to a possible increase in the forward pressure loss coefficient. However, in the complete SEC inlet setup (see Fig. 3.5) the reversed flow

will be guided into the cusp, because the diameter downstream of the center body is reduced. This is expected to increase the size of the observed recirculation region. In the experiment the main features of the flow are captured very well. However, due to the restriction of the measurement technique, the regions very close to the walls are not captured. Accordingly, the small separation region on the outside of the center body cannot be verified in the experimental data.

In order to quantitatively compare the experimental and numerical data and to validate the numerical model, the radial velocity profiles along the inlet and outlet of the fluidic diode are extracted and shown in Fig. 3.14 for the more important backward flow case. The position of the velocity profile coincides with the left

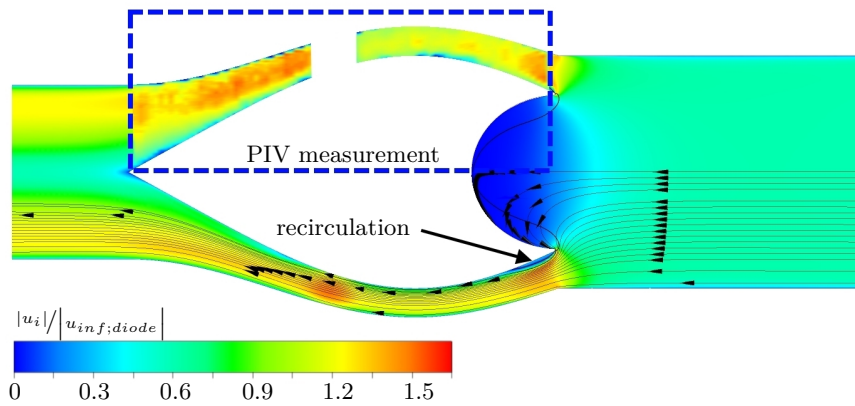


Figure 3.13: Flow field as measured by PIV (in the blue dashed rectangle) and calculated by the numerical simulation in the backward direction.

and right boundaries of the PIV measurement region, as shown in Fig. 3.13. The numerical simulation shows a very good agreement with the experimental results. On the “upstream” side (left boundary of the PIV measurement region in Fig. 3.13), shown in red, the numerical simulation is identical to the experimental results close to the outer wall. In the middle of the flow passage, the numerical simulation predicts a lower velocity with a more distinct peak on the outside of the channel. This deviation is likely to stem from a not perfect centering of the center body in the assembly process, which results in slight asymmetries in the flow field. At the “downstream” side (right boundary of the PIV measurement region in Fig. 3.13), shown in black, the numerical simulation is very close to the experimental results. Close to the center body, the small separation region that is predicted by the numerical simulations cannot be seen in the PIV measurements as it was already mentioned above. However, Fig. 3.14 gives confidence in the used numerical model for the given flow configuration, as the results of the numerical simulations and the experiments are in good agreement.

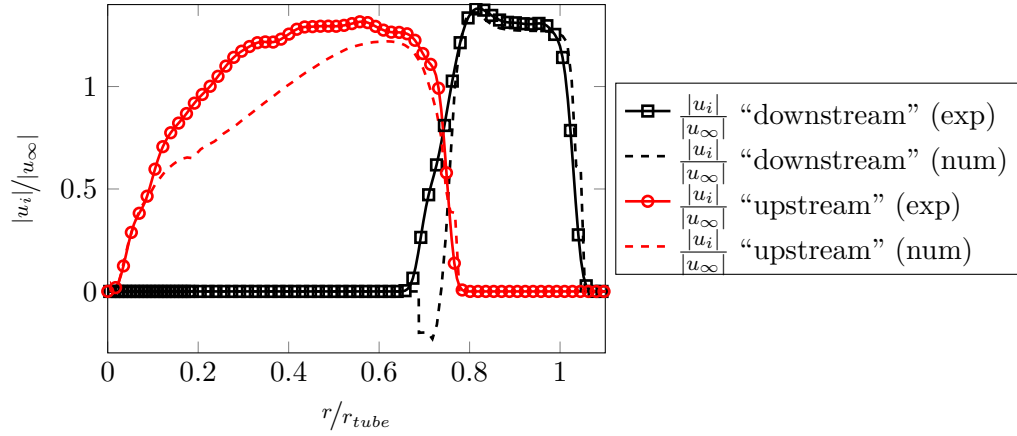


Figure 3.14: Velocity profiles at the inlet and outlet of the fluidic diode for the PIV measurements and the numerical simulation in the backward direction.

3.4 Transient Investigation

Subsequent to the presented investigation of the steady-state flow field and the validation of the numerical model, a numerical study of the transient behavior during a simulated ignition event is presented and discussed in this section. This investigation is based on the final geometry of the complete fluidic diode setup as it is shown in Fig. 3.5.

3.4.1 Computational Domain and Boundary Conditions

In the SEC process the fluidic diode is faced with an inherently transient process driven by pressure fluctuations due to the ignition events. In order to investigate the performance of the proposed fluidic diode geometry in this environment the complete geometry is numerically investigated. As for the steady-state validation case, the numerical model is based on the unsteady RANS formulation and the SST turbulence model, in this case for a compressible fluid. The computational grid was created using ICFM CFD and the numerical investigation was performed with the ANSYS CFX 14.5 software package. Figure 3.15 shows an overview of the computational domain including the regions for the different boundary conditions. The dimensions of the diode section itself are identical to the geometry of the steady investigation shown in Fig. 3.11, including the reference diameter of the combustion tube ($D = 40$ mm). The overall extent of the domain is increased to a length of 8 diameters and the convergent part of the fluidic diode geometry was added downstream of the center body. In addition, a new boundary condition region, which represents the wall film cooling (shown as two small blue lines at the step in the outer wall), is added. In this area an inlet with a 20% higher velocity than the main flow is defined to represent

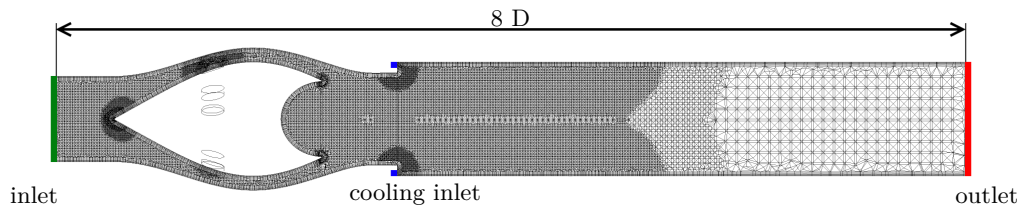


Figure 3.15: Overview of the computational domain including the regions for the boundary conditions (the colored lines) for the transient investigation of the fluidic diode.

the film cooling. This cooling is needed in the final SEC process to separate the combustible fresh charge from the hot boundaries of the combustion tube. The value of a 20% higher velocity was chosen to give an idea how the main flow is affected by the film cooling close to the inlet section. In the final SEC process this film cooling momentum must be further assessed: the cooling air has to cover the complete length of the fresh fuel–air charge. Additionally, the needed mass flow must be reduced to minimize the influence on the overall efficiency of the machine. The mesh is refined in the cooling region as well as at the sharp corners around the center body and its holding tacks. The calculations were again set to an adaptive time step scheme keeping the *rms*-value of the Courant number below a value of 1.5. This resulted in time steps around $7.5 \cdot 10^{-7}$ s. The simulated time corresponded to a single ignition event with a duration of 3.35 ms.

In contrast to the steady state investigation of Sec. 3.3 the numerical simulation was performed in two stages with different boundary conditions. The filling process of the combustion tube is simulated in a first stage using a pressure boundary inlet on the left side of the domain (shown as green line in Fig. 3.15) at a static pressure of 1400 Pa and an opening on the outlet side of the domain (see the red line in Fig. 3.15). Air at a temperature of 817 K is used, resulting in a Reynolds number of around 82,000 during this filling stage. Even though this Reynolds number is higher than the Reynolds number of the steady validation case, confidence in the qualitative reliability of the numerical model exists, because the flow is completely turbulent and dominated by a bluff–body separation downstream of the center body. In this stage of the numerical simulation the wall film cooling is activated. Subsequent to this initial state, one ignition event was simulated as follows. The pressure at the inlet was set to the surrounding reference pressure and the wall film cooling inlet was set to a non–slip wall. The boundary at the outlet of the domain was set to represent a pressure time trace as it is created by a single ignition at atmospheric pressure. In this way the combustion induced pressure rise is represented in the computational model. However, the temperature and density rise due to the constant volume combustion is not included in this investigation, because this section focuses on the flow field inside

the fluidic diode. The pressure time trace used in this simulation is obtained from an one-dimensional investigation of the ignition process using detailed chemistry carried out by Phillip Berndt¹. The numerical model used for the generation of this boundary condition is described in [15] and more deeply analyzed for its applicability on the investigated flow situations in [11]. It is based on an one-dimensional solver of the Euler equations including a thermally perfect equation of state and a reaction mechanism specially developed for the simulation of the SEC process (see [16]). The pressure at the upstream end of a fresh fuel-air charge over the time of the ignition process is obtained from this simulation. The corresponding time trace is shown in Fig. 3.16. As one can see, the combustion induced pressure rise is starting 0.35 ms

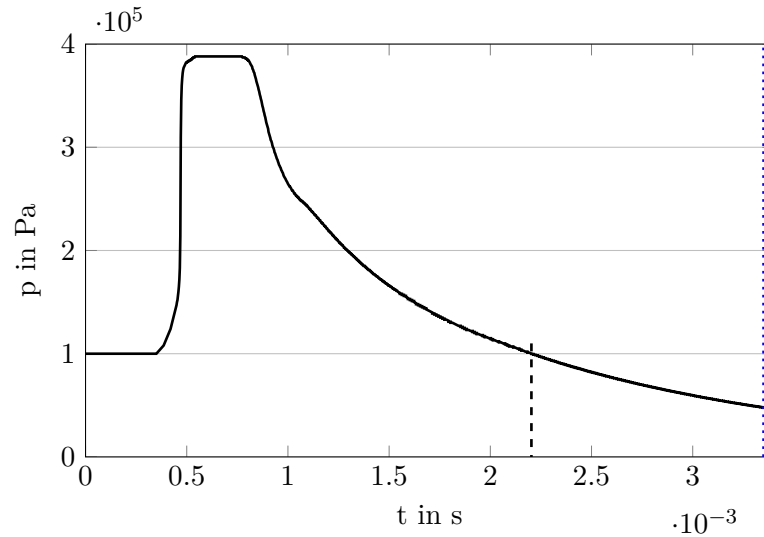


Figure 3.16: Pressure time trace of a single ignition event as it was used as boundary condition in the transient investigation.

after the initial state of the simulation. This is done to simulate at least a short ignition delay time. The real ignition delay time for an atmospheric ignition is longer by a factor of 100 (around 350 ms), which would increase the computational costs of the simulation without any further insights. After a duration of approximately 2.2 ms the pressure is already back to the atmospheric value from the beginning of the simulation. This instance in time is shown as a black dashed line in Fig. 3.16. Subsequently, the pressure is dropping below the initial pressure, which represents the suction wave that is created by the reflection of the combustion driven pressure wave at the open end of the combustor (see Sec. 1.1.1). Due to the high computational demands of this numerical model, the simulation is limited up to the time of 3.35 ms

¹ Freie Universität Berlin; FB Mathematik und Informatik; Institut für Mathematik

(as indicated by the blue dotted line). The results and findings of this simulation are presented and discussed in the following section.

Please note that the flow field induced by this “forced” boundary condition is a simplified view on the real transient process within the SEC combustor. In the real SEC process the pressure and density of a given fluid volume is increasing due to the chemical reaction, which is followed by a blow down of the higher pressure in both directions (i.e., upstream in the direction of the diode and downstream in the direction of the outlet). The dictated pressure at the outlet of the computational domain blocks all interaction with the pressure waves or velocities within the fluid domain. In addition, the boundary condition at the outlet of the computational domain corresponds to an infinite virtual volume of fluid with the given pressure, resulting in a possibly infinite backwards oriented flow into the combustion tube. This is, again, not a realistic representation of the SEC process, because there is only a finite fluid volume with higher pressure and density available to create a back flow. Unfortunately, the computational costs did not allow a more detailed and realistic numerical investigation within the framework of this project. Hence, the results of the numerical simulation subsequent to the moment when the pressure wave hits the fluidic diode and is reflected have to be considered with caution, keeping the mentioned simplifications in mind.

3.4.2 Flow Field During Ignition and Blow Down

The simulated ignition event and blow down is, as already mentioned, following an initial calculation of the filling process. The flow field of this initial state and the according static pressure distribution is shown in Fig. 3.17a. On the left side of this figure, the magnitude of the velocity is depicted in false colors, overlaid by streamlines in the displayed central plane of the computational domain. The streamlines are colored in black for a positive axial flow and white for a negative axial flow. The direction of the flow is additionally shown as arrowheads using the same color scheme. A black solid line without any symbols shows the locations with zero axial velocity (i.e., the location of back flow regions) within the domain. On the right side of Fig. 3.17a the static pressure within the computational domain is depicted as false colors. Note that both color maps are based on a logarithmic scale to gain visibility of the lower pressure and velocity regions. The described plot scheme is used throughout the remainder of this section to visualize the transient flow field within the fluidic diode.

The initial flow field in Fig. 3.17a shows the same main features as the flow field in the steady-state investigation. The flow follows the center body surface again without any separation. Downstream of the center body the recirculation region is present. As expected in the steady-state section, the axial extent of the recirculation region is reduced due to the convergent part of the fluidic diode assembly. Even though this creates a more even velocity profile within the combustor, the velocity on

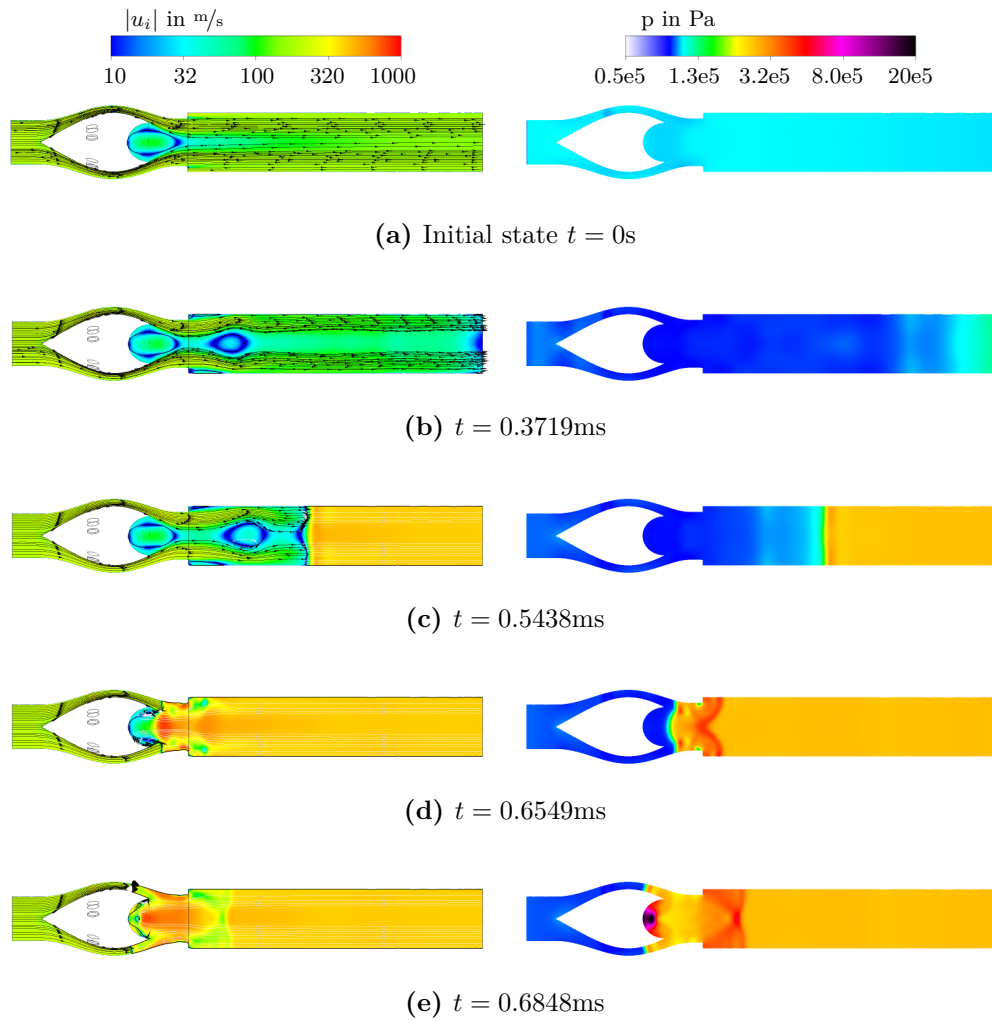


Figure 3.17: The flow and pressure field in the fluidic diode during one ignition event and the subsequent blow down (first part from initial state to the focusing of the pressure wave).

the center line of the combustor is still lower, than in the outer regions of the tube. This incision in the velocity profile is undesired, but will be significantly reduced by the fuel injection. The fuel in the SEC, is injected using spatially oscillating jets emanating inwards from the outer wall of the flow passage (see chapter 2). These oscillating jets collide in the center of the flow passage, creating very high turbulence levels. Hence, an even velocity profile at the inlet of the combustion tube is expected. At the inlet of the combustion tube, a sudden expansion in the cross section creates the necessary surface for the cooling inlet. The cooling flow is set to a 20% higher velocity than the main flow velocity. The region of high velocity close to the wall is visible in Fig. 3.17a. The pressure distribution reveals as expected a region of lower pressure at the downstream end of the center body. Subsequent to this initial condition, the pressure at the inlet of the computational domain is set to zero. The cooling flow inlet is additionally set to a non-slip wall in order to stop the wall film cooling flow. This is necessary in the SEC process to inhibit further movement or mixing of the fresh charge.

The consequences of this sudden closing of the cooling inlet can be seen in the second figure of the sequence shown in Fig. 3.17b. A recirculation bubble is separated from the fluidic diode due to the disturbance introduced by the sudden shut down of the cooling flow. This additional recirculation bubble is not desired in the SEC combustor because it is accompanied by additional axial mixing. The fuel injection is expected to reduce the main recirculation zone extent in the final SEC and, thus, suppress the additional recirculation zone. The main flow is still entering the computational domain from the left driven by the inertia of the fluid. In the final SEC process and the atmospheric ignition investigations the fluid velocity will be reduced prior to the ignition event. This is achieved by either the slight pressure wave from the prior ignition (in the real SEC process) or the fluidic switch (in the atmospheric ignition investigation). Unfortunately, no velocity or pressure time traces corresponding to this behavior were available for the developed geometry to include this effects in the numerical model. Downstream of the cooling flow inlet two small recirculation regions are established close to the wall. The pressure at the outlet is already increased to approximately 120 kPa. After 0.5438 ms in Fig. 3.17c the pressure wave has reached the middle of the simulated combustion tube, together with the backwards oriented flow, which is following this pressure rise. Fluid is still entering the domain in the left half of the computational domain. This counter flow situation results in a pressure peak of 290 kPa at the stagnation line. The second recirculation region mentioned in the preceding state of the flow has slightly moved downstream (i.e., to the right) but is still present in the domain.

Figure 3.17d corresponds to the moment when the pressure wave has just passed the cooling flow inlet in the upstream direction. Since the cooling flow inlet is treated as a non-slip wall in this simulation, the pressure wave is partly reflected at this surface and results in a funnel shaped pressure peak of around 460 kPa. This reflection will have a much lower amplitude in the real SEC test rig, because there the

cooling flow inlet is an opening. Accordingly, it has a significantly lower reflectivity. The backwards oriented flow has already reached the cusp of the center body in the fluidic diode. The flow is directed into said cusp creating regions of severe streamline curvature at its rim, due to the convergent fuel injection section. This flow situation creates a very high pressure loss in this flow direction. Still the main flow enters the computational domain from the left and is colliding with the backwards oriented flow right downstream of the center body.

One of the main features of the fluidic diode in the SEC concept is the pressure focusing cusp of the center body. This cusp prevents misfiring events, due to an ignition failure. As visible in Fig. 3.17d, the fluid is pushed back into the cusp by the incoming pressure wave. During a misfiring event, this pressure wave will be much lower, due to the failed ignition, but still it will push the fresh fuel–air mixture into the cusp as it was expected in Sec. 3.2. In Fig. 3.17e the pressure wave has reached the center of the cusp as well. As depicted by the pressure field on the right side of the picture, the pressure wave is reflected by the walls and focused into the focal point. In this point a peak pressure of 2,022 kPa (i.e., over 20 bar) is reached. This value corresponds to a pressure magnification factor of around 5 in comparison to the pressure at the outlet boundary condition. This value might be exaggerated by the numerical model, but already a significantly smaller pressure magnification will assure a reliable ignition of any remaining fuel–air mixture. Similar pressure amplification levels were found in literature, for example by Kulkarni who experimentally investigated the focusing of weak shock waves at surfaces with different curvatures [58]. He observed a peak pressure amplification factor of around 5 in his work as well. Even though, this emergency ignition is inside the inlet section and thus at a more upstream position than desired, a complete burn of the fuel is of more importance. If a misfired fuel–air charge leaves the combustor and is ignited at hot surfaces or exhaust gases in the turbine inlet it may harm the delicate turbine blades. This potential danger might be inhibited by the developed geometry. In the combustion tube the residuals of the pressure reflection at the cooling flow inlet are still visible traveling in the downstream direction. On the left side of Fig. 3.17e the collapse of the streamlines into the focal point of the focusing cusp is observable. The backwards oriented flow penetrates already into the passage around the center body, while the main inlet flow is still unaffected by the outlet boundary condition.

The second part of the transient investigation is shown in Fig. 3.18. It depicts the stages from the reflection of the pressure wave at the center body (Fig. 3.18a) up to the point where the inflow of the next filling process is established in Fig. 3.18e. The reflected pressure wave has just left the center body focusing cusp in the first figure of said second picture (Fig. 3.18a). The accompanying flow in the downstream direction (i.e., from left to right in the plots) has created a region of positive axial velocity located at the outlet side of the fluidic diode. While the reflected pressure wave is leaving the fluidic diode, it significantly reduces the velocity of the backwards oriented flow at its front. This is visible in the steep gradient of the velocity magnitude

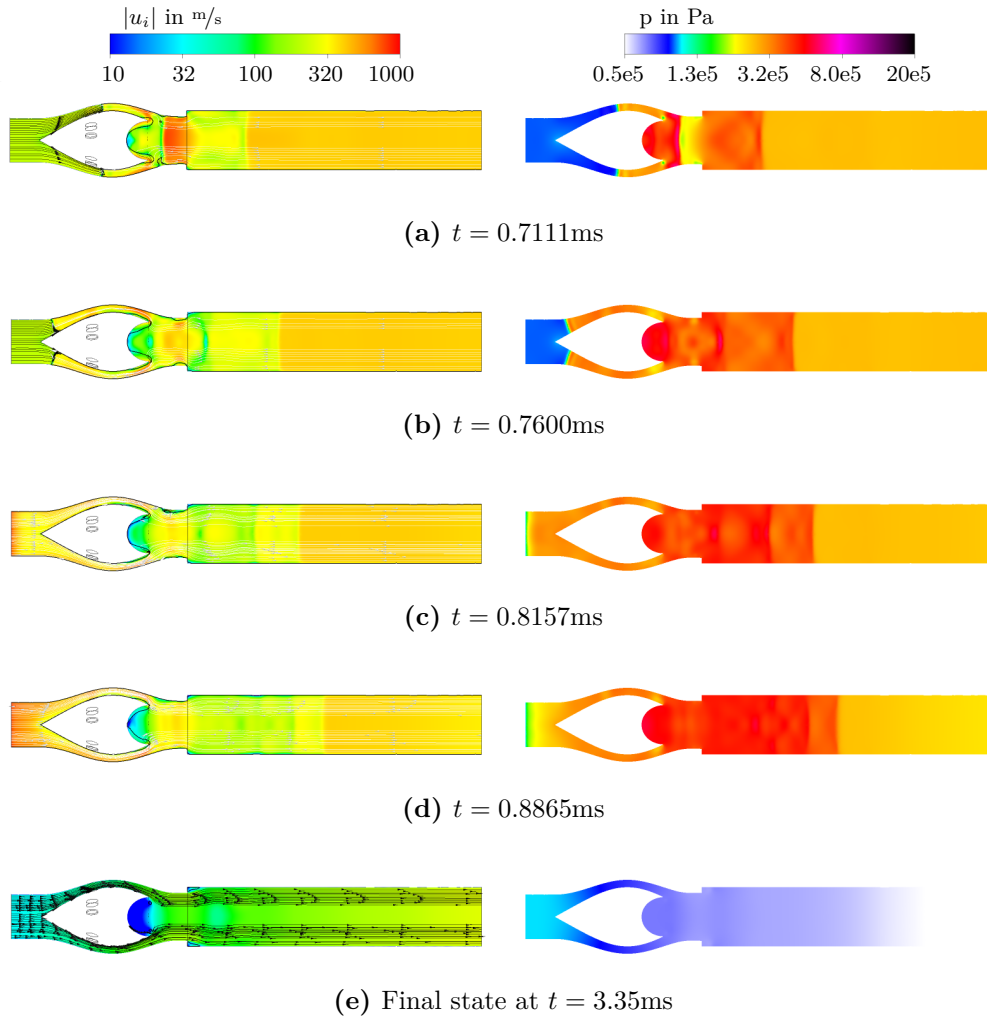


Figure 3.18: The flow and pressure field in the fluidic diode during one ignition event and the subsequent blow down (second part from the focusing of the pressure wave until final state of the simulation).

in Fig. 3.18a. The pressure on the right side clearly shows the reflected pressure wave with a peak pressure of around 645,000 Pa, which is still slightly higher than the peak pressure at the outlet boundary condition (see Fig. 3.16). Additionally, the upstream traveling pressure wave is visible in the flow path around the center body. Still the main inlet flow in the downstream direction is visible on the left side of this pressure wave. In the subsequent pictures (Fig. 3.18b-3.18d) both of the mentioned pressure waves can be observed traveling in their respective directions. As the upstream traveling pressure wave has reached the inlet, a negative axial flow is established throughout the whole computational domain. Accordingly, the flow field in the fluidic diode is similar to the one observed in the steady-state investigation (see Sec. 3.3). However, this high negative mass flow is, as already mentioned in the boundary condition section, partly exaggerated due to the boundary condition. In a real SEC ignition event the fluid volume undergoing the combustion induced pressure rise is finite, whereas an infinite virtual volume of high-pressure fluid is represented by the outlet boundary condition in this numerical investigation.

In the final state of the presented transient investigation (Fig. 3.18e) at $t = 3.35\text{ms}$, the pressure at the outlet boundary has already dropped below the inlet pressure (see Fig. 3.16) and the filling of the next combustion charge is in progress. The negative pressure gradient along the computational domain is causing an inflow into the combustion tube. The flow field within the fluidic diode is similar to the one of the initial state, but since the cooling flow is not activated yet, the two small recirculation regions at the cooling flow inlet are present. The main recirculation region in the focusing cusp of the fluidic diode is slightly smaller than at the initial state and the flow is accelerated along the combustion tube due to the higher negative pressure gradient. In the real SEC process the cooling flow will be switched on and the fresh fuel-air charge will be filled at this state of the combustor.

The presented numerical simulation is only a simplified model of a single ignition event inside the SEC combustor, but several conclusions can be drawn from the descriptions above. First, the fluidic diode was not able to completely block the flow in the upstream direction. From the conducted numerical study this effect cannot be quantified, since the simplified downstream boundary condition has a significant influence on this effect. The actual fluid volume available to generate a backwards oriented flow is finite in reality in contrast to the infinite virtual fluid volume generated by the boundary condition. In order to quantify this existing reversed mass flow an experimental investigation of an actual ignition event should be performed in future work. However, it might not be possible to completely block the reversed flow of such a homogeneous auto-ignition event without a mechanical blocking of the flow path. Experimental investigations of the complete SEC process must be conducted to identify the tolerable limits of this reversed mass flow.

The second finding from the numerical investigation is the capability of the fluidic diode to reflect the combustion induced pressure wave. Together with the third finding, the amplification of said pressure wave by a factor of around 5, the main

design features of the fluidic diode regarding this pressure wave reflection were confirmed. The presented inlet section of the SEC combustor is able to preserve the pressure fluctuations necessary for the SEC process and prevent misfiring events by means of pressure focusing.

3.5 Intermediate Conclusion

The reliable flow rectification for an unsteady combustion process, especially for high firing frequencies, is one of the key factors for a successful application of such a combustion technique. Regarding the SEC process, no traditional valves or other flow control devices exist that are able to switch or control the inflow of the combustion tube at a temperature of approximate 800 K and a firing frequency of around 250 Hz. The involved temperature and combustion induced pressure fluctuations would either destroy any traditional mechanical valve or limit the lifetime of the device significantly. Thus, traditional parts are not able to fulfill this task, in contrast to a fluidic diode without any moving parts.

In the last century several types of fluidic diodes were invented. They were reviewed regarding their applicability in the SEC test rig. Beginning from the first known fluidic diode, the “tesla diode”, the vortex, cascade, and scroll diodes were evaluated. Even though the cascade diode has the highest diodicity (i.e., the highest ratio between the forward and backward pressure loss coefficient) it is not suitable for the SEC process since the pressure fluctuations needed for the SEC process are not sufficiently reflected by the geometry of the diode. The same is expected for the “Tesla” and the vortex diode. Solely the scroll diode is expected to allow for a sufficient reflection of the pressure and suction waves due to its center body in the flow path. Based on the idea of the scroll diode, a fluidic diode was developed and designed that is not only able to reflect the pressure fluctuations but also is able to prevent misfiring events in the combustion process. The design is based on a streamlined center body that creates a very low pressure loss in the forward direction. This is accomplished by a constant cross-sectional area within the diode section and the absence of any flow separation on the surfaces of the center body. The low pressure loss in the forward direction is necessary to allow the fast filling process. On the downstream side of the center body a spherical cusp not only increases the pressure loss in the backward direction but also acts as a pressure focusing device. If, due to whatever reason, the auto-ignition fails, the pressure wave within the combustor is focused, creating a pressure peak in one single point. This pressure peak serves as an ignition source and ignites the combustible mixture. Downstream of the center body the fuel injection and wall film cooling is integrated in the device. This assures a compact, rigid and reliable inflow section of the SEC combustor without any moving parts.

An investigation of the steady state flow field was conducted based on this design using, experimental and numerical techniques. The performance (i.e., diodicity) of

the proposed design was assessed by means of pressure loss measurements in both flow directions. A diodicity value of 5.9 as defined by Eq. 3.1 was found, which is slightly lower than the value of 6.6 for the original scroll diode (see [8]). As desired during the design phase, a “clean” flow around the center body was observed without any undesired flow separation. In the backward direction the flow separated from the surface of the center body directly on the downstream side, due to the strong deflection of the flow. This separation and the following decrease in the effective passage height are, besides the sudden constriction of the cross-sectional area, the main driving factors for the increased pressure loss in the backward direction. The numerical simulation and the experimental measurements are in good agreement and, thus, this steady state investigation can also be seen as a validation of the numerical model.

A single ignition event was investigated using the validated numerical model. Since a simulation of a “real” homogeneous auto-ignition including the changes in the density, temperature, and pressure in a given flow volume was not possible within this project, a simplified approach was employed. From an one-dimensional simulation of the combustion process including detailed chemistry, a pressure time trace within the fuel-air mixture undergoing auto-ignition was obtained. This pressure time trace was used as outlet boundary condition of the computational domain in order to investigate the behavior of the pressure and flow field in the fluidic diode section. This approach implies several deviations from the real process. First, the combustion induced changes in density and temperature are not included in the simulation. Second, due to the nature of a pressure boundary condition, an infinite volume of fluid at elevated pressure was virtually present downstream of the computational domain. Hence, an infinite mass flow from the outlet to the inlet side of the computational domain was possible. This behavior is not reasonable regarding the real process, because only a finite fluid volume undergoes auto-ignition. However, the numerical simulation gave a nice view into the pressure and flow field within the combustion tube in the presence of a pressure wave.

It was shown, that the developed inlet section (including the fluidic diode) was not able to completely block the reversed flow. However, this effect could not be quantified, because the simplifications of the numerical model are introducing errors in this phenomenon. The quantification of this back flow and the tolerable limits of this effect in the SEC process must be evaluated experimentally in future work. Nevertheless, the numerical investigation revealed that the desired effects regarding the reflection of the incoming pressure wave were present. The developed geometry is not only able to reflect an incoming pressure wave with a sufficient amplitude, but also focuses said pressure wave in one single point, creating a pressure amplification factor of around 5. This behavior is able to prevent misfiring events within the SEC process, since it creates a single spot of high-pressure as ignition source if the homogeneous auto-ignition fails.

By changing the geometry of the center body and its positioning within the flow path, it may be possible to alter the three found parameters: diodicity, pressure wave reflection, and pressure focusing. A shallower cusp for example, might increase the backward pressure loss coefficient and move the focal point of the pressure amplification downstream. A larger maximum diameter of the center body may be positive for the diodicity of the presented diode. However, the developed geometry represents the optimum trade-off for the tested designs. The shift of the focal point to a more downstream position will create a pressure peak within the fresh fuel-air mixture for every little disturbance in the pressure field. This may lead to premature ignition and needs to be avoided by all means. A larger maximum diameter in the center body will result in a reduced height of the flow passage, due to the constant cross-sectional area. This increases the pressure loss in both flow directions and thus is not desired during the filling process of the combustor. As one can see, every little change in the geometry of the fluidic diode may have positive and negative effects and must be evaluated with caution. The presented geometry was chosen from the investigated versions in order to give the best performance regarding the SEC process.

Summarizing the findings of the different sections it was possible to fulfill almost every demand that was created by the SEC process as claimed in the geometric design section (see Sec. 3.2). Even though it was not possible to completely block the reversed flow, the diodicity of the presented fluidic device may reduce the back flow sufficiently. This must be investigated in future work. The other 4 requirements, namely the reflection of the pressure wave, a minimal inlet pressure loss, mechanical integrity and integrability of the device into a gas turbine system, are completely met. In addition, a special geometrical feature was integrated into the fluidic diode that provides a pressure amplification in a single point. This prevents misfiring events due to failed auto-ignition. All these features are integrated into a compact inlet section design without any moving parts that is expected to withstand the harsh environment of a SEC combustor for a more than sufficient time.

CHAPTER 4

Fluidic Switch

In the previous chapters fluidic devices were proposed to resolve two of the main challenges of the *SEC* process. Since the ignition time delays are strongly dependent on the static pressure inside the combustion tube, it is not possible to realize the complete *SEC* process at atmospheric conditions with a tube of reasonable length. However, in order to investigate the sensitivities, dynamics and underlying effects of a homogeneous auto-ignition, an atmospheric test rig is designed and built (see chapter 5). Due to the mentioned long ignition delay times under atmospheric pressure, it is necessary to stop the flow inside the combustion tube once the fuel is injected. Otherwise, the fresh fuel-air charge will move out of the combustor prior to ignition. This stopping of the flow inside the combustor and, hence, the device presented in this section, is only needed for the investigation of ignition events at atmospheric conditions. Two challenges arise from this task. On one hand, no valve is known to the author that is able to withstand an airflow with a maximum temperature of around 1000 K. On the other hand, the electrical air heater used requires a minimum airflow of 25 kg/h in order to prevent internal overheating. Accordingly, a device is needed that allows to switch a minimal air mass flow of 25 kg/h with a temperature of maximal 1000 K from the combustion tube to a bypass path in less than 50 ms. In the complete *SEC* process the combustor is “breathing” its oxidizer by itself from the compressor plenum. Unfortunately, this “breathing” process cannot be employed in the atmospheric test rig due to the minimum airflow of the heater and the extremely long ignition delay times. In this chapter a control device based on the bistable fluidic switch (see Sec. 1.1.2) fulfilling this task is presented, numerically simulated, and tested.

4.1 State of the Art

The fluidic amplifier was the first fluidic device invented in the late 1950s with the purpose of creating fluid driven logical circuits. The idea behind this device is to

deflect a large main jet with only small control flows. In the year 1958 a patent named “Jet Propulsion Units” was granted to Kadosch *et al.* [47] in which they describe the idea of steering a jet between two different outlet paths of a jet engine by either obstacles in the flow or small control flows. The sketch of his idea is shown in Fig. 4.1. In this figure, the main jet, which is coming from the bottom, is redirected

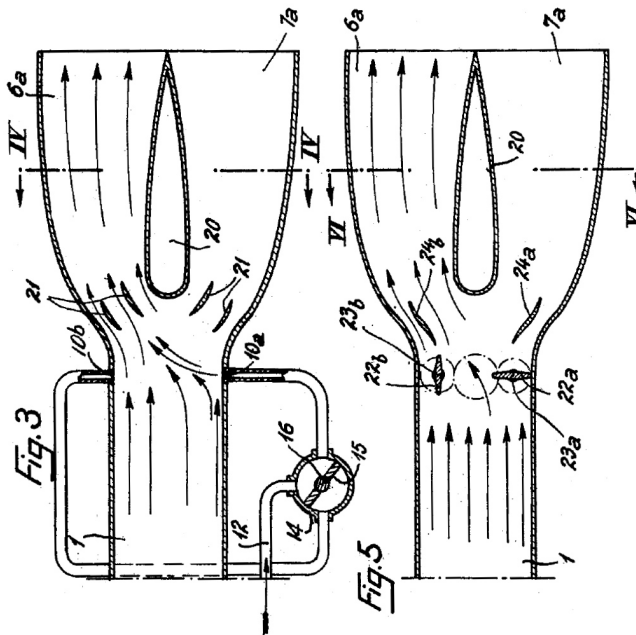


Figure 4.1: Idea of a fluidic amplifier as sketched by Kadosch *et al.* in their patent [47].

either by small obstacles in the flow (see right side of Fig. 4.1) or by a flow from one of the two small control ports (left side of Fig. 4.1). Based on the idea of jet deflection with small control jets, the fluidic amplifier was invented. An example of such an amplifier is shown in Fig. 4.2a. It represents an “analog” device where the ratio of the outlet flows can be adjusted by the feeding pressures at the control ports. From the first publication of the fluidic amplifier in the beginning of the 1960s, a broad variety of investigations and models arose around the globe. Several analytical models for the amplification characteristics of the “analog” amplifier were proposed and evaluated with respect to experimental data. Based on these first investigations, staged setups were derived to create fluidic amplifiers with even higher gain factors. One example of such a setup is shown in Fig. 4.2b. A broad overview on both, the different concepts and mathematical modeling approaches of fluidic amplifiers, can be found in [55]. During the investigations of the fluidic amplifier, it was observed that it was not possible to deflect a jet within a closed environment perfectly proportional to the control pressures, because the COANDĂ-Effect causes the jet to attach to a

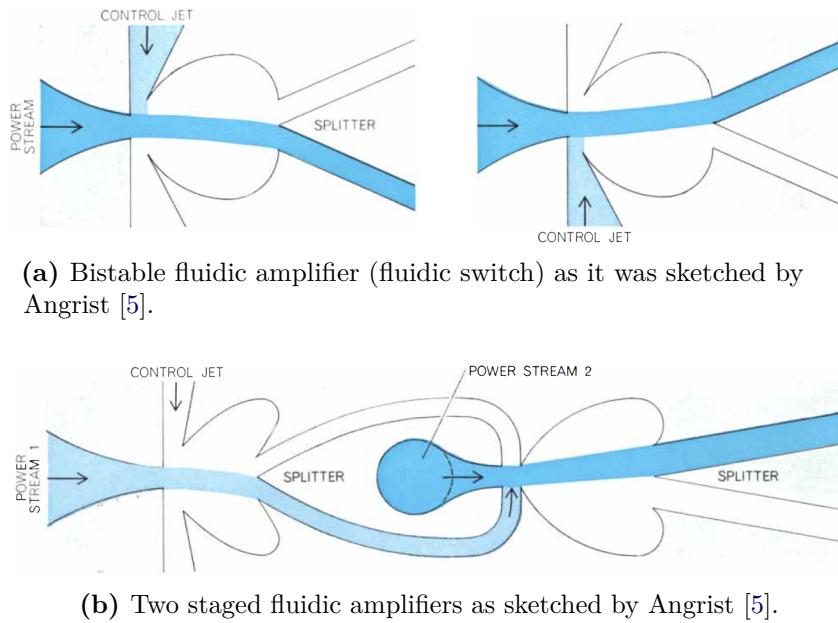


Figure 4.2: Sketches of an “analog” fluidic amplifier (4.2a) and two staged fluidic amplifiers 4.2b as presented in [5].

close surface¹. This effect was already described in the year 1800 by Thomas Young [108] as he discovered that an air stream is deflected towards a nearby body. In a letter to Edward Whitaker Gray, he described the effect as follows:

“The lateral pressure which urges the flame of a candle towards the stream of air from a blowpipe, is probably exactly similar to that pressure which causes the inflection of a current of air near an obstacle. Mark the dimple which a slender stream of air makes on the surface of water; bring a convex body into contact with the side of the stream, and the place of the dimple will immediately show that the current is inflected towards the body;...” — THOMAS YOUNG 1800

As already mentioned, this observation was later named the COANDĂ-Effect. Even though this effect rendered the idea of an ideal “analog” amplifier void, it creates the possibility of a more “digital” fluidic device, the bistable fluidic switch. A sketch of a simple example of such a bistable fluidic switch was already shown in the background chapter of this thesis (see Fig. 1.4). In the bistable fluidic switch two walls are placed close to the main jet exit to allow the attachment of the main jet to these walls. Starting from this simple device, several fluidic switches were invented and

¹ In order to avoid this effect the “heart”-shaped inclined wall is inserted in the fluidic amplifiers in Fig. 4.2

investigated in the last decades. In 1962 Levin and Manion presented an analytical model for the jet attachment distance inside such devices for constructing controlling circuits [61]. This work was later extended by Sher in 1964 [85] as well as Goto *et al.* [34]. Other research groups published studies on the influence and design of certain geometrical parameters inside these devices. In 1962 Warren published a work on the influence of the main geometric parameters affecting the switching behavior and overall performance of such bistable fluidic amplifiers [102]. He condensed his findings into one picture, shown in Fig. 4.3. As for all fluidic parts, every change in

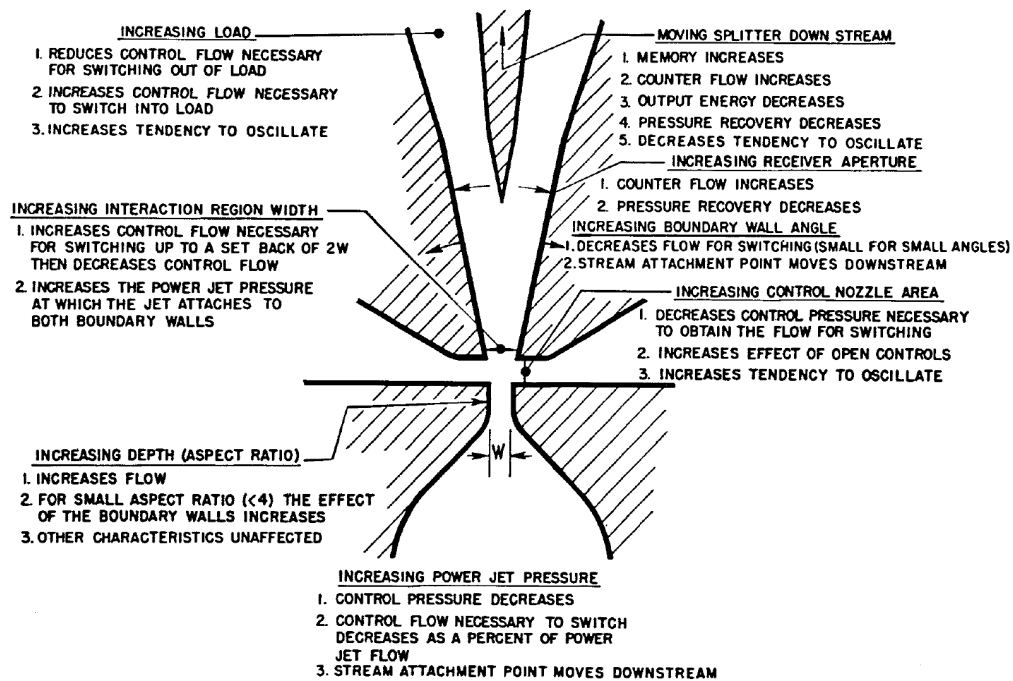


Figure 4.3: A summary of the parameters influencing the properties of a bistable fluidic amplifier as published by Warren in 1962 [102].

the geometry of the bistable amplifier goes along with more or less drastic changes in the performance of the device. Later investigations deal mainly with the influence of a specific region inside the switch (e.g., [38]), the design of improved or adapted geometries (e.g., [22, 92–94]), or the application of such devices (e.g., [46, 56, 92, 93]). Again, a nice overview on the early research regarding the bistable fluidic switch including several modeling approaches can be found at Kirshner and Katz [55].

4.2 Geometric Design

In the SEC test rig a bistable switch is needed that is able to switch the hot main air flow with temperatures up to 1000 K from the test section to the bypass in less than

50 ms. In addition, some other characteristics must be fulfilled in order to ensure the demanding process of the homogeneous auto-ignition. First, no vents or other openings to the environment can be utilized in the device, because the homogeneous auto-ignition imposes strict requirements to the fuel-air mixture and mass flow rate accuracy. Any opening to the environment other than the main flow paths may alter the main mass flow and, thus, the equivalence ratio, preventing the required accuracy in the filling process. Second, a choked nozzle inside the main air path is needed in order to prevent the penetration of pressure pulses into the electrical air heater. If, for example, a shock wave that is induced by a misfire event travels upstream into the air heater it will be destroyed due to the mechanical stresses on the heating coils. Both tasks, switching the hot air flow and creating a choked nozzle in the main air path, should be accomplished by the fluidic switch.

The geometry of the device used was derived from the geometry of Tesař *et al.* [95] that was in turn derived from a geometry used by Tesař [90] and later Perera and Syred [74]. A rendered picture of the CAD-model and a drawing of the inner dimensions is shown in Fig. 4.4 and Fig. 4.5, respectively.

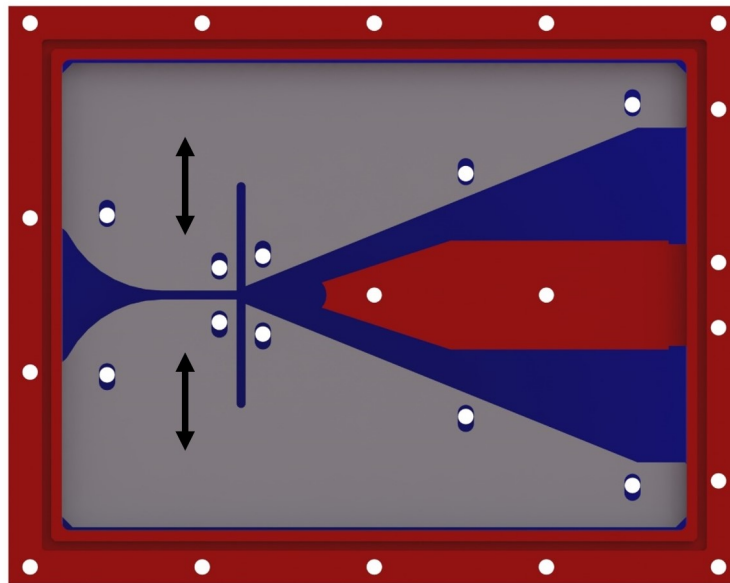


Figure 4.4: Rendered picture of the CAD-model, consisting of the bottom plate (blue), the two sliders (grey) and the outer frame (red). The white points are holes throughout the device.

In Fig. 4.4 the parts of the fluidic switch are shown in false colors. The top cover plate is not shown to allow the view on the inside geometry of the device. The flow enters the power nozzle from the left through the outer frame (shown in red). The

bottom plate of the switch is shown in blue behind the two gray sliders. The flow is accelerated in the power nozzle up to the speed of sound and then enters the interaction region (i.e., the region between the two control ports and the splitter cusp). In order to lower the pressure drop across the device for higher mass flow rates it is possible to adjust the cross-sectional area of the power nozzle by moving the two sliders. The flow attaches to one of the outer inclined walls and is directed into one of the two outlets on the right hand side of the switch in Fig. 4.4. The splitter features a cusp to create a self-stabilizing mechanism for the attached main jet. If the jet starts to detach from the inclined surface a small portion of the jet is “peeled” off and redirected in the upstream direction by the cusped splitter. This vortical flow pushes the main jet back to the outer wall, increasing the stability of the switched state. This effect was shown and explained by Tesař and Bandalusena [94].

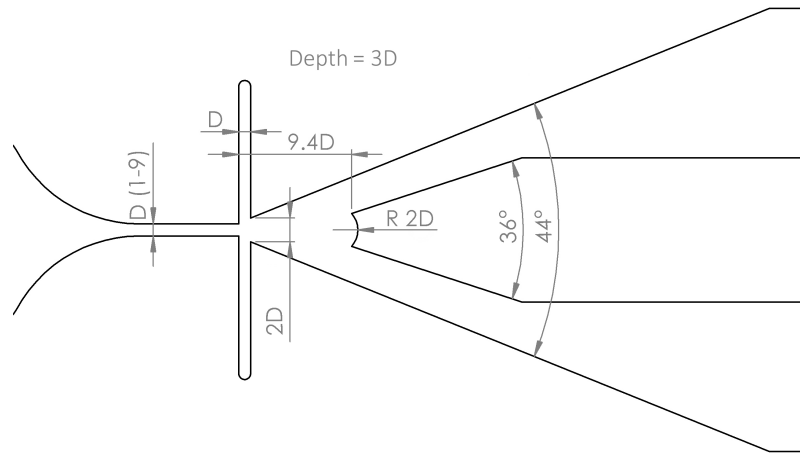


Figure 4.5: Drawing of the inner geometry including the main dimensions.

The main dimensions of the geometry used are shown in Fig. 4.5. All dimensions are based on the baseline power nozzle diameter $D = 5$ mm. The two sliders can be moved in or out to adjust the power nozzle diameter, as already mentioned. However, this adjustment does not affect all of the other dimensions inside the fluidic switch. The dimensions were based on the model of Tesař *et al.* [95] and adapted following the findings of Warren [102] in order to realize the desired switching parameter. The area of the control ports was increased to decrease the control port pressure needed for switching. The splitter was moved slightly downstream to decrease the oscillation tendency of the switch whereas the width of the interaction region (distance between the two outer inclined walls) was increased to further stabilize the attached flow. Finally, the angle between the two outer attachment walls was increased to create the needed distance between the two outlet ports at a reasonable overall length of the device. Additionally, the width of the two outlet ports was

increased sufficiently far downstream of the interaction region to create the needed area for the transition pieces. The large divergence angle at this widening was chosen due to the manufacturing process.

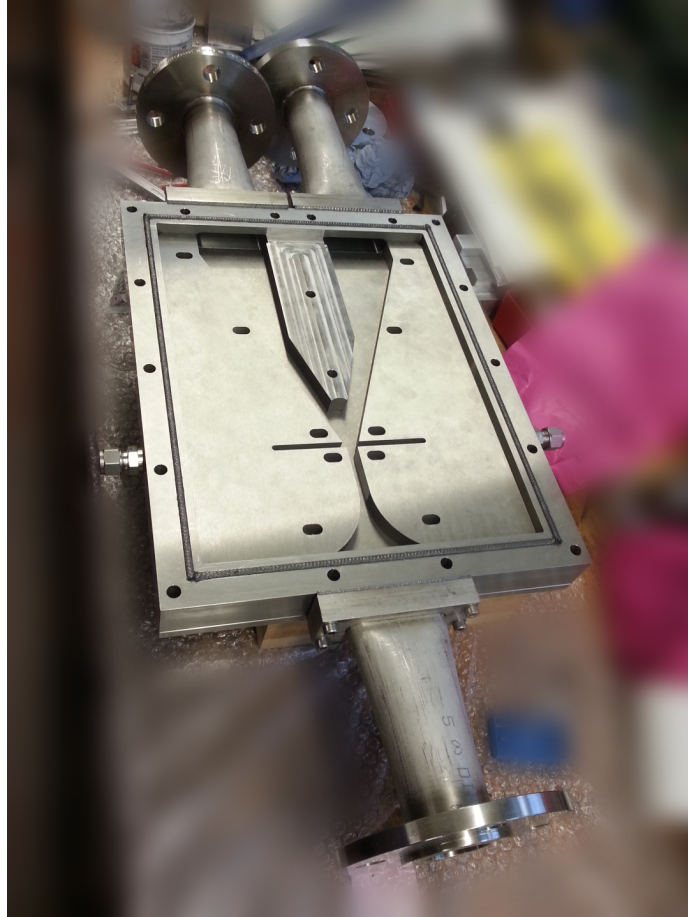


Figure 4.6: Photograph of the final device (without the top plate) including the inlet and outlet transition pieces.

A photograph of the manufactured device with attached transition pieces is shown in Fig. 4.6. In addition to the switch itself, the picture shows the connectors for the control flow on the outside of the outer frame, the inlet and outlet flanges, and the graphite sealing cord on top of the outer frame. The entire device was manufactured out of refractory stainless steel and has an overall weight of about 50 kg. The connectors to the control ports are made from stainless steel tubing with an inner diameter of 6 mm.

4.3 Investigation of the Switching Process

The bistable fluidic switch was investigated both numerically and experimentally to assess the performance and switching boundaries (i.e., the minimal control flow for switching) and the internal flow structures. Since the device was manufactured from steel, it was not possible to perform measurements inside the fluidic switch itself. However, the switching process was experimentally investigated by means of pressure probe measurements at the outlet of the device.

4.3.1 Experimental Investigation

The main inlet of the switch was fed with pressurized air at ambient temperature. The air mass flow rate was measured and adjusted using a Coriolis-type mass flow meter and a proportional valve. The two control ports were each connected to an 8 bar pressure reservoir via two sinusoidal, automotive valves. These two valves were connected in a parallel manner to decrease the pressure loss in the control line, because these automotive valves are designed for very low mass flow rates. For five different power nozzle diameters D the main mass flow was increased from 15 kg/h up to the mass flow rate at which the switching process failed. For all operating conditions the minimal opening time of the control valves needed was determined. To investigate if the switching process is reliable for a given opening time, four switching instances (two for each side) were initiated for every test case. A sketch of the experimental setup used is depicted in Fig. 4.7. A list of the investigated operating conditions is shown in Tab. 4.1.

The velocities in the two outlets of the device were measured using two Prandtl-probes connected to differential pressure transducers. The velocities are captured at arbitrary positions close to center of each outlet of the device. A high-speed data acquisition and control system was used to measure the pressure signals as well as to control the solenoid valves in the control ports at a data acquisition frequency of 1 MHz. One example of such a test case is shown in Fig. 4.8.

The data shown was obtained for test case 18, employing the baseline power nozzle width (5 mm), a main mass flow of 50 kg/h at 290 K, and a control valve opening time of 5 ms. As one can see, the velocity at the active outlet 2 drops as the control pressure is applied to the control port 2 at 1.5 s. The resulting change in the velocity time trace seems pretty slow regarding the needed switching time of less than 50 ms. However, note that a certain time lag between the internal switching and the drop in the velocity signal to zero exists. This time lag is the sum of the time needed for the development of the flow, the convective time lag between the interaction region and the outlet, and the time lag of the pressure signal between the Prandtl-tube and the pressure transducer. Even though, the internal switching of the device is already completed long before the mentioned transitions are completed and the main jet velocity has reached the other outlet in the measurements. During the measurements

Table 4.1: Investigated operating conditions of the bistable switch for the switching limits test.

no.	D	mass flow	$v_{\max;\text{theory}}$	momentum flux	$t_{\text{valves};\text{min}}$
(-)	in mm	in kg/h	in m/s	$(\dot{m} v_{\max;\text{theory}})$ in kg m/s ²	in ms
1	2	15	115.35	0.48	2
2	2	20	153.80	0.85	2
3	2	30	230.69	1.92	2
4	2	40	307.59	3.42	5
5	2	50	384.49	5.34	17
6	3.5	15	65.91	0.27	2
7	3.5	20	87.88	0.49	2
8	3.5	30	131.82	1.10	2
9	3.5	40	175.77	1.95	5
10	3.5	50	219.71	3.05	10
11	3.5	60	263.65	4.39	17
12	5	15	46.14	0.19	2
13	5	20	61.52	0.34	2
14	5	30	92.28	0.77	2
15	5	40	123.04	1.37	5
16	5	50	153.80	2.14	5
17	5	60	184.55	3.08	12
18	5	70	215.31	4.19	25
19	6.5	15	35.49	0.15	5
20	6.5	20	47.32	0.26	5
21	6.5	30	70.98	0.59	5
22	6.5	40	94.64	1.05	5
23	6.5	50	118.30	1.64	5
24	6.5	60	141.97	2.37	7
25	6.5	70	165.63	3.22	13
26	6.5	80	189.29	4.21	30
27	8	15	28.84	0.12	5
28	8	20	38.45	0.21	5
29	8	30	57.67	0.48	5
30	8	40	76.90	0.85	5
31	8	50	96.12	1.34	5
32	8	60	115.35	1.92	7
33	8	70	134.57	2.62	13
34	8	80	153.80	3.42	25

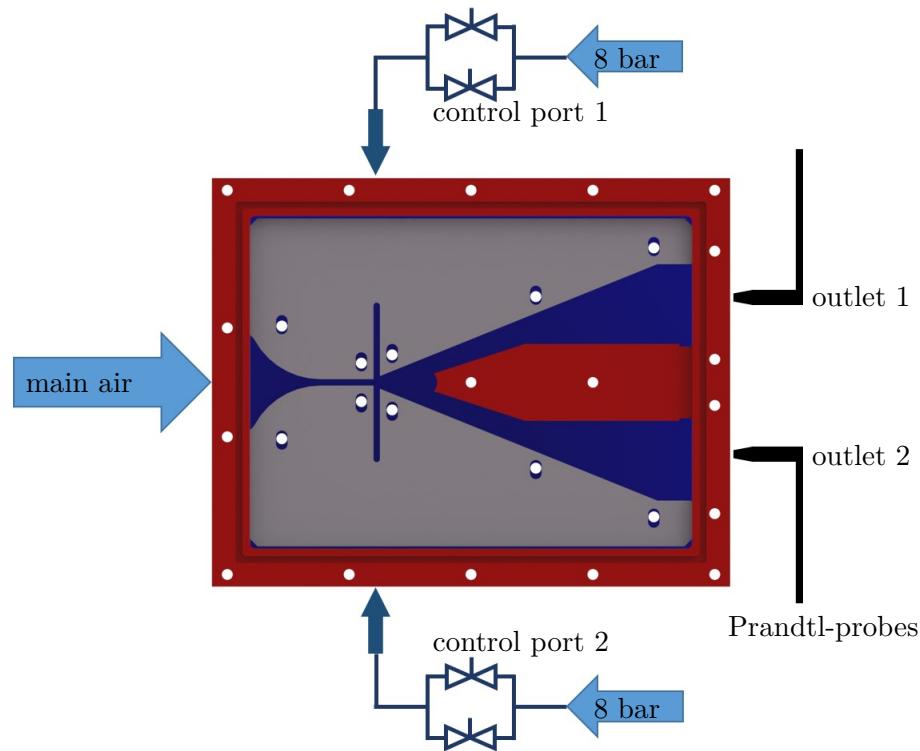


Figure 4.7: Experimental setup for the investigation of the switching limits.

an additional effect was observed. Due to the lower pressure in the interaction region a reversed flow in the inactive outlet was created, which is not measured by the Prandtl-probes. This reversed flow will be shown in more detail in the numerical investigation of the fluidic switch.

The minimal control valve opening times needed to initiate the switching process are summarized in Fig. 4.9. The successful switching attempts are shown as green circles, whereas red crosses indicate failed switching attempts. The color scale in the background denotes the needed minimal opening time of the control valves. The resulting switching limit is shown by a white dashed line. As one can see, the limit for successful switching depends on the mass flow rate and the main nozzle diameter. Since the main switching mechanism in this device is expected to be the momentum exchange in the interaction region, it is suspected that this switching limit is directly related to the momentum ration of the main and the control jet. To investigate this dependency, the momentum flux is used. This value is defined as the mass flow rate multiplied with the theoretical jet velocity. These values are already shown in Tab. 4.1. Based on this value, the switching limit tests were reevaluated and plotted against the momentum flux. The resulting plot is shown in Fig. 4.10. It is visible

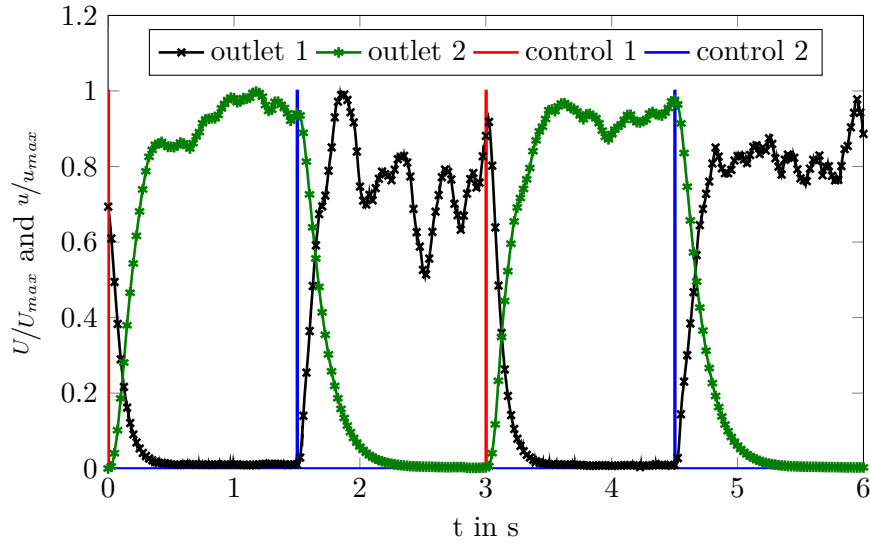


Figure 4.8: Example measurement of the switching process at operating condition 18 and a control valve opening time of 5 ms.

that the switching attempts are successful up to a certain value of the momentum flux. This limit value is slightly larger for smaller nozzle diameters. However, based on this threshold, it is possible to estimate the maximum main jet volumetric flow rate at which the switching is successful for a given nozzle diameter. Note that even for longer opening times of the control valves, it was not possible to successfully switch the main jet from one outlet to the other. This behavior indicates, that the governing switching mechanism inside the fluidic switch is based on a certain minimum momentum ratio between the main jet and the control jets in contrast to the switching mechanism of the fluidic oscillator (see Sec. 2). The momentum of the control jets was constant in these experiments due to the static pressure upstream of the valves and their pressure loss. It is expected that the determined limits of reliable switching may be increased by using control valves with a lower pressure loss or increasing the static pressure upstream of the control valves.

Following these findings, the nozzle diameter for the desired high-temperature operating condition was selected. The outlet temperature of 817 K and mass flow rate of 25 kg/h result in a momentum flux of 1.77 kg m/s^2 at a nozzle diameter of 5 mm. According to the findings in Fig. 4.10, the switching is successful with a valve opening time of 5 ms for these conditions. This was confirmed in a test at elevated temperature for this operating condition.

Since the internal dynamics of the fluidic switch during the switching process shall be numerically simulated, the inlet flow velocity in the control port is needed as a boundary condition. Due to the unknown inner diameter of the automotive valves,

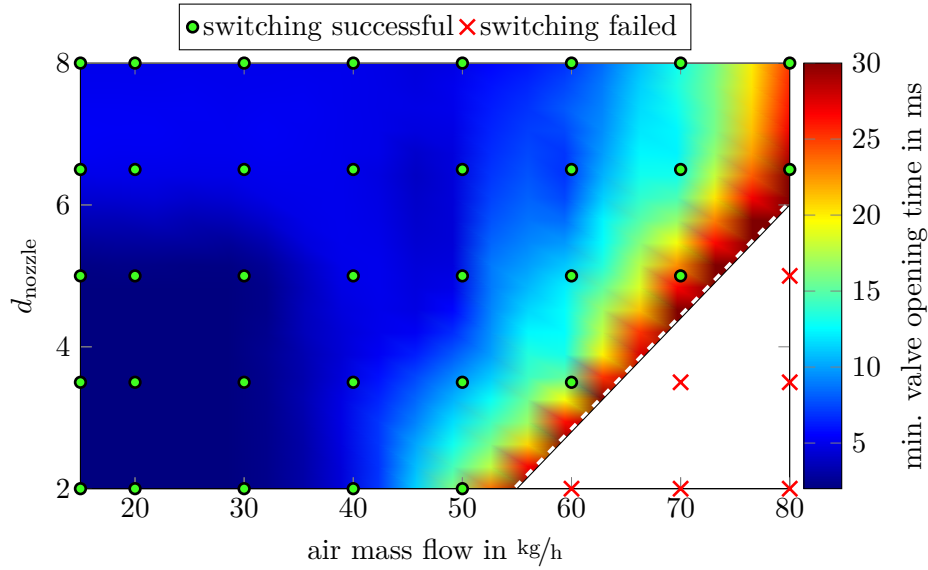


Figure 4.9: Limits of successful switching instances for different nozzle diameters and mass flows.

this velocity time trace was measured in the experimental setup using a hotwire probe. The steel tubing connector was removed from the fluidic switch itself and the velocity was measured at the open end of the tube (i.e., the control port inlet) with identical tubing and pressure as for the switching investigations. This time trace is shown in Fig. 4.11 for a control valve opening duration of 5 ms. The control valve voltage, shown as a black dashed line, rises at $t = 0$ s creating the necessary electro-magnetic field to open the valve. The valves open with a small time delay. The control flow reaches the control port inlet and thus the hotwire probe approximately 2.5 ms after the valve control signal was set to “open”. This time lag is the sum of the convective time delay between the valve and the control port inlet as well as the inertia induced time lag of the valve. The control port velocity is shown as a red solid line with cross markers. The valve control voltage drops down to zero after the set 5 ms opening time. Again, the control flow follows this signal with a certain time lag, due to the inertia of the valves and the convective time delay between the valves and the control port inlet. The control flow velocity is back to $|u_i| = 0$ m/s shortly before 10 ms, resulting in a control flow duration of approximately 7 ms. The bumps visible in Fig. 4.11 subsequent to this time correspond to an oscillation of the velocity around zero. The source of this oscillation in the hotwire signal is not perfectly clear. It may emerge from an oscillation within the fluid volume downstream of the control valve, the internal dynamics of the control valve itself, or the dynamic response of the hotwire measurement system. However, this velocity time trace is used in the numerical investigation (see next section) as the control port boundary condition initiating

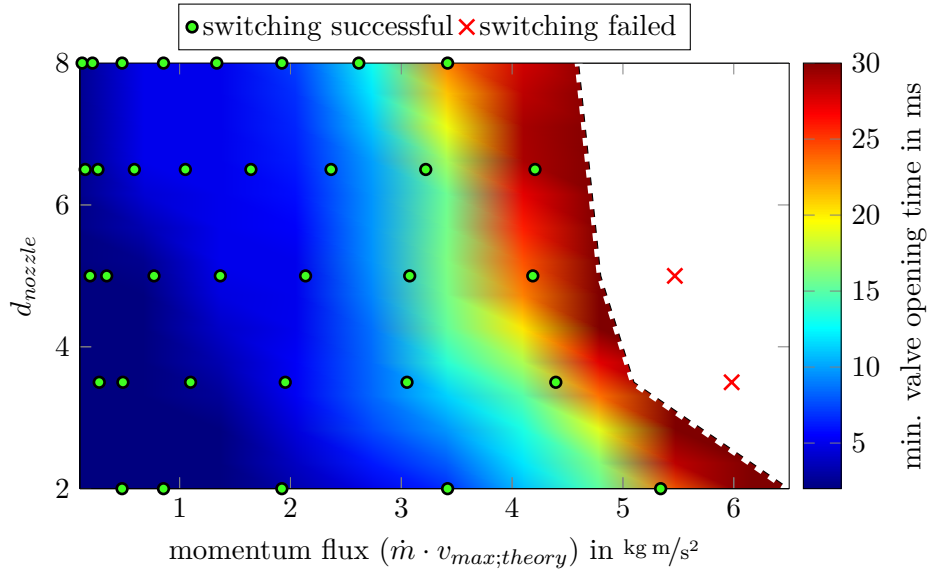


Figure 4.10: Limits of successful switching instances for different nozzle diameters and main jet momentums.

the switching process. To allow reasonable computational costs and avoid possible errors in the measurement subsequent to the closing of the valve, the oscillations in the control port velocity were omitted. This created a boundary condition inflow identical to the measured velocities, including the time lags of the solenoid valve.

In order to further investigate the internal dynamics of the bistable switch in both the steady and the transient state, a numerical study was performed. The setup of this study and the results are presented in the following section.

4.3.2 Numerical Investigation

Following the experiments, the switching process at the desired operating condition is investigated numerically. Since the inner geometry of the bistable fluidic switch is a two-dimensional structure, the numerical simulation is conducted using a two-dimensional approach. This simplification is additionally supported by the fact that the same approach was successfully validated for the geometry of the fluidic oscillator (see Sec. 2.3). The employed numerical model is based on the RANS approach and the SST turbulence model for a compressible fluid as it is described in Sec. 1.1.3. As in the previous numerical studies, the numerical investigations were performed using the commercial program package ANSYS CFX 14.5. The computational grid was generated with ICFM CFD 14.5. The grid was created in an unstructured manner with a depth of one cell. An overview on the mesh is shown in Fig. 4.12.

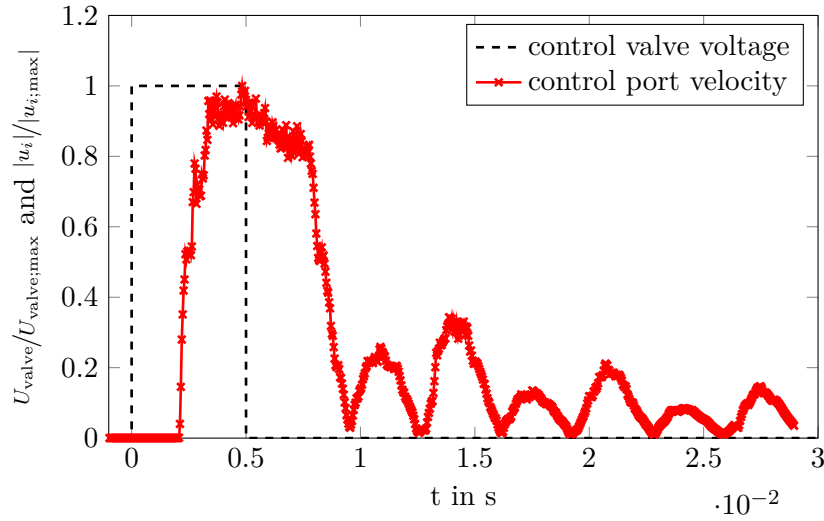


Figure 4.11: Time trace of control valve signal and the corresponding control port inlet velocity for a valve opening time of 5 ms.

The flow enters the domain from the left where the desired mass flow rate (25 kg/h) and temperature (817 K) were set as the inlet boundary condition. The walls were treated as adiabatic non-slip walls, and the outlets were defined as zero gradient openings to ambient pressure and 817 K temperature. The two control ports were either closed or defined as inlets with a certain velocity time trace to initiate the switching process. In the depth of the geometry, a symmetry boundary condition was used to simulate a device of infinite depth. The computational grid is refined in the interaction region to sufficiently resolve the local turbulence effects, resulting in a total grid size of 366,336 nodes.

Subsequent to a steady-state initialization simulation, the switching process was simulated in three stages. Initially, the device was simulated with closed control ports using the unsteady RANS formulation until a steady flow simulation was observed at the outlets. In the next stage of the simulation process, the boundary condition at the control port on the side where the jet is attached is set to an inlet with the measured control velocity time trace to simulate the control valve opening. The resulting velocity time trace includes the opening and closing of the valve and has a time duration of around 7 ms (see Fig. 4.11). This longer time results from the inertia of the control valve. The short pulse results in the detachment of the main jet from the wall and pushes the jet to the other side of the switch. In the final phase of the numerical simulation, the opened control port was closed again, and the simulation was continued until a steady flow situation was observed again. This step was necessary to assure that the switching process was successful even when the control flow is switched of again. The simulation results are presented in the

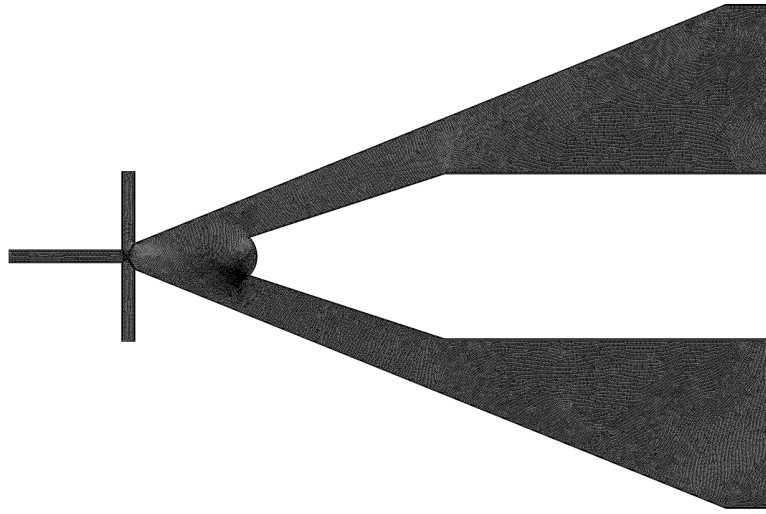


Figure 4.12: Overview on the computational grid used for the numerical investigation of the switching process.

form of color plots in the domain in Figs. 4.13-4.16. Each of these simulation steps was performed employing an adaptive time step scheme to keep the rms-value of the Courant number below a value of 5, resulting in time steps of around $1 \cdot 10^{-5}$ s. All unsteady simulations were performed for a compressible ideal gas, due to the high velocities inside the device, especially during the switching process. Unfortunately, it was not possible to validate the presented numerical study, because it was not possible to directly measure the flow structures inside the oscillator. However, since the numerical model used was successfully validated for the flow inside the fluidic oscillator, it is expected to give a reliable qualitative overview of the internal flow in the fluidic switch.

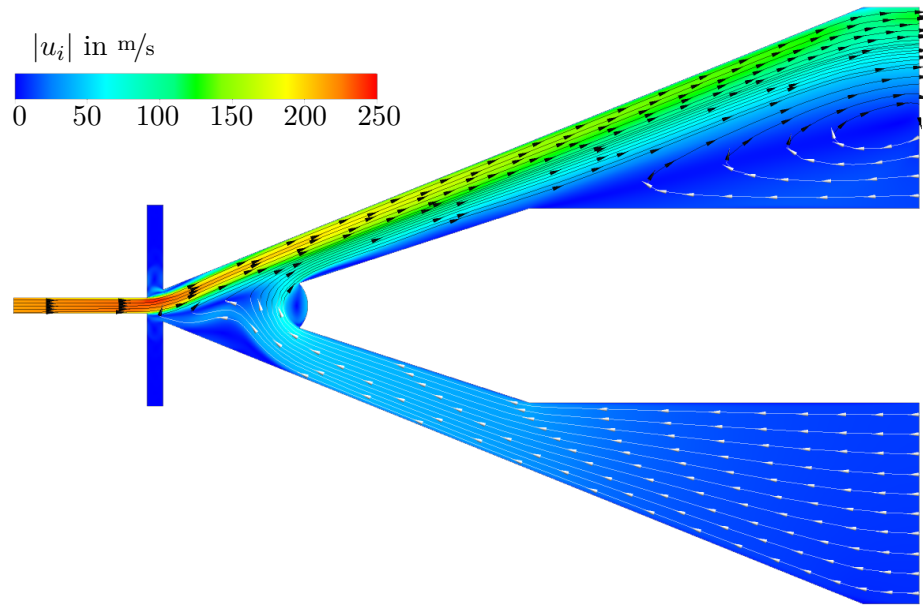


Figure 4.13: Velocity distribution inside of the fluidic switch at the end of simulation stage 1.

The internal velocity distribution of the fluidic switch at the end of the first simulation stage is shown in Fig. 4.13. The colors denote the velocity magnitude and the streamlines indicate the direction of the flow. The streamlines are color coded with the sign of the axial velocity u_1 so that white streamlines denote a negative axial velocity whereas black lines indicate a positive axial flow. In this simulation stage both control ports of the bistable switch are closed and the main jet is attached to the upper outside wall. The main jet leaves the device through the upper outlet port, creating a large recirculation region close to the outlet. This recirculation stems from the outlet boundary condition. The transition pieces that are connected to the outlets in the SEC test rig are assumed to reduce the mentioned recirculation region by blocking the inflow from ambient air and smoothing out the flow downstream of the device. Hence, the mentioned transition pieces are expected to create the necessary even inflow into the diode section in the SEC test rig. Downstream of the upper control port, a small recirculation region is formed (see also Fig. 4.15a). Due to the wide outlet ports in the design, the main jet is able to enter the upper outlet without attaching to the inner wall of the receiver port. Accordingly, no part of the jet is “peeled” off by the splitter cusp as it was observed by Tesař *et al.* [92, 94, 95] and no “spill over flow” in the inactive outlet is present either. This behavior changes for larger power nozzle diameters. If the power nozzle diameter is set to its maximum value of 9 mm, the main jet is wider and is expected to “fill”

the complete receiver port. However, a significant reversed flow is observed in the inactive outlet. This back flow was also noticed in the experimental investigations of the switch. It originates from the connection of the static pressure opening at the inactive outlet and the lower pressure at the interaction region. The distribution of the relative static pressure inside the fluidic switch at the end of simulation stage one is shown in Fig. 4.14. The low pressure region in the active outlet port is visible above the splitter cusp.

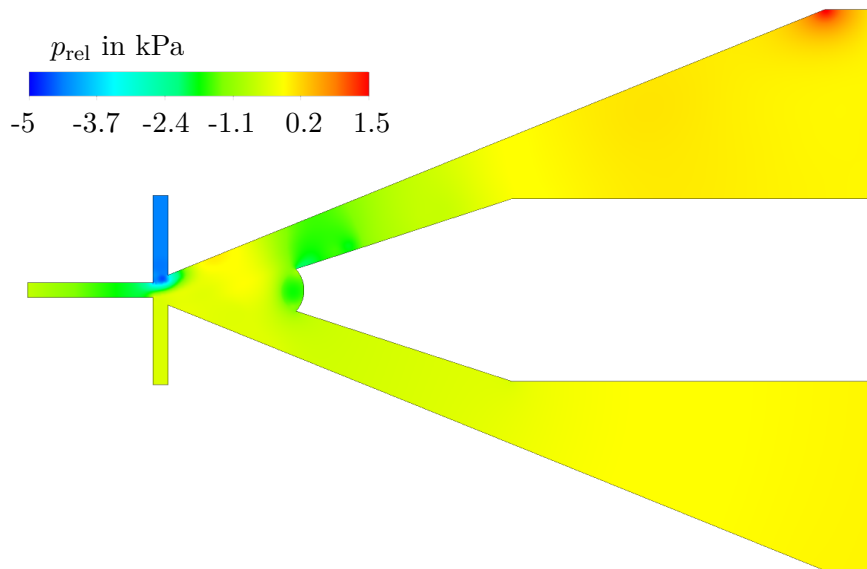


Figure 4.14: Relative static pressure distribution inside of the fluidic switch at the end of simulation stage 1.

This reversed flow creates an additional mass flow through the active outlet port which is not acceptable for the application in the SEC test rig. Thus, thin metal foils were attached downstream of the combustion and bypass tube in order to stop this back flow. This will be shown in more detail in chapter 5. Note, that for the selected operating condition (i.e., power nozzle width) the power nozzle is not choked and, thus, it is possible that pressure waves may travel through the power nozzle into the air heating device. This decision was made to minimize the needed control flow. For the SEC process the temperature in the combustion tube must be adjusted as accurately as possible. Since cold air is used for the control flow due to the temperature limitations of the control valves, a large amount of cold air would be introduced in the system for higher main jet velocities. It is expected that most of the combustion induced pressure wave is reflected by the fluidic diode, whereas the

residual pressure distortion will leave the system through the inactive outlet of the fluidic switch.

In the next step of the simulated switching process, the experimentally obtained velocity time trace is set at the upper control port as inlet boundary condition. The subsequent transient movement of the main jet in the interaction region is shown in Figs. 4.15. Starting the moment of the valve opening, the internal state is plotted each 0.75 ms up to the point where the jet is attached to the other side (Figs. 4.15a-4.15e). The last picture (Fig. 4.15f) corresponds to the moment when the control flow has just stopped. Like for the overview of the initial state, the colors denote the velocity magnitude inside the device. The direction of the flow is indicated by arrows. White arrows correspond to negative axial velocity ($u_1 < 0$) and black arrows indicate positive axial flow direction. In the plot of the initial state (see Fig. 4.15a) the same flow structure, as described for Fig. 4.13, is shown. The main jet is attached to the upper wall and a significant reversed flow is present in the inactive lower outlet. With the opening of the control valve, the control flow enters the switch through the upper control port and the recirculation bubble downstream of said control port grows as the jet detaches from the upper wall. This growing of the recirculation region strongly resembles the oscillation mechanism of the fluidic oscillator as it was described in chapter 2. This similarity was not expected, since it was expected from the experimental switching tests that the direct momentum exchange between the main and the control jet is the dominant switching mechanism. Looking at the results of the numerical simulations, this assumption needs to be reviewed in future work. Since the presented numerical data is not validated and, thus, not reliable enough to further analyze the underlying mechanism, it was not possible to quantify the role of the two mechanisms within this thesis. However, the reversed flow in the inactive outlet is still visible in Fig. 4.15b 0.75 ms after the control valve is opened. Due to the ongoing control flow, the main jet bends further to the other side in the subsequent phases of the switching process. 1.5 ms after the control flow has started (Fig. 4.15c), the reversed flow in the inactive outlet is still present, whereas the main jet is already attached to the lower wall downstream of the control ports. The jet is bent strongly inside the interaction region but still leaves the device completely through the upper outlet. In the following plot (Fig. 4.15d) the reversed flow has stopped. The recirculation region has grown even further and covers the complete interaction region. The main jet is attached to the lower wall directly downstream of the control ports, but detaches shortly after and follows the surface of the splitter cusp. A small portion of the main jet is now “peeled off” by the lower edge of the splitter cusp and leaves the switch through the lower outlet port. In the upper outlet port a reversed flow is visible on the inside of the flow path, creating a long, but narrow vortex in this outlet port. This vortex vanishes in the following stages as the reversed flow gains intensity in the upper, now inactive, outlet. The main jet attaches to the lower wall further downstream after 3 ms (Fig. 4.15e). The still ongoing control flow thickens the main jet and thus a part of this flow is “peeled” off by the splitter

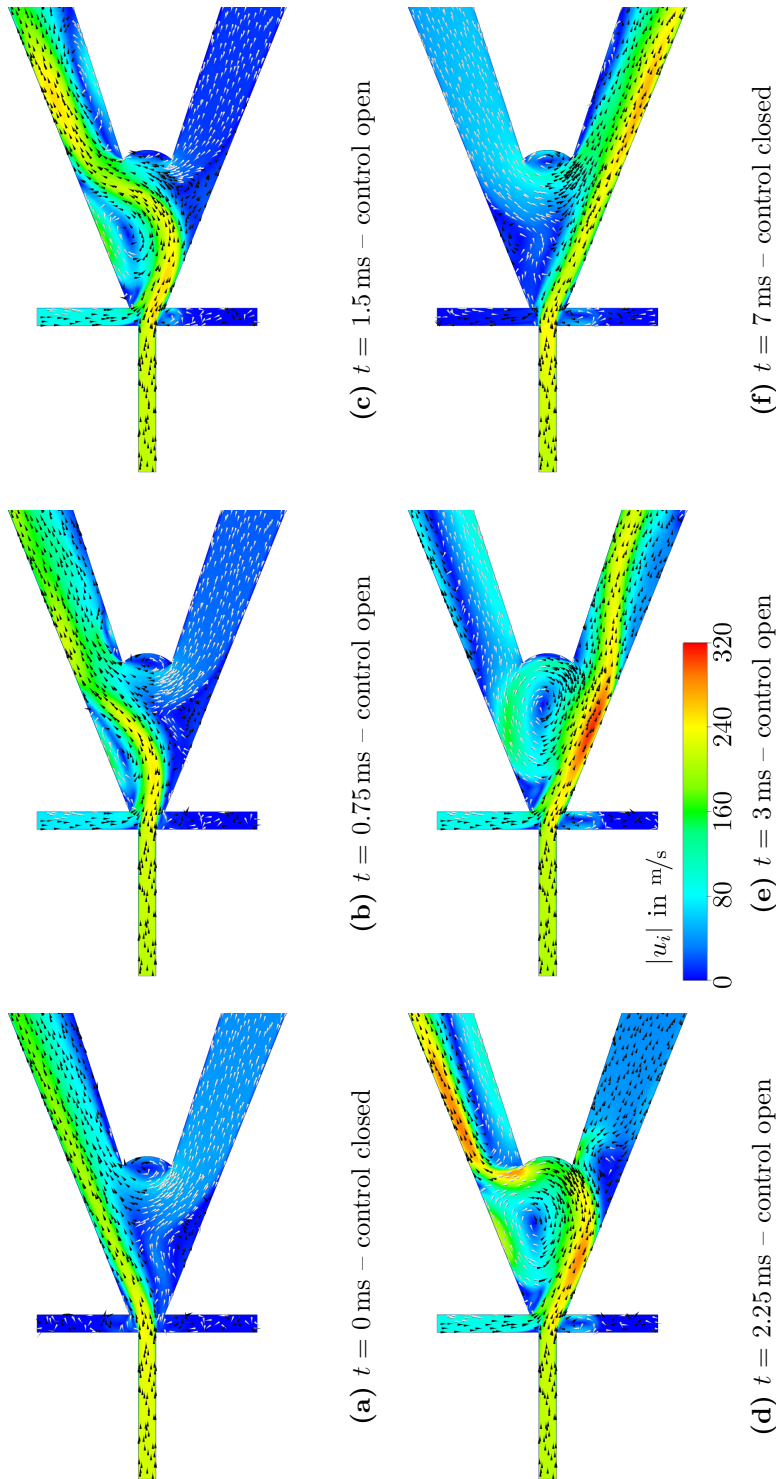


Figure 4.15: Velocity distribution inside the bistable fluidic switch during the switching process. The displayed time steps are determined from the moment of the valve opening.

cusps, creating a large feedback vortex in the interaction region. This vortex was already observed by Tesař *et al.* for this geometry [92, 94, 95]. The vortex is desired, because it induces a flow directed to the outer walls directly downstream of the control ports. Hence, this vortex represents an important stabilization mechanism for the main jet directly after the switching process. In the following time steps, the main jet attaches completely at the lower wall and the control flow is stopped 7 ms after the opening of the control valve. This event corresponds to Fig. 4.15f. The large vortex in the interaction region has disappeared and the main jet leaves the switch through the lower outlet port. The flow state of the device is now the same as for Fig. 4.15a but mirrored at the centerline of the switch. Accordingly, the reversed flow is now located in the upper outlet, and a small recirculation region is created at the lower wall directly downstream of the control ports. An overview of the flow through the device in this final state of the switching process can be found in Fig. 4.16.

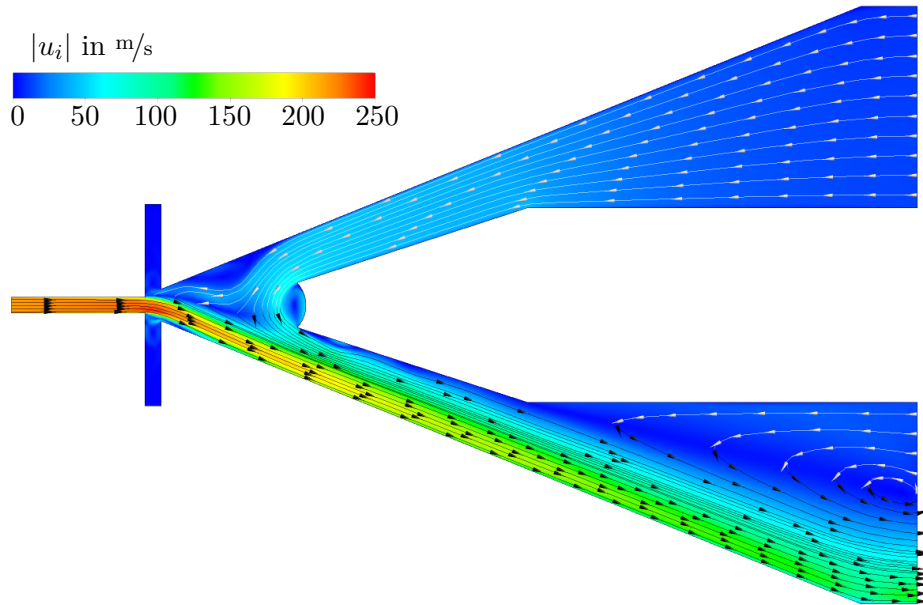


Figure 4.16: Velocity distribution inside the fluidic switch at the end of the switching process.

The presented numerical simulation of the internal flow structures during the transient switching process revealed several main findings. First, the internal switching of the jet is as short as 7 ms and, thus, short enough to fulfill the needed switching time criterion of 50 ms. Second, the reversed flow that was observed during the experimental tests is clearly visible in the numerical simulations. This behavior must

be suppressed by an appropriate boundary condition downstream of the test rig (in this case sheets of thin metal foils). Third, the internal mechanisms found by Tesař [92, 94, 95], for example, the large feedback vortex in the interaction chamber, were observed during the switching process of the used geometry as well. However, due to the wider receiver ports these effects are not visible in the stable “positions” of the fluidic switch. Finally, the internal mechanism is reminiscent of the switching mechanism of the fluidic oscillator as it was found in chapter 2. This resemblance is not totally surprising, since both the bistable fluidic switch as well as the fluidic oscillator were derived from the fluidic amplifier. However, the presence of the growing main vortex in the interaction region was not expected to be this pronounced as the direct momentum exchange between the main and the control jet was suspected to be the governing switching mechanism. The rates of these two mechanisms need to be further investigated in future work. Nonetheless, the numerical simulation of the switching process provides a nice preliminary overview of the internal structures.

4.4 Intermediate Conclusion

The long ignition delay times under atmospheric pressure creates the need to stop the flow in the SEC test rig in order to investigate the ignition event of auto-ignitions. Unfortunately, no valve is known to the author that is able to handle an air mass flow of 25 kg/h at a temperature of 817 K. Additionally, a constant flow through the electrical air heater is needed to prevent overheating of this device. Hence, a way to switch the hot main air flow between a bypass and the combustion tube is needed. In the final SEC process this bypass and switching is not necessary. The suction wave created by the process itself will suck the hot air, emanating from the compressor of the gas turbine, into the combustor. Hence, the inflow must not be switched between flow paths as the process itself will assure the inflow of oxidizer.

One of the first fluidic devices ever created, the fluidic switch, was proposed to fulfill this task. Based on the comprehensive work of Tesař *et al.* [92, 94, 95] and the findings of Warren [102], a fluidic switch was designed to not only switch the main flow between the two flow paths, but also to create a choked nozzle in the flow path. This choked nozzle is needed to prevent shock waves that might be generated by misfiring events from traveling upstream into the air heater and destroying this expensive device. The nozzle width in the fluidic switch was designed to be adjustable to keep the pressure loss of the choked nozzle at a reasonable level even for higher mass flow rates.

The developed fluidic switch was tested experimentally in both hot and cold conditions. With cold air as the working fluid, the limits of reliable switching were investigated for various mass flow rates and main nozzle widths. It was found that the governing parameter limiting a reliable switching is the ration between the main and control jet momentum. Accordingly, the switching limits can be derived from

main jet momentum flux for a given control flow momentum. Even for longer opening times of the control valves, it is not possible to switch the main jet to the other outlet if this momentum flux is too high, which indicates that the direct momentum exchange plays an important role in the switching process. Based on the determined switching limits, the inner nozzle diameter for the desired hot operating condition was selected. In order to reduce the needed control flow, an operating condition without a choked inflow was chosen for the ignition tests. However, the presented device is able to switch the main jet for a choked inflow as well. As expected, the switching was possible at elevated temperatures with the minimal control valve opening time obtained by the measured data.

Unfortunately, a significant reversed flow in the inactive outlet was observed during the experiments. In order to investigate this behavior and the internal flow structures during the switching process, a numerical simulation of the flow inside the device was performed. After a first simulation stage with boundary conditions representing closed control ports, a control flow velocity was set as the boundary condition at one control port. The time trace of this control flow was taken from hotwire measurements in the control port of the actual device. The switching event was successfully simulated. The simulations revealed a large growing recirculation region inside the interaction zone during the switching process. This recirculation region was similar to the one observed for the fluidic oscillator (see chapter 2), indicating that the direct momentum exchange between the main and the control flow is not the only mechanism responsible for the switching process. Additionally, the reversed flow observed in the experiments was found to be created by the connection between the static surrounding and the low pressure (high velocity) region in the interaction chamber. By narrowing the receiver ports, it might be possible to decrease this effect, but simultaneous a significant “spill over flow” may be introduced (see Tesař *et al.* [92, 94, 95]).

The numerical simulations revealed that the internal switching is as fast as 7 ms and, thus, the presented fluidic switch is able to fulfill the switching task of the hot main flow in less than the desired 50 ms. This outstanding performance is even present for very hot air flows and due to the avoidance of moving parts for an almost infinite life time of the switch itself. Accordingly, it was shown that the developed adjustable fluidic switch is able to sufficiently meet all the requirements for the SEC test rig and can be used to investigate auto-ignition events, as it will be shown in the following chapter.

CHAPTER 5

Shockless Explosion Combustion Ignition

The investigation of the SEC imposes several strict demands on the test rig, the mixing, and the accuracy of the fuel injection system. Three of the main requirements were addressed in the three preceding chapters of this thesis. For each of these requirements a fluidic device was developed and tested regarding their specific tasks. The long ignition delay times at atmospheric pressure do not allow to realize the complete SEC cycle in the given test facilities. For the given ignition delay times of around 300 ms and a mean temperature of 1100 K in the combustor a tube length of around 50 m would be required. However, the ignition can be investigated using single-shot experiments. This chapter is dedicated to these first single-shot auto-ignition tests for the SEC process. The developed test rig, employing all the previously investigated fluidic devices, will be described in full detail together with the used measurement and control equipment. Required fuel injection curves and timings will be presented and discussed subsequently. Finally the results and findings of the ignition tests will be presented in the last part of this chapter.

5.1 The Shockless Explosion Combustion Test Rig

The test rig for the SEC ignition tests was designed to provide a high flexibility in order to allow for a broad investigation of possible regimes for homogeneous auto-ignition. An overview of the test rig is shown in Fig. 5.1. In order to enhance the visibility of the most important parts, the surrounding infrastructure (e.g., air and fuel lines, valves, electrical wires, etc.) and the measurement equipment is not included into the depicted CAD model whereas the different parts in the main air path are shown in different (false) colors. The air is provided from a central air compressor and is entering the main air path through the air heater, which is shown in green in Fig. 5.1. The used high temperature electrical air heater is able to supply an air stream with a temperature up to 1170 K for mass flow rates between 25-120 kg/h consuming 36 kW electrical power. Directly downstream of the

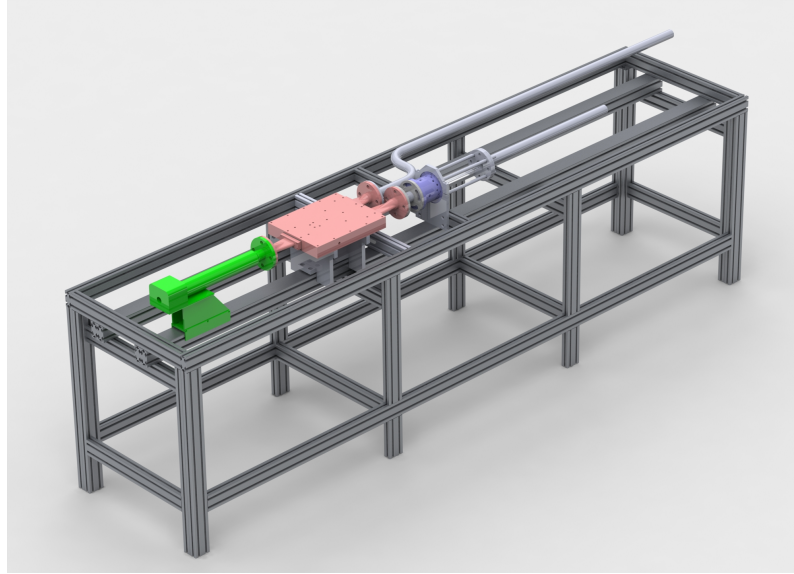


Figure 5.1: Overview of the Shockless Explosion Combustion test rig based on the different fluidic devices.

air heater, the fluidic switch (see chapter 4) is connected (shown in red in Fig. 5.1). It switches the main air flow between the combustion tube (the right path including the blue diode section) and the bypass path (the plain tube on the left). In order to suppress the reversed flow that is created in the inactive outlet of the switch small sheets of thin metal foil are attached on both outlets of the test rig. Due to the lower pressure in the inactive outlet, these foil sheets close the outlet and sufficiently seal it from the surrounding air. At one outlet of the fluidic switch, the SEC inlet section including the fluidic Diode (see chapter 3) and the fuel injection using fluidic oscillators (see chapter 2) is attached. This inlet section is shown in blue in Fig. 5.1 and is responsible for the flow rectification and the fuel-air mixing. The fluidic diode as shown in Fig. 3.6 was manufactured out of stainless steel. In contrast to the water channel experiments the center body is fixed by only four tacks due to a different manufacturing process. The injection disk inside this inlet section (shown in yellow in Fig. 3.6) is replaceable to allow the flexible investigation of different injector geometries. The ignition investigations presented in this thesis are conducted using the same fluidic oscillator geometry as proposed in chapter 2. The inlet section (shown in blue) is directly connected to the combustion tube. The combustion tube is divided into two sections. The first section with a length of 0.5 m is made out of silica glass in order to provide the optical assessment of the ignition process. Due to availability issues, this silica glass has an inner diameter of 35 mm. Since the wall cooling of the inlet section is not activated for the single ignition tests, the small step that is accompanied by this change in the diameter has

no significant influence on the flow field in the measurement section. Downstream of this section a stainless steel tube with a diameter of $D = 40\text{mm}$ is connected to guide the combustion products into the exhaust system of the laboratory (not shown in the picture). All of the mentioned parts in the main flow path upstream of the combustion tube are insulated to the environment in order to reduce the loss of air temperature prior to the combustion tube. On the bypass side a plain stainless steel tube guides the air directly into the exhaust hood. In later setups it is possible to attach a second combustor to the bypass side in order to allow for a faster systematic investigation of the ignition process.

Air is used as oxidizer in the current first investigation of the auto-ignition. Its mass flow rate is controlled and metered using a coriolis type mass flow meter and an electrically driven proportional valve. The air heater is equipped with two thermocouples for the control and observation of the air temperature. The fuel used in the presented first investigations is pure dimethylether (DME). The reason for the choice of this gas and its special characteristics are discussed in the subsequent chapter. Due to the fact that the vapor pressure of DME at ambient temperature is only about 5 bar, a complex vaporization system was installed in the lab in order to vaporize and heat up the liquid DME from the gas container to a temperature of around 330 K. From this system, the DME is guided to the test rig through a heated pipe. The mass flow rate of the fuel is controlled using a high-speed control valve that is mounted as close as possible to the fuel injection. The used valve is able to control a gas flow with a full-span delay (0-100%) of less than 3 ms at an inlet pressure of 8 bar, which is exceptionally fast. The fuel valve as well as the measurement equipment is controlled using a high-speed data acquisition system, which is able to read and write at a sampling rate of 1 Mhz. The ignition event is investigated by 5 photomultiplier tubes (PMT), detecting the light emission (chemiluminescence) of the flame as it ignites within the combustion tube. Downstream of the silica glass combustion tube, 6 piezo-type pressure transducers are mounted to measure the combustion induced pressure wave. A more detailed view on the measurement section and the setup is shown in Fig. 5.2 as a rendered picture of the CAD-model.

The 5 photomultiplier tubes are depicted above the measuring section. Their respective fields of view are arranged alongside the measuring section with an axial distance of 9 cm between each of them. In addition to these optical measurements, the temperature is measured by two 1.5 mm type K thermocouples upstream and downstream of the combined inlet and measuring section. These thermocouples are also used to control the temperature of the airflow prior to the fuel injection. The used piezo-type pressure transducers are connected downstream of the thermocouple and are not shown in the rendered CAD-model. A photograph of the test rig including the piezo-type pressure transducers is presented in Fig. 5.3. On the left side in the photograph the fluidic diode including the fuel injection tubing can be found. The fluidic diode as well as the other parts upstream of the combustion tube are covered in approximately 10 cm of thermal insulation to keep the temperature gradient as

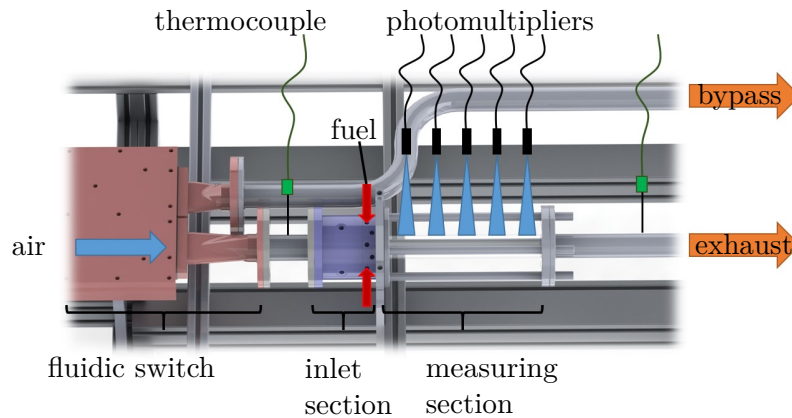


Figure 5.2: Measurement section including the employed measurement equipment for the first ignitions.

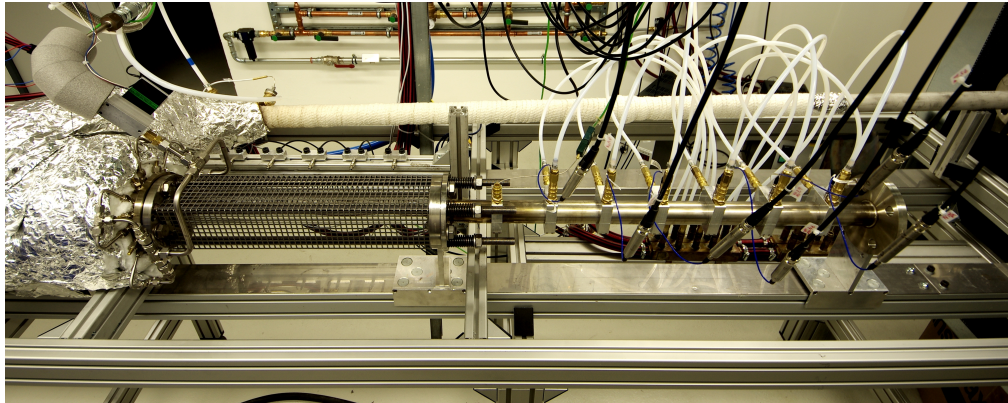


Figure 5.3: Photograph of the used test setup including the 5 optical fibers for the photomultiplier tubes, the six pressure transducers and the two thermocouples.

low as possible. The fuel injection valve is located on top the fluidic diode to ensure the shortest possible fuel path downstream of the valve. A protection cover grid made of steel is mounted around the measuring section to protect the measurement equipment from fragments in case of a bursting of the silica glass combustion tube. The optical fibers for the photomultiplier tubes are visible behind the measurement section. Due to their divergent field of view, the blockage of the line of sight by the protection cover is not significant. Downstream of the silica glass measuring section, seven multi purpose mounts are axially distributed attached to the exhaust pipe. These mounts are able to accommodate either thermocouple probes or the mentioned piezo-type pressure transducers. In the most upstream mount, the thermocouple shown in Fig. 5.2 is installed. This mount is not connected to any cooling. The

other six mounts are water cooled at a constant temperature of 320 K to protect the pressure transducers. The pressure transducers are arranged with an axial distance of 10 cm between each other. At the downstream open end, a flange is connected to the exhaust tube. This flange is used to mount the thin metal foil to block the reversed flow that is created by the fluidic switch (see chapter 4 for details). This foil and the downstream end of the exhaust tube can be seen more clearly from a different angle in Fig. 5.4. In this photograph the protective cover of the combustion

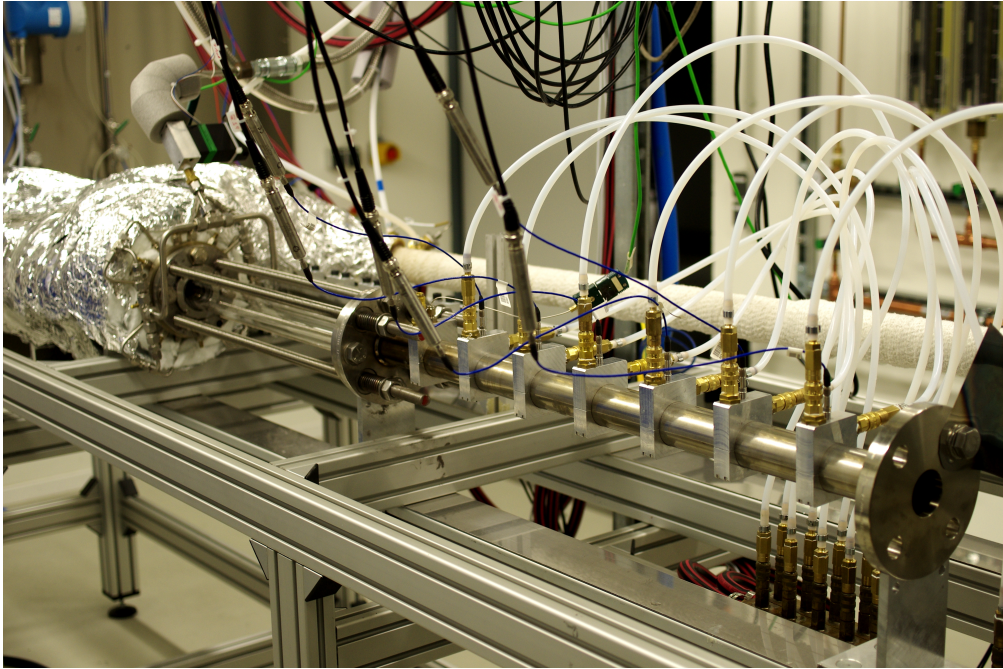


Figure 5.4: Photograph of the used test setup (without the protection grid) in the upstream direction including the metal foil cover at the outlet of the exhaust tube .

tube was removed to show the silica glass tube. The mentioned thin metal foil is mounted on the downstream flange on the right side of the picture. During startup and cool down of the test rig this foil is moved out of the flow path as shown in the picture. An identical metal foil is mounted on the bypass flow path.

The installed measurement equipment allows to identify the performance of the developed fluidic devices in the following way: First, the spatial homogeneity of the auto-ignition would give a first idea of the fuel injection performance. If no satisfactory result is achieved, the interchangeable injection disks allow for the investigation of different fuel injection configurations.

Second, the performance of the fluidic diode can be determined by the pressure measurements. If a homogeneous auto-ignition is achieved, the resulting pressure wave and its reflection at the fluidic diode end can be measured. As previously

stated, the quantitative measurement of the ignition induced reversed flow is to be conducted in future work.

Finally, the fluidic switch can be evaluated employing the photomultiplier tubes and the pressure signals. A reliable adjustment of the axial position of the fresh fuel–air charge inside the combustion tube by changing the switching times, is a qualitative indicator for the performance of the fluidic switch. The PMTs enable the detection of the axial position of the reaction. In addition, the pressure inside the measurement path will be reduced during the switching event. As shown in chapter 4, the inactive outlet is connected to the low pressure region inside the fluidic switch, which results in a pressure decrease in this outlet.

5.2 Fuel Injection Curves and Timings

The preparation of a fresh fuel–air charge that undergoes a homogeneous auto–ignition is based on several important parameters. First, the fuel and the oxidizer must be defined. For the presented ignition tests, dimethylether (DME) is used as fuel and air as oxidizer. This definition yields the needed temperature and the equivalence ratio range for an auto–ignition charge. Beside these curves and dependencies, the timings of the test rig control signals (switch and fuel injection) are presented in this section.

5.2.1 Fuel Injection Curve

Based on the definition of the fuel and the oxidizer, the temperature of the fresh fuel–air charges in the combustion test rig is defined. In order to explain the selection of the operating conditions in the test rig, the ignition delay times for DME in air are presented in Fig. 5.5.

All shown and discussed ignition delay time curves and the final equivalence ratio stratification curve for the ignition tests are obtained by making use of a one–dimensional calculation of the flow and ignition inside the SEC combustor. The used numerical solver was written and the simulations were performed by Phillip Berndt¹, whereas the detailed numerical chemistry model was developed by Liming Cai². The solver itself is described in [14] and [11]. The reaction mechanism used was published in [16].

In Fig. 5.5 the ignition delay time is plotted against the temperature for different equivalence ratios (see Eq. 1.1 for the definition of Φ). The NTC behavior of DME in air is visible in a normalized temperature range of 1.3–1.55. Recall that the negative temperature coefficient (NTC) behavior means an increase in the ignition delay time for increasing temperatures, which is the maximum range in which the SEC ignition

¹ Freie Universität Berlin; FB Mathematik und Informatik; Institut für Mathematik

² RWTH Aachen University; Institut für Technische Verbrennung

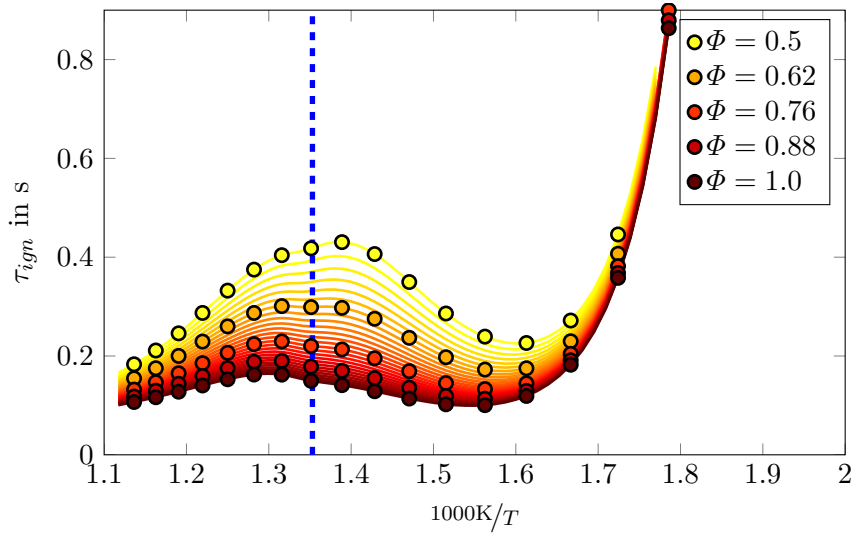


Figure 5.5: Calculated ignition delay times of DME in air at atmospheric pressure.

can be achieved if only a minimal temperature dependency of the ignition time delay is acceptable. In order to further decrease the temperature dependency of the ignition delay time, the temperature used in the investigations was set to the region of local maximum in the ignition time delay curve at around 739 K mixture temperature. This temperature is depicted in Fig. 5.5 as a dashed blue line. At this temperature the sensitivity of the ignition delay time to a change of temperature is reduced to ~ 2 ms for ± 5 K. Following this, the difference of the ignition delay time for $\Phi = 1$ and $\Phi = 0.5$ at 739 K mixture temperature defines the maximum ignition delay time difference within the stratified mixture. This ignition delay time range defines in turn the residence time of the different parts of the mixture in the combustion tube. The maximum possible range of ignition delay times is shown in Fig. 5.6. The residence times must be within the range of 0.15-0.42 s in order to allow for a homogeneous auto-ignition. This plot also visualizes the impossibility to investigate a complete SEC cycle at atmospheric conditions. Given the acoustic time scales within the used combustor, a firing frequency of approximately 250 Hz is needed. The ignition delay times only allow a maximum firing frequency of around 1-3 Hz, which is significantly lower than the needed frequency. It might be possible to reduce the resonance frequency of the combustor by using a longer combustion tube, but in order to match the chemical time scales of the auto-ignition at atmospheric pressure a tube with a length of ~ 50 m is needed.

However, knowing the inlet flow velocity the required equivalence ratio range can be calculated for a fuel-air charge with a given axial extent. The used air heater imposes a minimal air mass flow rate, which results in an inlet velocity of at least 12 m/s . Since this mass flow rate must be assured under all circumstances, an inlet

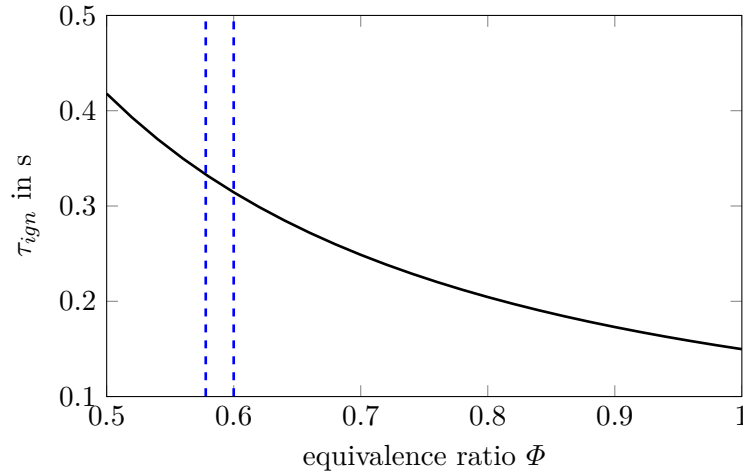


Figure 5.6: Calculated ignition time delays of DME in air at atmospheric pressure and a temperature of 739 K for various Φ .

air mass flow rate of 30 kg/h was selected resulting in an inlet velocity of 15.14 m/s. In order to create a fuel–air charge that fits into the silica glass combustion chamber, a maximum filling time of 18.5 ms was selected. This time corresponds to the ignition time delay difference between the first and last portion of the fresh fuel–air charge. Using Fig. 5.6 this difference can be transferred to an equivalence ratio difference. In order to keep the temperature dependency as low as possible, an optimal equivalence ratio range of 0.5775 – 0.6 was calculated by an optimization algorithm. This range is indicated in Fig. 5.6 by two blue dashed lines. Together with the known air mass flow rate, it is possible to calculate the required equivalence ratio and fuel mass flow rate curve, which are shown in Fig. 5.7. The target fuel mass flow rate and, thus, the equivalence ratio within the fresh charge almost rises linearly from the beginning of the fuel injection up to the closing of the fuel valve. Note that the time on the abscissa denotes the injection time and not the axial coordinate of the mixture in the tube. The goal is to fill the combustion tube with the derived fuel–air charge at a mixture temperature of 739 K by making use of the designed fuel injection and the high speed inlet valve. Unfortunately, it is not possible to preheat the fuel to temperatures above 330 K due to temperature limitations of the fuel injection valve. Thus, the temperature of the mixture must be adjusted by the air temperature for a constant fuel temperature of around 320 K. Due to the different fuel mass flows during the injection process, the temperature in the fresh fuel–air charge would slightly change for a constant air temperature. This effect is already included and corrected for in the presented fuel mass flow rate curve.

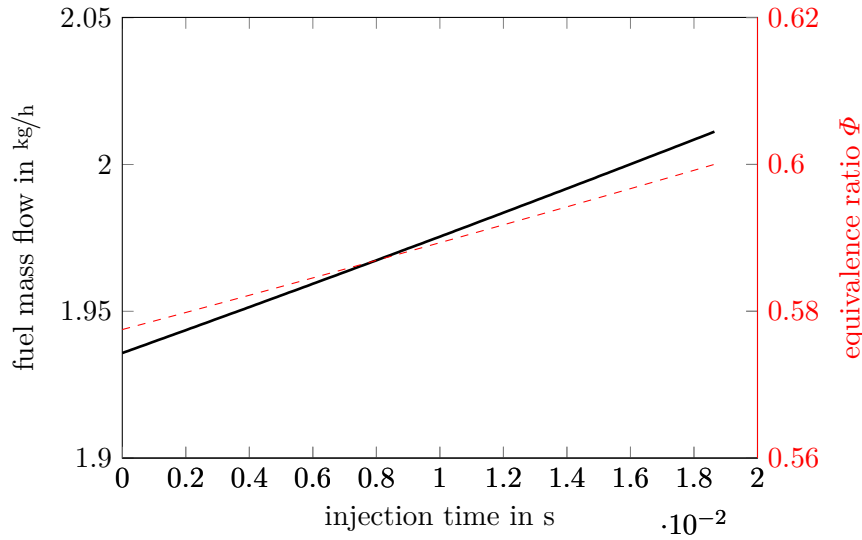


Figure 5.7: Target curve of equivalence ratio Φ and the fuel mass flow rate at the injection position as a function of the injection time.

5.2.2 Fuel Valve Response

As shown in the prior section, the fuel needs to be precisely controlled in a very short time to create the required equivalence ratio stratification. Hence, a high speed proportional valve is used to control the fuel mass flow. Due to the hot main flow and the absence of optical accessibility, it is not possible to measure the instantaneous fuel flow downstream of the fuel injection in the complete setup. However, knowing the valve response for a given pressure difference and valve control signal, it is possible to calculate a valve transfer function. This function can then be used to translate the required fuel mass flow rate curve to the corresponding valve control signal. In order to investigate the valve response, the velocity downstream of the high speed valve was measured. Air was used as working fluid with a pressure of 5 bar upstream of the valve. The pressure of 5 bar was chosen, as this is the pressure available in the used fuel supply system. Downstream of the valve a 100 mm long tube with an inner diameter of 10 mm was attached to create an even velocity profile at the end of the tube. The velocity time trace at the end of the attached tube was measured using a hotwire probe for different valve control signals. A data acquisition system with a sampling rate of 1 MHz was used to control the valve and to record the voltage signal of the hotwire probe.

The first investigated part of the valve response is the delay time between the control signal and the actual movement of the mechanical parts in the valve. According to the technical specifications of the valve, it responds to a full-span (0-100%) step with a response delay of less than 3 ms at an upstream pressure of 8 bar. Since only

an upstream pressure of 5 bar is available in the fuel supply line, this response time must be reevaluated. The response delay was determined employing a 400 ms long control signal pulse for a completely opened valve. The result of this measurement is shown in Fig. 5.8. The control signal (shown as red dashed line) rises to 100 % at 10 ms and is followed by the outlet velocity (shown as black solid line) after a short time delay. The measured velocity is normalized with its maximum value. Directly subsequent to the valve opening, the high pressure upstream of the valve creates an overshoot in the velocity time trace before the velocity reaches a steady state for the remainder of the valve opening. After 400 ms the valve control signal drops back to zero and the velocity signal follows after a short delay time.

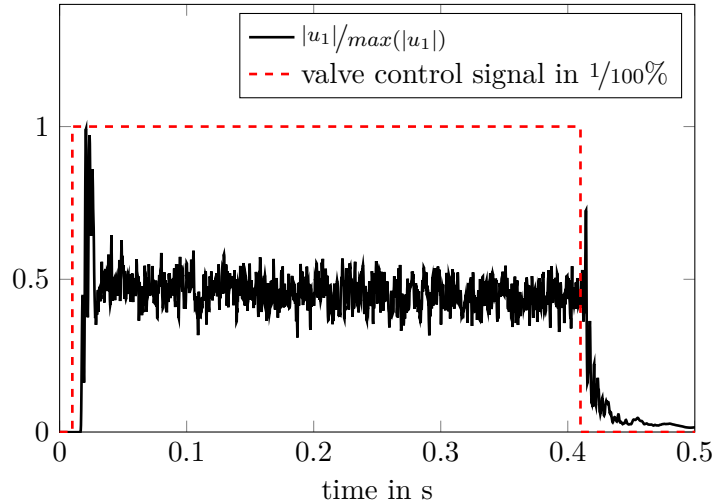


Figure 5.8: Velocity time trace downstream of the fuel valve for a 400 ms pulse at 100 % valve opening.

In Fig. 5.9, the first 38 ms of the valve opening are plotted to allow for a more detailed investigation of the valve opening response. Again, the valve control signal is shown as a red dashed line, whereas the normalized velocity is depicted as a black solid line. Between the valve control signal and the velocity response a time delay of 7 ms is observable in Fig. 5.9. This time delay corresponds to the time delay of the valve and the convective time delay between the valve outlet and the measurement location at the end of the attached tube. However, due to the lower available upstream pressure it is expected that the response time of the fuel valve is longer than 3 ms because the pressure difference across the valve influences the movement of the mechanical parts inside the valve.

Subsequent of the valve opening an undesired effect sets in. At the moment the valve opens, an oscillatory hotwire signal can be seen in Fig. 5.9 between 17 ms and 27 ms. This oscillation has several possible reasons. First, it may result from the inner dynamics of the valve itself. Second, it might stem from the pressure wave

which is created when the valve opens. Third, an oscillation in the hotwire bridge circuit might be excited by the sudden opening of the valve. However, the result of this behavior is a very unsteady velocity for the first 10-15 ms of the valve opening. The mentioned behavior can also be observed for a ramp-like control signal of the

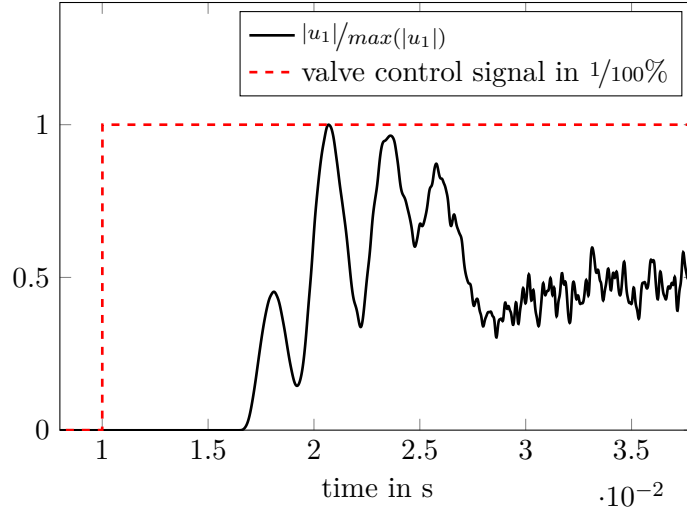


Figure 5.9: Velocity time trace downstream of the fuel valve at the beginning of a 400 ms pulse at 100 % valve opening.

valve. The corresponding time traces are shown in Fig. 5.10. In this case a ramp between 40 % and 100 % in 20 ms was set as control signal. This signal is close to the desired control signal for a homogeneous auto-ignition charge. The already determined response time between the valve control signal and the velocity time trace of approximately 7 ms is present in this case as well. The oscillatory behavior is also observed for this control signal, although no velocity overshoot can be found. The desired ramp in the velocity is vaguely present but superimposed by the mentioned oscillations.

The presented results of the fuel valve response investigation are not very promising for the ignition investigations. The observed oscillatory behavior subsequent to the valve opening prevents the calculation of the required valve transfer function. Hence, a precise fuel injection and stratification of the equivalence ratio in the short time available for the filling process is not possible. Additionally, changes in the flow path downstream of the fuel valve will significantly influence the mentioned phenomena. In order to create a homogeneous auto-ignition, the fuel mass flow rate must be precisely controlled between 1.94 kg/h and 2.08 kg/h (see Fig. 5.7). With the found velocity time traces in the fuel injection system, this curve will be superimposed by oscillations in the range of at least $\pm 10\%$, which inhibits the required precision for a homogeneous auto-ignition. Hence, the equivalence ratio and fuel mass flow rate curves presented in the previous section are not used in the succeeding ignition

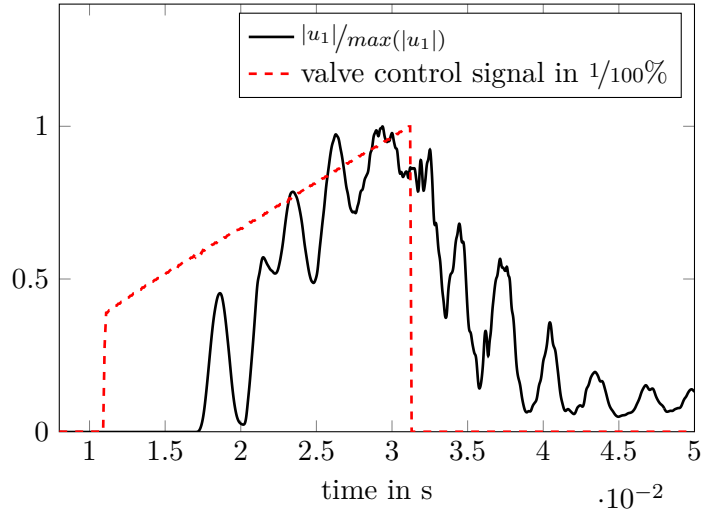


Figure 5.10: Velocity time trace downstream of the fuel valve for a ramp between 40-100% valve opening in 20 ms.

investigations. However, the performance of the developed fluidic devices within the SEC test rig is evaluated using non-homogeneous auto-ignition events. The first ignition tests within the presented SEC test rig are conducted without the equivalence ratio stratification, which is necessary for a homogeneous auto-ignition. Constant valve control signals of different durations and for different overall control signal timings were used for the fuel control valve. The resulting control signals and their timings will be presented in the following section.

5.2.3 Timing of Test Rig Control Signals

The initiation of controlled auto-ignition event is a challenging task, because several steps must be performed within a very short time. The presented test rig accomplishes this employing the developed fluidic devices. A sketch of the flow paths and the required components of the test rig is shown in Fig. 5.11. The default flow path for heating up the test rig and in between the ignition events is the measurement path (the lower flow path in Fig. 5.11).

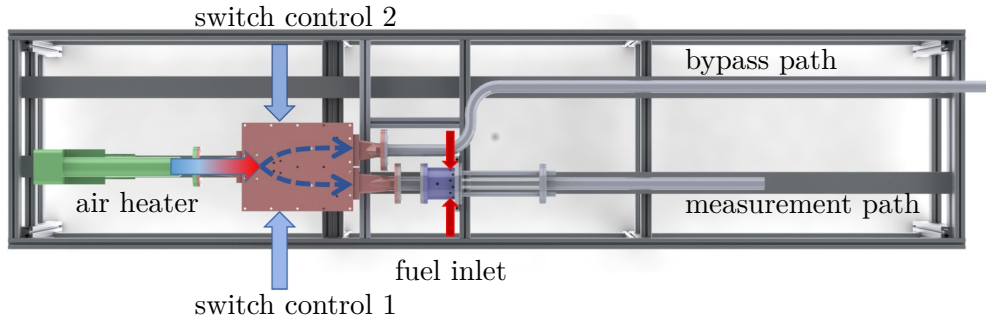


Figure 5.11: Flow paths and control devices in the SEC test rig.

Accordingly, the following initiation of a single ignition event is based on the main air flow through the measurement path. When the test rig is heated up, three main steps must be performed to create the ignition within the measurement volume:

1. The fuel is injected in the hot main air (cross) flow.
2. The main flow is switched from the measurement path to the bypass path in order to stop the flow within the measurement volume
3. Subsequent to the ignition event the flow is switched back to the measurement path.

The complete initiation process takes place in less than 1 s in the presented test rig. The corresponding three control signals are shown in Fig. 5.12. At $t = -10$ ms the measurement equipment is started in order to detect and acquire the complete ignition event. After a delay time of 10 ms the fuel injection is activated. Due to the undesired oscillations in the flow velocity downstream of the fuel control valve (see Sec. 5.2.2), only square pulses are employed in the presented ignition tests. The control signal of the fuel valve is shown on the top of Fig. 5.12. The corresponding fuel mass flow rate was measured for a given steady control current in the complete setup and is around $\dot{m} = 3.4$ kg/h, which results in an equivalence ratio of $\Phi = 1$. Subsequent to the fuel injection, the flow in the combustion tube must be stopped. This is done by the fluidic switch that switches the main air flow into the bypass path (see the “switch control 1” signal in Fig. 5.12). If the flow is not stopped fast enough the fresh fuel air charge will move out of the measurement volume or even out of the combustor. Beginning from a switching simultaneously to the closing of the fuel valve (as denoted by the vertical blue dash-dotted line in Fig. 5.12), several time delays between these two actions were investigated (as indicated in the middle of Fig. 5.12), in order to determine the ignition limits and to evaluate the performance of the fluidic switch. The different time delays are denoted as Δt_{switch} , where $\Delta t_{\text{switch}} = 0$ corresponds to the mentioned simultaneous switching. After the switching of the main air path, the fresh fuel–air charge is stopped inside the measurement volume

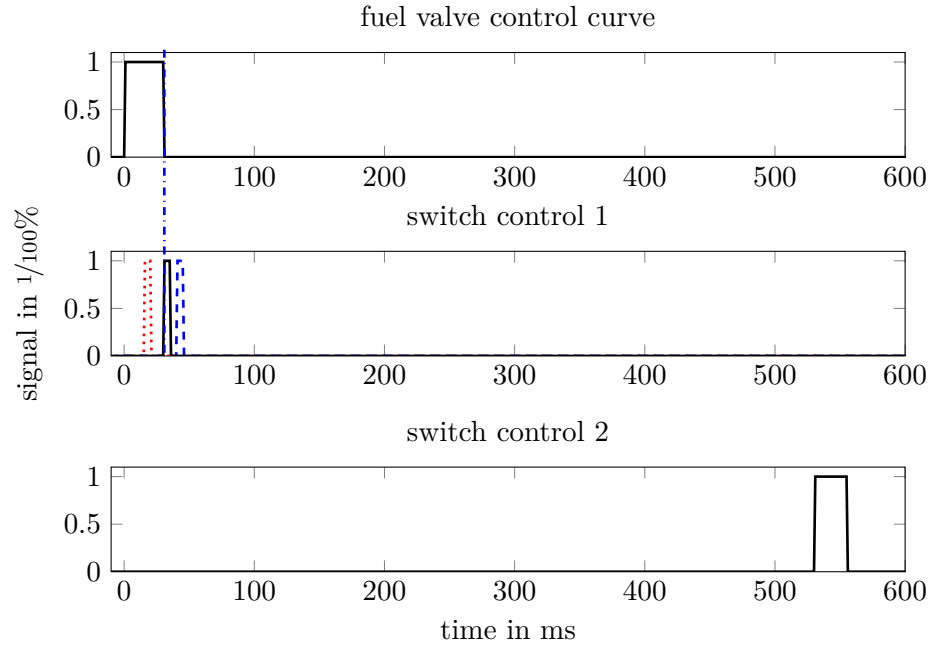


Figure 5.12: Timings of the three control signals: fuel valve (top), switch control 1 (middle), and switch control 2 (bottom).

for around 500-600 ms. Within this time the auto-ignition occurs and is detected by the photomultiplier tubes and the pressure transducers. Finally, the main flow is switched back to the measurement path purging the combustor. The corresponding control signal is shown on the bottom of Fig. 5.12. In order to ensure the switching back to the measurement path, the control signal for this side of the fluidic switch was set to 25 ms in contrast to the minimal 5 ms used for the switch control 1. However, the switching process was successful for all switching events in both directions.

The necessary severe heating of the test rig to around 800 K is accompanied by a disintegration of the dimethylether (DME) in the last part of the fuel line and the fuel injection disk. DME starts to disintegrate to lower hydrocarbons at around 500 K and, thus, the ignition behavior changes significantly. By subsequently firing 5 ignitions with a delay of less than a second between them, the heating of the fuel in the injection system was minimized. Accordingly, sequences of five ignition attempts for each change in the timings or operating condition (e.g., different Δt_{switch}) were initiated to ensure the inflow of “fresh” fuel. Nevertheless, with a bulk flow velocity of 15.14 m/s inside the combustion tube, the exhaust gases were completely transported out of the test rig prior to each filling. The results of these first ignition events within the developed SEC test rig are presented and discussed in the following section.

5.3 Ignition Investigations

After investigating the different parts of the SEC test rig, the system was assembled and set up for the first ignition investigations. Using the air heater, the measurement path of the test rig was heated up to match the required air inlet temperature of 793 K. Since, the temperature sensor for the combustor inlet temperature control was located upstream of the fluidic diode inlet section, the air was heated to around 820 K at this position. The additional temperature needed was estimated knowing the heat losses between the air heater outlet, the inlet temperature and the temperature downstream of the measurement volume. Due to the limited insulation in the measurement section (optical access was needed), a temperature difference between the inlet of the combustor and the measurement downstream of the measurement volume of around 100 K is present. This loss in flow temperature (measured in the center of the tube) is expected to stem from the very cold ambient air, which is sucked into the laboratory by the exhaust fan. A more efficient insulation of the complete test rig (including the measurement flow path) or an additional heating of the air around the combustor may reduce this parasitic loss of heat energy. Another possible solution may be to compensate the temperature loss with an adapted equivalence ratio curve. All of these potential solutions are left for further investigations, as it was not possible to investigate them within the current project. Together with the undesired outlet flow of the fuel control valve (see Sec. 5.2.2), this temperature gradient prevented the initiation and investigation of homogeneous auto-ignition events. However, as stated before, non-homogeneous auto-ignition events were investigated to assess the performance of the developed fluidic devices within the SEC combustor.

5.3.1 Ignition Characteristics

In the presented test campaign with the new SEC test rig, 121 successful auto-ignitions were initiated, out of 205 ignition attempts. The first one or two ignition attempts in the sequences of 5 attempts mostly fail due to the degeneration of the DME within the hot fuel supply, as mentioned in Sec. 5.2.3. Several timings and operating conditions were tested throughout this measurement campaign, which are presented in more detail later. However, all of the successful ignition events observed in the test rig can be categorized into the following categories:

1. The flame ignites close to the injection position and subsequently travels through the measurement volume.
2. A first ignition occurs close to the injection position, whereas a second ignition occurs with a short delay at a more downstream position.
3. A flame is ignited within the measurement volume and then travels in both axial directions.

Within one 5-shot sequence the ignition category mostly stays the same. The only shift in the ignition category within such a sequence were changes from 1-2 or 2-3 respectively. No sequence including category 1 and category 3 ignition were observed throughout the measurement campaign. Most of the successful ignitions were of category 1. A plot of the photomultiplier tube (PMT) time traces is shown in Fig. 5.13. The PMT signals are normalized by their saturation intensity, whereas the control signals are denoted in $1/100\%$. The ignition attempt begins with the fuel control

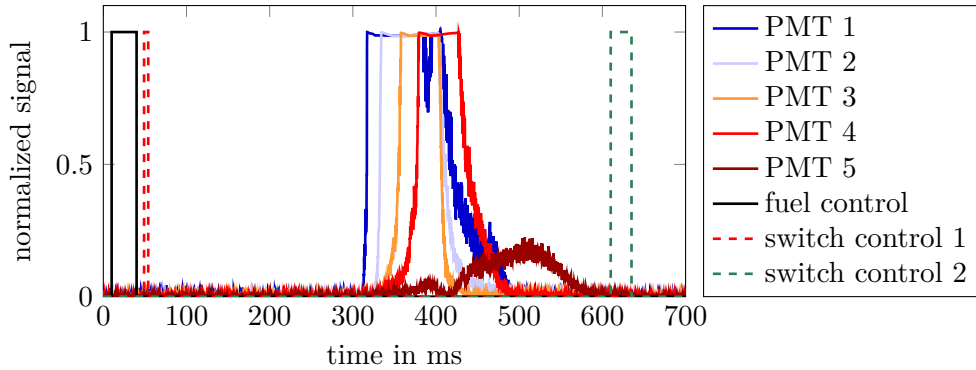


Figure 5.13: Time traces of the axially distributed photomultiplier tubes (normalized with their saturation limit) and the test rig control signals for a Category 1 auto-ignition.

signal, which completely opens the fuel valve at 10 ms for a duration of 30 ms. The fluidic switch switches the main flow to the bypass path of the test rig, 9 ms after the closing of the fuel valve. Hence, the delay time between these two signals is $\Delta t_{\text{switch}} = 9$ ms, as defined in Sec. 5.2.3. After an ignition delay time of around 300 ms, the fuel-air mixture undergoes auto-ignition in the vicinity of the injection location. This can be seen in the increase of the signal of the first PMT, which is located most upstream. The photomultiplier tubes were set to a very high sensitivity in order to capture very low intensity light emissions of the reaction. Thus, the PMT signal saturates shortly after the first increase in intensity. However, since the PMTs are not calibrated, no additional information would be obtained by the quantification of the maximum in the signal. Subsequent to the increase in the first PMT signal, the flame propagates through the measurement volume as it is detected by the other PMTs. The velocity of the propagating flame front is not constant in the presented case and varies between 4-6 m/s between the different measurement locations.

A representative measurement of a category 2 auto-ignition is plotted in Fig. 5.14. In this case, the ignition starts close to the injection position again. Surprisingly, the initial ignition delay time is around 215 ms and, thus, significantly lower than for the shown category 1 ignition. This is likely to stem from the earlier switching initiation in the category 2 auto-ignition. In this case, the switch control signal was already started 15 ms prior to the closing of the fuel valve (i.e., $\Delta t_{\text{switch}} = -15$ ms).

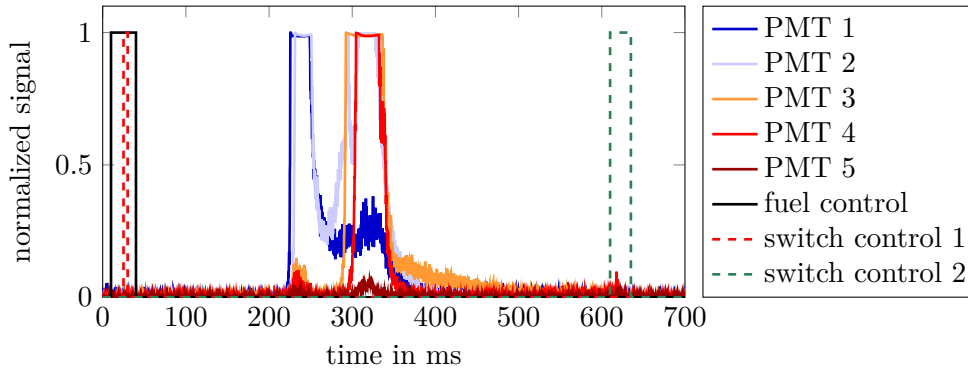


Figure 5.14: Time traces of the axially distributed photomultiplier tubes (normalized with their saturation limit) and the test rig control signals for a Category 2 auto-ignition.

Even including the delay time of the control valve and the switching time of the fluidic switch, this will create a stagnation of the air flow in the measurement path, while fuel is still injected. Hence, a region of higher equivalence ratio is created at the injection position resulting in a reduction of the ignition delay time. However, subsequent to the first ignition close to the injection, a second ignition kernel is observed in the PMT 3 and 2 signal. This second ignition takes place after an ignition delay time of around 280 ms, which is close to the ignition delay time of the category 1 auto-ignition. The flame front of the second ignition kernel travels through the measurement volume in both directions. The signals of PMT 2 and 4 reach the saturation level almost at the same time after the second ignition.

The third category of auto-ignition in the presented test rig is the most interesting as it corresponds to an auto-ignition somewhere in the measurement volume. Unfortunately, this type of auto-ignition was observed only for cases employing a significantly longer fuel injection. The corresponding plot is shown in Fig. 5.15. In this sequence fuel was injected into the main air flow for a period of 90 ms and the switch control was set to a time delay of $\Delta t_{\text{switch}} = -15$ ms. No ignition close to the injection position was observed in this case. This is expected to be a result of the longer fuel injection duration. Since the fuel valve is opened for a time significantly longer than 15 ms a steady fuel injection is expected, which may result in different equivalence ratios close to the injection position (see Sec. 5.2.2). However, after some weak light signals at PMT 1 and 2, the main ignition takes place at around 500 ms. This significantly longer ignition delay time was observed for all category 3 auto-ignitions. The reason for this increase in the ignition delay time is likely to stem from the heat loss in the combustor. Since the ignition kernel close to the hot injection position is not present as an ignition source, the fresh fuel-air charge is cooled down prior to ignition and the ignition delay time increases. An additional

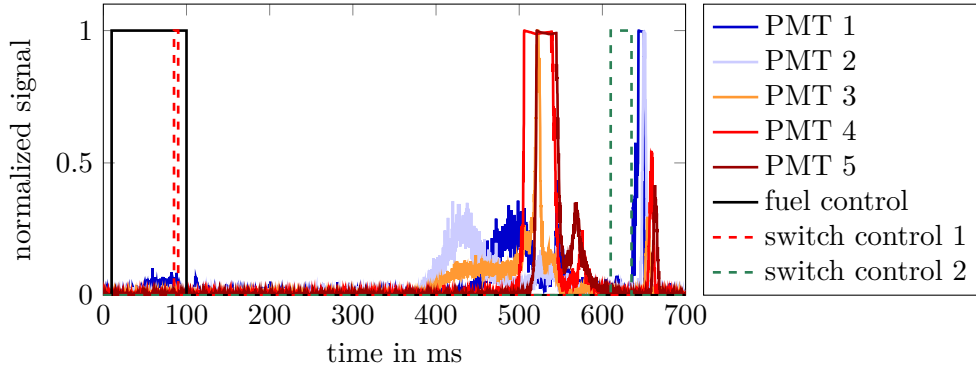


Figure 5.15: Time traces of the axially distributed photomultiplier tubes (normalized with their saturation limit) and the test rig control signals for a Category 3 auto-ignition.

result of the long fuel injection duration can be found subsequent to the switch control 2 signal. Residual fuel is ignited in the hot inlet section and is transported with the reactivated main flow through the measurement tube.

For all auto-ignitions investigated in these ignition tests only a marginal pressure increase of around 0.1 bar was observed. This is not surprising because the inhomogeneity of the auto-ignition gives the reactants enough time to expand during the combustion process. The expected pressure increase for the SEC is only present if the auto-ignition takes place homogeneously. However, two different influences on the ignition behavior are investigated in more detail in this ignition test campaign.

Influence of Duration of Fuel Injection

The first investigated parameter is the influence of different fuel injection durations on the ignition behavior. This is done to determine the minimal duration for fuel injection. The resulting numbers are listed in Tab. 5.1. For this test a switching delay time Δt_{switch} of -15 ms was selected in order to keep the fresh charge close to the hot combustor inlet. For each test, several ignition events were measured and the representative values are summarized in the table. All of the investigated ignition events are of category 2 or 3. Category 3 auto-ignitions have been observed for the first four test numbers, but since they were not as often as category two for numbers 1, 3, and 4 they are only listed in Tab. 5.1 for test number 2. However, the ignition delay time is decreasing for decreasing durations of fuel injections. This is assumed to stem from the undesired fuel valve behavior. As stated in Sec. 5.2.2, the fuel valve creates an overshoot in the outlet velocity for the first 15 ms of the valve opening. For significantly longer valve opening times, the high equivalence ratio accompanied by this overshoot in fuel mass flow rate is transported out of the measurement volume prior to auto-ignition. Hence, the decrease in the ignition time

Table 5.1: Influence of the duration of the fuel injection on the ignition delay time and the auto-ignition category

no.	fuel inj. in ms	Δt_{switch} in ms	valve control in %	τ_{ign} in ms	category
1	100	-15	100	377	2
2	90	-15	100	495	3
3	80	-15	100	339	2
4	70	-15	100	304	2
5	60	-15	100	259	2
6	50	-15	100	252	2
7	40	-15	100	244	2
8	30	-15	100	214	2

delay τ_{ign} is assumed to be a result of the increase in equivalence ratio due to the fuel mass flow rate overshoot.

Influence of Switching Time Delay Δt_{switch}

Subsequent to the investigation of the fuel injection duration, the influence of the switching delay time Δt_{switch} is investigated for the minimal valve opening. During the ignition tests it was observed that no auto-ignition event occurs, if the switching delay time is longer than 9 ms. This was expected as, the fresh fuel-air mixture is transported into the exhaust tube within the ignition delay time for longer switching delay times. Thus, the fresh charge is lost before it can undergo auto-ignition. In order to investigate the influence of the switching delay time, it was varied between -15 ms up to 9 ms. The results of this test are summarized in Tab. 5.2.

All of the investigated auto-ignitions are of category 1 or 2, whereby a transition between these two categories is observed for increasing switching time delays. The reasons for this transition and the differences in the ignition delay times are not completely understood and should be investigated in future work. However, the presented investigation allows to investigate the performance of the fluidic switch within the SEC test rig. The different switching delay times will change the axial position of the fresh charge, which is shown in Sec. 5.3.2.

Table 5.2: Influence of the switching time delay on the ignition delay time and the auto-ignition category

no.	fuel inj. in ms	Δt_{switch} in ms	valve control in %	τ_{ign} in ms	category
1	30	-15	100	214	2
2	30	-14	100	188	2
3	30	-13	100	193	2
4	30	-12	100	197	1/2
5	30	-11	100	211	1/2
6	30	-10	100	230	1
7	30	-9	100	214	2
8	30	-8	100	199	1
9	30	-7	100	202	1
10	30	-6	100	220	1
11	30	-5	100	196	1
12	30	-4	100	199	1
13	30	-3	100	219	1
14	30	-2	100	208	1
15	30	-1	100	207	1
16	30	0	100	226	1
17	30	1	100	282	1
18	30	2	100	285	1
19	30	3	100	317	1
20	30	4	100	296	1
21	30	5	100	258	1
22	30	6	100	245	1
23	30	7	100	272	1
24	30	8	100	303	1
25	30	9	100	306	1

5.3.2 Performance of the Fluidic Devices

The investigation of the performance of the developed fluidic devices within the SEC test rig was the main goal of the presented preliminary ignition tests. Due to the unforeseen characteristics regarding the fuel control valve and the temperature loss in the measurement section, no initiation of homogeneous auto-ignitions in the presented first ignition tests was possible. Hence, the performance of the fluidic oscillators for fuel injection could not be assessed in the final setup. However, since the mixing characteristics of the inlet section were thoroughly investigated in Sec. 2.4, it can be assumed that their performance within the SEC framework is as expected. Regarding the fluidic diode, the absence of homogeneous auto-ignitions and, thus,

the absence of a significant pulse like pressure rise (i.e., more than 0.1 bar), prevents an analysis of the reflected pressure wave using the pressure transducer data. Even though the temperature sensors in the measurement path indicated that the fluidic diode is blocking a significant portion of the combustion induced back flow, their data is not reliable enough to be presented here. Hence, the performance of the inlet section including the fluidic oscillators and the fluidic diode in the surrounding of the SEC test rig must be investigated in future work.

In contrast to that, the performance of the fluidic switch in the SEC test rig can be reviewed using the optical and the pressure measurements. The first criterion was the general function of the fluidic switch. As stated in chapter. 4, the fluidic switch is necessary to stop the flow in the measurement path. Otherwise the fresh reactants will be transported out of the test rig within the ignition delay time. This was confirmed since no auto-ignition was observed for a switching delay time longer than $\Delta t_{\text{switch}} = 9 \text{ ms}$. In addition, the performance of the switch can be assessed using the pressure signal during the ignition event and the data of the photomultiplier tubes. The pressure time trace of the most upstream pressure transducer for the ignition event shown in Fig. 5.15 is plotted in Fig. 5.16. The plot on the top of

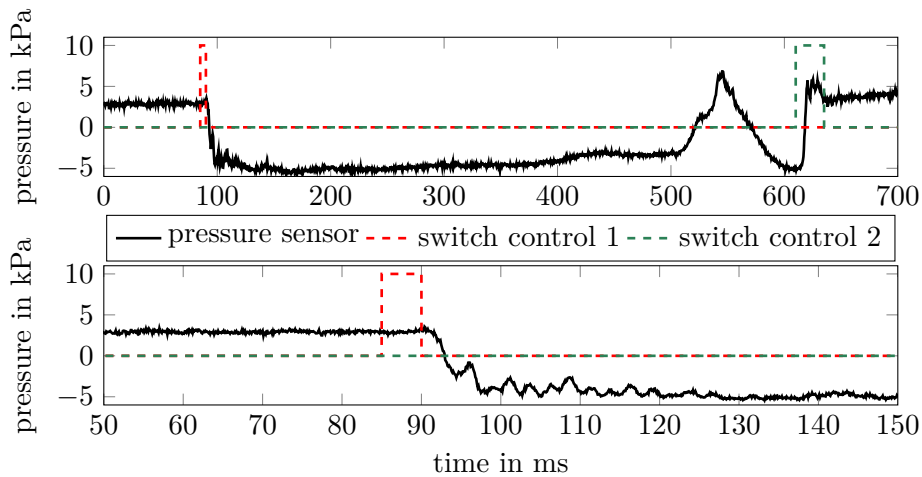


Figure 5.16: Time traces of the pressure signal during the initiation of an ignition event (the switching controls are shown in arbitrary units for visualization).

Fig. 5.16 shows the complete time history of the ignition event, whereas the plot on the bottom shows the the switching event from the measurement path to the bypass path. The switching control signals are shown here in arbitrary units to visualize the timing of the signals. In both plots the switching process is clearly visible in the pressure signal. As described in chapter 4, a lower pressure level is established in the inactive outlet. This decrease in static pressure is visible directly subsequent to the first switching control signal at around 90 ms. Between 400-560 ms the ignition event is detected as an increase in pressure. At 630 ms the main air flow is switched back to

the measurement path and the pressure level is increased again. In the more detailed plot of the first switching (Fig. 5.16 on the bottom), the delay between the switch control signal and the decrease in the pressure level can be determined. The pressure starts to decrease 7 ms after the rising edge of the switching control signal. This delay time is identical to the numerically determined switching time (see chapter 4).

The second way to determine the performance of the fluidic switch are the ignition events with different switching delay time Δt_{switch} . For a longer Δt_{switch} the fresh fuel–air charge will move further downstream prior to ignition. This behavior can be detected by the photomultiplier tubes. The corresponding plots of the PMT signals (normalized by the saturation value) for three different switching delay times (i.e., $\Delta t_{\text{switch}} = -15$ ms, 0 ms, and 9 ms) are shown in Fig. 5.17. The increase in intensity is visible for the most downstream photomultiplier as the switching delay time increases. This increase in intensity is a direct indicator that the axial position of the fresh fuel–air charge has changed. Together with the pressure signals that show the switching process, this finding confirms the performance of the fluidic switch. For all switching attempts in the presented ignition tests the switching of the main mass flow between the two air paths was successful, underlining the outstanding reliability and performance of the developed fluidic device.

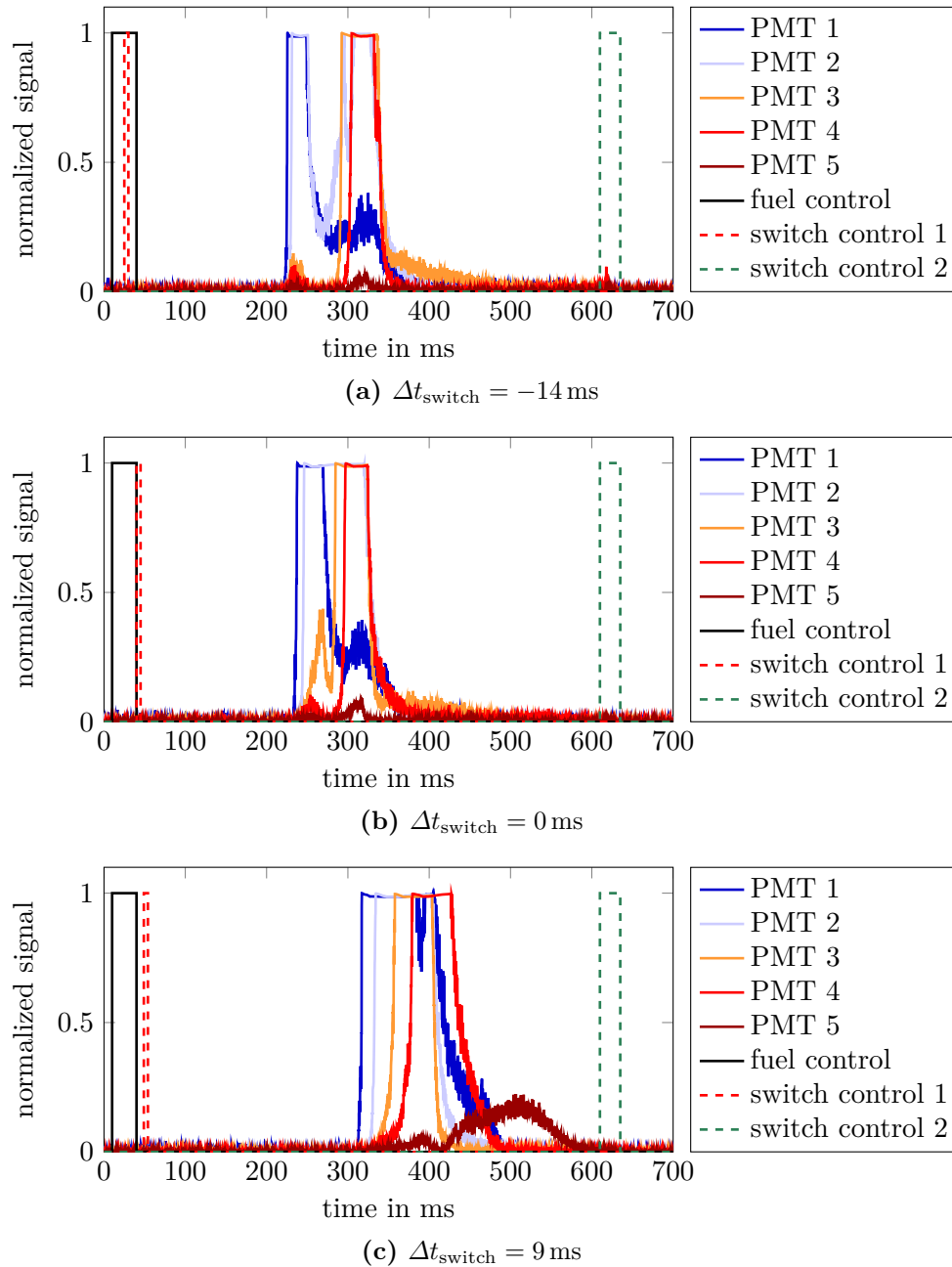


Figure 5.17: The PMT signals of the ignition event for different switching delay times Δt_{switch} .

5.4 Intermediate Conclusion

Based on the findings and developed fluidic devices, a test rig for the initiation and investigation of auto-ignition events was developed and built. Emanating from the electrical air heater the flow path includes all three developed and investigated fluidic devices. The fluidic switch is integrated to switch the main air flow between the measurement and the bypass path, stopping the fluid in the measurement volume. The fluidic diode and the fluidic oscillators, as fuel injection devices, were combined in the inlet section of the combustion tube. Employing a silica glass combustion tube enabled optical measurements using photomultiplier tubes. This measurement technique allows to detect the location of the reaction zone and the ignition with the necessary sampling frequency. Together with piezo-type pressure transducers the *PMTs* allowed for a reliable detection and investigation of the ignition events in the developed test rig.

Based on the one-dimensional numerical simulations of the ignition event¹ the control curves of the equivalence ratio and the corresponding fuel mass flow rate were determined and presented. In order to translate this required fuel mass flow rate curve to a valve control current, the valve response should be determined by making use of velocity measurements. During these tests an unwanted behavior was observed in the velocity time traces at the valve outlet. Subsequent to the valve opening, an oscillatory velocity is present downstream of the fuel valve, which obstructs the precise adjustment of the fuel mass flow rate in the first 15 ms after the valve opening. Together with the temperature loss observed in the measurement path, this behavior prevents the initiation of homogeneous auto-ignitions in the presented ignition tests. Accordingly, only constant fuel mass flow rates resulting in an equivalence ratio of around $\Phi = 1$ were investigated in the presented work. After reaching the needed operating conditions 121 successful auto-ignitions were initiated and investigated. Based on the optical *PMT* measurements, it was possible to categorize the ignition events in three categories with different ignition characteristics.

Due to the absence of homogeneous auto-ignitions, it was not possible to determine the performance of the inlet section including the fluidic diode and the fuel injection (i.e., fluidic oscillators) further than presented in the previous chapters. However, the data acquired by the *PMTs* and the pressure transducers allowed for the confirmation of the performance of the fluidic switch. All switching events of the hot air mass flow were successful and the numerically obtained switching time of 7 ms was confirmed in the *SEC* test rig. In addition, it was possible to axially move the fresh fuel-air charge in the combustion tube as it was confirmed by the optical *PMT* measurements. Even though, the performance of the other two fluidic devices could not be completely

¹ The numerical simulations were performed by Phillip Berndt with a detailed chemical reaction mechanism developed by Liming Cai.

verified in the presented first ignition tests, the great performance of the fluidic switch and the promising performance of the overall test rig gives confidence in the performance of the developed and implemented fluidic devices.

In order to create homogeneous auto-ignition events in the presented test rig two challenges must be addressed in future work. First, the fuel control valve must be assessed in detail to allow a precise control of the injected fuel mass flow rate. To do so, the velocity at the outlet of the fuel injection disk must be investigated in the complete setup, which is challenging due to the hot cross flow in the combustor. By employing concentration measurements of a tracer gas (e.g., Acetone-PLIF) it might be possible to determine the instantaneous equivalence ratio in the combustion tube and, thus, calibrate the fuel valve for a given equivalence ratio curve. Second, the temperature gradient inside the measurement path must be reduced. Beside the possibility to add insulation around the measurement volume, which requires changes in the measurement equipment, one may add a second tube around the measurement path. The annulus between these two tubes can be fed with hot air, creating a homogeneous temperature distribution throughout the complete measurement path.

Following the findings of this chapter, the main goal of developing fluidic devices that enable to investigate auto-ignition events regarding the innovative SEC process in a test rig was successful. An auto-ignition test rig was designed based on these devices and first preliminary tests were performed. Using the new test rig it is possible to reliably initiate auto-ignition events. The interchangeable fuel injection disks allow for a flexible investigation of different fuel injection geometries, including the possibility to implement a liquid fuel injection into the developed test rig. The excellent performance of the fluidic switch allow to stop the fresh fuel-charge at a specific axial position in the combustion tube, which creates the possibility to shift the reaction zone into the optimal measurement position. Hence, the new test rig allows for flexible, economic and efficient investigations of the auto-ignition behavior of almost every fuel and at different operating conditions.

CHAPTER 6

Concluding Remarks

In order to increase the efficiency of energy conversion systems, the constant volume combustion is a promising technique to achieve a step-change in the gas turbine technology. Employing a completely different thermodynamical cycle and utilizing unsteady effects in gas turbine systems, these concepts also enable new additional possibilities for further improvement. However, the known *CVC* processes are accompanied by several drawbacks, such as shock waves or difficult mechanical integration. The new shockless explosion combustion (*SEC*) concept presented in this work overcomes many of this drawbacks, but also is accompanied by new challenges. The *SEC* concept is based on a homogeneous auto-ignition that is created by an equivalence ratio stratification in the combustor. Due to the required quality in the fuel-air mixing and the incorporation of high frequency flow oscillations at high temperatures, traditional parts are not able to fulfill the arising tasks.

The presented thesis introduced the *SEC* and evaluated its challenges and advantages. In contrast to known *CVC* approaches, five outstanding main benefits arise from the *SEC* concept:

1. Smooth pressure rises
2. Lower exergy losses due to kinetic energy
3. No detonation to deflagration transition losses
4. Mechanical integrity
5. Inherent filling process against the positive pressure gradient

On the other hand, two main challenges arise from the *SEC* concept. First, an almost instantaneous mixing of fuel and air is required and second, the flow rectification of a 800 K air flow at a frequency of around 250 Hz must be realized. Additionally, the long ignition delay times at atmospheric pressure induce the need for a mechanism to stop such a high temperature flow in the required test rig. These tasks can not

be accomplished by traditional parts. Hence three fluidic devices were developed, investigated, and integrated the new auto-ignition test rig.

Fluidic devices are able to withstand the demanding conditions of such a combustion chamber and performing their specific task for an almost infinite lifetime. For each of the imposed requirements in the surrounding of an atmospheric SEC ignition test rig, a special fluidic device was presented. The test rig, which was designed based on the developed fluidic devices, enables the possibility of a flexible and efficient investigation of the auto-ignition event for relevant fuels. With the presentation of preliminary auto-ignition investigations using the developed test rig it was shown that the developed fluidic devices are able to reliably perform their specific task within the SEC environment.

Introducing the presented test rig and following the findings regarding the fluidic devices a first step towards the realization of the SEC process is achieved. Employing the test rig it is now possible to efficiently investigate not only the auto-ignition behavior of different fuels, but also it is possible to investigate different fuel injection systems, combustor geometries, and perform other parametric studies regarding the ignition behavior. The optical access allows for the detailed investigation of the flow and heat release during the auto-ignition event. Hence, the results and findings of this thesis will accelerate the development and integration of the SEC process in future generations of gas turbine systems.

Besides the SEC concept, the presented findings enable possible improvements in other applications. The significant improvement of the mixing quality may be employed in current combustion systems, such as stationary gas turbines or aero-engines. The presented mechanisms and sensitivities regarding the fluidic oscillator allow for an efficient adaption of such devices to other applications. The same holds for the other two developed fluidic devices. The fluidic diode cannot only be used as a flow rectification devices in the framework of the SEC process, but might also be useful for example in general piping systems or the cooling of surfaces facing severe pressure oscillations. The fluidic switch provides an extremely reliable and robust way to switch a fluid flow between different flow paths, which, for example, might be used in cooling circuits or other fluid distribution networks.

Following the results and findings of the presented thesis it is possible to fulfill the challenges and tasks imposed by the innovative SEC combustion process employing the developed fluidic devices. Accordingly, the presented results and the developed test rig allow for further investigations and developments in the field of constant volume combustion systems.

Bibliography

- [1] O. V. Achasov, S. A. Labuda, V. V. Kondrashov, O. G. Penyaz'kov, R. M. Pushkin, A. I. Tarasov, and S. I. Shabunya. Focusing of shock waves on reflection from concave curvilinear surfaces. *Journal of Engineering Physics and Thermophysics*, 65(5):1073–1077, 1993. ISSN 1062-0125. doi: [10.1007/BF00862034](https://doi.org/10.1007/BF00862034).
- [2] O. V. Achasov, S. A. Labuda, O. G. Penyaz'kov, P. M. Pushkin, and A. I. Tarasov. Initiation of detonation in reflection of a shock wave from a concave curvilinear surface. *Journal of Engineering Physics and Thermophysics*, 67(1-2):739–744, 1994. ISSN 1062-0125. doi: [10.1007/BF00853325](https://doi.org/10.1007/BF00853325).
- [3] P. Akbari, R. Nalim, and N. Mueller. A Review of Wave Rotor Technology and Its Applications. *Journal of Engineering for Gas Turbines and Power*, 128(4):717, 2006. ISSN 07424795. doi: [10.1115/1.2204628](https://doi.org/10.1115/1.2204628).
- [4] J. Andreopoulos. On the structure of jets in a crossflow. *Journal of Fluid Mechanics*, 157:163–197, 1985. doi: [10.1017/S0022112085002348](https://doi.org/10.1017/S0022112085002348).
- [5] S. W. Angrist. Fluid Control Devices. *Scientific American*, 211:80–89, December 1964. ISSN 0036-8733.
- [6] ANSYS Inc. ANSYS CFX-Solver Theory Guide ANSYS CFX Release 11.0. Technical report, ANSYS inc., 2006.
- [7] G. Arwatz, I. Fono, and A. Seifert. Suction and Oscillatory Blowing Actuator Modeling and Validation. *AIAA Journal*, 46(5):1107–1117, May 2008. ISSN 0001-1452. doi: [10.2514/1.30468](https://doi.org/10.2514/1.30468).
- [8] P. J. Baker. A comparison of fluid diodes. In *Proceedings of the 2nd Cranfield Fluidics Conference*, pages 88–126, 1967.
- [9] J. Barber. A Method of Rising Inflammable Air for the Purposes of Procuring Motion, and Facilitating Metallurgical Operations. *United Kingdom Patent*, (1791-1833), 1791.

- [10] P. Bauer. Fluidic Oscillator Flowmeter. *United States Patent*, (US1981-4,244,230), 1981.
- [11] P. Berndt. On the Use of the HLL-Scheme for the Simulation of the Multi-Species Euler Equations. *Finite Volumes for Complex Applications VII - Elliptic, Parabolic and Hyperbolic Problems*, 78:809–816, 2014.
- [12] B. C. Bobusch, R. Wozidlo, J. M. Bergada, C. N. Nayeri, and C. O. Paschereit. Experimental study of the internal flow structures inside a fluidic oscillator. *Experiments in Fluids*, 54(6):1559, June 2013. ISSN 0723-4864. doi: [10.1007/s00348-013-1559-6](https://doi.org/10.1007/s00348-013-1559-6).
- [13] B. C. Bobusch, R. Wozidlo, O. Krüger, and C. O. Paschereit. Numerical Investigations on Geometric Parameters Affecting the Oscillation Properties of a Fluidic Oscillator. *Proceedings of the 21st AIAA Computational Fluid Dynamics Conference*, 2013.
- [14] B. C. Bobusch, P. Berndt, C. O. Paschereit, and R. Klein. Shockless Explosion Combustion – An Innovative Way of Efficient Constant Volume Combustion in Gas Turbines –. *Combustion Science and Technology*, 186(10-11):1680–1689, 2014. doi: [10.1080/00102202.2014.935624](https://doi.org/10.1080/00102202.2014.935624).
- [15] B. C. Bobusch, P. Berndt, C. O. Paschereit, and R. Klein. Investigation of Fluidic Devices for Mixing Enhancement for the Shockless Explosion Combustion Process. In Rudibert King, editor, *Active Flow and Combustion Control 2014*, volume 127 of *Notes on Numerical Fluid Mechanics and Multidisciplinary Design*, pages 281–297. Springer International Publishing, 2015. ISBN 978-3-319-11966-3. doi: [10.1007/978-3-319-11967-0_18](https://doi.org/10.1007/978-3-319-11967-0_18).
- [16] L. Cai and H. Pitsch. Tailoring Fuels for a Shockless Explosion Combustor. In Rudibert King, editor, *Active Flow and Combustion Control 2014*, volume 127 of *Notes on Numerical Fluid Mechanics and Multidisciplinary Design*, pages 299–315. Springer International Publishing, 2015. ISBN 978-3-319-11966-3. doi: [10.1007/978-3-319-11967-0_19](https://doi.org/10.1007/978-3-319-11967-0_19).
- [17] N. Caldwell and E. Gutmark. Performance analysis of a hybrid pulse detonation combustor/gas turbine system. *44th AIAA/ASME/SAE/ASEE Joint Propulsion Conference and Exhibit Aerospace Sciences Meeting and Exhibit*, (AIAA 2008-4880), 2008.
- [18] C. J. Campagnuolo, C. Chase, and S. O. Rutstein. Fluidic Oscillatory System Insensitive to Pressure and Temperature. *United States Patent*, US1970-350:1–5, January 1970. ISSN 00694770. doi: [10.1177/006947707000800108](https://doi.org/10.1177/006947707000800108).

- [19] C. Cerretelli and E. Gharaibah. An Experimental and Numerical Investigation on Fluidic Oscillators For Flow Control. *37th AIAA Fluid Dynamics Conference and Exhibit*, (AIAA 2007-3584), 2007.
- [20] C. Cerretelli and K. Kirtley. Boundary Layer Separation Control With Fluidic Oscillators. *Journal of Turbomachinery*, 131(4), 2009. ISSN 0889504X. doi: 10.1115/1.3066242.
- [21] C. Cerretelli, W. Wuerz, and E. Gharaibah. Unsteady Separation Control on Wind Turbine Blades using Fluidic Oscillators. *AIAA Journal*, 48(7):1302–1311, July 2010. ISSN 0001-1452. doi: 10.2514/1.42836.
- [22] V. J. Chadwick and B. C. Dye. A fluidic wall-attachment amplifier of improved sensitivity. *Journal of Scientific Instruments*, 44:683–685, 1967.
- [23] A. E. Clarke, A. J. Gerrard, and L. A. Holliday. Some experiences in gas turbine combustion chamber practice using water flow visualization techniques. *Symposium (International) on Combustion*, 9(1):878–891, 1963.
- [24] M. L. Coleman. Overview of pulse detonation propulsion technology. *Chemical Propulsion Information Agency*, 2001.
- [25] P. V. Danckwerts. The definition and measurement of some characteristics of mixtures. *Applied Scientific Research, Section A*, 3:279–296, 1952.
- [26] A. Eroglu and R. E. Breidenthal. Structure, penetration, and mixing of pulsed jets in crossflow. *AIAA journal*, 39(3):417–423, 2001. doi: 10.2514/2.1351.
- [27] Douglas Feikema and Dennis Culley. Computational Fluid Dynamic Modeling of a Fluidic Actuator for Flow Control. *46th Aerospace Sciences Meeting and Exhibit*, (AIAA 2008-557), 2008.
- [28] S. Gaertlein, R. Wozidlo, F. Ostermann, C. Nayeri, and C. O. Paschereit. The Time-Resolved Internal and External Flow Field Properties of a Fluidic Oscillator. In *52nd Aerospace Sciences Meeting*, Reston, Virginia, January 2014. American Institute of Aeronautics and Astronautics. ISBN 978-1-62410-256-1. doi: 10.2514/6.2014-1143.
- [29] U. Gebhard, H. Hein, and U. Schmidt. Numerical investigation of fluidic micro-oscillators. *Journal of Micromechanics and Microengineering*, 6:115–117, 1996. doi: 10.1088/0960-1317/6/1/028.
- [30] B. Goelling, M. Bauer, and W. Nitsche. Fluid Actuator for Influencing the Flow Along a Flow Surface, as well as Blow-Out Device and Flow Body Comprising a Like Fluid. *International Patent*, (WO/2012/048853 A1), 2012.

- [31] S. A. Gokoglu, M. A. Kuczmariski, D. E. Culley, and S. Raghu. Numerical Studies of a Fluidic Diverter for Flow Control. *39th Fluid Dynamics Conference and Exhibit*, (AIAA-2009-4012), 2009.
- [32] S. A. Gokoglu, M. A. Kuczmariski, D. E. Culley, and S. Raghu. Numerical Studies of a Supersonic Fluidic Diverter Actuator for Flow Control. *5th Flow Control Conference*, (AIAA-2010-4415), 2010.
- [33] S. A. Gokoglu, M. A. Kuczmariski, D. E. Culley, and S. Raghu. Numerical Studies of an Array of Fluidic Diverter Actuators for Flow Control. *41st Fluid Dynamics Conference and Exhibit*, (AIAA-2011-3100), 2011.
- [34] J. M. Goto and T. M. Drzewiecki. An analytical model for the response of flueric wall attachment amplifiers. *Harry Diamond Laboratories Report (HDL-TR-1598)*, 1972.
- [35] J. W. Gregory and M. N. Tomac. A Review of Fluidic Oscillator Development. *43rd Fluid Dynamics Conference*, (AIAA 2013-2474), June 2013. doi: 10.2514/6.2013-2474.
- [36] J. W. Gregory, J. P. Sullivan, and S. Raghu. Visualization of jet mixing in a fluidic oscillator. *Journal of Visualization*, 8(2):169–176, June 2005. ISSN 1343-8875. doi: 10.1007/BF03181660.
- [37] J. W. Gregory, J. P. Sullivan, G. Raman, and S. Raghu. Characterization of the Microfluidic Oscillator. *AIAA Journal*, 45(3):568–576, March 2007. ISSN 0001-1452. doi: 10.2514/1.26127.
- [38] W. S. Griffin. Design of a Fluid Jet Amplifier with Reduced Receiver-Interaction-Region Coupling. *NASA Technical Note (TN D-3651)*, 1966.
- [39] D. Guyot, C. O. Paschereit, and S. Raghu. A Fluidic Actuator for Active Combustion Control. *ASME Turbo Expo 2008*, (GT2008-50797), 2008.
- [40] D. Guyot, C. O. Paschereit, and S. Raghu. Active Combustion Control Using a Fluidic Oscillator for Asymmetric Fuel Flow Modulation. *International Journal of Flow Control*, 1(2):155–166, 2009. doi: 10.1260/175682509788913335.
- [41] W. H. Heiser and D. T. Pratt. Thermodynamic Cycle Analysis of Pulse Detonation Engines. *Journal of Propulsion and Power*, 18(1):68–76, January 2002. ISSN 0748-4658. doi: 10.2514/2.5899.
- [42] P. Holmes, J. L. Lumley, and G. Berkooz. *Turbulence, coherent structures, dynamical systems and symmetry*. Cambridge University Press, 1998.
- [43] H. Holzwarth. Rotary Combustion Engine. *United States Patent*, (US1905-783434), 1905.

- [44] H. Johari. Scaling of Fully Pulsed Jets in Crossflow. *AIAA Journal*, 44(11): 2719–2725, November 2006. ISSN 0001-1452. doi: 10.2514/1.18929.
- [45] H. Johari, M. Pacheco-Tougas, and J. Hermanson. Penetration and Mixing of Fully Modulated Turbulent Jets in Crossflow. *AIAA Journal*, 37(7):842–850, July 1999. ISSN 0001-1452. doi: 10.2514/2.7532.
- [46] J. W. Joyce. Fluidics: basic components and applications. *Harry Diamond Laboratories Report (HDL-SR-83-9)*, 1983.
- [47] M. Kadosch, F. G. Paris, J. Le Foll, and B. Jean. Jet Propulsion Units. *United States Patent*, (US 2,825,204), 1958.
- [48] K. Kailasanath. Recent Developments in the Research on Pulse Detonation Engines. *AIAA Journal*, 41(2):145–159, February 2003. ISSN 0001-1452. doi: 10.2514/2.1933.
- [49] Y. Kamotani and I. Greber. Experiments on a turbulent jet in a cross flow. *AIAA journal*, 10(11):1425–1429, 1972. doi: 10.2514/3.50386.
- [50] J. F. Keffer and W. D. Baines. The round turbulent jet in a cross-wind. *Journal of Fluid Mechanics*, 15(4):481–496, 1963. doi: 10.1017/S0022112063000409.
- [51] J. A. C. Kentfield. Thrust Augmenting Fluid Rectifier for a Pulsed Combustor. *United States Patent*, (US 4,033,120), 1977.
- [52] J. A. C. Kentfield and M. O’Blenes. Methods for achieving a combustion-driven pressure gain in gas turbines. *Journal of Engineering for Gas Turbines and Power*, 110:704–711, 1988.
- [53] J. A. C. Kentfield, A. Rehman, and J. Cronje. Performance of Pressure-Gain Combustors Without Moving Parts. *Journal of Energy*, 4(2):56–63, March 1980. ISSN 0146-0412. doi: 10.2514/3.62460.
- [54] R. Khelifaoui, S. Colin, S. Orieux, R. Caen, and L. Baldas. Numerical and Experimental Analysis of Monostable Mini- and Micro-Oscillators. *Heat Transfer Engineering*, 30(1-2):121–129, January 2009. ISSN 0145-7632. doi: 10.1080/01457630802293548.
- [55] J. M. Kirshner and S. Katz. *Design Theory of Fluidic Components*. Academic Press In., 1975. ISBN 978-0124102507.
- [56] B. Koli, J. W. Chew, N. J. Hills, and T. Scanlon. CFD Investigation of a Fluidic Device for Modulation of Aero-Engine Cooling Air. *Proceedings of ASME Turbo Expo 2014: Turbine Technical Conference and Exposition*, (GT2014-26221), 2014.

- [57] O. Krüger, B. C. Bobusch, R. Woszidlo, and C. O. Paschereit. Numerical Modeling and Validation of the Flow in a Fluidic Oscillator. In *21st AIAA Computational Fluid Dynamics Conference*, Reston, Virginia, June 2013. American Institute of Aeronautics and Astronautics. doi: 10.2514/6.2013-3087.
- [58] V. A. Kulkarni. *An Experimental Investigation on Focussing of Weak Shock Waves in Air*. PhD thesis, California Institute of Technology, 1975.
- [59] A. Lacarelle and C. O. Paschereit. Increasing the Passive Scalar Mixing Quality of Jets in Crossflow With Fluidics Actuators. *Journal of Engineering for Gas Turbines and Power*, 134(2), 2012. ISSN 07424795. doi: 10.1115/1.4004373.
- [60] A. Lacarelle, G. Sebastian, and C. O. Paschereit. A Quantitative Link Between Cold-Flowscalar Unmixness and NOX Emissions in a Conical Premixed Burner. *ASME Turbo Expo 2010*, (ASME GT2010-23132), 2010.
- [61] S. G. Levin and F. M. Manion. Fluid Amplification: 5. Jet Attachment Distance as a Function of Adjacent Wall Offset and Angle. *Harry Diamond Laboratories Report (HDL-TR-1087)*, 1962.
- [62] V. A. Levin, J. N. Nechaev, and A. I. Tarasov. A New Approach to Organizing Operation Cycles in Pulsed Detonation Engines. In Gabriel D. Roy, Sergei M. Frolov, David W. Netzer, and Anatolii A. Borisov, editors, *High-Speed Deflagration and Detonation; Fundamentals and Control*, pages 223–238. ELEX-KM Publishers, Moscow, 2001.
- [63] F. Lu, E. Braun, L. Massa, and D. Wilson. Rotating Detonation Wave Propulsion: Experimental Challenges, Modeling, and Engine Concepts. In *47th AIAA/ASME/SAE/ASEE Joint Propulsion Conference & Exhibit*, Reston, Virginia, July 2011. American Institute of Aeronautics and Astronautics. ISBN 978-1-60086-949-5. doi: 10.2514/6.2011-6043.
- [64] A. Mellling. Tracer particles and seeding for particle image velocimetry. *Measurement Science and Technology*, 8(12):1406–1416, 1997. doi: 10.1088/0957-0233/8/12/005.
- [65] F. R. Menter. Zonal two equation $k-\omega$ turbulence models for aerodynamic flows. In *24th Fluid Dynamics Conference*, 1993.
- [66] S. Mondal, A. Mukhopadhyay, and S. Sen. Dynamic Characterization of a Laboratory-Scale Pulse Combustor. *Combustion Science and Technology*, 186(2):139–152, February 2014. ISSN 0010-2202. doi: 10.1080/00102202.2013.851078.

- [67] A. Nakayama, F. Kuwahara, and Y. Kamiya. A two-dimensional numerical procedure for a three dimensional internal flow through a complex passage with a small depth (its application to numerical analysis of fluidic oscillators). *International Journal of Numerical Methods for Heat & Fluid Flow*, 15(8): 863–871, 2005. ISSN 0961-5539. doi: [10.1108/09615530510625129](https://doi.org/10.1108/09615530510625129).
- [68] L. Narayanaswami and G. A. Richards. Pressure-gain combustion: Part I — Model development. *Journal of Engineering for Gas Turbines and Power*, 118(3):461–473, 1996. doi: [10.1115/1.2816668](https://doi.org/10.1115/1.2816668).
- [69] G. J. Nathan, J. Mi, Z. T. Alwahabi, G. J. R. Newbold, and D. S. Nobes. Impacts of a jet’s exit flow pattern on mixing and combustion performance. *Progress in Energy and Combustion Science*, 32(5-6):496–538, September 2006. ISSN 03601285. doi: [10.1016/j.pecs.2006.07.002](https://doi.org/10.1016/j.pecs.2006.07.002).
- [70] T. S. Norton, G. A. Richards, K. H. Casleton, and L. C. Jenkins. NO_x and CO Emissions from an Aerovalve Pulse Combustor. *Fall Technical Meeting of the Eastern Section of the Combustion Institute*, 1993.
- [71] K. Oberleithner and C. O. Paschereit. Low Amplitude Excitation of Moderately Swirling Jets at High Reynolds Numbers. *47th AIAA Aerospace Sciences Meeting*, (AIAA 2009-577), 2009.
- [72] F. Ostermann, R. Woszidlo, S. Gaertlein, C. Nayeri, and C. O. Paschereit. Phase-Averaging Methods for a Naturally Oscillating Flow Field. In *52nd Aerospace Sciences Meeting*, Reston, Virginia, January 2014. American Institute of Aeronautics and Astronautics. ISBN 978-1-62410-256-1. doi: [10.2514/6.2014-1142](https://doi.org/10.2514/6.2014-1142).
- [73] D. E. Paxson. A Simplified Model for Detonation Based Pressure-Gain Combustors. *46th AIAA/ASME/SAE/ASEE Joint Propulsion Conference & Exhibit*, (AIAA 2010-6717), July 2010. doi: [10.2514/6.2010-6717](https://doi.org/10.2514/6.2010-6717).
- [74] P. C. Perera and N. Syred. A coanda switch for high temperature gas control. *American Society of Mechanical Engineers, Winter Annual Meeting*, (Paper 83-WA/DSC-26), 1983.
- [75] E. Phillips, R. Woszidlo, and I. Wygnanski. The Dynamics of Separation Control on a Rapidly Actuated Flap. *5th Flow Control Conference*, (AIAA 2010-4246), 2010.
- [76] M. W. Plesniak and D. M. Cusano. Scalar mixing in a confined rectangular jet in crossflow. *Journal of Fluid Mechanics*, 524:1–45, February 2005. ISSN 0022-1120. doi: [10.1017/S0022112004001132](https://doi.org/10.1017/S0022112004001132).

- [77] A. A. Putnam, F. E. Belles, and J. A. C. Kentfield. Pulse combustion. *Progress in Energy and Combustion Science*, 12(1):43–79, January 1986. ISSN 03601285. doi: 10.1016/0360-1285(86)90013-4.
- [78] S. Raghu. Feedback-free fluidic oscillator and method. *United States Patent*, (US 6,253,782), 2001.
- [79] G. Raman and S. Raghu. Cavity resonance suppression using miniature fluidic oscillators. *AIAA Journal*, 42(12):2608 – 2611, 2004. doi: 10.2514/1.521.
- [80] G. A. Richards, J. Yip, R. S. Gemmen, M. C. Janus, T. Norton, and W. A. Rogers. Pressure-gain combustion. In *Joint contractors meeting on advanced turbine systems, fuel cells and coal-fired heat*, 1993.
- [81] G. D. Roy, S. M. Frolov, A. A. Borisov, and D. W. Netzer. Pulse detonation propulsion: challenges, current status, and future perspective. *Progress in Energy and Combustion Science*, 30(6):545–672, January 2004. ISSN 03601285. doi: 10.1016/j.pecs.2004.05.001.
- [82] F. Schauer, J. Stutrud, and R. Bradley. Detonation Initiation Studies and Performance Results for Pulsed Detonation Engine Applications. *39th AIAA Aerospace Sciences Meeting & Exhibit*, (AIAA 2001-1129), 2001.
- [83] R. Seele, P. Tewes, R. Woszidlo, M. A. McVeigh, N. J. Lucas, and I. J. Wygnanski. Discrete Sweeping Jets as Tools for Improving the Performance of the V-22. *Journal of Aircraft*, 46(6):2098–2106, November 2009. ISSN 0021-8669. doi: 10.2514/1.43663.
- [84] R. Seele, E. Graff, M. Gharib, L. Taubert, J. Lin, and I. Wygnanski. Improving Rudder Effectiveness with Sweeping Jet Actuators. *6th AIAA Flow Control Conference*, (AIAA 2012-3244), 2012.
- [85] N. C. Sher. Jet attachment and switching in bistable fluid amplifiers. *Fluids Engineering Conference*, (Paper-No. 64-FE-19), 1964.
- [86] S. H. Smith and M. G. Mungal. Mixing, structure and scaling of the jet in crossflow. *Journal of Fluid Mechanics*, 357:83–122, February 1998. ISSN 00221120. doi: 10.1017/S0022112097007891.
- [87] C. E. Spyropoulos. A Sonic Oscillator. *Harry Diamond Laboratories Report*, pages 27–51, 1964.
- [88] RD Stouffer. Oscillating spray device. *United States Patent*, (US 4,151,955), 1979.

- [89] L. Taubert and I. Wygnanski. Preliminary Experiments Applying Active Flow Control to a 1/24 th Scale Model of a Semi-Trailer Truck. *The Aerodynamics of Heavy Vehicles II: Trucks, Buses and Trains*, 41:105–113, 2009.
- [90] V. Tesař. A mosaic of experiences and results from development of high-performance bistable flow-control elements. In *Process control by power fluidics*, Sheffield, Great Britain, 1975.
- [91] V. Tesař. Fluidic Control of Molten Metal Flow. *Acta Polytechnica*, 43(1): 15–22, 2003.
- [92] V. Tesař. Fluidic Valves for Variable-Configuration Gas Treatment. *Chemical Engineering Research and Design*, 83(9):1111–1121, September 2005. ISSN 02638762. doi: 10.1205/cherd.04283.
- [93] V. Tesař. No-moving-part valve for automatic flow switching. *Chemical Engineering Journal*, 162(1):278–295, August 2010. ISSN 13858947. doi: 10.1016/j.cej.2010.04.028.
- [94] V. Tesař and H. C. H. Bandalusena. Bistable diverter valve in microfluidics. *Experiments in Fluids*, 50(5):1225–1233, October 2010. ISSN 0723-4864. doi: 10.1007/s00348-010-0983-0.
- [95] V. Tesař, C. Hung, and W. B. Zimmerman. No-moving-part hybrid-synthetic jet actuator. *Sensors and Actuators A: Physical*, 125(2):159–169, January 2006. ISSN 09244247. doi: 10.1016/j.sna.2005.06.022.
- [96] N. Tesla. Valvular Conduit. *United States Patent*, (US1920-1,329,559), 1920.
- [97] P. Tewes, L. Taubert, and I. Wygnanski. On the Use of Sweeping Jets to Augment the Lift of a Lambda-Wing. *28th AIAA Applied Aerodynamics Conference*, (AIAA 2010-4689), 2010.
- [98] D. Thoma. Fluid Lines. *United States Patent*, (US 1,839,616), 1929.
- [99] O. Uzol and C. Camci. Experimental and computational visualization and frequency measurements of the jet oscillation inside a fluidic oscillator. *Journal of Visualization*, 5(3):263–272, 2002. doi: 10.1007/BF03182334.
- [100] V. N. Vatsa, M. Koklu, I. J. Wygnanski, and E. Fares. Numerical Simulation of Fluidic Actuators for Flow Control Applications. *6th AIAA Flow Control Conference*, (AIAA 2012-3239), 2012.
- [101] H. Viets. Flip-Flop Jet Nozzle. *AIAA Journal*, 13(10):1375–1379, October 1975. ISSN 0001-1452. doi: 10.2514/3.60550.

-
- [102] R. W. Warren. Some parameters affecting the design of bistable fluid amplifiers. In *Fluid Jet Control Devices; Papers presented at the winter annual meeting of the ASME*, pages 75–82, 1962.
- [103] R. W. Warren. Fluid Oscillator. *United States Patent*, (US1962-3,016,066), 1962.
- [104] R. P. Weston and F. C. Thames. Properties of aspect-ratio-4.0 rectangular jets in a subsonic crossflow. *Journal of Aircraft*, 16(10):701–707, 1979. doi: [10.2514/3.58592](https://doi.org/10.2514/3.58592).
- [105] E. Wintenberger and J. E. Shepherd. Thermodynamic Cycle Analysis for Propagating Detonations. *Journal of Propulsion and Power*, 22(3):694–698, May 2006. ISSN 0748-4658. doi: [10.2514/1.12775](https://doi.org/10.2514/1.12775).
- [106] P. Wolański. Detonative propulsion. *Proceedings of the Combustion Institute*, 34(1):125–158, January 2013. ISSN 15407489. doi: [10.1016/j.proci.2012.10.005](https://doi.org/10.1016/j.proci.2012.10.005).
- [107] R. Wozidlo. *Parameters Governing Separation Control with Sweeping Jet Actuators*. PhD thesis, The University of Arizona, 2011.
- [108] T. Young. Outlines of Experiments and Inquiries Respecting Sound and Light (In a Letter to Edward Whitaker Gray, M. D. Sec. R. S). *Philosophical Transactions of the Royal Society of London*, 90:106–150, 1800.